UNIVERSITY OF OKLAHOMA
GRADUATE COLLEGE

SPATIAL FILTERING OF CLUTTER USING PHASED ARRAY RADARS FOR OBSERVATIONS OF THE WEATHER

A DISSERTATION
SUBMITTED TO THE GRADUATE FACULTY
in partial fulfillment of the requirements for the
Degree of
DOCTOR OF PHILOSOPHY

By

KHOI LE
Norman, Oklahoma
2009

SPATIAL FILTERING OF CLUTTER USING PHASED ARRAY RADARS FOR OBSERVATIONS OF THE WEATHER

A DISSERTATION APPROVED FOR THE
SCHOOL OF ELECTRICAL AND COMPUTER ENGINEERING

BY

Dr. Robert Palmer

Dr. Evgeni Fedorovich

Dr. Sebastian Torres

Dr. Tian-You Yu

Dr. Mark Yeary

Dr. Dusan Zrnic

Acknowledgments

The completion of this dissertation was only achieved with the assistance of many individuals, for which I am sincerely thankful and grateful of:

Personally, I would like to thank my parents (Khien V. Le and Thanh T. Pham) for their unwavering support and complete belief in me even though, for the most part, they only know that I am some sort of engineer. Yet, they still and will love me for who I was, who I am, and who I will become. It is then with tremendous honor that I dedicate this dissertation to them so that it will be forever documented of their sacrifices for me. Next, I would like to thank my brothers and sisters (Dung, Khoa, Hanh, and Khang). I hope that, with this work, they can physically grasp and will optimistically dream of the possibilities that their sons and daughters can become. With some brain power, luck, good friends, and a lot of hard work, I believe that everything is possible. I would also like to thank my advisor, Bob Palmer, for his love of me, his belief in me, and the opportunities that he has created for me. I know that without his help and patience, none of this would have happened. I would only hope that my future works reflect well on him and that he will be honored by me, both professionally and as an individual. Finally, I would like to thank my best friends, Pin-Lin Fang and Boon-Leng Cheong, for being my friends.

Professionally, I would like to thank my committee members: Dr. Robert Palmer, Dr. Evgeni Federovich, Dr. Sebastian Torres, Dr. Tian-You Yu, Dr. Mark Yeary, and Dr. Dusan Zrnic. I would also like to acknowledge that my research was funded by the NSSL (grant `NA17RJ1227`), and that Steven Frasier, F. Lopez-Dekker, and Mike Hoffman contributed to the original TEP data that I used. Finally, I would like to thank the staff at the SOM, the ARRC (in particular, Kristyn Bailey and Krysta Bruehl), and the ECE office (Lynn Hall) for their assistance in the little things.

Contents

List Of Tables

List Of Figures

Abstract

Phased array radars are attractive for weather surveillance primarily because of their capacity for extremely rapid scanning through electronic steering. When combined with the recently developed beam multiplexing technique, these radars can provide significantly improved update rates, which are necessary for monitoring rapidly evolving severe weather. A consequence of beam multiplexing, however, is that a small number of contiguous time series samples are typically used, creating a significant challenge for temporal/spectral filters typically used for clutter mitigation. As a result, the accurate extraction of weather products can become the limiting performance barrier for phased array radars that employ beam multiplexing in clutter-contaminated scattered fields. By exploiting the spatial correlation among the signals from the elements of the phased array antenna, the effect of clutter contamination can be reduced through a processed called *spatial filtering*. In contrast to conventional temporal filtering, spatial filtering is used to adaptively adjust the antenna beam pattern to produce lower gain in the directions of the undesired clutter signals. In this dissertation, the effect of clutter mitigation using spatial filtering was studied using numerical simulations of a tornadic environment and an array antenna configuration similar to the NSSL NWRT Phased Array Radar for changes in signal-to-noise ratio, clutter-to-signal ratio, number of time series samples, and diagonal loading for three types of clutter sources that include nearly stationary ground clutter, moving targets such as aircraft, and wind turbine clutter, which has recently been documented to be increasingly problematic for radars. Since such data are not currently available from a horizontally pointed phased array weather radar, experimental validation was applied to an existing data set from the Turbulent Eddy Profiler (TEP) developed at University of Massachusetts, which is a vertically pointed phased array radar. Results will show that spatial filtering holds promise for the future of phased array radars for the observation of the weather in a clutter environment.

Chapter 1

Observing the Atmosphere Using Radars

1.1 The Atmosphere: A Brief Review

The atmosphere is composed of a mixture of gases that surrounds the earth (Wallace and Hobbs 1977; Lutgens et al. 1979; Miller et al. 1983; Ahrens et al. 2001). The vertical temperature profile shown in Figure 1.1 for the standard condition reveals that the atmosphere has five distinct layers. The lowest layer, called the troposphere, is characterized by surface heating and a decreasing vertical temperature, which results in instability and favorable conditions for convection. The next layer starts at approximately 20 km and is called the stratosphere. The layer has a temperature profile that increases with height as a result of elevated concentration of ozone gas at approximately 35 km. Near the top of the atmosphere are the mesospheric and thermospheric layers, where space debris attracted by the gravitational field of the earth are ablated and atmospheric gases with low densities are observed. While additional atmospheric layers beyond these heights exist, most of the important processes that do occur are localized within these five layers.

The mixture of gases found within the atmosphere are either *permanent* or *variable*. The average contribution of each constituent near the surface as measured in terms of percentage of the total volume is listed in Table 1.1. Nitrogen and oxygen gases are the primary constituents, and are *permanent* constituents that combine to contribute approximately 99% of the total volume. The primary *variable* constituent is water vapor and it contributes up to 4% of the total volume. Even though water vapor contributes to only a small percentage to the atmospheric volume, it is a constituent of the atmosphere that is responsible for weather in the tropospheric layer due to its capability to transport energy in the form of phase change through latent heat release/absorption.

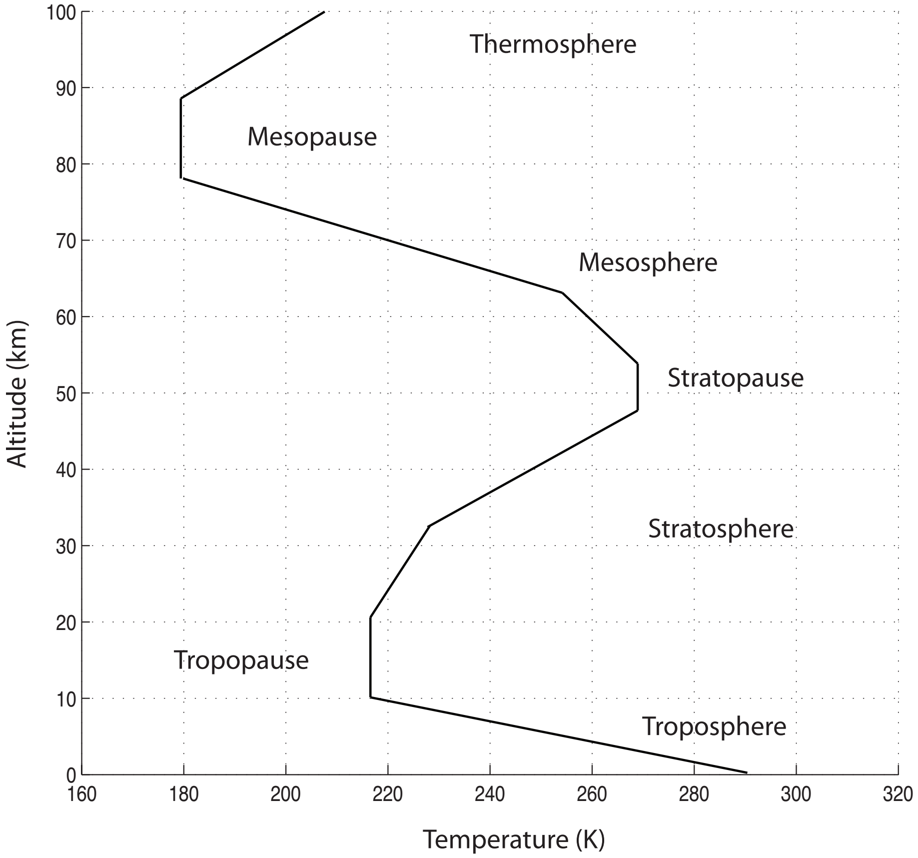

Figure 1.1: Profile of air temperature (Wallace and Hobbs 1977). The atmosphere is a mixture of gases that is mostly concentrated near the surface. Its structure can be revealed using a vertical profile of the air temperature.

Table 1.1: Atmospheric Composition (measured at sea surface level in % volume) (Miller et al. 1983)

Permanent Constituents (averaged concentrations)		Variable Constituents	
Nitrogen	78.08	Water vapor	< 4
Oxygen	20.95	Ozone	$<0.07 \times 10^{-4}$
Argon	0.93	Sulfur dioxide	$<1 \times 10^{-4}$
Carbon dioxide	0.032	Nitrogen dioxide	$<0.02 \times 10^{-4}$
Neon	18.2×10^{-4}	Ammonia	Trace
Helium	5.24×10^{-4}	Carbon monoxide	0.2×10^{-4}
Krypton	1.14×10^{-4}	Dust	$< 10^{-5}$
Xenon	0.087×10^{-4}	Water	< 1
Hydrogen	0.5×10^{-4}		
Methane	1.5×10^{-4}		
Nitrogen Oxide	0.5×10^{-4}		
Radon	6×10^{-18}		

1.2 Radars for Sensing the Atmosphere

Radars use radio frequencies to scatter energy from distinct targets such as hydrometeors or from inhomogeneities in the refractive index, and are one of the many instruments used to observe the atmosphere (Lutgens et al. 1979; Ahrens et al. 2001; Wallace and Hobbs 1977; Miller et al. 1983). For atmospheric applications, radars provide observations of the scatterers at very high temporal and spatial resolutions and are generally very sensitive to the scatterers. There are at least three types of radars: (1) precipitation radars, (2) cloud radars, and (3) radars for sensing the clear-air. Detailed reviews of various radar types are provided in Harper and Gordon (1980); Balsley and Gage (1980); Kropfli (1981); Chadwick and Gossard (1983); Atlas (1990); Doviak and Zrnić (1993). In this section, a short discussion is provided of atmospheric radars.

1.2.1 Precipitation Radars

Precipitation radars generally operate with frequencies between 3 and 10 GHz, transmit with peak power from a few hundred kilowatts to several megawatts, and typically use a rotating parabolic antenna. These radars provide observations of any liquid or solid water particles (Wallace and Hobbs 1977; Lutgens et al. 1979; Miller et al. 1983; Ahrens et al. 2001). Measurements provided by precipitation radars are important because precipitation is an indicator of accumulating water vapor and the later stages of cloud formation (Miller et al. 1983).

Some of the earliest precipitation radars constructed prior to the 1950s were built from excess military parts. The early radars were crude and measured only the scattered power. An example of an early precipitation radar is the AN/APQ-13, which was an improved version of the British H2S radar that was used during WWII to map the ground (Guerlac 1987). The AN/APQ-13 was employed after the war as the first "weather radar" (Whiton et al. 1998). Another example of an early precipitation radar is the AN/APS-2F that used S-band and transmitted approximately 50 kW of peak power. The AN/APS-2F used the acronyms WSR-1, WSR-1a, WSR-3, and WSR-4 that stood for Weather Surveillance Radars.

The first radars designed and developed for observing the weather were the AN/CPS-9 Storm Detection radars (Whiton et al. 1998). The AN/CPS-9 radars, pictured in Figure 1.3(a), were engineered by the Signals Corps Engineering Laboratories in Belmar, New Jersey and manufactured by the Raytheon Manufacturing Company. Compared to the AN/APQ-13 and AN/APS-2F, the AN/CPS-9 was much more sensitive and performed better. 56 AN/CPS-9 were installed at military bases worldwide between 1953 and 1954 (Whiton et al. 1998).

The technology of precipitation radars up to the early 1950s was in the early stages, and the network that comprises these radars was sparse (Rockney and Jay 1953; Battan 1962; Bigler et al. 1962). As a result, key features of synoptic systems that lead to significant damages without warnings were often undetected. In the late 1950s, the federal government allocated funding to develop a dense network of radars that led to the development of WSR-57. These radars, shown in Figure 1.3(b), were more sensitive than their predecessors and could provide long range surveillance up to approximately 900 km. The design of the WSR-57 was completed by 1957, and the first radar was installed in Miami, Florida in 1959.

Approximately 20 years later in 1976, the Weather Bureau, now renamed the National Weather Service (NWS), received additional funding to replace 82 aging local radars (Whiton et al. 1998). The NWS used the funding to develop the WSR-74C and WSR-74S. As development of the WSR-74C and WSR-74S were made, a major effort was made to incorporate measurements of Doppler velocity as advances in

Figure 1.2: Distribution of radars operated by Weather Bureau in 1953 (Rockney and Jay 1953). The network of radars consisted mainly of AN/APS-2F and was used to provide observations of severe weather. Due to the geographical setup of these radars, the network mainly provided surveillance only to the eastern half of the continental United States.

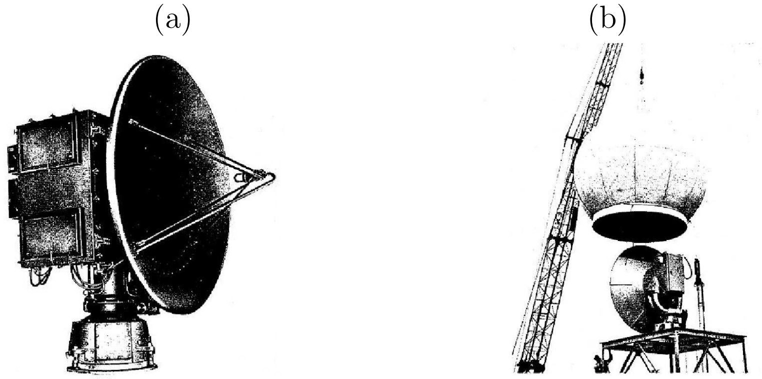

(a) (b)

Figure 1.3: (a) AN/CPS-9 and a (b) WSR-57 (Battan 1962). Two of the earliest radars used for monitoring precipitation. Designed and developed in between the 1940s and 1950s, these early radars demonstrated the potential of using radars to observe potentially damaging severe weather.

Figure 1.4: Distribution of WSR-57 radars operated by the Weather Bureau in 1962 (Bigler et al. 1962). With the addition of the AN/CPS-9, the radar network of the Weather Bureau in 1962 became more dense. However, its coverage capability was still limited, and was still mainly focused on the central plains and the eastern coast.

semiconductor fabrication and signal processing (namely the R-meter (Rutkowski and Fleisher 1955), fast Fourier transform (Cooley and Tukey 1965), pulse pair processor (Rummler 1968), and color displays (Jagodnik et al. 1975; Gray et al. 1975)) made it possible to incorporate the Doppler velocity capability. Additionally, the Departments of Commerce, Defense, and Transportation combined efforts and between 1977-1979 conducted a large-scale operation to investigate the possibility of using real-time Doppler observations to provide surveillance of tornadic storms (Brown and Lewis 2005). Doppler radars from the National Severe Storms Laboratory (NSSL) and the Air Force Geophysics Laboratory were used to provide observations that showed tornado warnings lead time could be enhanced by up to 21 min when Doppler was used. As a result, the Joint System Program Office in 1980 recommended that a network of S-band radars with Doppler capabilities be acquired. This led to the Next-Generation Radars (NEXRADs) network, which is a collection of modern surveillance radars. The NEXRAD network consists of 158 S-band radars with Doppler capability, and the positions of these radars are shown in Figure 1.5.

Figure 1.5: Distribution of radars operated by the NWS in 2009 (`roc.noaa.gov`). Located in all 50 states and consisting of 158 sensitive S-band Doppler radars, the current network operated by the National Weather Service aims to provide surveillance, forecasts, and warnings of all severe weather events.

Since the milestone of Doppler capability, radar development has focused on obtaining polarimetric measurements to improve hydrometeor classification and precipitation estimation (Zrnić and Ryzhkov 1999). A large campaign, called the Joint Polarization Experiment (JPOLE), was conducted in 2003 to collect precipitation data from 98 weather events. The NSSL Cimarron and NWS KTLX, KINX, KVNX, and KFDR WSR-88D radars, as well as rain gauges from the Oklahoma Climate Survey Mesonet and ARMS Micronet (Ryzhkov et al. 2005), were used to collected the data as well as two hail-intercept vehicles from the South Dakota School of Mines and Technology and upper air data. The results of this campaign showed that improved rainfall estimation, data quality, hydrometeor discrimination could be obtained by using polarimetric radars (Scharfenberg et al. 2005).

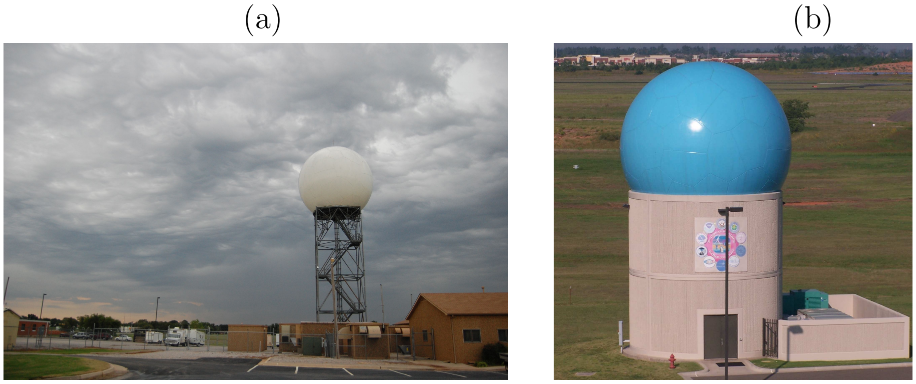
(a)

(b)

Figure 1.6: (a) NSSL Polarimetric Radar (courtesy of Boon-Leng Cheong) and (b) NWRT PAR (courtesy of Adam Smith). Used primarily for developing and testing weather algorithms, these two radars are located in the NSSL Oklahoma testbeds. The improvements made using these radars are then transferred to the operational NWS WSR-88D radars.

Despite past successes, modern radars are still mechanically driven and are bounded by these limitations (Weber et al. 2007; Zrnić et al. 2007). One of the primary problem is the limited scanning strategies that cannot be easily adapted to rapidly evolving weather phenomena, but can be overcome by using a phased array radar (Weber et al. 2007; Zrnić et al. 2007). As a result, a phased array radar (PAR) located at the National Weather Radar Testbed NWRT) in Norman, Oklahoma is being currently demonstrated. The NWRT PAR was developed by a government/university/industry team consisting of the National Oceanic and Atmospheric Administration's National Severe Storms Laboratory, the Tri-Agencies' (Department of Commerce, Defense & Transportation) Radar Operations Center (ROC), the United States Navy's

Office of Naval Research, Lockheed Martin Corporation, the University of Oklahoma's Electrical Engineering Department and School of Meteorology, the Oklahoma State Regents for Higher Education, and the Federal Aviation Administrations William J. Hughes Technical Center (Forsyth et al. 2002). The NWRT PAR, pictured in Figure 1.6(b), consists of a converted U.S. Navy SPY-1A phased array antenna, a modified WSR-88D transmitter, and a custom-designed controller-processor (Forsyth et al. 2002; Zrnić et al. 2007; Forsyth et al. 2007). Additionally, improvements such as incorporating the Matrix PC, Real Time Controller, Uninterruptible Power Source, multi-channel receiver, data visualization tools, along with algorithm development have been implemented to the radar (Forsyth et al. 2008). Additionally, other advanced radars such as the Naval Post Graduate School and ProSensing, Inc. (PopStefanija et al. 2005) radar, Collaborative Adaptive Sensing of the Atmosphere (CASA) radars, and the TRMM shown in Figure 1.7 can be used to overcome the limitations imposed by conventional dish radars. Compared to the NWRT PAR, these radars aim to provide close-up and above surface observations of the weather.

1.2.2 Radars for Measuring Features of Clouds

Cloud radars generally operate at millimeter wavelengths and transmit with peak powers ranging from a few kilowatts to hundreds of kilowatts (Pazmany et al. 1994; Mead et al. 1994; Moran et al. 1998). They are directed vertically and provide observations of the clouds as the clouds propagate across the radar beam. The measurements are important as they provide insight into the early stages of cloud formation (Miller et al. 1983). Additionally, the data are useful for both weather and climatological observations.

The earliest cloud radars were the AN/TPQ-6, AN/TPQ-11, and APS-34. These radars were built between 1940 and 1960 using surplus military parts. The radars operated between 28 GHz and 35 GHz and used a bistatic configuration with a spatially separated transmitter and receiver. While data that were obtained were useful, the radars often unreliable. As a matter of fact, the hardware problem eventually halted the development and research of cloud radars between the 1960s and 1970s (Kollias et al. 2007).

Resurgence of cloud radars eventually came about in the 1980s and were led by Pasqualucci et al. (1983), Hobbs et al. (1985), and Lhermitte (1987). While still built using excess military parts, these radars were more reliable. The radar built by Pasqualucci et al. (1983) is shown in Figure 1.8(a) and consisted of two spatially

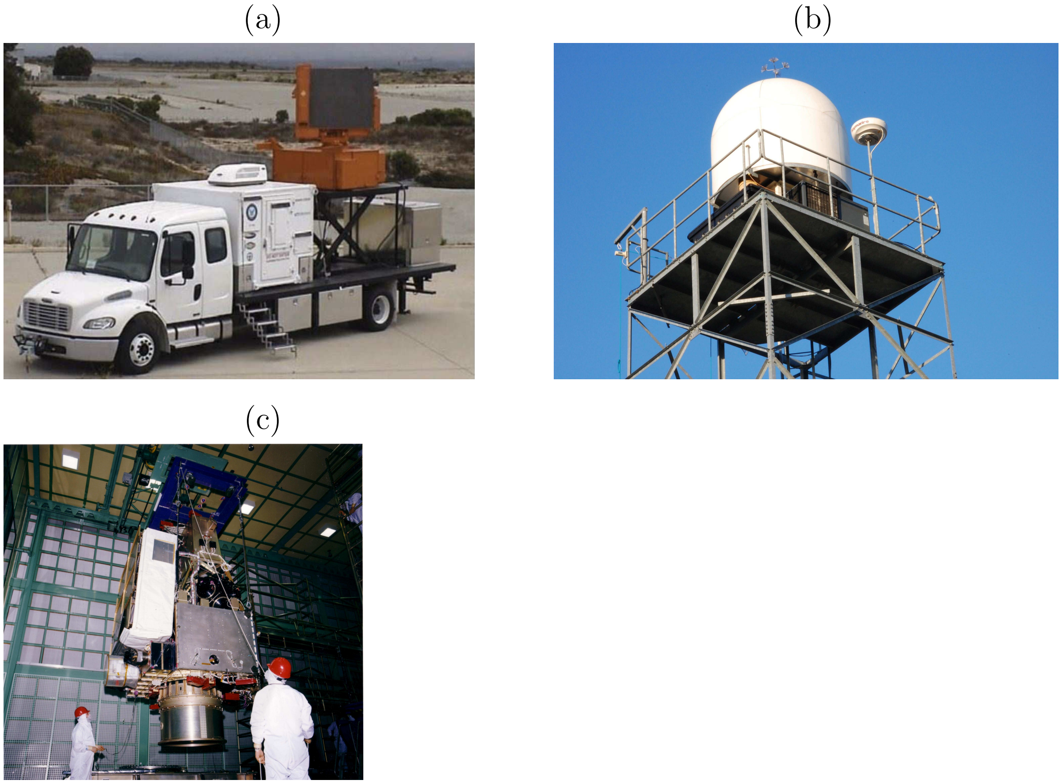

Figure 1.7: Examples of future platforms that can be used to provide surveillance of the weather: (a) Naval Post Graduate mobile phased array (PopStefanija et al. 2005), (b) CASA (courtesy of Boon-Leng Cheong), and (c) TRMM (`trmm.gsfc.nasa.gov`). By observing the weather from a different perspective as compared with the current NWS WSR-88D network of radars, these devices offer the possibility of additional observations and enhanced coverage.

separated Cassegrainian antennas that were individually used for transmission and receiving. The whole system was capable of transmitting up to 160 kW of peak power, and was used to collect data on the kinematic and microphysics of clouds during the 1981 Cooperative Convective Precipitation Experiment in Montana. The radar built by Hobbs et al. (1985) was a modified version of the military AN/TPQ-11 and had Doppler capability. However, its setup was similar to the one of Pasqualucci et al. (1983). Lhermitte (1987), on the other hand, was the first to construct a cloud radar that operated at 94 GHz. The radar, shown in Figure 1.8(b), was also bistatic and transmitted only 1 kW of peak power.

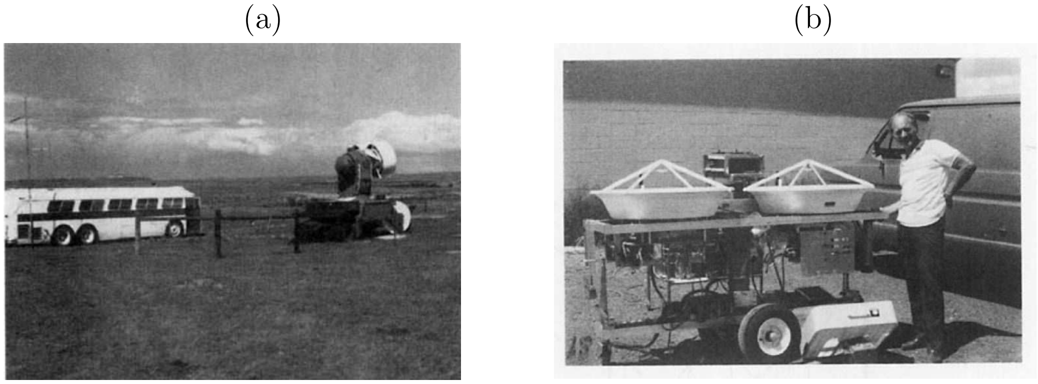

Figure 1.8: Two early radars that were used to provide sensing of clouds: (a) 35 GHz (Pasqualucci et al. 1983) (b) and 94 GHz (Lhermitte 1987) cloud radars. While providing the first observations of clouds, these devices were plagued with reliability issues.

Since the construction of these three radars, many cloud radars have since been designed and built (Mead et al. 1994; Kollias et al. 2007) including instruments such as the Advanced Multi-Frequency (AMF) and CloudSAT, as examples. The AMF shown Figure 1.9(a) was developed by the University of Massachusetts in 2001 and operates at 13.4, 35.6 and 94.9 GHz (Sekelsky 1995). Additionally, it uses a Klystron amplifiers over the traditional magnetron amplifier and transmits simultaneous H-V over the three frequencies. Another cloud radar shown in Figure 1.9(b) observes the clouds from an altitude of 705 km and operates at 94 GHz. The radar was jointly developed by NASA, JPL, the Canadian Space Agency, Colorado State University, and the US Air Force (Im et al. 2005). The radar is primarily used to improve the understanding and impact of clouds on climate change.

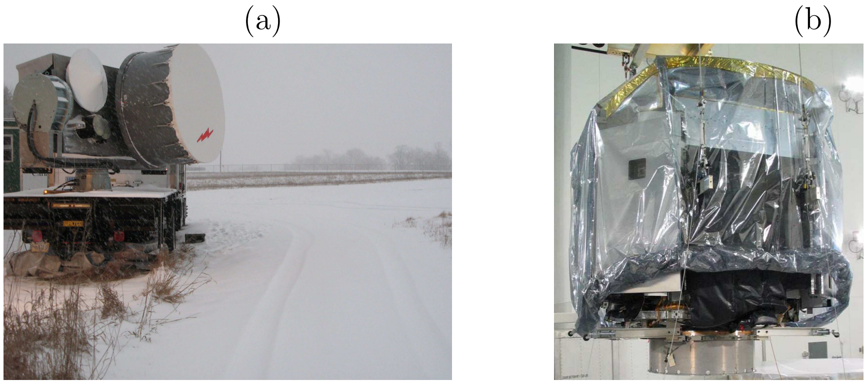

Figure 1.9: Modern radars used for sensing clouds: (a) AMF (`mirsl.ecs.umass.edu`) and (b) CloudSAT (`jpl.nasa.gov`). Some use multiple frequencies and are able to provide particle size distribution.

1.2.3 Radars for Sensing the Clear-Air Environment

Refractive index variations in the atmosphere, caused by gradients in temperature and moisture, can be sensed using radio frequencies by instruments called wind profilers (Martner et al. 1993; Rogers et al. 1993; Gage et al. 1994). These instruments are radars that typically operate at UHF and VHF frequencies and transmit with powers ranging from a few kilowatts to as high as a few megawatts. The data that can be obtained provide estimates of the 3-D wind and are useful in forecasting to infer regions of moisture convergence.

Some of the earliest wind profilers were Mesosphere-Stratosphere-Troposphere (MST) radars that were used to observe the middle and upper regions of the atmosphere. Some of these radars include the Jicamarca, SUNSET, SOUSY, Poker Flat, and the Middle and Upper (MU) radars. One such radar is the fixed-beam phased array located in Jicamarca, Peru. The radar, pictured in Figure 1.10(a) (`jicamarca.ece.cornell.edu`), operates at 50 MHz and consists of an antenna array with 18,432 half-wave dipoles. The array is arranged into 64 separate modules of 12 x 12 crossed half-wave dipoles and phasing of each module is achieved by changing its cable length. Another early profiling radar was the SUNSET radar located in Sunset, Colorado (Figure 1.10(a)). The radar was used to observe the mesosphere-stratosphere-troposphere (MST) and stratosphere-troposphere (ST) and consists of an array of 16 north-south lines of 12 half-wave dipoles (Green et al. 1975). Another early radar was the SOUSY radar located in the Harz mountains of Germany, which operated at 53.5 MHz and had an antenna array that consisted of 196 Yagi elements (Czechowsky et al. 1976). Other radars include the Poker Flat and the MU radars.

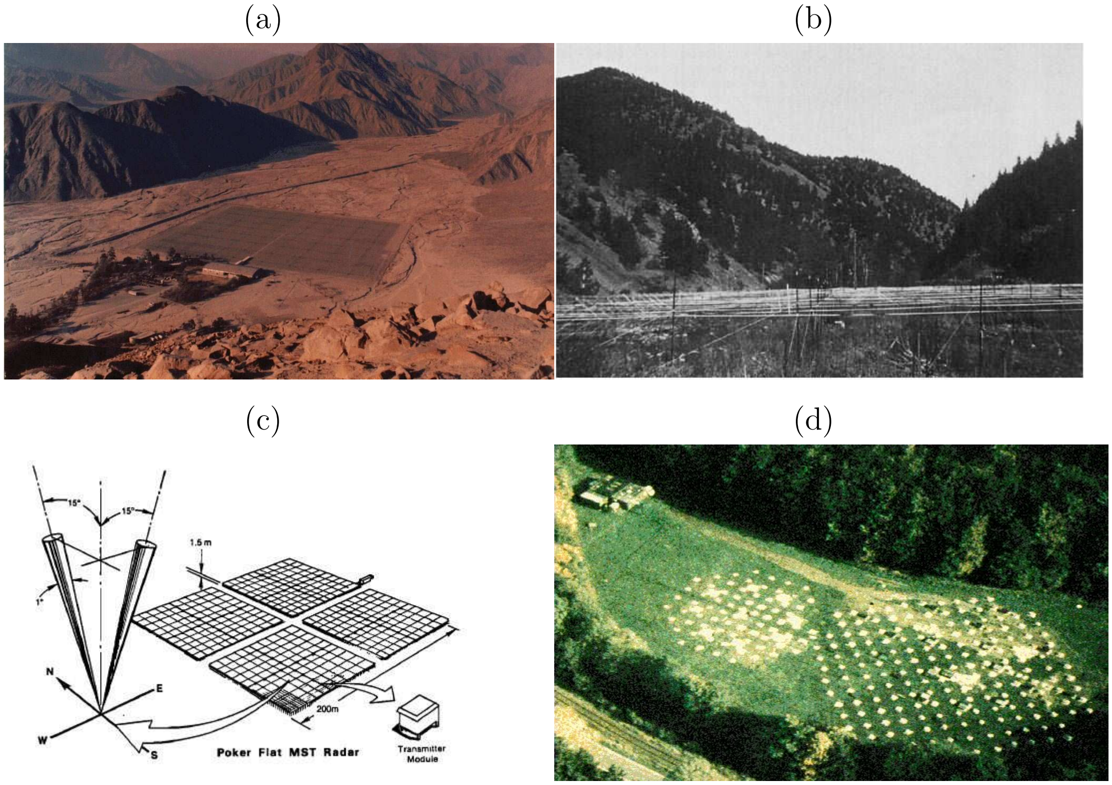
(a)
(b)
(c)
(d)

Figure 1.10: Some examples of wind profiling radars: (a) Jicamarca, Peru, (b) SUNSET (Gage and Balsley 1978), (c) Poker Flat (Balsley et al. 1980) and (d) SOUSY (`www.rssd.esa.int`). These radars collected many of the early data sets on wind flow and operated mainly using a mechanical phase shifting network for beamforming.

The Poker Flat radar, located in Alaska, operates at 49.9 MHz and has an antenna composed of 32 separate coaxial collinear elements. It is used to provide measurements of the wind up to 80 km. The MU radar, pictured in Figure 1.11, operates at 46.5 MHz and has an antenna that consists of 475 Yagi elements (Fukao et al. 1980). It is considered one of the most advanced wind profilers in the world.

Figure 1.11: Middle and Upper atmospheric radar (`www-lab26.kuee.kyoto-u.ac.jp`). Located in Kyoto, Japan, the device shown is considered one of the most advanced wind profilers of its kind with a received antenna that consists of 475 Yagi elements. The radar is used to investigate atmospheric phenomena and plasma dynamics that occur at high altitudes.

Other wind profiling radars such as the NOAA Profiling Network (NPN) (Weber et al. 1990), the Turbulent Eddy Profiler (Mead et al. 1998), and the active phased array described in Hashiguchi et al. (2004) observe only the lowest several kilometers. The NPN is located across the continental United States and consists of a total of 37 Doppler radars that operate at 404 MHz and 449 MHz. Data obtained by the NPN radars are used for forecasting the weather and inputs into numerical weather prediction models. The Turbulent Eddy Profiler is pictured in Figure 1.13 and is a digital beamforming phased array radar (Mead et al. 1998; Palmer et al. 2005; Cheong et al. 2006). The transmit antenna is a horn antenna that illuminates a large 20° swath and the receive antenna consists of an array of microstrip-elements.

Figure 1.12: NPN Profilers (`profiler.noaa.gov`). Located mainly in the continental United States, this network of vertically pointing radars provides hourly estimates of the wind that are used for observation and forecasting the weather.

Hashiguchi et al. (2004) also presented an active radar that operates at 1.3 GHz, transmits with 2 kW of peak power, and has an antenna array that consists of 24 elements.

1.3 Radars and Clutter Contamination

Radar signals often contain *clutter* in addition to signals from desired atmospheric scatterers. In the atmospheric radar environment, typically clutter sources include the ground, birds, planes, and more frequently wind turbines. References to these clutter sources can be found in Sekine (1996); Bachmann (2008); Haykin et al. (1979, 1991); Doviak and Zrnić (1985); Durden et al. (2001); Rico-Ramirez and Cluckie (2008); Hanado and Ihara (1992); Billingsley (2002); Isom et al. (2009). The presence of the clutter biases the radar signal and masks the underlying weather features. As a result, the clutter signal is undesired and needs to be mitigated. In this section, some examples of clutter sources for weather radars (as weather is clutter in other radars) and clutter filtering methods are presented.

Figure 1.13: Turbulent Eddy Profiler (courtesy of Boon-Leng Cheong). This bistatic radar operated at 915 MHz and was used to investigate phenomena occurring in the boundary layer.

1.3.1 Contamination by Quasi-Stationary Clutter Sources

Quasi-stationary clutter sources, which are contamination caused by approximately stationary clutter, are some of the most pervasive sources of clutter (Long 2001; Billingsley 2002; Curtis 2009). Quasi-stationary clutter sources include buildings, trees, power lines, and non-atmospheric scatterers near the surface, as well as the ground itself. They are observed in the radar signal when the radar beam is steered near the ground or in conditions when the beam is bent toward the ground. They are generally characterized with high reflectivity values, near-zero Doppler velocities, and spectrum width values less than 0.3 ms^{-1} (Hubbert et al. 2009). The amplitude return is often modeled using a Rician distribution, while the spatial distribution is modeled using a Weibull distribution of the quasi-stationary ground clutter (Hubbert et al. 2009).

A model of radar returns from quasi-stationary ground clutter is shown in Figure 1.14. Based on empirical modeling of extensive ground clutter data collected with multiple radars in the Alberta region, the model uses three inter-dependent components (Billingsley 2002) to represent the observed spectrum. The DC component is centered at the zero velocity and is used to characterize the return from static scatterers; the quasi-AC component models the returns from wind blow scatterers and is located near the zero velocity; while the AC component is used to characterize the effects of clustering caused by wind blown scatterers.

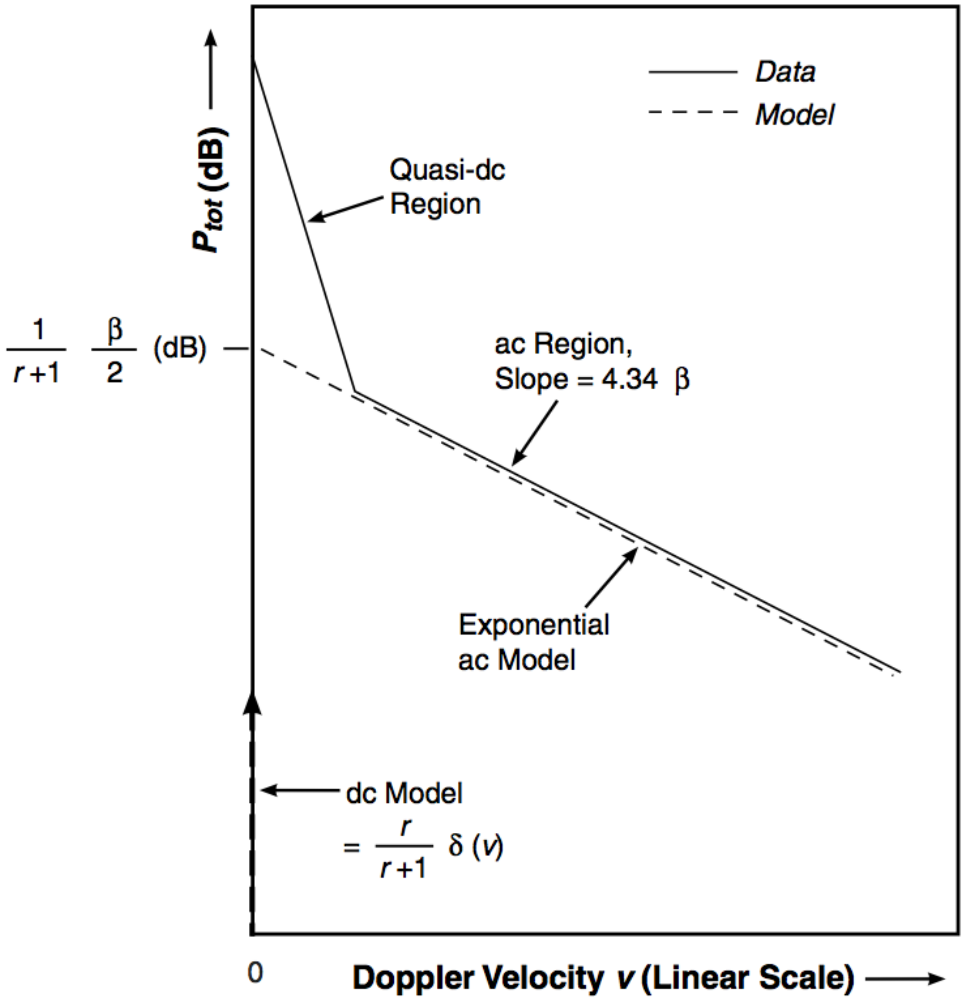

Figure 1.14: Quasi-stationary clutter model (Billingsley 2002). Constructed using empirical data, this model consists of three components that each describe a different spectral signature of the clutter.

1.3.2 Contamination by Non-Stationary Clutter Sources

Clutter can also be produced by *non-stationary* sources such as birds and insects. Birds generally are most active at sunrise and sunset and are found from the ground up to 1000 m. Birds typically flock in groups with densities that range from 10^{-7}-10^{-6} m^{-3} and increase up to 10^{-5} m^{-3} when large social groups are observed (Skolnik 2001). These scatterers generally fly in the same direction as the wind with speeds that can be up to 15 ms^{-1} faster (Martin and Shapiro 2007). Insects, on the other hand, typically fly closer to the surface with speeds that differ up to 5 ms^{-1}. While larger insects, such as grasshoppers and moths, are generally nocturnal, insects that are smaller often migrate during the day. Insects also travel in groups with densities that range from 10^{-5}-10^{-4} m^{-3} and increase up to 10^{-3}-10^{-4} m^{-3} when insects converge. While backscattered cross-sections for birds are not well understood, values of backscattered cross-sections for some insects are illustrated in Figure 1.15.

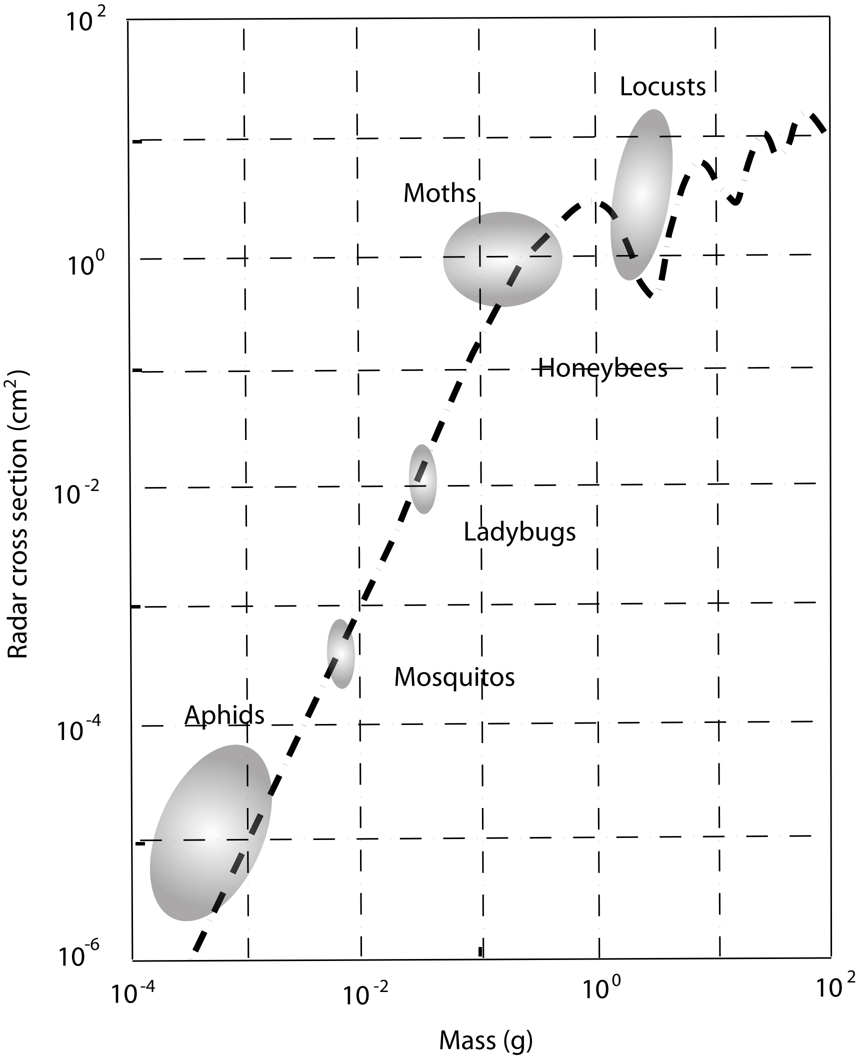

Figure 1.15: Radar cross-section of insects (Skolnik 2001). With values ranging from 10^{-5} to 10^1 cm^2, the radar cross-section of some common insect species are shown. They are present in both the Rayleigh and Mie scattering regimes of the radar.

Wind turbines, which consist of a tower, a nacelle, and typically three blades, are another source of non-stationary clutter. Generally, wind turbines are clustered into *wind farms* with hundreds of individual wind turbines. In the weather radar environment, wind farms typically produce return signatures that resemble isolated storms with large shear (Isom 2007; Isom et al. 2009). An example of a wind farm clutter signature is shown in Figure 1.16. The signature has reflectivity values on the order of the weather scatterers and appears similar to an isolated storm. With expected construction of many wind farms to meet the desired energy needs, the problem of wind turbine clutter is expected in the weather radar environment to become more problematic in the near future.

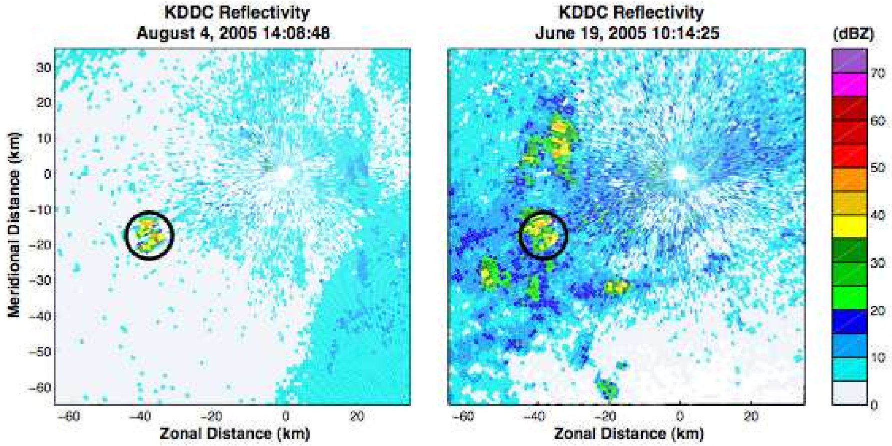

Figure 1.16: Contamination by wind farms (Isom et al. 2009). The scattering signature produced by these clutter sources resembles single celled storms.

1.4 Mitigation of Clutter Contamination

Contamination by clutter adversely affects the scattered signal by changing the expected moments of the desired signals (Haykin et al. 1991; Torres and Zrnić 1999; Billingsley 2002; Rico-Ramirez and Cluckie 2008). As a result, clutter mitigation is important for quality assurance and can be achieved by exploiting statistical differences between the weather and clutter, which include time, frequency, and location. Ideally, clutter is mitigated and the weather is preserved. In this section, some clutter mitigation schemes are presented.

1.4.1 Clutter Mitigation for Single-Receiver Radar Systems

Averaging Filtering: Strauch et al. (1984) presented a simple technique to remove speckle interferers in signals obtained from weather scatterers based on averaging alone. A block diagram of the filter used in this technique is shown in Figure 1.17. The filter exploits the temporal and spatial discontinuity of the interferers and the spectral and temporal continuity of returns by weather scatterers. The filter attenuates the clutter contamination by averaging over the spectral returns in which the intermittent clutter was observed while using a window with a short length to preserve the structure of the weather.

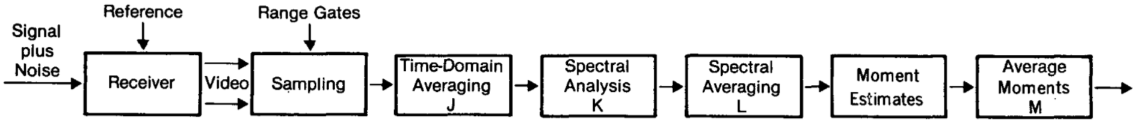

FIG. 1. Data processing steps for wind profiling Doppler radars.

Figure 1.17: Averaging filter (Strauch et al. 1984). A block diagram of an averaging filter is shown. It consists of a combination of temporal and spatial averaging schemes. These filters exploit the temporal and spatial correlation differences between the weather and clutter signals to remove the clutter.

Temporal Filtering: Temporal filtering such as finite impulse response (FIR) and infinite impulse response (IIR) filters can be used to remove clutter. The design of some of these techniques are discussed in Haykin (1996); Kay (1988); Oppenheim and Schafer (1989), among others. Depending on the clutter-to-signal ratio, these techniques may require long sample sizes that depend on the length of their impulse response. While generally useful, these filters are not practical for signals with small number of samples or non-contiguous samples collected by phased array systems.

Gaussian Model Adaptive Processing: Siggia and Passarell, Jr. (2004) presented an iterative technique for estimating the weather spectrum contaminated by ground clutter. An illustration of the filtering scheme is shown in Figure 1.18. The technique operates using a Hamming window to estimate the contaminated spectrum. The three points closest to the zero velocity of the spectrum are assumed to be the components of ground clutter, and the power of these three points is calculated. The other points are assumed to be from the weather return and their power is calculated as well. A clutter to weather signal ratio is then computed, and this value is used to determine whether a re-estimation of the contaminated spectrum is needed using a more aggressive window.

When it is determined that a sufficient window has been selected, a Gaussian model based on the weather spectral components is used to replace the three points that were removed. Operationally, only the Blackman window is used to estimate the spectral component and adaptive windowing was shown to not work properly.

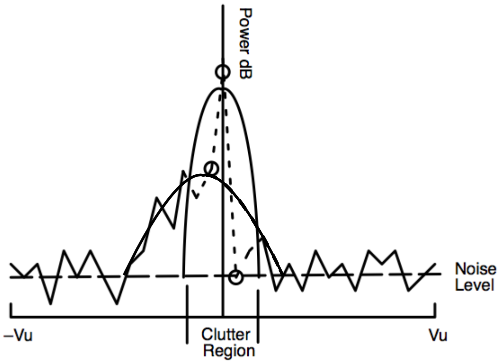

Figure 1.18: Gaussian Model Adaptive Processing (Siggia and Passarell, Jr. 2004). A spectral ground clutter filter is shown, which uses an iterative technique to replace the central three spectral components with estimates of the weather spectra via a Gaussian model. Values of the weather spectra are obtained through a series of windowing applications and Gaussian fits.

Spectral Filtering: Bachmann and Zrnić (2008) presented a technique that uses adaptive spectral processing to remove weather radar data contaminated by bird clutter; an example of a spectrum with bird clutter is shown in Figure 1.19. The technique first uses a Blackmann-exact window to estimate the contaminated power spectrum. After the velocity of the bird clutter sources are located, spectral notches are then placed at these locations to remove the contamination. Additionally, Cornman et al. (1998) presented a fuzzy logic technique to obtain the moments of the weather contaminated for a variety of clutter sources. The approach uses a combination of fuzzy logic and image processing to determine the location of the weather. The moments of the weather scatterers are then estimated using many membership functions and image processing techniques. Additionally, a confidence value of each retrieved moment is also provided that can be used as a censoring measure. An example is presented in Figure 1.20 of some results.

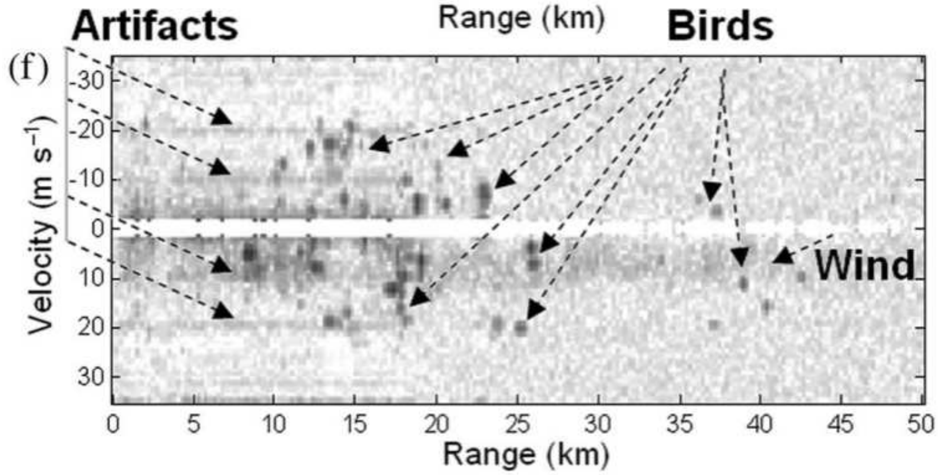

Figure 1.19: Spectrogram with birds in clear-air (Bachmann and Zrnić 2008). A bird clutter filter is shown. The technique uses a spectral approach to estimate the Doppler velocity of the bird contaminant. The power of the bird clutter at these locations are then replaced with notches in the spectrum.

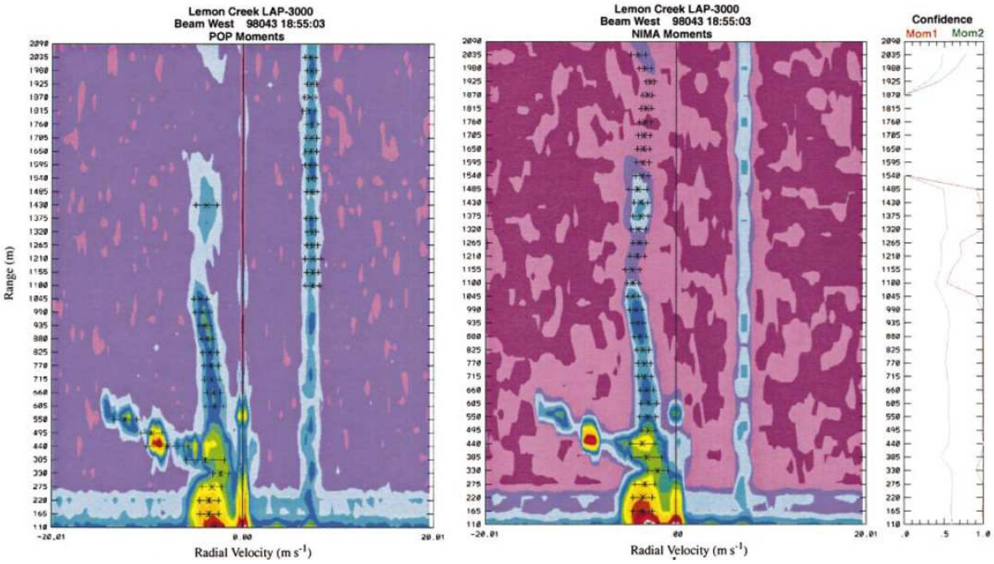

Figure 1.20: Spectrogram with clutter scattering using a boundary layer radar (Morse et al. 20002). The original contaminated field and an overlay of the mean Doppler velocity and spectrum width moments obtained using conventional estimation techniques is shown in the left panel. At locations where there is dominant clutter, the moments are biased. On the right is the processed field overlaid with moments obtained using a fuzzy logic filtering scheme and their corresponding confidence intervals. The moments obtained using this technique is more visibly reasonable compared to the results obtained using the conventional estimation technique.

Wavelet Filtering: Jordan et al. (1997) presented a technique for filtering ground and intermittent clutter using wavelet analysis. The two-step process involves the application of the wavelet clutter filter in both the temporal and spatial domains, and was used to remove contamination from ground and moving clutter. In the first step, a Daubecies 20 wavelet was used to decompose the contaminated signals, and the ground clutter was removed by replacing the slow moving harmonics with interpolated values of nearby weather scatterers. The filtered signal was then transformed back to the time domain, and its spectral components were decomposed using another wavelet filter. This time, the fast moving harmonics representative of moving clutter were replaced.

Regression Filtering: Torres and Zrnić (1999) presented a fitting scheme for removing contamination caused by ground clutter. The technique assumes that the time series signal of the ground clutter is slowly moving and that a low-order polynomial can be used to fit this contamination. A mean squared fit is used to obtain the coefficients of the polynomial, and the fitted ground clutter signature is then subtracted from the contaminated signal. The residual signal is then assumed to the the desired weather signal.

Parametric Time Domain Filtering: Nguyen et al. (2008) presented an iterative technique, illustrated in Figure 1.21, for retrieving weather signals contaminated by ground clutter. The technique uses two Gaussian models: a non-zero mean Gaussian spectrum for the weather return and a zero-mean Gaussian spectrum for the ground clutter return. A non-linear iterative scheme of Nelder and Mead (1965) is then used to obtain the optimal parameters that fits the Gaussian models based on the measured autocorrelation values. The initial noise and clutter power is obtained from the system noise level and a least square fit of the expected ground clutter power, respectively. The power and mean velocity of the weather signals are then obtained by minimizing the difference between the measured and modeled correlation functions. While the technique of Nguyen et al. (2008) was presented in 2008, a parametric time domain technique based on the autocorrelation function was previously applied to retrieve stratospheric signals in the presence of ground clutter by Sato and Woodman (1982).

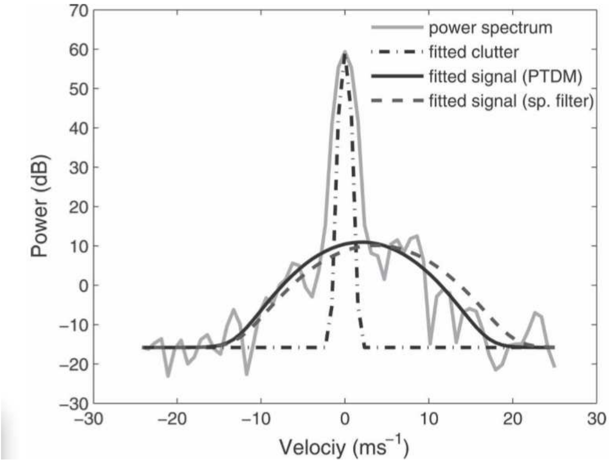

Figure 1.21: Parametric Time Domain Filtering (Nguyen et al. 2008). Using the assumption that the weather and ground clutter can be modeled by two Gaussian processes, this technique retrieves characteristics of the weather and ground clutter from finite radar data via an iterative technique that fits the measured with the expected data. The ground clutter is filtered by neglecting the retrieved values of the ground clutter.

1.4.2 Approaches for Multiple-Receiver Systems

Adaptive Sidelobe Canceling: Kamio and Sato (2003) implemented a simple sidelobe canceler shown in Figure 1.22 with the MU radar. The main array, which consists of 475 Yagi elements, is located in the center, and uses non-adaptive spatial windowing to steer its antenna beam. The received signal obtained using this setup, as a result, is contaminated when clutter is in either the mainlobe or sidelobe by the radiated beampattern. Clutter filtering of the contaminated signal is achieved by adaptively combining signals from the seven elements located around the main array. The weights of the sidelobe cancelers are obtained using a power minimization scheme that includes a constraint such that the magnitude sum of the adaptive weights squared is below 0.5. From processing real data, Kamio and Sato (2003) showed that contamination caused by ground clutter and aircrafts could be significantly attenuated while the signature from the weather was preserved.

Fully Adaptive Canceling: Palmer et al. (1998) were the first to implement a fully adaptive beamforming technique for atmospheric radars. They used the linear minimization technique of Capon (1969) to obtain the filter weights of the antenna elements and implemented this algorithm on signals obtained using the MU atmospheric

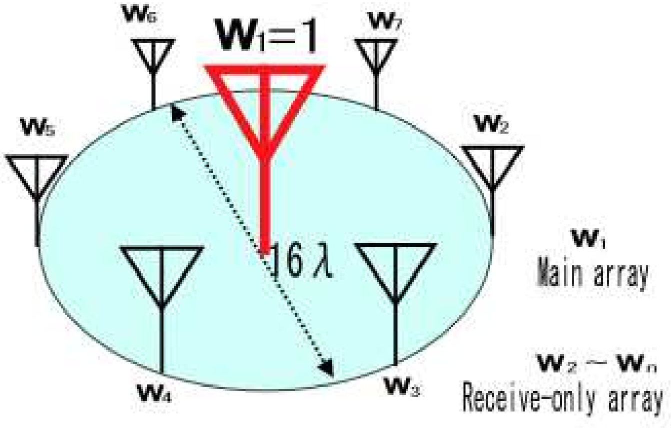

Figure 1.22: Sidelobe canceling configuration (Kamio and Sato 2003). Using adaptive weighting of the signals from the seven elements located around the main antenna, this array setup was able to mitigate clutter that contaminated the main array from the ground and possible moving targets.

radar. They observed turbulence and stratiform precipitation, and noted that enhanced resolution of the scatterers in terms of anisotropic details compared to those obtained using traditional Fourier beamforming using the adaptive technique. Using the same minimization technique, Palmer et al. (2005) observed small-scale interaction between precipitation and clear-air turbulence using the Turbulent Eddy Profiler. They investigated the interaction of a case with light rain passing through a turbulent layer and another case with dissipating rain passing through a turbulent layer. Additionally, Cheong et al. (2006) also applied the technique to remove biological clutter using the Turbulent Eddy Profiler. Particularly, they designed an antenna array configuration such that a null was obtained in the locations of the grating lobes, resulting in an improved clutter suppression capability.

An extension of the fully adaptive beamforming technique, called range imaging (Palmer et al. 1995), was investigated by Yu and Palmer (2001). The technique extended upon the spatial beamforming by incorporating adaptive weighting to both frequency and spatially sampled signals. Via simulations of the 49.3, 49.83 and 50.50 MHz, they examined the capabilities of this technique for improving the range and angular resolution of the MU radar configuration. They modeled the reflectivity field with blob-like scatters and simulated the technique. The results of some of these simulations are shown in Figure 1.23.

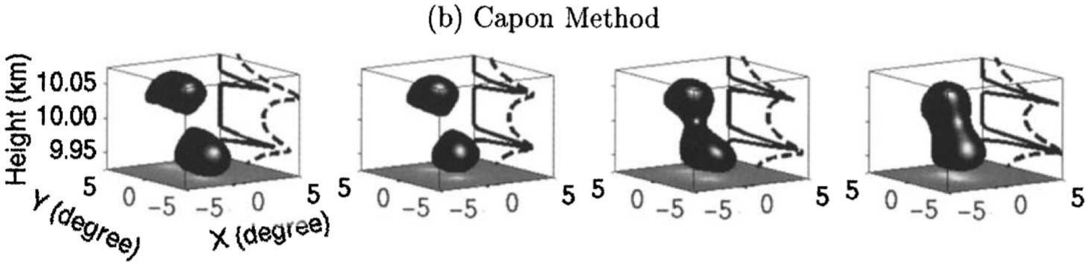

Figure 1.23: Three-dimensional imaging results (Yu and Palmer 2001). By adaptively combining spatial and frequency weighting, this imaging scheme showed that enhanced resolution could be obtained with a phased array.

1.5 Motivation and Outline of Dissertation

As presented, current clutter mitigation algorithms for weather radars operate on signals from a single receiver and attempt to separate the weather signal in either the temporal or spatial domains. These techniques exploit either the long correlation time of clutter signals and/or the Gaussian spectrum of the weather signal in order to retrieve the weather component (Strauch et al. 1984; Siggia and Passarell, Jr. 2004; Jordan et al. 1997; Torres and Zrnić 1999; Nguyen et al. 2008). When the weather and clutter can be separated, these techniques work well to estimate the spectral moments of the weather. However, the results obtained can be unexpected when the above assumptions are not fully satisfied. In the special case of a short number of contiguous time samples, the current clutter mitigation algorithms should not be applied because the temporal and spectral resolutions are poor (Harris 1978; Oppenheim and Schafer 1989; Haykin 1996; Stoica and Moses 2005). As a result, other approaches beside temporal or spectral filters are needed.

Phased array radar with agile electronic beam steering is a candidate to replace the aging NEXRAD network and resolve some of the limitations imposed with mechanically steered and fixed radiation pattern radars (Weber et al. 2007; Zrnić et al. 2007). The technology is being tested in Norman, Oklahoma with the National Weather Radar Testbed phased array radar (Forsyth et al. 2002, 2007). Details of the NWRT PAR have been presented in Forsyth et al. (2002, 2007); Zrnić et al. (2007), among others, while references of general phased array radars are presented in Skolnik (1990, 2001); Brookner (2002); Van Trees (2002); Mailloux (2005); Brookner (2008). An advantage of phased array radars in weather applications is their capability to revisit discrete parts of the atmosphere. The capability provides the opportunity to quickly gather decorrelated time samples and provide statistically improved estimates using the same number of samples as compared with conventional scanning methods (Zrnić 1977, 1979; Doviak and Zrnić 1993). The approach of revisiting certain parts of the weather environment when decorrelated samples can be obtained is called *beam multiplexing*, which is detailed in Yu et al. (2007). As a result, a short number of contiguous samples, as low as two, is obtained during each visit, which is problematic for the current clutter mitigation algorithms that requires sufficient temporal or spectral separation to retrieve the weather component.

With the addition of a multi-channel receiver that is being developed for the NWRT PAR, real-time access to the time series signals of the main array and six auxiliary elements will soon be available (Yeary et al. 2008). When completed, spatial processing techniques can be implemented. These techniques require only spatial separation between the clutter and weather signals and can be used even when non-contiguous samples are observed (Billetter 1989; Mailloux 2005; Nicholas 2000; Van Trees 2002; Monzingo et al. 2004). A study is needed that examines the performance of the spatial filters under various operational scenarios which include dwell time, relative clutter position, and clutter characteristics. In general, very little is known about the effects of clutter mitigation using sidelobe canceler in the phased array radar environment because of the classified nature of these devices (Brookner 2008). As a result, the completed study could provide improved understanding of the advantages as well as limitations of spatial array processing techniques. In this dissertation, a thorough examination is attempted by observing the effect of clutter filtering for a simulated and real phased array radars. The results will show that clutter filtering can be obtained even for as few as two samples. However, there are trade-offs that are observed, some of which result in filtered signals that may be unusable.

Following this introductory chapter, a more in-depth review of precipitation radars with a single receiver is provided in Chapter 2. Topics that are discussed in the review include the radar environment, scattering condition, and signal processing approaches used in such a radar setup. From here, an extension to phased array with multiple antenna elements is provided in Chapter 3. An introduction is given of a simple narrowband signal model, as well as conventional and adaptive filtering techniques, for partially adaptive and fully adaptive arrays. With the signal model described, approaches for simulating and validating the filters for a weather radar environment are introduced in Chapter 4. In this part of the dissertation, the simulator for generating the time series signals, the parameters for controlling the adaptive array processing algorithms, and the approach for validating the spatial filtering schemes are introduced. In Chapter 5, the clutter filtering techniques are applied to a numerical generated weather radar event and also to real data obtained from a field campaign, and the results of the analysis from both sets of data are discussed. The dissertation ends with conclusions of spatial filtering with phased arrays in the weather radar environment and some important recommendations for related future studies.

Chapter 2

Doppler Radar Theory for Observing the Atmosphere

2.1 Key Developments in Radar Technology

Radars (RAdio-Detection-And-Ranging) are devices that typically operate at frequencies from 3 Hz to 300 GHz and have the capability to detect and locate targets (Atlas 1990; Doviak and Zrnić 1993; Guerlac 1987; Richards 2005; Sauvageot 1992; Skolnik 1990, 2001). The RADAR term was first suggested by S. M. Taylor and F. R. Furth in 1940 and universally adopted in 1943 by the Allied Forces (Doviak and Zrnić 1993). Radars were relatively simple in their early development, consisting of a powerful incoherent transmitter, a parabolic dish antenna, and a basic analog display. These devices were primarily used to detect and track aircrafts and missiles, and operated by military personnel who served to interpret the observed backscattered signals. Modern radars have evolved significantly from the early devices; they are now coherent, built with sophisticated transmit/receive antennas, possess powerful signal processors, and have high-resolution digital displays. These radars provide services to both the military and for civilian use that include but are not limited to: collision avoidance, navigation, and weather monitoring. End-users now act as quality-control specialists who determine the accuracy of the processed products.

While radars have significantly evolved since the first prototypes, the concept upon which these devices operate is still the same and originates from the principle of electromagnetic wave propagation, which was established by James Maxwell and is expressed with the following equations:

$$\begin{aligned} \overrightarrow{\nabla} \times \overrightarrow{E} &= -\overrightarrow{M} + \frac{\partial(\mu \overrightarrow{H})}{\partial t}, \quad \nabla \cdot (\epsilon \overrightarrow{E}) = \rho_e \\ \overrightarrow{\nabla} \times \overrightarrow{H} &= \overrightarrow{J} + \frac{\partial(\epsilon \overrightarrow{E})}{\partial t}, \quad \nabla \cdot (\mu \overrightarrow{H}) = \rho_m. \end{aligned} \tag{2.1}$$

The Maxwell's equations relate the electric $\overrightarrow{E}$ and magnetic $\overrightarrow{H}$ fields, electric $\overrightarrow{J}$ and magnetic $\overrightarrow{M}$ current densities to the electric ρ_e and magnetic ρ_m charge densities, where in these equations μ is the magnetic permeability and ϵ is the electric permittivity. The equations were originally published in 1864 in a memoir to the Royal Society entitled "A Dynamical Theory of the Electromagnetic Field" (Selvan 2007), again published in 1873 in the book *Treatise on Electricity and Magnetism*, and are now commonly found in all electromagnetic textbooks. In weather radar applications, the Maxwell's equations are used to characterize the propagating fields, the interactions of the fields with atmospheric scatterers, and the scattered fields.

From Maxwell's theories, the transition to application is credited to George FitzGerald, Oliver Lodge, and Heinrich Hertz, among others who developed means for detecting and transmitting electromagnetic waves. Fitzgerald and Lodge, for example, conceptualized that an oscillating electric current produced electromagnetic waves and developed devices that generated electromagnetic energy other than light between 1879 and 1883 (Sengupta and Sarkar 2003). Hertz, additionally, completed the transmission/receiving process in 1887 using a simple resonant circuit pictured in Figure 2.1 that made detecting electromagnetic waves a reality. Contributions such as from FitzGerald, Lodge, and Hertz are fundamental to the building blocks of modern radars.

The next progress of modern radars was to use the waves to detect scatterers. The accomplishment is credited to Christian Hulsmeyer for his invention of the "telemobiloscope", which is illustrated in Figure 2.2. The device consisted of a spark gap amplifier and an array of dipole receivers, and it operated by radiating a beam of electromagnetic waves away from a ship and ringing a bell when foreign ships were present in the path of the radiated energy.

The final component of a modern radar is ranging and it was accomplished between 1920 and 1940. The capability was motivated by: (1) point-to-point surveying and geodetic measurements; (2) altimeters for aircrafts; and (3) exploration of the Kelley-Heaviside layer (Guerlac 1987). One experiment of ranging included using two

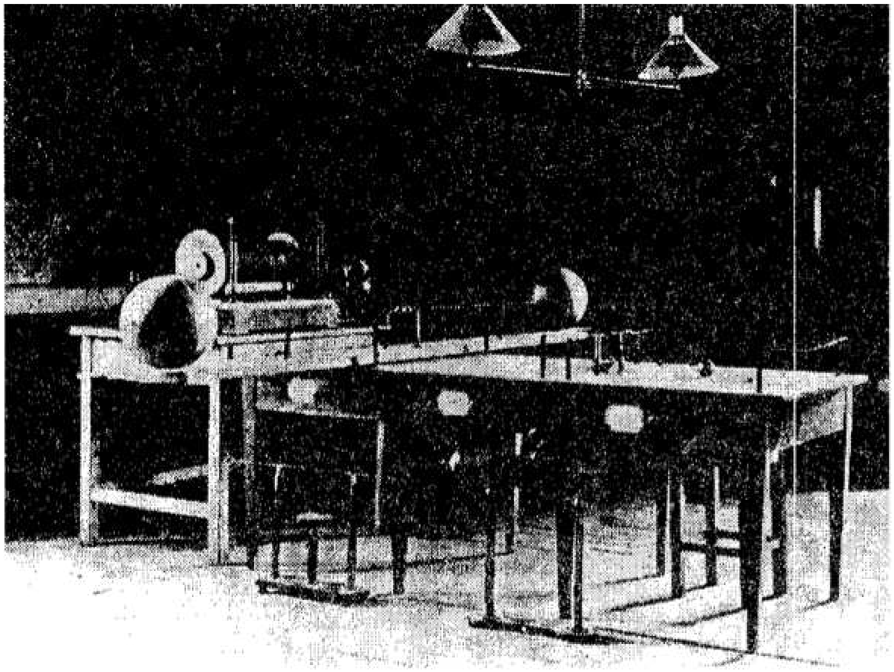

Figure 2.1: Apparatus of Hertz experiment (Cichon and Wiesbeck 1995). Hertz used the above equipment to demonstrate simultaneously the concept of transmission and reception of electromagnetic waves. He is credited as the first person to accomplish this achievement.

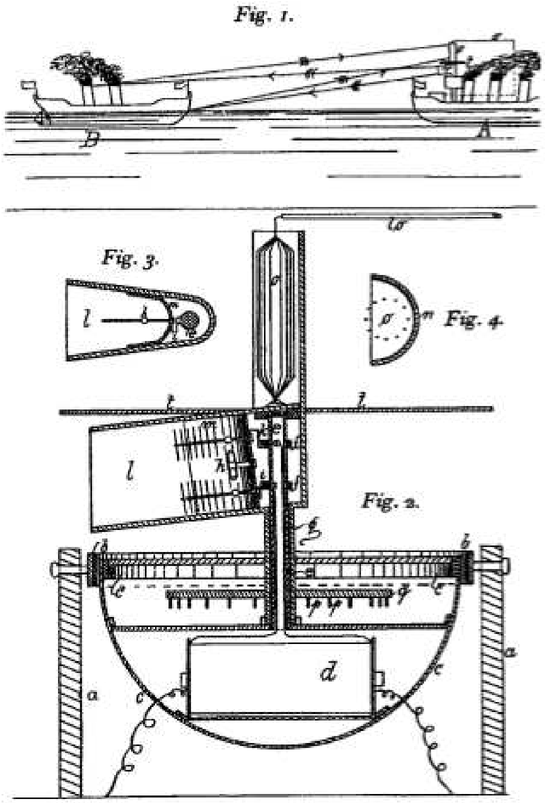

Figure 2.2: Christian Hulsmeyer Telemobiloscope (van Loon 2005). Hulsmeyer patented this device as a mean for preventing the collision between ships. Using a directive radio beam, this device operates by ringing a bell when a ship is detected in its field-of-view.

frequencies and examining the phase differences to estimate propagational distances between the North Caucasus mountains, the Black Sea, and Lake Ilmen (Guerlac 1987). Other ranging techniques that were explored included using radiation patterns and triangulation to measure the altitudes of aircraft. Two ranging methods that eventually became standards for modern radars are the frequency modulation of E. V. Appleton and M. A. F. Barnett and the pulsed Doppler technique of G. Breit and M. A. Tuve. The two techniques employ temporal or phase delay characteristics of the return signals to estimate the range of the scatterers. With ranging, the foundation of radar was built.

2.2 Pulsed Modulated Doppler Radar: Basic Concepts

Most weather radars are coherent and pulse-modulated (Doviak and Zrnić 1993; Skolnik 1990, 2001; Richards 2005). They consist of a transmitter responsible for generating a powerful RF pulse and a receiver that is responsible for processing the scattered signal and producing an output signal. A simplified block diagram that illustrates the details of a generic weather radar is shown in Figure 2.3. The transmitter is outlined in the upper part of the block diagram while the receiver is outlined in the lower part. Coherency between the two components is achieved using a stable local oscillator (STALO). In the setup, the outputs signal of the radar consists of $I(t)$ and $Q(t)$, which are in-phase $I(t)$ and quadrature $Q(t)$ signals, respectively. These signals are used to estimate the properties of the scatterers such as their reflectivity and Doppler motion.

The transmitter shown in the upper half of Figure 2.3 is responsible for producing a powerful RF waveform. This component of the radar is important because the waveform affects the signal-to-noise ratio (SNR), range resolution, Doppler velocity resolution, ambiguity in range and Doppler, range and Doppler side lobes, and range-Doppler coupling (Griffiths et al. 1998; Richards 2005), and determines the characteristics and performance of the radar. The effects of the waveform through the transmitter can be examined by observing the path it propagates through the transmitter. The path starts at the waveform generator with a trigger signal, where a pulse is generated, modulated, and then amplified to frequencies from 2 MHz to 100 GHz. For typical atmospheric applications, frequencies between 100 MHz to

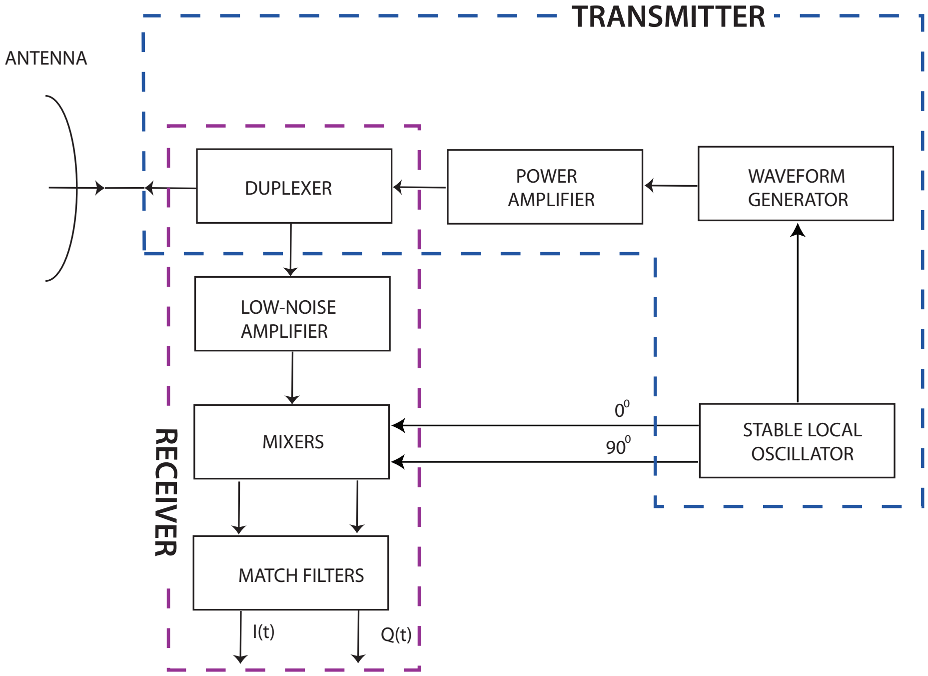

Figure 2.3: Block diagram of a Doppler radar. The diagram shows that the Doppler radar consists of two main components: the transmitter and the receiver. The first device operates by amplifying a transmit waveform and transmitting it into space. The second device then senses for the weak energy that is scattered back. Through a local stable oscillator, the Doppler frequency of the backscattered signal is measured.

1 GHz, 3-10 GHz, 30 GHz, and 95 GHz are used as these frequencies are most sensitive to water vapor concentration. The waveform after modulation is then radiated into space through an antenna. While specific details were not given, the above outline illustrates the basic functions of a transmitter.

Table 2.1: Radar Frequencies and Wavelengths

Band	Frequencies	Wavelengths
HF	2-30 MHz	100-10 m
VHF	30-300 MHz	10-1 m
UHF	300 MHz-1 GHz	1 m-30 cm
L	1-2 GHz	30-15 cm
S	2-4 GHz	15-7.5 cm
C	4-8 GHz	7.5-3.7 cm
X	8-12 GHz	3.7-2.5 cm
K	18-26.5 GHz	1.7 cm-1.1 mm
Q	33-50 GHz	9.1-6 mm
V	40-60 GHz	7.5-5 mm
W	56-100 GHz	5.4-3 mm

For specifics related to the radar waveform and the radar output signals, observe the relationship shown in Figure 2.4 of a timing diagram for a pulsed Doppler radar that transmits an identical train of pulses. Each pulse is identical, has an amplitude of A, width τ_s, and is repeated every T_s. Its peak power is A^2 while its average power of $A^2\tau_s/T_s$. Over the period T_s, the radar has a duty cycle of $\tau_s/T_s \times 100$ % and is active over τ_s while being inactive over $T_s - \tau_s$. In general, a large $A\tau_s$ is desired since the sensitivity of the radar depends on A. However, $A > A_b$, which is called the breakdown potential, causes ionization of gas in the waveguide and limits the maximum value of A. According to Naidu and Kamaraju (1996),

$$A_b \;=\; 24.22\frac{293pd}{760T} + 6.08\left(\frac{293pd}{760T}\right)^{1/2} \tag{2.2}$$

for dry air, where pd is torr-cm, and T is temperature. For example, the breakdown potential is 30.3 kV at 1013 mbar, 293 K, and over a 1 cm gap.

At the receiver, the scattered signal is first amplified by a low-noise amplifier to increase its power. The signal is then demodulated to baseband using a stable local oscillator and sent through a pulse-matched filter to produce $I(t)$ and $Q(t)$.

Additionally, while not shown, $I(t)$ and $Q(t)$ can be further processed to obtain information about the scatterers. The setup shown in Figure 2.3 uses a homodyne detection scheme with a single stage mixer. However, modern receivers generally use a superheterodyne detection scheme with multiple mixing stages to provide improved conversion loss, improved sensitivity, and decreased flicker noise (Richards 2005).

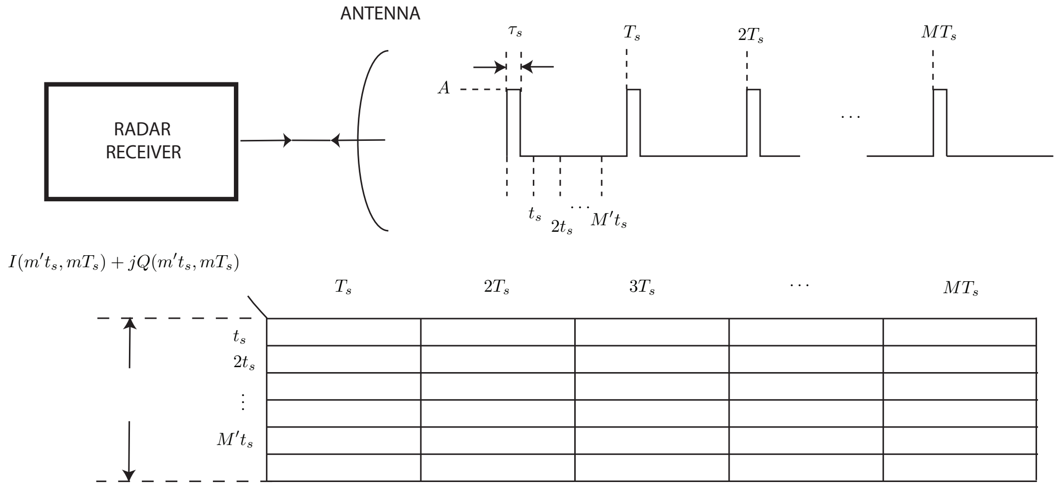

Figure 2.4: Radar sampling schedule. The data are grouped into a two-dimensional matrix where one dimension represents range samples and the other represents time samples at fixed range locations. In general, signals along the range samples are assumed to be independent, and signals along the pulse samples are assumed to be correlated. In this setup, the spectral moments are calculated along the pulse samples dimension.

The output signals of the radar $I(t)$ and $Q(t)$ are generally continuous. As a result, they need to be sampled and the process is illustrated in Figure 2.4. The sampling of $I(t)$ and $Q(t)$ is achieved using a slow "sample time" rate, T_s, and a fast "range time" rate of t_s. The sampled signals, denoted $I(m't_s, mT_s)$ and $Q(m't_s, mT_s)$ where $m = \{1, 2, ..., M\}$ and $n = \{1, 2, ..., N\}$ are then grouped into a two-dimensional matrix, where the $m^{'}$ index is associated with the $m^{'}ct_s/2$ range and the m index is associated with the time mT_s. Moment estimation of each range gate is then applied along the m dimension and the index $m^{'}$ is implied and dropped.

2.2.1 Sampling and Aliasing Effects

From the sampling strategy previously described, a range

$$\hat{R} \;=\; \frac{1}{2}\left(2R_{\text{true}} - cT_s\left\lfloor\frac{2R_{\text{true}}}{cT_s}\right\rfloor\right), \tag{2.3}$$

is assigned to the scattered signal, where the true range is R_{true} and $\lfloor \cdot \rfloor$ is the floor function. Listed in Table 2.2 are examples of the estimated range for scatterers located from 0 to 425 km with an aliasing range ($R_a = cT_s/2$) of 150 km. Using the above sampling approach, targets closer than $cT_s/2$ are correctly estimated, while targets located outside $cT_s/2$ will be estimated with values less than $cT_s/2$. This ambiguity effect is called range aliasing and is used to describe the maximum range to which targets can be unambiguously estimated.

Table 2.2: Effect of Range Aliasing for $cT_s/2 = 150$ km

Unambiguous Range		Ambiguous Range	
R_{true}	$\hat{R}$	R_{true}	$\hat{R}$
0	0	150	0
25	25	175	25
50	50	200	50
75	75	225	75
100	100	250	100
125	125	275	125
		300	0
		325	25
		350	50
		375	75
		400	100
		425	125

A similar aliasing effect is observed when estimating the Doppler velocity and can be derived from the scattered spherical wave, $A\exp\left[j\left(2\pi f(t - 2R/c) + j\Psi_s\right)\right]$, where Ψ_s is the phase shift produced by the scatterer. Now, substitute $\lambda \equiv \dfrac{c}{f}$, and the phase at the output of the synchronous detector is

$$\Psi_e \equiv -\frac{4\pi R}{\lambda} + \Psi_s. \tag{2.4}$$

The time rate of change of Ψ is

$$\begin{aligned} \frac{d\Psi_e}{dt} &= -\frac{4\pi}{\lambda}\frac{dR}{dt} \\ &= -\frac{4\pi}{\lambda}v_r \end{aligned} \tag{2.5}$$

where v_r is the radial velocity and is defined as dR/dt. The Doppler frequency is also defined as $2\pi f_D = -\dfrac{4\pi}{\lambda}v_r$ and then rearrange to get $f_D = -2v_r/\lambda$.

From sampling theory,

$$|f_D| \;\leq\; \frac{1}{2T_s} \tag{2.6}$$

is needed to unambiguously estimate the Doppler frequency. The above observation implies that $\left|-\frac{2v_r}{\lambda}\right| \leq \frac{1}{2T_s}$, and solving for v_r gives

$$|v_r| \;\leq\; \frac{\lambda}{4T_s}. \tag{2.7}$$

Obviously, aliasing ($v_r \equiv v_a$) occurs when $|v_a| = \frac{\lambda}{4T_s}$.

The aliasing effect is illustrated in Figure 2.5 for the continuous signal $S_c(v)$. From sampling theory, $S_c(v)$ is repeated at $2v_a m$, where $m = \{\cdots, -1, 0, 1, \cdots\}$, in the spectral domain. The spectral contents of $S_c(v)$ do not overlap and filtering is applied to unique components of $S_c(v)$ when $|v_r| \leq v_a$, while $S_c(v)$ is aliased and filtering is applied to overlapping components of $S_c(v)$ when $|v_r| \geq v_a$.

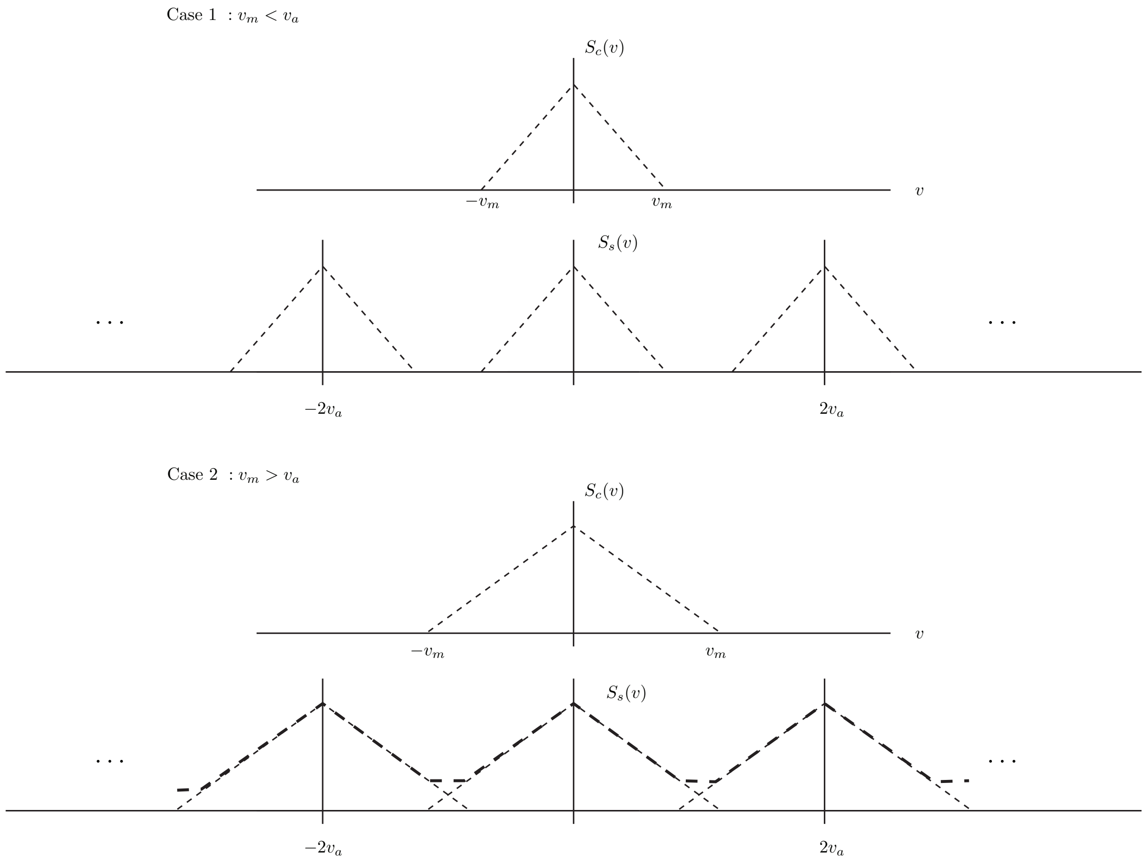

Figure 2.5: Examples of measured Doppler spectra under conditions of aliasing. In this case, the measured spectrum can overlap onto itself and cause errors in spectral moment estimates.

A special effect is observed when the two aliasing phenomena of range and Doppler velocity are multiplied. The following constant is produced

$$\begin{aligned} R_a \times |f_D| &\leq \frac{cT_s}{2} \times \frac{\lambda}{4T_s} \\ &= \frac{1}{8}. \end{aligned} \tag{2.8}$$

The effect associated with this constant is called the "range Doppler dilemma" and it implies that a trade-off between the maximum aliasing range and maximum Doppler velocity must be obtained; By increasing one parameter, the other is inherently reduced.

2.3 The Radar and Its Environment

2.3.1 The Radar Range Equation

One basic formula that can be used to describe the radar environment is the radar range equation (Doviak and Zrnić 1993; Richards 2005; Skolnik 1990, 2001). The equation connects the instantaneous power measured by a radar to the characteristics of the scatterers. For a single point target, the radar range equation as given by Skolnik (1990) has the expression

$$P_r = \frac{P_t G_t}{4\pi R^2 l} \times \frac{\sigma(D)}{4\pi R^2 l} \times A_e. \tag{2.9}$$

where the received signal power is P_r, the transmitted power is P_t, the antenna gain is G_t, the propagation loss is l, the radar cross section is $\sigma(D)$, the diameter of the target is D, and the effective aperture of the received antenna is A_e. The first term on the right hand side is the power density at a distance R for a radar with P_t and G_t, while the second term depends on the target characteristics. When the two terms are combined, a new term which describes the power density returned to the radar is obtained. When the term is applied to an antenna with $A_e = G_r\lambda^2/4\pi$ where λ is the wavelength (Doviak and Zrnić 1993), the return power is

$$P_r = \frac{P_t G_t}{4\pi R^2 l} \times \frac{\sigma(D)}{4\pi R^2 l} \times \frac{G_r \lambda^2}{4\pi}. \tag{2.10}$$

For atmospheric radars, Sauvageot (1992) showed that the average received power is meaningful,

$$\begin{aligned} \bar{P}_r &\approx \frac{P_t G_t}{4\pi R^2 l} \times \frac{\eta \triangle V}{4\pi R^2 l} \times \frac{G_r \lambda^2}{4\pi} \\ &\approx \frac{P_t \lambda^2 G_t G_r}{(4\pi)^3 R^4 l^2} \eta \triangle V, \end{aligned} \tag{2.11}$$

where the average radar cross-section per unit volume (reflectivity)

$$\eta = \int_0^\infty \sigma_b(D)N(D)dD. \tag{2.12}$$

In this expression, $\sigma_b(D)$ is the backscattered cross section and $N(D)$ is the drop size distribution. For atmospheric scatterers, some $N(D)$ are given in Straka et al. (2000).

The above radar range equation can be simplified to a standard form by including an approximate radar resolution volume. Assuming that the volume is that of a cylinder, $\triangle V = \frac{c\tau}{2}\pi\frac{R^2\theta_1^2}{4}$ with the pulse width τ and the one-way half-power beamwidth θ_1,

$$\begin{aligned} \bar{P}_r &\approx \frac{P_t\lambda^2 G_t G_r}{(4\pi)^3 R^4 l^2}\eta\frac{c\tau}{2}\pi\frac{R^2\theta_1^2}{4} \\ &\approx \frac{P_t\lambda^2 G_t G_r}{(4\pi)^3 R^2 l^2}\eta\frac{c\tau}{2}\pi\frac{\theta_1^2}{4}. \end{aligned} \tag{2.13}$$

For scattering from turbulence, Doviak and Zrnić (1993) showed

$$\eta = 0.38\lambda^{-1/3}C_n^2, \tag{2.14}$$

where the turbulence structure parameter is C_n^2, with values of $C_n^2 \approx 6 \times 10^{-17}$ m$^{-2/3}$ when turbulence is weak, $C_n^2 \approx 2 \times 10^{-15}$ m$^{-2/3}$ when it is intermediate, and $C_n^2 \approx 3 \times 10^{-13}$ m$^{-2/3}$ when it is strong.

2.3.2 Backscattered Cross-Section

Examples of radar backscattered cross-sections for some common scatterers are listed in Table 2.3, which include birds, insects, humans, trucks, bicycles, and planes. The values listed are quite variable with magnitudes that range from 10^{-1} cm^2 to 10^6 cm^2.

Table 2.3: Radar Cross Section (Richards 2005)

Object	σ (cm^2)
Jumbo jet	10^6
Pickup truck	2×10^6
Bicycle	2×10^4
Man	10^4
Bird	10^2
Insect	10^{-1}

Since the main scatterers for precipitation radars are rain droplets, the backscattered cross-section of these scatterers are examined in more detail. Using complex dielectric constants of 79.4+j24.9, 62.1+j38.1 and 42.0+j40.8 for the 3, 5, and 10 cm wavelengths, respectively, cross-section values of precipitation particles are numerically calculated using Mie and Rayleigh scattering. The results are plotted in Figure 2.6 for particles with diameters of up to 50 mm although rain drops rarely reach diameters greater than 9 mm. For particles with small diameter to wavelength ratios, the cross sections using Mie and Rayleigh scattering match. The values differ as the diameter increases beyond a few mm. The values obtained using Rayleigh scattering is initially below that of Mie scattering; however the magnitude of the curves switch order when the ratio of the diameter to wavelength is increased further.

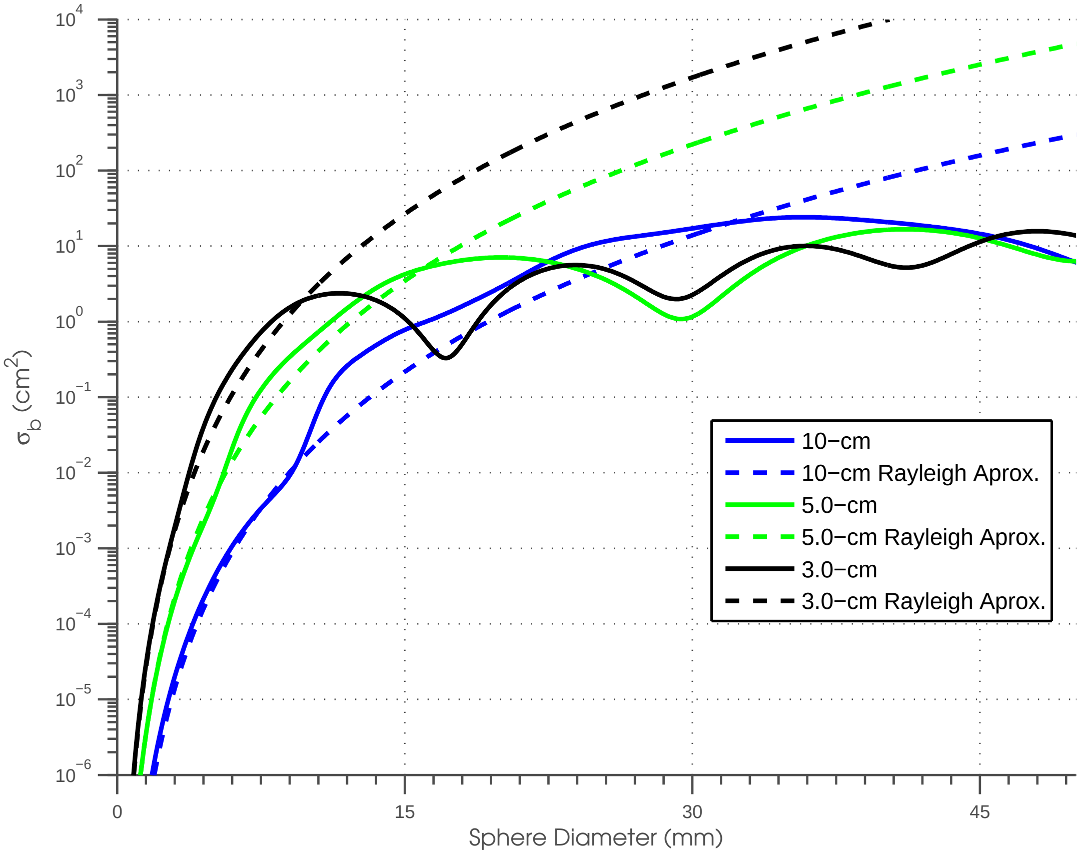

Figure 2.6: Radar backscattered cross-sections (Matlzer 2002). The radar backscattered cross-sections are shown for spheres with diameters of up to 50 mm for the 3, 5, and 10 cm wavelengths. These values were calculated using Mie and Rayleigh scattering and with complex dielectric constants of 79.4+j24.9, 62.1+j38.1 and 42.0+j40.8.

When rain droplets have diameter $D \leq \lambda/16$ and are spherical, their backscattered cross section can be simply expressed as

$$\sigma_b(D) \approx \frac{\pi^5}{\lambda^4}|K_m|^2 D^6, \tag{2.15}$$

where $K_m = (m^2 - 1)/(m^2 + 2)$ and m is the complex refractive index of water (Doviak and Zrnić 1993). The cross-section is proportional to D^6 and is a function of the complex refractive index of water. The reflectivity of volume scatterers then becomes

$$\begin{aligned} \eta &\equiv \int_0^\infty \frac{\pi^5}{\lambda^4}|K_m|^2 D^6 N(D) dD \\ &\approx \frac{1}{\triangle V}\sum_i \frac{\pi^5}{\lambda^4}|K_m|^2 D_i^6. \end{aligned} \tag{2.16}$$

A "volume reflectivity factor" $Z \equiv \frac{1}{\triangle V}\sum_i D_i^6$ is used to relate the reflectivity to the rate of intensity of precipitation. Some examples of the volume reflectivity factor in logarithmic units are listed in Table 2.4. These values range from 18 dBZ for light rain, corresponding to a rain rate of 0.49 mm/hr to values above 57 dBZ corresponding to rain rates above 133.2 mm/hr.

Table 2.4: Rainfall to dBZ Rates (Richards 2005)

Rainfall rates (mm/hr)	Z (dBZ)	Category
0.49 to 2.7	18 to < 30	Light mist
2.7 to 13.3	30 to < 41	Moderate
13.3 to 27.3	41 to < 46	Heavy
27.3 to 48.6	46 to < 50	Very heavy
48.6 to 133.2	50 to < 57	Intense
133.2 and greater	57 and above	Extreme

Calculations of the reflectivity factor use an assumption of spherical drops to obtain the backscattered cross-section. However, precipitation particles are no longer purely spherical when $D > 3.5$ mm. In these cases, the shape of the precipitation particle is changed by an unequal pressure development produced as they fall through the air (Spilhaus 1948). A negative pressure develops over the top and side, and a positive pressure develops at the bottom of the falling precipitation particles. The pressure drop then deforms the falling particle by reducing the ratio of its area of cross-section to perimeter in the vertical plane to balance the internal pressure and surface tension. As a result, the shape of the precipitation particles become more oblate than spherical and a spheroidal scattering model, which is more representative of a falling precipitation droplet, must be used (Doviak and Zrnić 1993).

2.3.3 Propagational Attenuation

The propagational attenuation, which is a parameter that describes the loss of the transmit signal, is defined in a precipitating environment as

$$l = \exp\left[\int_0^R \int_0^\infty N(D,r)\sigma_e(D) dD dr\right], \tag{2.17}$$

where the extinction cross-section is $\sigma_e(D)$ and the particle drop size distribution as a function of range is $N(D,r)$. The propagational attenuation is a function of the extinction cross-section and the number of the precipitation particles that the transmit signal interacts with along the path. At range R, the parameter is obtained by integrating the scattering along the transmitted path.

A component of the propagational attenuation is the extinction cross-section and can be numerically calculated for precipitation particles. Using complex dielectric constants at 0°C of 79.4+j24.9, 62.1+j38.1 and 42.0+j40.8 for the 3, 5, and 10 cm wavelengths, respectively, values of the extinction cross-section for particles up to 50 mm were obtained and plotted in Figure 2.7. The cross-sections for the three wavelengths and precipitation particles larger than 30 mm have approximately the same values. The values diverge at smaller diameters with the extinction cross-section being larger when the wavelength is changed from 10 cm to 3.2 cm.

In particular, the propagational attenuation can be used to calculate a rate loss incurred by the transmitted signal. The parameter is called *specific attenuation* and has been calculated for rainfall rates up to 100 mm/hr, particle distribution of Laws and Parsons (1943), and wavelengths of 3.2, 5.0, and 10.0 cm. The values are plotted in Figure 2.8 and show that *specific attenuation* ranging from 3×10^{-6} dB/km to 30 dB/km are observed with values that are larger for shorter wavelengths. An order of magnitude in the *specific attenuation* is observed when one of the selected wavelengths is changed.

In addition, attenuation is observed when the transmit wave interacts with water vapor and oxygen particles. While this loss can be significant at some frequencies, it is relatively insignificant at the frequencies typically used for observations of precipitation and can be neglected. It should be noted that the loss caused by water vapor

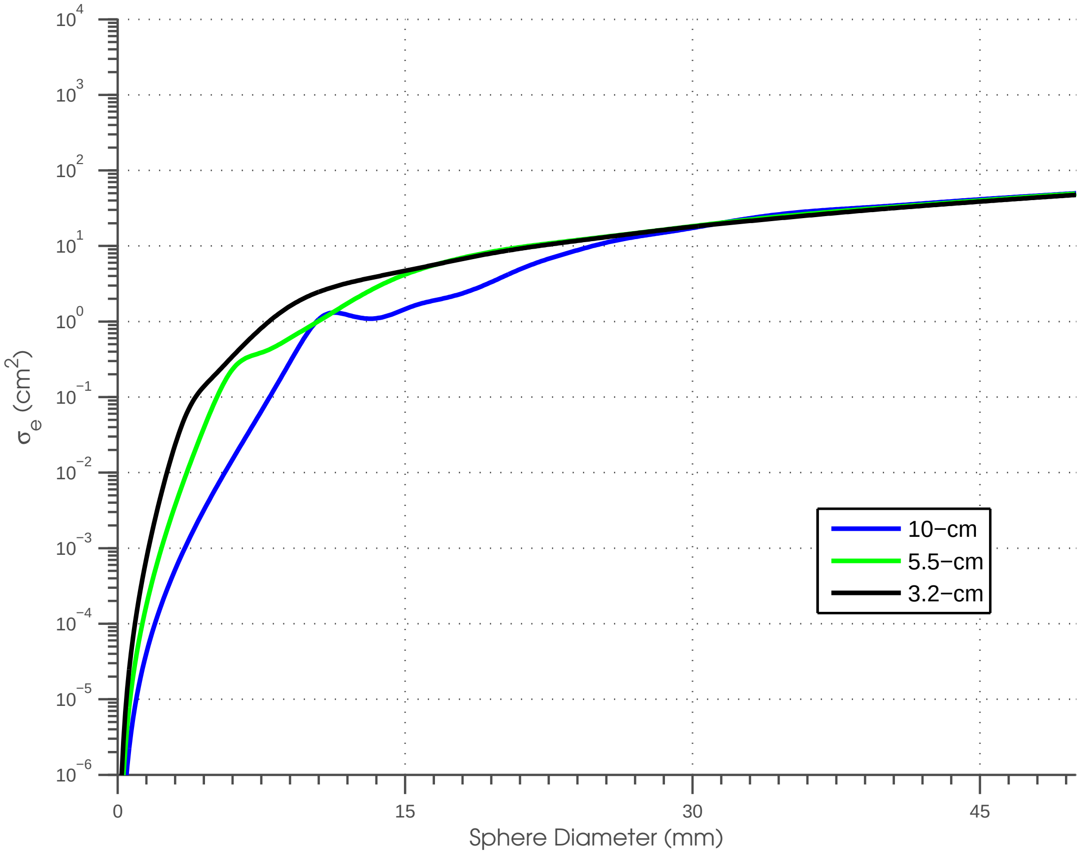

Figure 2.7: Extinction cross-section (Matlzer 2002). The extinction cross-sections are shown for spheres with diameters up to 50 mm for the 3, 5, and 10 cm wavelengths. These values were calculated using Mie and Rayleigh scattering and with complex dielectric constants of 79.4+j24.9, 62.1+j38.1 and 42.0+j40.8, respectively.

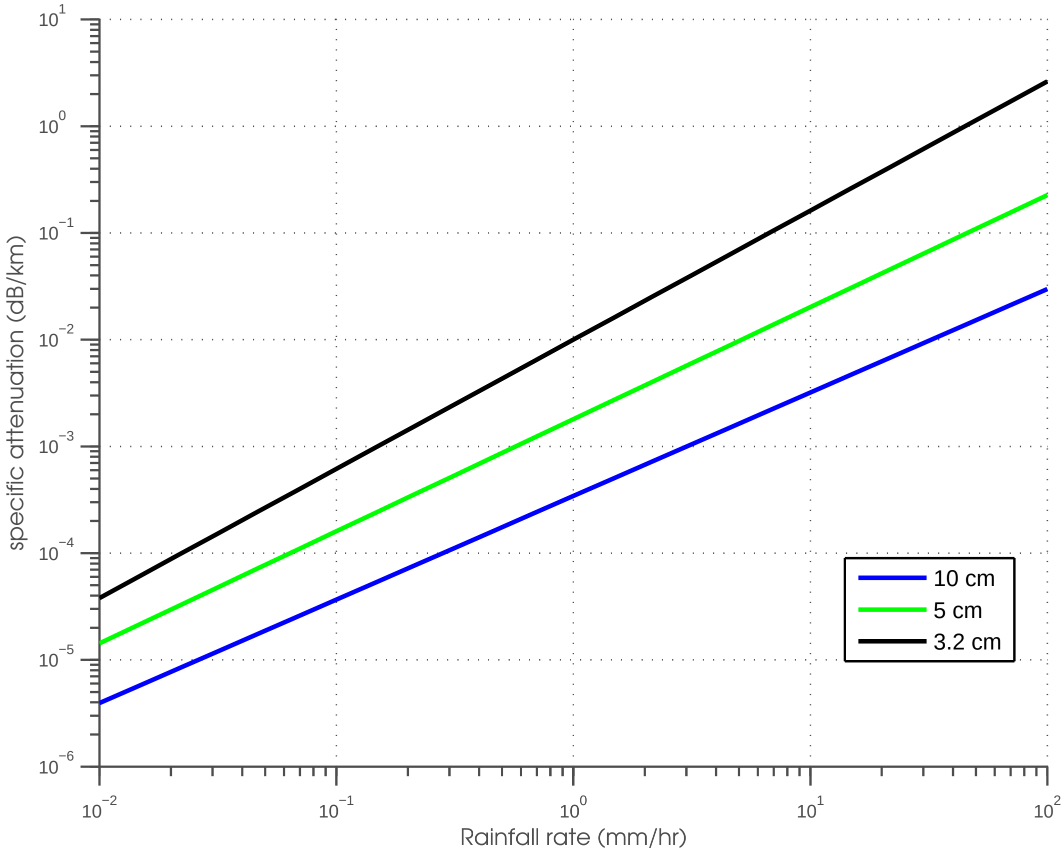

Figure 2.8: Rainfall and specific attenuation. Some specific attenuations are calculated using the drop size distribution of Laws and Parsons (1943) for the 3.2, 5.0, and 10.0 cm wavelengths. The difference in path loss can be an order of magnitude when the wavelength is varied between these ranges.

and oxygen particles is generally much smaller than the loss due to the interaction with precipitation particles.

2.3.4 Propagation Path

Since the atmosphere is inhomogeneous, radar signals traveling away from the radar do not follow a straight path (Doviak and Zrnić 1993; Richards 2005; Skolnik 1990, 2001). The projection of the radar path depends on the composition of the atmosphere and is characterized using a "refractivity" N factor, which has the expression

$$N \approx \frac{77.6}{T}\left(P + \frac{4810 P_w}{T}\right), \tag{2.18}$$

where the air temperature is T, air pressure is P, and partial pressure of water vapor is P_w. The gradient of N with height is

$$\begin{aligned} \frac{dN}{dh} &= \frac{77.6}{T}\left(\frac{-P}{T} - \frac{9620 P_w}{T^2}\right)\frac{dT}{dh} + \\ & \frac{77.6}{T}\frac{dP}{dh} + \frac{77.6}{T^2}(4810)\frac{dP_w}{dh}. \end{aligned} \tag{2.19}$$

The value is a function of T, P, P_w and also of $\frac{dT}{dh}$, $\frac{dP}{dh}$, and $\frac{dP_w}{dh}$.

Some examples of the radar paths through the standard atmosphere with a beam that has a 3-dB beamwidth of 1° are plotted in Figure 2.9. The paths are obtained using the following refractivity profile (Doviak and Zrnić 1993)

$$N(h) = 313 \times 10^6 \exp\left[-0.1439 h\right]. \tag{2.20}$$

The values are shown for distances up to 400 km, heights up to 14 km, and elevations angles of 0.0°, 1.0°, 3.0°, and 10.0°. The results show the beam generally bends away from the surface and its width increases with range.

In general, $dN/dh \approx -40$ km^{-1} for the standard atmosphere and the radar path follows the above curves. In some special conditions such as when ducting, temperature inversion, subsidence, and advection are observed, the radar signal can be trapped near the surface or forced to propagate away from the surface at a faster rate. In the first case, $dN/dh < -157$ km^{-1} and the situation allows for further observations of weather events near the surface for many hundreds of kilometers. In the second case, $dN/dh > -40$ km^{-1} and the situation decreases the range of the radar. Special discussion of this topic is found in Hall et al. (1996)

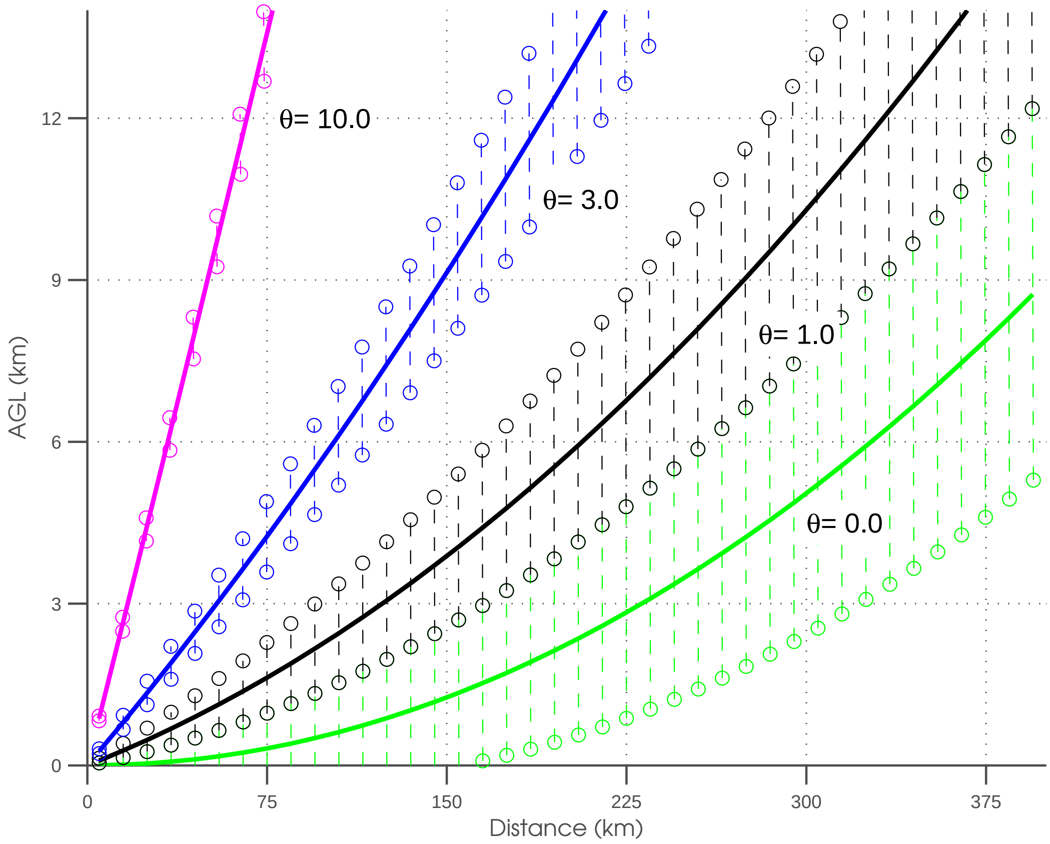

Figure 2.9: Propagation paths in the standard atmosphere. Radar signals travel through the atmosphere in a curved path that depends on the refractivity profile. In the standard atmosphere, the paths for elevations of 0°, 1°, 3°, and 10.0° are plotted in addition to the upper and lower paths of a radar beam with a 1.0° beamwidth.

2.4 Signal Processing for Radars that Observe the Atmosphere

For coherent radars that observe the atmosphere, the signal measured at the receiver $V(mT_s)$ depends on many factors and can be expressed using the radar range equation. Following Capsoni and D'Amico (1998), the echo signal has in-phase and quadrature components with the form

$$I(mT_s) = H\sum_i \left[\frac{\sqrt{\sigma_{bi}}|W_i|}{R_i^2 l_i} f^2(\theta_i,\phi_i)\cos(\gamma_i)\right] \tag{2.21}$$

$$Q(mT_s) = H\sum_i \left[\frac{\sqrt{\sigma_{bi}}|W_i|}{R_i^2 l_i} f^2(\theta_i,\phi_i)\sin(\gamma_i)\right] \tag{2.22}$$

where $\gamma_i = (4\pi R_i/\lambda) + (4\pi v_i m T_s/\lambda) - \psi_i - \beta_i$, $H = \sqrt{P_t G_t G_r/(4\pi)^2}$, $f(\theta_i,\phi_i)$ is the antenna directivity function, and W_i is the range weighting function. In particular, ψ_i is the phase contribution to the range weighting function, and β_i is the phase contribution to the scattering function. In (2.21) and (2.22), the signals are composed of an amplitude and a phase contribution from each scatterer that is illuminated in the radar resolution volume. The combined signal is called the echo voltage and has the form

$$V(mT_s) = I(mT_s) + jQ(mT_s). \tag{2.23}$$

2.4.1 Basic Statistics of the Radar Signal

Since the radar resolution volume is large $\left(\frac{c\tau}{2}\pi R^2\theta_1^2 4 \gg \lambda^3\right)$ and a significant number of scatterers exist within the volume, the received signal is described by a random process (Doviak and Zrnić 1993). The characteristics of the received signal can be derived by applying the central limit theorem to the contribution from each scatterer. In Doviak and Zrnić (1993), the statistics of the received voltage were derived for scatterers that are uniformly distributed, have directional flow, and are illuminated by a Gaussian radiating and receiving pattern. The results show that the statistics of the received voltage are due solely to the radiation pattern.

Under the Gaussian radiation pattern assumption, the statistics of the amplitude of the in-phase and quadrature components of the received voltage has a joint Gaussian distribution with the form

$$P(I,Q) = \frac{1}{2\pi\sigma^2}\exp\left[-\frac{I^2}{2\sigma^2} - \frac{Q^2}{2\sigma^2}\right], \tag{2.24}$$

where σ is the standard deviation of the I and Q amplitudes. These in-phase and quadrature components are independent, and their densities are the same. Additionally, the phase of each signal is independent with a uniform distribution that ranges from 0 to 2π.

The amplitude of the received voltage, $|V| = \sqrt{I^2 + Q^2}$, is calculated by taking the magnitude of the in-phase and quadrature components. It has a Rayleigh distribution with a cumulative distribution function that is derived by integrating the probability density function of the received voltage from $0 \leq |V| \leq |v|$,

$$\begin{aligned} F(|V| \leq |v|) &= \int_0^{|v|} \frac{1}{2\pi\sigma^2} \exp\left[-\frac{|v'|^2}{2\sigma^2}\right] 2\pi|v^{'}|dv' \\ &= \int_0^{|v|} \frac{|v^{'}|}{\sigma^2} \exp\left[-\frac{|v'|^2}{2\sigma^2}\right] dv'. \end{aligned} \tag{2.25}$$

The integrand is the probability distribution function of V with a Rayleigh distribution that has a mean of $\sigma\sqrt{\frac{\pi}{2}}$ and variance of $\sigma^2\frac{4-\pi}{2}$.

The power of the received voltage, $P = |V|^2$, is obtained by taking the square of the magnitude of the received voltage. It has an exponential probability density function, and a probability distribution function that can be obtained by integrating

$$\begin{aligned} f_P(p) &= \left.\frac{f_{|V|}(|v|)}{|dp/d|v||}\right|_{|v|=\sqrt{p}} \\ &= \frac{\frac{\sqrt{p}}{\sigma^2}\exp\left[-\frac{p}{2\sigma^2}\right]}{2\sqrt{p}} \\ &= \frac{\exp\left[-\frac{p}{2\sigma^2}\right]}{2\sigma^2}. \end{aligned} \tag{2.26}$$

The probability density function of the power is valid for $0 \leq p \leq \infty$, and has a well-known mean of $2\sigma^2$ and a variance of $4\sigma^4$.

2.4.2 Spectral Signatures of Radar Signals

Another estimate of the received signal statistics is its *power spectrum.* This parameter, which is a power-weighted distribution of the Doppler velocities, can be used to infer the radial motion of the scatterers within the radar resolution volume. For uniform shear, the power spectrum was derived by Doviak and Zrnić (1993) who showed that its shape is primarily caused by the transmit and receive radiation patterns. Since most radars that are used to observe the atmosphere use a single parabolic dish antenna with an exponential radiation pattern, the spectrum is expected to have a

Gaussian shape. This assumption was confirmed by Janssen and Van der Spek (1985) using a phased array radar to observe precipitation particles. More recently, Yu et al. (2009) investigated the Doppler spectrum of a tornadic supercell and showed that non-Gaussian Doppler spectra were often observed.

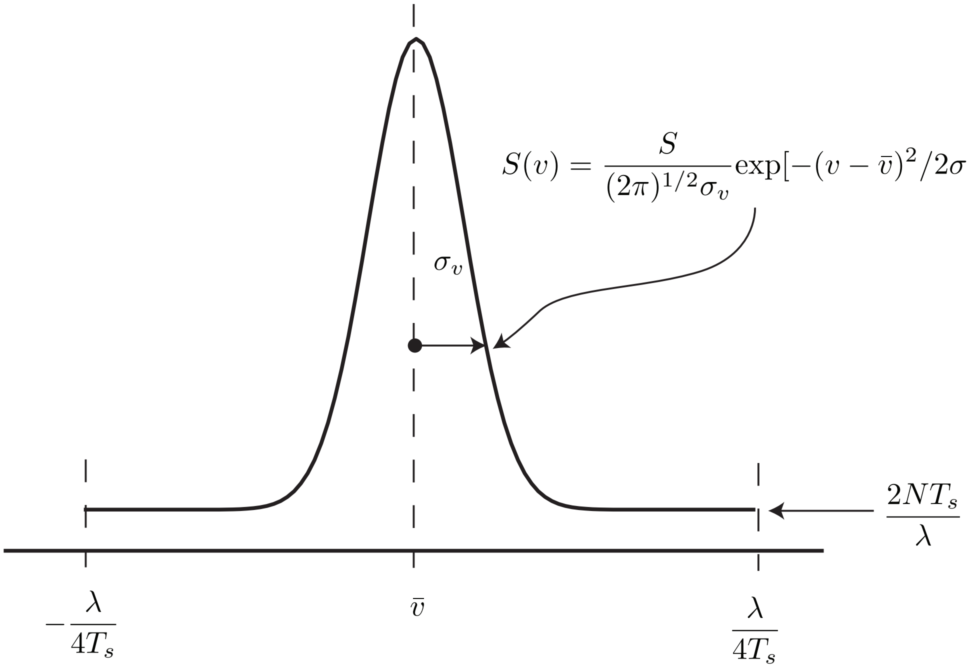

Figure 2.10: Gaussian spectral model. A model of a weather spectrum is shown. It is based on the assumption of an exponential radiation pattern and a uniform shear field. Under these assumptions, the weather spectrum can be completely described by knowing S, σ_v, $\bar{v}$, and N.

Assuming a narrow spectrum width compared to v_a, an unaliased power spectrum with a Gaussian shape is plotted in Figure 2.10. Its shape is defined by the equation

$$S(v) \quad = \quad \frac{S}{(2\pi)^{1/2}\sigma_v}\exp[-(v-\bar{v})^2/2\sigma_v^2] + \frac{2NT_s}{\lambda}, \qquad -\frac{\lambda}{4T_s} \leq v \leq \frac{\lambda}{4T_s}, \tag{2.27}$$

where S is the total power contributed from the scatterers, $\bar{v}$ is the mean velocity, σ_v is the spectrum width, and N is the receiver noise power. The amplitude of the power spectrum ranges from $\frac{2NT_s}{\lambda}$ to $\frac{S}{(2\pi)^{1/2}\sigma_v} + \frac{2NT_s}{\lambda}$, and is centered at $\bar{v}$ and has a width of σ^2. In particular, σ_v^2 is a sum of several parameters, namely

$$\sigma_v^2 \quad = \quad \sigma_s^2 + \sigma_\alpha^2 + \sigma_d^2 + \sigma_o^2 + \sigma_t^2, \tag{2.28}$$

where σ_s^2 is due to shear, σ_α^2 to antenna motion, σ_d^2 to different hydrometeor fall speeds, σ_o^2 to hydrometeor orientation and vibration, and σ_t^2 to turbulence (Doviak and Zrnić 1993). As a result, retrieving a particular σ_v value is difficult since not all of the parameters can be estimated at one time.

The autocovariance function for the above power spectrum sampled at T_s has the form

$$R(mT_s) \;=\; S\exp[-8(\pi\sigma_v mT_s/\lambda)^2]\exp[-j4\pi\bar{v}mT_s/\lambda] + N\delta(mT_s). \tag{2.29}$$

The first term expresses the autocovariance function of the atmospheric scatterers and has a Gaussian shape. It has a peak value of S at lag 0 and its magnitude decreases with increasing lag values. The second term expresses the autocovariance of the noise component and has a value of N that exists only at lag 0. These two terms are independent, and when summed, express the autocovariance function of the power spectrum of the received signal.

2.4.3 Moment Estimation Using the Autocovariance Function

The autocovariance function previously derived can be used to estimate the spectral moments of radar signals with Gaussian power spectra (Doviak and Zrnić 1993; Rummler 1968; Hyde and Perry 1958). The first three lags of the autocovariance function can be used to obtain the power, mean velocity, and spectrum width (Doviak and Zrnić 1993). Ideally, a long dwell time that produces good estimate the three lags is used. However, an estimate of the function is used when a finite sequence of echo signals is available. The estimate of the autocovariance function at lag k with M samples is

$$\hat{R}(kT_s) \;=\; \frac{1}{M-k}\sum_{m=0}^{M-k-1} V^*(mT_s)V([m+k]T_s). \tag{2.30}$$

The power is obtained by subtracting the noise power from the autocovariance function at lag 0,

$$\hat{S} \;=\; \hat{R}(0) - N. \tag{2.31}$$

The estimate of the mean velocity can be obtained from lag 1,

$$\hat{v} \;=\; -(\lambda/4\pi T_s)\arg[\hat{R}(T_s)]. \tag{2.32}$$

The spectrum width estimator is obtained from lags 0 and 1,

$$\hat{\sigma}_v \;=\; \frac{\lambda}{2\pi T_s\sqrt{2}}\left|\ln\left(\frac{\hat{S}}{|\hat{R}(T_s)|}\right)\right|^{1/2}\operatorname{sgn}\left[\frac{\hat{S}}{|\hat{R}(T_s)|}\right]. \tag{2.33}$$

The estimator uses the sgn function as a means to censor statistically inappropriate values such as when $\hat{S}$ is smaller than $|\hat{R}(T_s)|$. Additionally, lags 1 and 2, which is discussed in Doviak and Zrnić (1993), can also be used to estimate the spectrum width. Derivation of the above three equations can be found in Doviak and Zrnić (1993), and their statistical analysis can be found in Doviak and Zrnić (1993); Zrnić (1979, 1977)

2.4.4 Moment Estimation Using Spectral Analysis

Spectral moments of the radar signal can also be retrieved from the power spectrum. Like with the autocovariance function, an estimate of the power spectrum is needed for finite samples. In this case, a basic technique, called the "periodogram", which has the expression

$$\hat{S}(v) \quad = \quad \frac{1}{M}\left|\sum_{m=1}^{M} V(mT_s)\exp[j8\pi v/\lambda m T_s]\right|^2, \tag{2.34}$$

is used to estimate the true power spectrum $S(v)$. Note that the discrete-time Fourier Transform (DTFT) is used (2.34) so the velocity variable is continuous over $\pm v_a$. Additionally, a modification to the above equation can be made by adding a windowing function. The performances of a variety of windowing functions have been analyzed in Harris (1978).

The power of the radar signal is obtained by subtracting the noise power from the integrated power,

$$\hat{S} = \int_{-v_a}^{v_a} \hat{S}(v)dv - \hat{N}. \tag{2.35}$$

The mean velocity is estimated by calculating the first moment of the power spectrum,

$$\hat{v} = \frac{\int_{-v_a}^{v_a} v\hat{S}(v)dv}{\int_{-v_a}^{v_a} \hat{S}(v)dv}, \tag{2.36}$$

and the spectrum width is obtained by taking the square root of the second moment of the power spectrum,

$$\hat{\sigma}_v = \left[\frac{\int_{-v_a}^{v_a} (v-\hat{v})^2\hat{S}(v)dv}{\int_{-v_a}^{v_a} \hat{S}(v)dv}\right]^{1/2}. \tag{2.37}$$

While the equations for estimating the spectral moments from the power spectrum are relatively straightforward, the estimation of the power spectrum itself is not so. There are many such techniques, and references of some of these techniques include

Kay (1988); Haykin et al. (1991); Stoica and Moses (2005); Oppenheim and Schafer (1989).

Chapter 3

Phased Array Radars for the Atmosphere: Fundamental Theory

3.1 Review of Key Developments

Phased array radars use a collection of discrete elements as an antenna and a phasing network to control the radiation pattern (Skolnik 1990; Johnson and Dudgeon 1993; Galati 1993; Tang and Burns 1993; Haykin 1996; Nicholas 2000; Manolakis et al. 2000; Skolnik 2001; Monzingo et al. 2004; Balanis 2005; Mailloux 2005). In modern applications, the phasing is electronically controlled and the radiation pattern can be rapidly switched. As a result, phased array radars are considered to be multifunctional and can be used to provide "simultaneous" detection, tracking, and engagement of multiple targets on a pulse-to-pulse basis. While phased array radars are sophisticated devices, the basic underlying concept that these radars use is based on directive antennas which has been well understood since the mid-1920s with antennas such as the Beverage and Yagi-Uda (Beverage 1921; Uda 1926; Yagi 1928). The transition from directive antennas to early phased array systems used mechanical means to steer the beam and it was not until the mid-1950s, when ferrite phase shifters, electronic computers, and microwave printed circuits became available, that phased array system with full electronic beam steering became possible (Sarkar et al. 2006). For atmospheric applications with long wavelengths (1-6 m), phased array radars have been widely used for MST research (Hocking 1997; Palmer et al. 1998; Fukao 2007). Additionally, phased array radars are now being introduced to provide surveillance of the weather (Forsyth et al. 2002; National Research Council 2002; Forsyth et al. 2007; Zrnić et al. 2007; Weber et al. 2007). In this section, a brief introduction of key developments of the phased array radar technology is presented.

One of the earliest uses of a multiple antenna array was that of Friis (1925). The system is pictured in Figure 3.1 and consisted of an array of two loop antennas. Beam steering was obtained using a series of mechanical phase shifters and induction networks. The system was used to improve the reception of broadcast systems located in Philadelphia, New Jersey by reducing the interferences from local thunderstorms, radio transmitting ships in the Atlantic Ocean, and radio stations along the New Jersey coast. When an optimal phase shift was applied, the system was able to reduce the interferences by 8-10 dB.

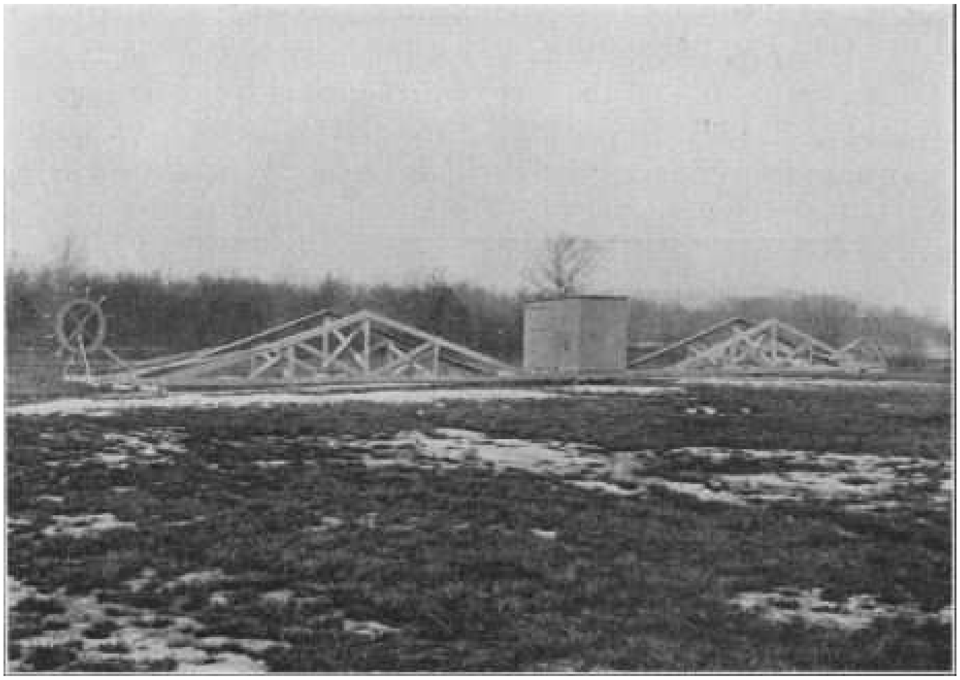

Figure 3.1: Two-loop array of Friis (1925). An early multiple antenna system. The receiving system consisted of two loop antennas, and used coherent summing to provide and improved received signal. This was achieved by phasing one of the received signal and using a condenser network to sum the other signal with it.

The concept of beam steering was extended to six more antennas by Friis and Feldman (1937). The array is pictured in Figure 3.2 and consisted of six rhombic antennas. Like its predecessor, it used a series of condenser and inductor network to phase and combine the signals from the antenna elements. The above setup was used to reduce fading by constructing a more directive receive beampattern. Compared to the results obtained using only one antenna from a signal transmitted from Rugby, England, the system was able to provide an improvement of 7-8 dB in the SNR.

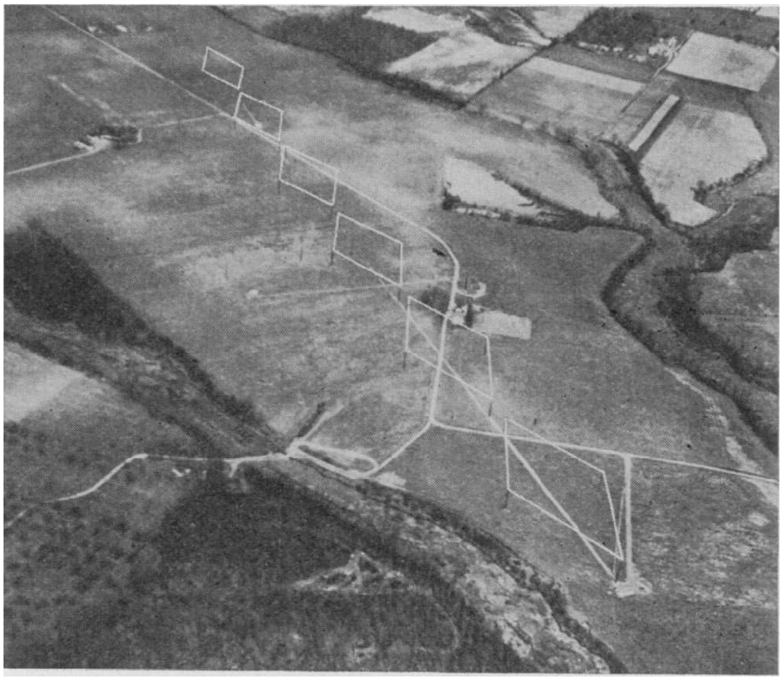

Figure 3.2: Multiple Unit Steerable Antenna (Friis and Feldman 1937). An advanced early multiple antenna system. This system consisted of six rhombic antennas, and the signals were combined using a sophisticated system of condensers and inductors. An improvement of 7-8 dB in the SNR was achieved using this system.

The use of multiple antennas in a radar system was first achieved between 1930 and 1940 using the Chain Home radars. These were military surveillance radars located along the eastern coast of Great Britain that were use for detecting and tracking incoming German aircrafts. A picture of a Chain Home radar is shown in Figure 3.3. The transmitting elements consisted of a stack of half-wave dipoles located on the metal tower. It operated by continuously flooding large swaths with pulses of electromagnetic energy. The receiving antennas were located on smaller wooden towers and sensed for the scattered energy. By comparing the ratio of the echo power between two of the received antennas an expected ratio of their radiation patterns, an angular estimate of the aircraft could be made (Scannlan 1993).

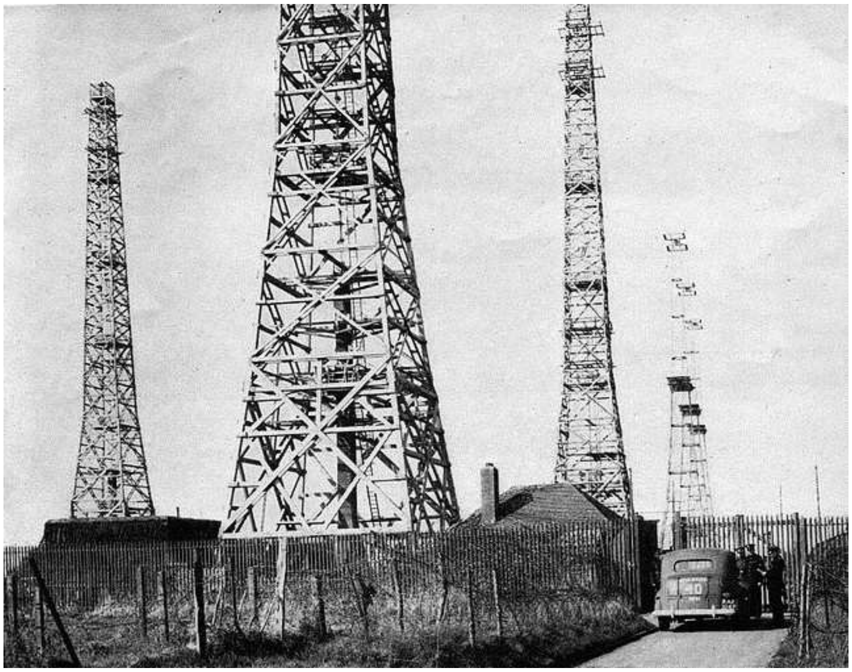

Figure 3.3: Chain Home radar (`www.ventnorradar.co.uk`). One of a collection of surveillance radars located along the eastern coast of Great Britain that was used to detect and track incoming aircrafts. These radars used multiple receive antennas to locate the targets both in elevation and azimuth. The concept that was used by these radars involved relating a ratio of the received power obtained by two antennas to the expected ratio of the received beampattern.

The next transition after the Chain Homes radar was phased array radars with mechanically driven beam steering (Fowler 1998). Some early examples were the FH Musa Shipboard Mark VII Fire Control Radar, the Foster scanner, and the Scarlzchild antenna. The FH Musa Shipboard Mark VII Fire Control Radar consisted of an end-fire Polyrod antenna and provided beam steering using mechanical means. The Foster scanner used a rapidly rotating cone inside a fixed cone to achieve phasing and beam steering, while the Scharlzchild antenna used a small secondary reflector to shift the focal point and steer its beam. These early scanners were small advances that eventually led to phased array radars with full electronic scanning.

The early development of phased array radars with full electronic scanning came after 1950. Two such early devices were the Hughes UHF AN/SPS-32 and the ARPA/Rome Air Development Center Electronically Steerable Array Radar (ESAR). The Hughes UHF AN/SPS-32 consists of a wide rectangular antenna array and is used to provide air surveillance for the US Navy. The radar was installed on the USS Long Beach and USS Enterprise and uses frequency and phase shifting to scan in 2-D. The ARPA/Rome Air Development Center Electronically Steerable Array Radar (ESAR) has a transmitter with 5,184 elements, a receiver with 19,500 elements, and stands approximately 13 stories high. The radar uses frequency translation and tapped delay lines to provide beam steering (Fowler 1998). According to `www.globalsecurity.org`, it was the first phased-array radar system designed to detect and track objects in space and could detect targets with a range in excess of 37,000 km.

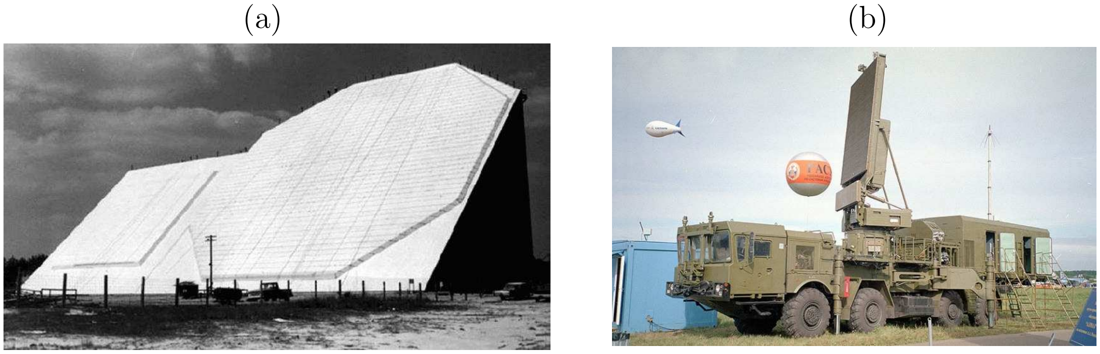
(a) (b)

Figure 3.4: (a) ESAR (`www.globalsecurity.org`) and (b) Big Bird (`ausairpower.net`). Early phased array radars with full electronic beam steering capabilities. Mostly used by the military, these radars could detect, track, and engage foreign targets such as aircraft and missiles at far ranges and with great precision.

Numerous phased array radars now exist, while most are operated by the military. From Brookner (2002), most of these radars are included in Table 3.1. In the U.S., they include passive devices such as the AN/TPN-25, AN/GPN-22, COBRA

DANE, COBRA JUDY, PATRIOT, AEGIS SPY-1, B-1, AN/TPQ-37, and AN/TPQ-36. There are also active devices such as the PAVE PAWS, BMEWS, AN/TPS-59, ROTHR. Internationally, they include passive devices such as the Italy/UK EMPAR, France ARABEL, Sweden ARTHUR, Russia FLAP LID, India SAM, and France RBE2. As for active devices, there are the Sweden ERIEYE, UK MARTELLO, Israel PHALCON, and the Israel ATBM EL/M.

Table 3.1: Phased Array Radars (Brookner 2002)

USA	
Passive	Active
AN/TPN-25 (18)	PAVE PAWS (4)
AN/GPN-22 (60)	BMEWS (2)
COBRA DANE (1)	AN/TPS-59 (50)
COBRA JUDY (1)	ROTHR
PATRIOT (173)	
AEGIS SPY-1 (234)	
B-1 (100)	
AN/TPQ-37 (102)	
AN/TPQ-36 (243)	
INTERNATIONAL	
Passive	Active
Italy/UK EMPAR	Sweden ERIEYE
France ARABEL	UK MARTELLO
Sweden ARTHUR	Israel PHALCON
Russia FLAP LID (<100)	Israel ATBM EL/M
India SAM	
France RBE2	

3.2 Basic Design Concepts of Phased Array Radars

Phased array radars use a collection of discrete elements as an antenna and a phasing network to obtain a directive radiation pattern. Usually, the radiation pattern of each discrete element is relatively wide and its gain is low. By combining the signals from each element in an optimal fashion called *beamforming*, a highly directive radiation pattern can be achieved (Balanis 2005). The general design of phased arrays are categorized using three basic designs: analog-passive, analog-active, and digital beamformer (Mailloux 2005). Each design is distinguished by how the power is distributed to the discrete elements. Specific details of the designs are further discussed in Billetter (1989); Skolnik (1990); Parker and Zimmermann (2002); Mailloux (2005); Bhattacharyya (2006).

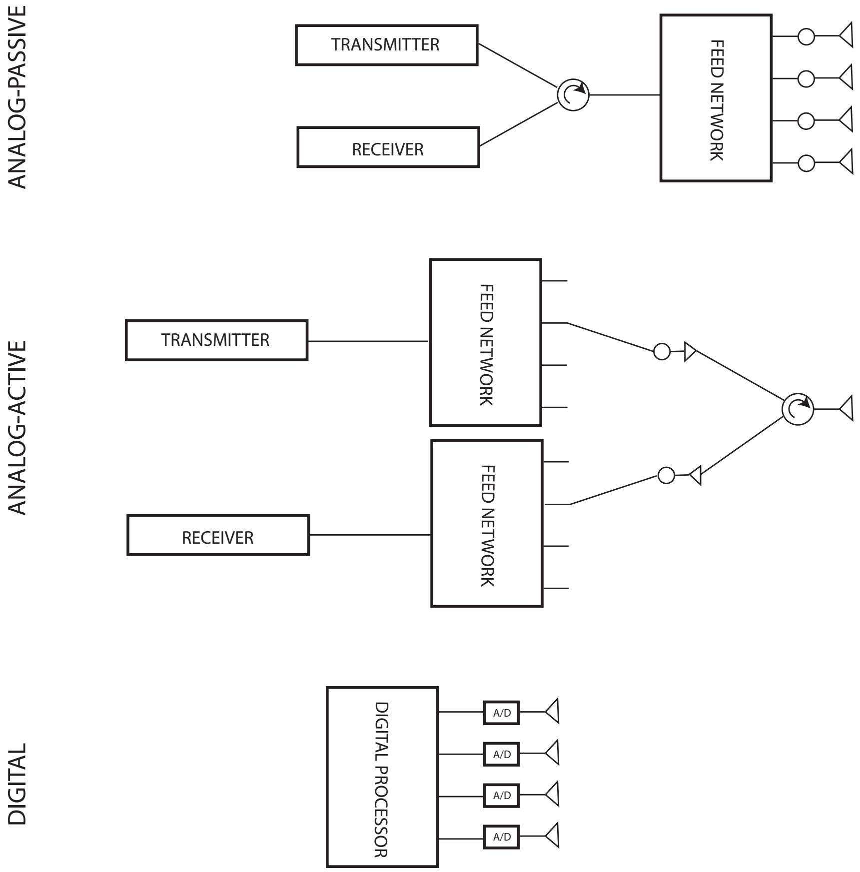

Figure 3.5: Architectures of phased array radars (Mailloux 2005). The three basic designs of phased array radars are shown. The designs are different based on the location and size of the transmitter.

The analog-passive design shown at the top of Figure 3.5 is the most common architecture used in modern phased array radars. The design is characterized by a central transmitter and is constructed to minimize system losses. To accomplish this, a single but powerful transmitter and low-loss waveguides are used. In the transmit mode, the transmitter outputs a high power pulse of radio energy and via a duplexer, the power is transfered to a feed network and distributed to each antenna. In the received mode, the scattered signal at each antenna element is phased and then transfered to the feed network that combines all the signals. The combined signal is then processed by the receiver.

The analog-active design shown at the middle of Figure 3.5 is a less commonly used architecture. While each element contains an amplifier and a transmit/receive feed network, many of the same components found in the analog-passive architecture are still used. A powerful central transmitter is not needed, but a central transmitter transmitter is used to provide a coherent input signal. In the transmit mode, the low power signal is distributed using a feed network to each antenna element, where the signal is then amplified, phased, and transmitted. In the received mode, the scattered signal at each element is amplified and phased, and each signal is combined via a feednetwork and sent to the receiver.

The digital beamforming design shown at the bottom of Figure 3.5 is the most unique and desirable. The layout is simple and consists of a digital processor, antenna elements, and individual means for controlling the amplitude and phase of each signal. In the transmit mode, the digital processor sends control signals to each amplifier and selects the transmit weighting pattern. Each antenna element then manufactures and radiates the selected transmit signal. In the received mode, the scattered signal at each element is individually demodulated to baseband and broadcasted to the digital processor that combines them in an optimal sense.

While many designs of phased array radars exist, the fundamental concept is phase shifting that produces a directive radiation pattern. The objective is obtained by examining the phase of a signal of wavelength λ transiting a line of length l at a velocity v,

$$\phi \quad = \quad 2\pi l/\lambda \quad = \quad 2\pi f/v \quad = \quad 2\pi f l\sqrt{\mu\epsilon} \tag{3.1}$$

where the frequency $f = v/\lambda$, $\mu =$ permeability and $\epsilon =$ permittivity. Phase shifting, as a result, can be accomplished by changing l, λ, f, μ or ϵ.

3.3 Signal Model for Phased Array Antennas

The signal model expresses the output signal of an antenna array in terms of the received signals. It is derived from basic electromagnetic theory and illustrates the processed signal that is obtained with a multi-element array. The derivation of the signal model starts by describing the radiation field of a single antenna element and then extending the result to an arbitrary array such elements. In the following, a signal model of a uniform linear array (ULA) is derived for an array of rectangular-shaped radiators commonly found in phased array radars. Extension of this signal model to an arbitrarily configured array is straightforward.

Consider the geometry of a rectangular aperture radiator shown in Figure 3.6 with an infinitesimally small width ($D_x/\lambda \ll 50$) and located at the origin. From Balanis (2005), the far-field electrical intensity $E_\theta(R)$ of the radiator at distance R is the inverse Fourier transform of the current distribution $A(y')$ over the face of the radiating element and has the expression

$$E_\theta(R) \approx j\eta_i \frac{2\pi \exp[-j2\pi R/\lambda]}{4\pi R} \sin(\theta) \left[\int_{-D_y/2}^{D_y/2} A(y') \exp\left[j2\pi y' \cos(\theta)/\lambda\right] dy' \right], \tag{3.2}$$

where the intrinsic impedance of space is η_i. At large R, incremental changes in R primarily affect the phase and only negligibly the magnitude of $E_\theta(R)$.

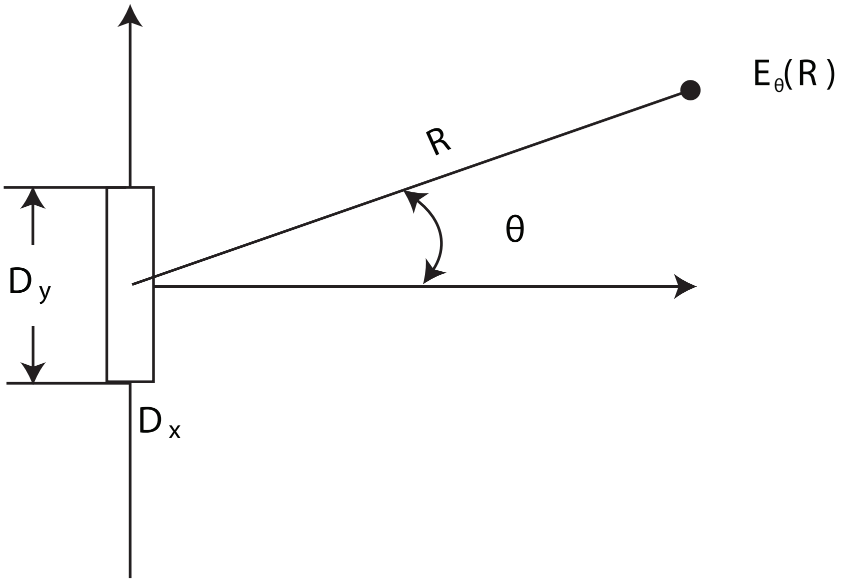

Figure 3.6: Far-field for a rectangular aperture radiator. A configuration for the electric field at far field is shown. For a fixed angle, the electric field depends only the range and wavelength. Additionally, for incremental changes of the range, the magnitude of the electric field is approximately constant while its phase changes with a rate that depends on the wavelength.

Now consider the geometry of an array of such rectangular aperture radiators shown in Figure 3.7. There are L elements, each element is separated by a distance d from its neighbor, and a single radiating source is located at the angle θ normal to the array. Suppose through reciprocity, the baseband voltage (also in reference

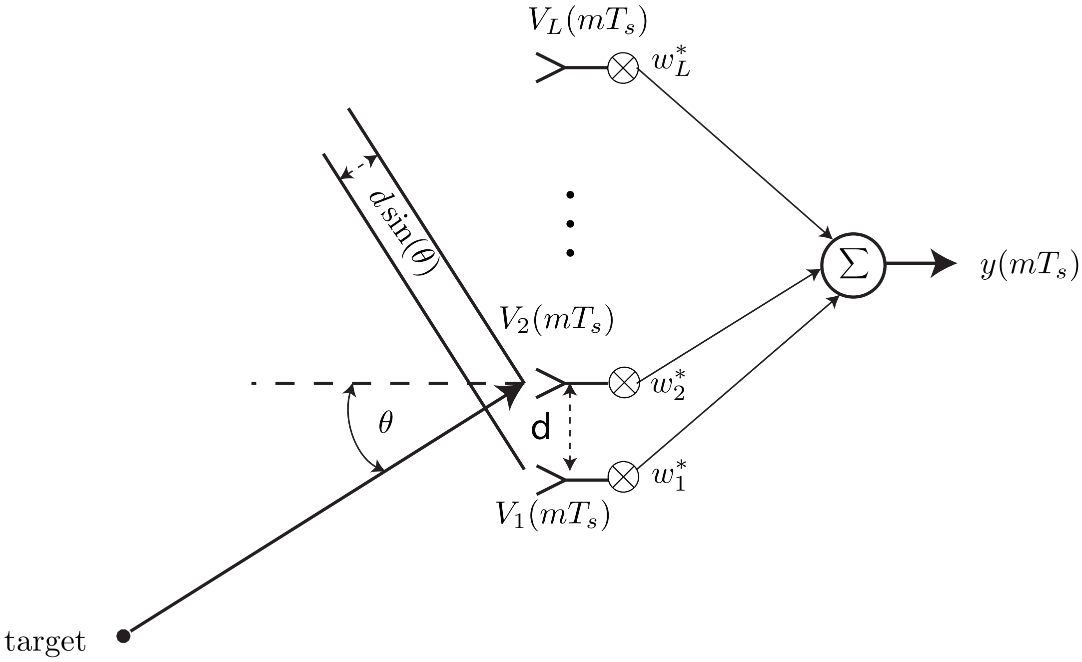

Figure 3.7: Configuration of a linear array. Assuming far-field propagation, the difference of the signal measure at each antenna is a phase. In this configuration, the output signal of the array is a weighted sum of the signals at each element.

to the in-phase and quadrature components) of a reference element is expressed as $V(mT_s) \propto E_\theta(R)$ and is weighted by a complex factor w^*. The output voltage of the array is

$$y(mT_s) \;=\; V(mT_s)\sum_l w_l^* \exp\left[-j2\pi\frac{(l-1)d\sin(\theta_i)}{\lambda}\right]. \tag{3.3}$$

where

$$AF(\theta) \;=\; \sum_l w_l^* \exp\left[-j2\pi\frac{(l-1)d\sin(\theta)}{\lambda}\right] \tag{3.4}$$

is called the *array factor* and it expresses the contribution of scatterers to the output signal.

With multiple radiating sources, the output signal is

$$\begin{aligned} y(mT_s) &= \sum_i V^i(mT_s)\sum_l w_l^* \exp\left[-j2\pi\frac{(l-1)d\sin(\theta_i)}{\lambda}\right] \\ &= \sum_l w_l^* \sum_i V^i(mT_s)\exp\left[-j2\pi\frac{(l-1)d\sin(\theta_i)}{\lambda}\right], \end{aligned} \tag{3.5}$$

where $V^i(mT_s)$ and θ_i denote the reference voltage measured for the i^{th} scatterer and its impinging angle, respectively. Let $V_l(mT_s) = \sum_i V^i(mT_s)\exp\left[-j2\pi\frac{(l-1)d\sin(\theta_i)}{\lambda}\right]$

denote the output signal measured at the l^{th} element in order to simplify the above expression to

$$y(mT_s) \quad = \quad \sum_l w_l^* V_l(mT_s). \tag{3.6}$$

Additionally, let $\mathbf{v}(mT_s) = \begin{bmatrix} V_1(mT_s) & \cdots & V_L(mT_s) \end{bmatrix}^T$ and $\mathbf{w} = \begin{bmatrix} w_1 & \cdots & w_L \end{bmatrix}^T$, where $(\cdot)^T$ is the transpose. The output voltage of the ULA can be expressed as a vector multiplication of the form

$$y(mT_s) \quad = \quad \mathbf{w}^H \mathbf{v}(mT_s). \tag{3.7}$$

The extension of the above equation for arbitrarily configured array can be obtained by changing the R of each element.

3.3.1 Implications of the Array Factor

Previously, the array factor was defined as

$$AF(\theta) \quad = \quad \sum_l w_l^* \exp\left[-j2\pi \frac{(l-1)d\sin(\theta)}{\lambda}\right]. \tag{3.8}$$

The usefulness of this parameter can be illustrated in an example using a uniform linear array with unity weights $w_l^* = 1$. Between the two closest elements, a phase difference of $2\pi d\sin(\theta)/\lambda$ is obtained. The phase difference is always less than π and is unique when d/λ is smaller than 1/2, while the phase difference can be larger than π and ambiguously measured when d/λ is larger than 1/2. An illustration of this angular aliasing phenomenon is shown in Figure 3.8 for three d/λ ratios of 1/2, 1, and 2. A unique phase is measured for each θ when $d/\lambda = 1/2$, while multiple phases can be observed for the same θ when $d/\lambda > 1/2$. The example shows that two θ values can be produced for the same phase when $d/\lambda = 1$ and four θ when $d/\lambda = 2$, etc. While simple, the results demonstrate tehe effects of aliasing when spatial undersampling is employed.

Additionally, the array factor of a ULA with L elements can be expressed as

$$AF(\theta) \quad = \quad \exp\left[j\frac{(L-1)\pi d\sin(\theta)}{\lambda}\right] \frac{\sin\left(\frac{Ld\pi\sin(\theta)}{\lambda}\right)}{\sin\left(\frac{d\pi\sin(\theta)}{\lambda}\right)} \tag{3.9}$$

with an absolute value of

$$|AF(\theta)| \quad = \quad \frac{\sin\left(\frac{Ld\pi\sin(\theta)}{\lambda}\right)}{\sin\left(\frac{d\pi\sin(\theta)}{\lambda}\right)}. \tag{3.10}$$

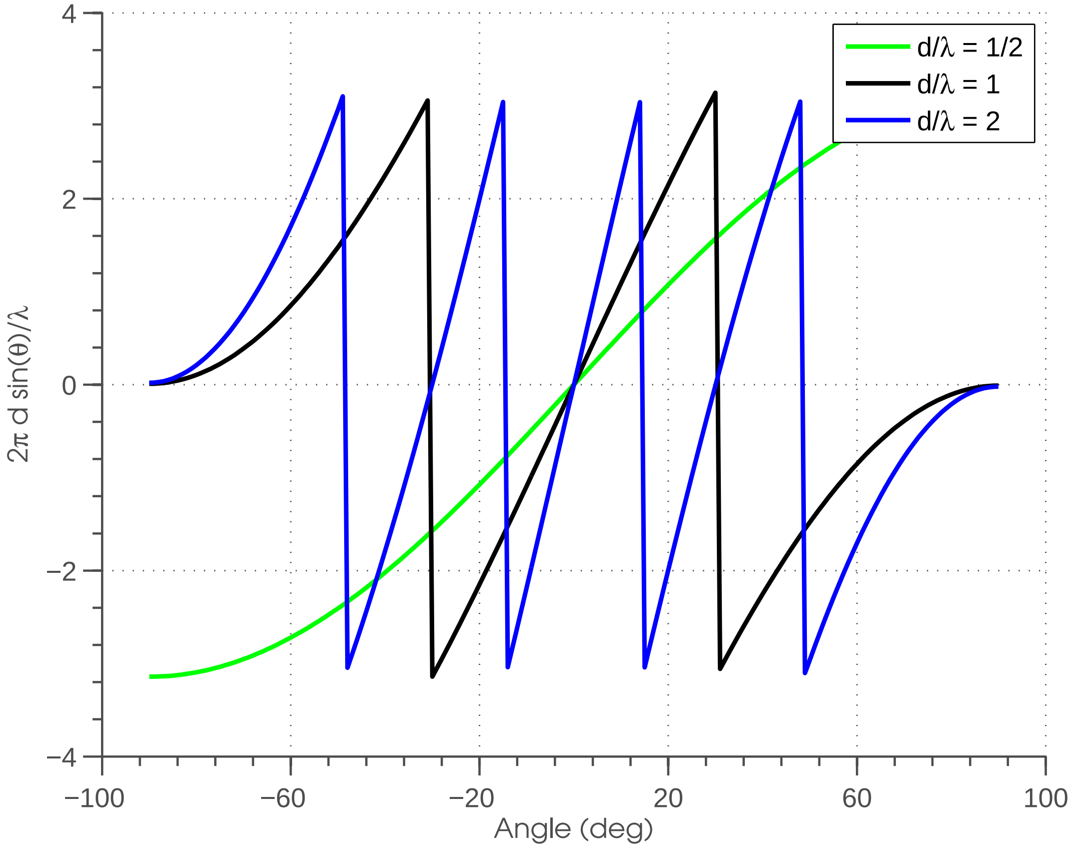

Figure 3.8: Plot of the phase difference between two antenna elements. The phase difference is plotted for three element spacing for different angle-of-arrivals. Phase wrapping occurs when the d/λ is greater than $1/2$. When this occurs, the same phase can be associated with multiple angles-of-arrival.

The latter parameter can be used as a proxy of the array resolution by considering the angle where the $|AF| = 0$, which is $\dfrac{Ld\pi \sin(\theta_{\text{null}})}{\lambda} = \pm\pi$. Solving for θ_{null} gives

$$\theta_{\text{null}} \quad = \quad \pm \sin^{-1}\left(\frac{\lambda}{Ld}\right). \tag{3.11}$$

θ_{null} decreases when λ becomes smaller or Ld becomes larger. Some examples of θ_{null} for a linear array with various L and d/λ are given in Figure 3.9.

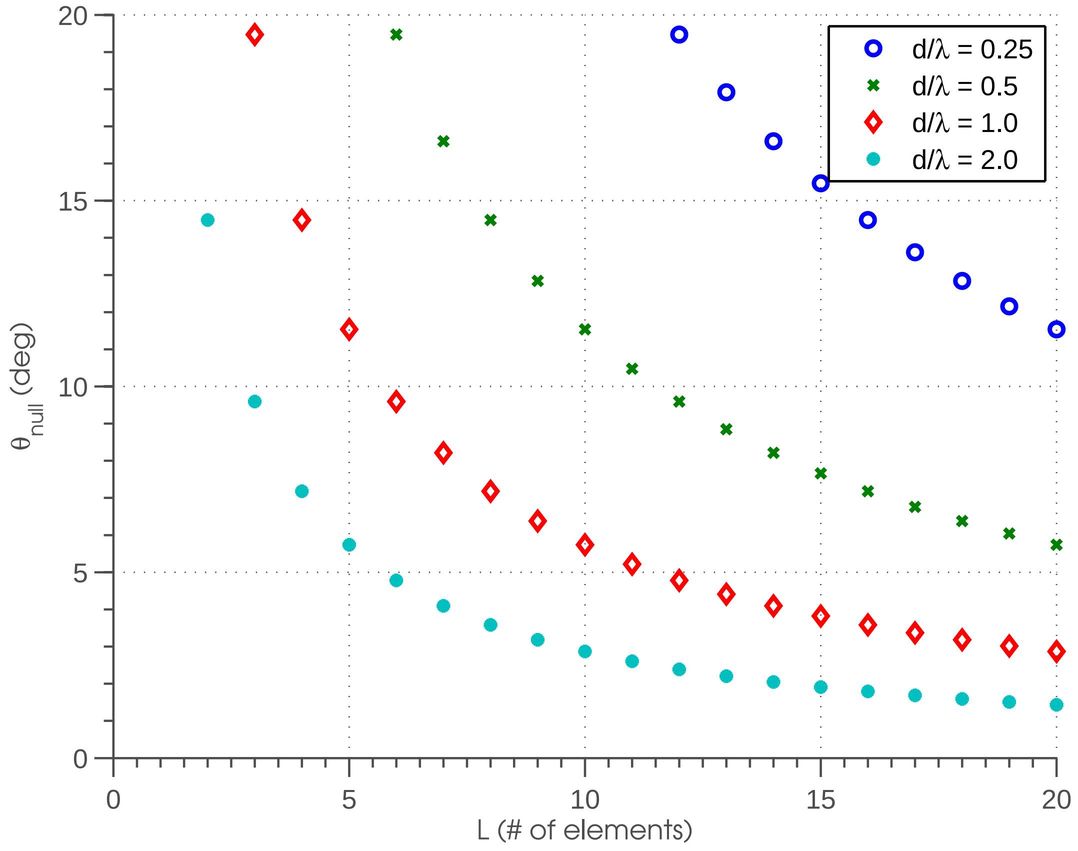

Figure 3.9: Illustration of resolution for a ULA. Equation (3.10) is plotted for various L and d/λ. This equation, which expresses the width of the mainlobe, is used as a proxy for the array resolution. As can be observed, the width of the mainlobe decreases with larger L or d/λ.

3.4 Spatial Processing for Phased Array Antennas

The array factor $AF(\theta)$ can be designed by choosing $\mathbf{w}^H$ under specific constraints. Methods for designing the weights include parametric and non-parametric techniques, while constraints that are commonly used include mainlobe gain and width, sidelobe suppression, locations of nulls, etc. References to some of the design techniques and constraints are discussed in details in Haykin (1996); Manolakis et al. (2000); Stoica and Moses (2005), among others. In cases of one and two-dimension arrays, the design of the array factor is similar in many respects to that of temporal filters. In other more complicated cases, the design of the array factor is not straightforward and iterative schemes may be needed. For atmospheric radar applications, the scatterers are randomly distributed and their motions cannot be easily modeled using parametric techniques. As a result, only non-parametric techniques are considered in this study.

3.4.1 Conventional Non-Adaptive Spatial Processing

One of the simplest techniques of designing the array factor is to choose $\mathbf{w}^H$ such that certain beampattern constraints are satisfied. The technique presented is based on a linear minimization of the noise gain ($\mathbf{w}^H\mathbf{w}$) and sidelobe levels, and is obtained using the expression

$$\min_{\mathbf{w}}\{\mathbf{w}^H\mathbf{w}\} \quad \text{subject to} \quad \mathbf{w}^H\mathbf{A}(\theta) = \mathbf{c}, \tag{3.12}$$

where the steering matrix is $\mathbf{A}(\theta) = \begin{bmatrix} \mathbf{a}(\theta_1) & \mathbf{a}(\theta_2) & \dots & \mathbf{a}(\theta_M) \end{bmatrix}$, steering vectors $\mathbf{a}(\theta)$, and the constraint vector is $\mathbf{c} = \begin{bmatrix} c_1 & c_2 & \dots & c_M \end{bmatrix}^T$. Assuming $M \leq L$, $\mathbf{w}^H\mathbf{a}(\theta_1) = c_1$, $\mathbf{w}^H\mathbf{a}(\theta_1) = c_2$, etc., the solution to (3.12) is given by Stoica and Moses (2005)

$$\mathbf{w}_o = \mathbf{A}(\theta)\left(\mathbf{A}(\theta)^H\mathbf{A}(\theta)\right)^{-1}\mathbf{c}^H, \tag{3.13}$$

which is unique when rank$(\mathbf{A}(\theta)^H\mathbf{A}(\theta)) = M$ and $\left(\mathbf{A}(\theta)^H\mathbf{A}(\theta)\right)^{-1}$ exists. Otherwise, a pseudo inverse of $\left(\mathbf{A}(\theta)^H\mathbf{A}(\theta)\right)$ can be used when rank$(\mathbf{A}(\theta)^H\mathbf{A}(\theta)) \leq L$.
The solution satisfies the constraint since

$$\begin{aligned}
\mathbf{w}_o^H\mathbf{A}(\theta) &= \left[\mathbf{A}(\theta)\left(\mathbf{A}(\theta)^H\mathbf{A}(\theta)\right)^{-1}\mathbf{c}^H\right]^H\mathbf{A}(\theta) \\
&= \mathbf{c}\left[\left(\mathbf{A}(\theta)^H\mathbf{A}(\theta)\right)^{-1}\right]^H\mathbf{A}^H(\theta)\mathbf{A}(\theta) \\
&= \mathbf{c}\left[\mathbf{A}(\theta)^H\mathbf{A}(\theta)\right]^{-1}\left[\mathbf{A}^H(\theta)\mathbf{A}(\theta)\right] \\
&= \mathbf{c}.
\end{aligned} \tag{3.14}$$

In order to see that the solution is optimal, let $\mathbf{w}_\triangle \in \mathcal{C}^{L\times 1}$ and notice that the constraint is satisfied in (3.14). Now, if $\mathbf{w} = \mathbf{w}_o + \mathbf{w}_\triangle$, and $\mathbf{w}_o^H\mathbf{A}(\theta) = \mathbf{c}$, then $\mathbf{w}_\triangle^H\mathbf{A}(\theta)$ must be $\mathbf{0}$. Therefore,

$$\mathbf{w}^H\mathbf{w} = \mathbf{w}_o^H\mathbf{w}_o + \mathbf{w}_\triangle^H\mathbf{w}_o + \mathbf{w}_o^H\mathbf{w}_\triangle + \mathbf{w}_\triangle^H\mathbf{w}_\triangle \tag{3.15}$$

Notice that $\mathbf{w}_{\triangle}^{H}\mathbf{w}_{\triangle} \geq 0$. Now, observe that

$$\begin{aligned}
\mathbf{w}_{\triangle}^{H}\mathbf{w}_{o} &= \mathbf{w}_{\triangle}^{H}\left[\mathbf{A}(\theta)\left[\mathbf{A}^{H}(\theta)\mathbf{A}(\theta)\right]^{-1}\mathbf{c}^{H}\right] \\
&= \mathbf{w}_{\triangle}^{H}\mathbf{A}(\theta)\left[\mathbf{A}^{H}(\theta)\mathbf{A}(\theta)\right]^{-1}\mathbf{c}^{H} \\
&= \mathbf{w}_{\triangle}^{H}\mathbf{A}(\theta)\left[\mathbf{A}^{H}(\theta)\mathbf{A}(\theta)\right]^{-1}\mathbf{c}^{H} \\
&= \mathbf{0}\left[\mathbf{A}^{H}(\theta)\mathbf{A}(\theta)\right]^{-1}\mathbf{c}^{H} \\
&= 0. \qquad (3.16)
\end{aligned}$$

Conversely, it is obvious that $\mathbf{w}_{o}^{H}\mathbf{w}_{\triangle} = 0$. From this, the perturbation produces positive values and implies that $\mathbf{w}_{o}$ is the optimal solution.

3.4.1.1 Fourier Beamforming

For the special case of a single constraint, (3.12) simplifies to

$$\min_{\mathbf{w}}\left\{\mathbf{w}^{H}\mathbf{w}\right\} \quad \text{subject to} \quad \mathbf{w}^{H}\mathbf{a}(\theta) = 1, \qquad (3.17)$$

which has the solution

$$\mathbf{w}_{o} = \mathbf{a}(\theta)/L, \qquad (3.18)$$

and is the weights commonly observed of the Fourier beamformer. The solution produces a unity gain at the steered direction and the minimum noise gain.

Some examples of spatial processing using the Fourier beamformer are shown in Figure 3.10. The Fourier beamformer was applied to a ULA with $d/\lambda = 1/2$ and $d/\lambda L = 16$ and steered at 0°, 15°, 30°, and 45°. The results show that the width of the mainlobe of the beamformer is smallest at 0° and increases as the steered angle is changed from 0° to 45°, while the sidelobe level stays the same except that is angle changes.

3.4.1.2 Spatial Windowing

The results in Figure 3.10 show that $\mathbf{w}^{H}\mathbf{a}(\theta_n) \neq 0$ when $\theta \neq \theta_n$ at most angles. The phenomenon is called spectral leakage and is observed for all finite-aperture arrays. The phenomenon is caused by the assumed periodic extension of the Fourier beamformer and manifests as non-zero gain away from the steered angle. The effects of spectral leakage can be reduced by windowing the Fourier beamforming weights to attenuate the first and second-order discontinuities at the edge of the array at the cost of an increase in the mainlobe width. Commonly used windows are discussed in Harris

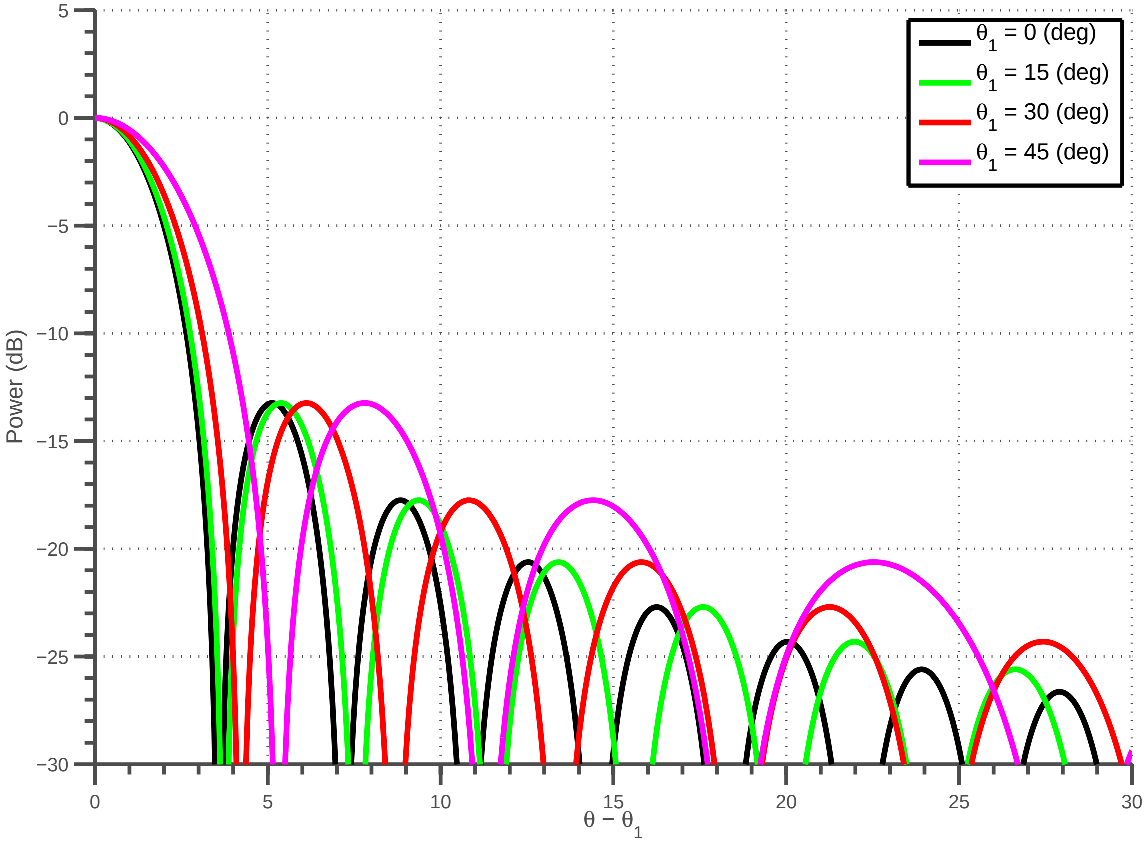

Figure 3.10: Fourier beamforming. Shown are some examples of the Fourier beampattern obtained for a ULA with $d/\lambda = 1/2$ and $d/\lambda L = 16$. As can be observed, the mainlobe increases when steered away from normal to the array.

(1978); Kay (1988); Oppenheim and Schafer (1989); Haykin et al. (1991); Stoica and Moses (2005), among others, and include the triangular, von Hann, Blackman, and Chebyshev windows. A plot of the beampatterns for a ULA array with $d/\lambda = 1/2$ and $d/\lambda L = 16$ that has the above windows applied is shown in Figure 3.11. The beampatterns show that a trade-off is obtained between spectral leakage and mainlobe resolution when the windows are applied.

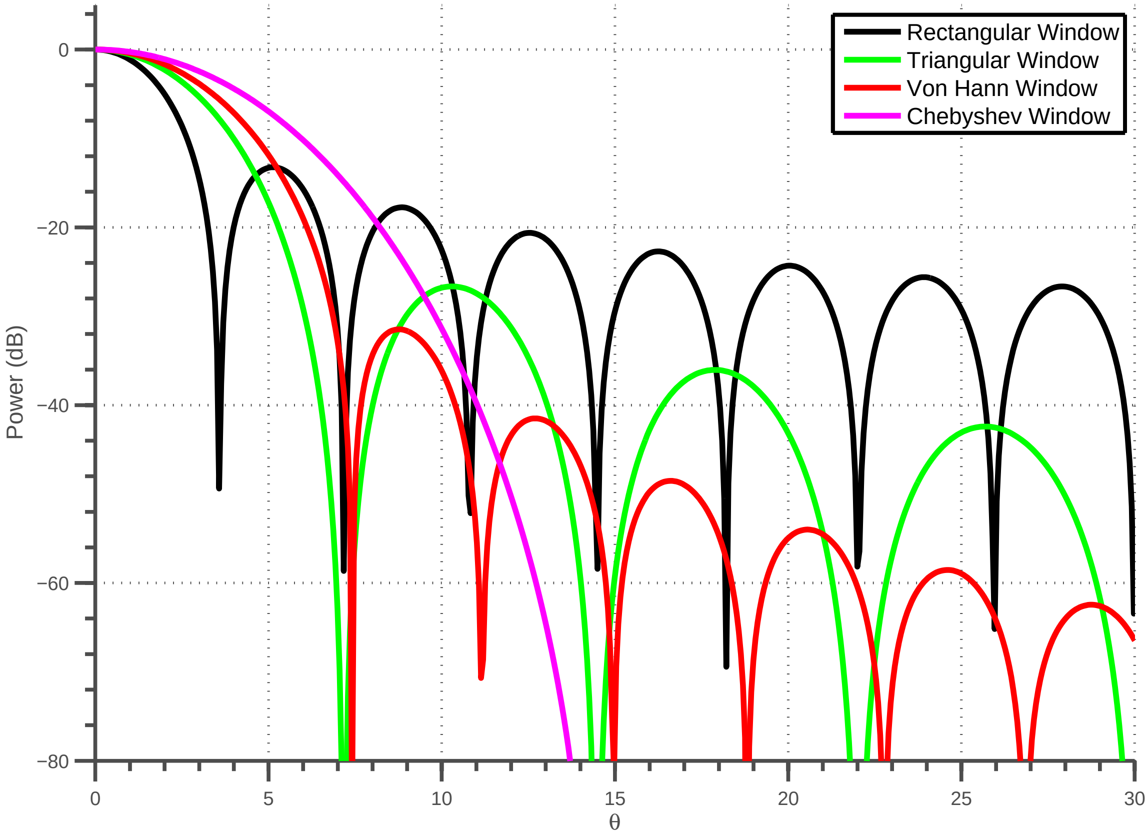

Figure 3.11: Windowing effects. A plot of the beampattern is shown for rectangular, triangular, von Hann, Blackman, and Chebyshev windows. As can be observed, a trade-off between sidelobe level and mainlobe width is obtained between the windows. In these cases, a small mainlobe width results in a larger sidelobe level, while a larger mainlobe width produces sidelobes with smaller gains.

3.4.2 Fully Adaptive Spatial Processing Using Linear Constraints

When time series data are available for an array of receivers, the signals can be used to obtain an optimal set of $\mathbf{w}^H$ with beampattern constraints. A commonly used minimization scheme for obtaining the weights is

$$\min_{\mathbf{w}}\left\{\mathbf{w}^H\mathbf{R}\mathbf{w}\right\} \quad \text{subject to} \quad \mathbf{w}^H\mathbf{A}(\theta) = \mathbf{c}, \tag{3.19}$$

where the covariance matrix is given by

$$\mathbf{R} \;=\; \mathrm{E}\left\{\mathbf{v}(mT_s)\mathbf{v}^H(mT_s)\right\} \tag{3.20}$$

and is assumed to be Hermitian positive definite. Under this assumption, the solution is unique and has the expression

$$\mathbf{w}_o \;=\; \mathbf{R}^{-1}\mathbf{A}(\theta)\left[\mathbf{A}^H(\theta)\mathbf{R}^{-1}\mathbf{A}(\theta)\right]^{-1}\mathbf{c}^H. \tag{3.21}$$

The optimal weights, therefore, depend on the covariance matrix and the received time series signals. Additionally, the solution is similar to the form observed in (3.13) with the covariance matrix being $\mathbf{I}$. To prove the solution is optimal, first observe that the solution satisfies the constraint,

$$\begin{aligned}
\mathbf{w}_o^H\mathbf{A}(\theta) &= \left[\mathbf{R}^{-1}\mathbf{A}(\theta)\left[\mathbf{A}^H(\theta)\mathbf{R}^{-1}\mathbf{A}(\theta)\right]^{-1}\mathbf{c}^H\right]^H\mathbf{A}(\theta)\\
&= \mathbf{c}\left[\mathbf{R}^{-1}\mathbf{A}(\theta)\left[\mathbf{A}^H(\theta)\mathbf{R}^{-1}\mathbf{A}(\theta)\right]^{-1}\right]^H\mathbf{A}(\theta)\\
&= \mathbf{c}\left[\left[\mathbf{A}^H(\theta)\mathbf{R}^{-1}\mathbf{A}(\theta)\right]^{-1}\right]^H\mathbf{A}^H(\theta)(\mathbf{R}^{-1})^H\mathbf{A}(\theta)\\
&= \mathbf{c}\left[\mathbf{A}^H(\theta)\left(\mathbf{R}^{-1}\right)^H\mathbf{A}(\theta)\right]^{-1}\mathbf{A}^H(\theta)\left(\mathbf{R}^{-1}\right)^H\mathbf{A}(\theta)\\
&= \mathbf{c}.
\end{aligned} \tag{3.22}$$

To see that $\mathbf{w}_o$ is a unique solution, let $\mathbf{w} = \mathbf{w}_o + \mathbf{w}_\triangle$. Because of the constraint, $\mathbf{w}_\triangle^H\mathbf{A}(\theta)$ must equal $\mathbf{0}$. Applying the weight perturbation to the output power gives

$$\mathbf{w}^H\mathbf{R}\mathbf{w} \;=\; \mathbf{w}_o^H\mathbf{R}\mathbf{w}_o + \mathbf{w}_\triangle^H\mathbf{R}\mathbf{w}_o + \mathbf{w}_o^H\mathbf{R}\mathbf{w}_\triangle + \mathbf{w}_\triangle^H\mathbf{R}\mathbf{w}_\triangle \tag{3.23}$$

Since $\mathbf{R}$ is positive definite, $\mathbf{w}_\triangle^H\mathbf{R}\mathbf{w}_\triangle \geq 0$. Now, observe that

$$\begin{aligned}
\mathbf{w}_\triangle^H\mathbf{R}\mathbf{w}_o &= \mathbf{w}_\triangle^H\mathbf{R}\left[\mathbf{R}^{-1}\mathbf{A}(\theta)\left[\mathbf{A}^H(\theta)\mathbf{R}^{-1}\mathbf{A}(\theta)\right]^{-1}\mathbf{c}^H\right]\\
&= \mathbf{w}_\triangle^H\mathbf{A}(\theta)\left[\mathbf{A}^H(\theta)\mathbf{R}^{-1}\mathbf{A}(\theta)\right]^{-1}\mathbf{c}^H\\
&= \mathbf{w}_\triangle^H\mathbf{A}(\theta)\left[\mathbf{A}^H(\theta)\mathbf{R}^{-1}\mathbf{A}(\theta)\right]^{-1}\mathbf{c}^H\\
&= \mathbf{0}\left[\mathbf{A}^H(\theta)\mathbf{R}^{-1}\mathbf{A}(\theta)\right]^{-1}\mathbf{c}^H\\
&= 0.
\end{aligned} \tag{3.24}$$

Similarly, it is easy to show that $\mathbf{w}_o^H \mathbf{R} \mathbf{w}_\triangle = 0$. From this, it can be observed that $\mathbf{w}_o$ provides the optimal solution.

3.4.2.1 Diagonal Loading

Diagonal loading is a commonly used technique in spatial processing for making adaptive algorithms robust. The process is needed when the elements of the arrays are miscalibrated or when the statistics of the covariance matrix is poorly estimated. In these situations, the optimal adaptive weights can produce results worse than applying conventional beamforming. To provide improved estimates, the adaptive algorithm is regularized and a constant diagonal matrix is generally added to the covariance matrix (Press et al. 1992). In this setup, the diagonal loading is denoted by the γ symbol, and the minimization problem of (3.19) with diagonal loading is expressed as

$$\min_{\mathbf{w}} \left\{ \mathbf{w}^H \mathbf{R} + \gamma \mathbf{I} \mathbf{w} \right\} \quad \text{subject to} \quad \mathbf{w}^H \mathbf{A}(\theta) = \mathbf{c}. \tag{3.25}$$

By substituting $\mathbf{R}^{'} = \mathbf{R} + \gamma \mathbf{I}$, the minimization problem with diagonal loading has the solution

$$\mathbf{w}_o \;=\; (\mathbf{R}^{'})^{-1} \mathbf{A}(\theta) \left[\mathbf{A}^H(\theta) (\mathbf{R}^{'})^{-1} \mathbf{A}(\theta) \right]^{-1} \mathbf{c}^H. \tag{3.26}$$

The solution has a similar expression as (3.21) except that $\mathbf{R}$ is now $\mathbf{R}^{'}$.

3.4.2.2 High Clutter-to-Signal Ratio

When γ is significantly larger than the actual noise power,

$$\mathbf{R} \;\approx\; \gamma \mathbf{I} + \mathbf{A}(\theta) \mathbf{S} \mathbf{A}^H(\theta), \tag{3.27}$$

where $\mathbf{S}$ is the source covariance matrix of the source echo voltage. Following Van Trees (2002) and using the matrix inversion lemma,

$$\begin{aligned}
\mathbf{R}^{-1} &\approx \left[\gamma \mathbf{I} + \mathbf{A}(\theta) \mathbf{S} \mathbf{A}^H(\theta) \right]^{-1} \\
&= \frac{1}{\gamma} \mathbf{I} - \frac{1}{\gamma} \mathbf{A}(\theta) \left[\mathbf{I} + \mathbf{S} \mathbf{A}^H(\theta) \frac{1}{\gamma} \mathbf{A}(\theta) \right]^{-1} \mathbf{S} \mathbf{A}^H(\theta) \frac{1}{\gamma} \\
&= \frac{1}{\gamma} \left[\mathbf{I} - \mathbf{A}(\theta) \left[\mathbf{I} + \mathbf{S} \frac{1}{\gamma} \mathbf{A}^H(\theta) \mathbf{A}(\theta) \right]^{-1} \mathbf{S} \frac{1}{\gamma} \mathbf{A}^H(\theta) \right]
\end{aligned} \tag{3.28}$$

If the sources are uncorrelated,

$$\mathbf{S} = \begin{bmatrix} \gamma_1 & & 0 & \\ & \gamma_2 & & \\ & 0 & \ddots & \\ & & & \gamma_M \end{bmatrix}, \tag{3.29}$$

then

$$\mathbf{R}^{-1} \approx \frac{1}{\gamma}\left[\mathbf{I} - \mathbf{A}(\theta)\left[\left(\mathbf{S}\frac{1}{\gamma}\right)^{-1} + \mathbf{A}^H(\theta)\mathbf{A}(\theta)\right]^{-1}\mathbf{A}^H(\theta)\right]. \tag{3.30}$$

When $\left(\mathbf{S}\frac{1}{\gamma}\right) >> \mathbf{A}^H(\theta)\mathbf{A}(\theta)$,

$$\mathbf{R}^{-1} \approx \frac{1}{\gamma}\left[\mathbf{I} - \mathbf{A}(\theta)\left[\mathbf{A}^H(\theta)\mathbf{A}(\theta)\right]^{-1}\mathbf{A}^H(\theta)\right]. \tag{3.31}$$

Let $\mathbf{P}^{\perp} = \left[\mathbf{I} - \mathbf{A}(\theta)\left[\mathbf{A}^H(\theta)\mathbf{A}(\theta)\right]^{-1}\mathbf{A}^H(\theta)\right]$, and notice that it is the projection orthogonal to the clutter subspace. So, $\mathbf{R}^{-1} = \frac{1}{\gamma}\mathbf{P}^{\perp}$ and includes only scale elements that are orthogonal to the clutter subspace.

3.4.2.3 Capon Beamforming

The minimization problem of Equation (3.19) simplifies to that of the Capon (1969) beamformer when a constraint of unity gain is applied for the steered direction. This setup has the expression

$$\min_{\mathbf{w}} \mathbf{w}^H\mathbf{R}\mathbf{w} \quad \text{subject to} \quad \mathbf{w}^H\mathbf{a}(\theta) = 1, \tag{3.32}$$

and the solution follows from (3.19) and is given by

$$\mathbf{w}_o = \frac{1}{\mathbf{a}^H(\theta)\mathbf{R}^{-1}\mathbf{a}(\theta)}\mathbf{R}^{-1}\mathbf{a}(\theta). \tag{3.33}$$

In the special case of high clutter-to-signal ratio with uncorrelated clutter sources, the output power of the Capon beamformer is

$$\begin{aligned} \mathbf{w}_o^H\mathbf{R}\mathbf{w}_o &= \left[\frac{1}{\mathbf{a}^H(\theta)\mathbf{R}^{-1}\mathbf{a}(\theta)}\mathbf{R}^{-1}\mathbf{a}(\theta)\right]^H \mathbf{R}\left[\frac{1}{\mathbf{a}^H(\theta)\mathbf{R}^{-1}\mathbf{a}(\theta)}\mathbf{R}^{-1}\mathbf{a}(\theta)\right] \\ &\approx \left[\frac{1}{\mathbf{a}^H(\theta)\frac{1}{\gamma}\mathbf{P}^{\perp}\mathbf{a}(\theta)}\frac{1}{\gamma}\mathbf{P}^{\perp}\mathbf{a}(\theta)\right]^H \mathbf{R}\left[\frac{1}{\mathbf{a}^H(\theta)\frac{1}{\gamma}\mathbf{P}^{\perp}\mathbf{a}(\theta)}\frac{1}{\gamma}\mathbf{P}^{\perp}\mathbf{a}(\theta)\right] \\ &\approx \left[\frac{1}{\mathbf{a}^H(\theta)\mathbf{P}^{\perp}\mathbf{a}(\theta)}\right]^2 \left[\mathbf{P}^{\perp}\mathbf{a}(\theta)\right]^H \mathbf{R}\left[\mathbf{P}^{\perp}\mathbf{a}(\theta)\right]. \end{aligned} \tag{3.34}$$

It can be observe that the output power contains signals that are in the subspace orthogonal to the strong scatterers' signals.

An example of spatial processing using Capon beamforming is shown in Figure 3.12. The beampattern is provided for a 32-element ULA with $d/\lambda = 1/2$ and $d/\lambda L = 16$. The steered angle is 0° while an undesired but uncorrelated clutter source is located at $\theta = -10^\circ$. In this setup, a unity gain is obtained at the steered direction while a null is placed at the angel of the clutter source. In comparison, the beampattern shown using conventional Fourier beamforming has a non-zero gain at the clutter source. Besides the difference at the location of the clutter, the two beampatterns have similar gains at other locations.

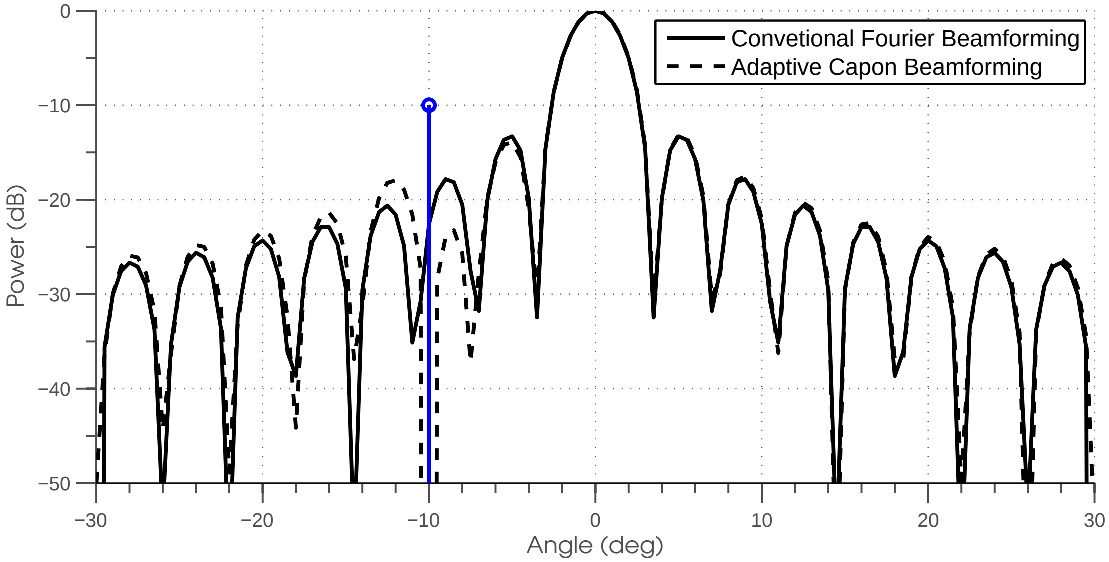

Figure 3.12: Example of a spatial response with the adaptive Capon beamformer. The steered direction is located at 0.0°, while the clutter source is located at -10°. Using the adaptive Capon beamformer, a null at the clutter source is obtained. In contrast, a non-zero gain at the clutter source is obtained using a conventional non-adaptive Fourier beamformer.

3.4.3 Partially Adaptive Spatial Processing Using Linear Constraints

Ideally, adaptive weights with the maximum number of degrees-of-freedom are used for all elements of the array. However, the complexity and added cost are primary factors that limit their use. Partially adaptive arrays (or sidelobe canceler, SLC) are simpler and more cost effective than fully adaptive arrays, and can be used to provide a measure of adaptivity (Widrow et al. 1967; Applebaum 1976). The SLC systems use fewer low-gain antenna elements in addition to a conventionally processed main array to provide the desired adaptivity at the cost of mainlobe clutter mitigation. In general, the elements are placed such that the baselines produced are perpendicular to the locations of the clutter sources and allow for nulls to be oriented in the direction of the clutter.

An example of a partially adaptive array is shown in Figure 3.13. Beam steering for the main antenna is accomplished with a conventional beamformer, and a single signal denoted by the symbol $X(mT_s)$ is obtained. The signal contains mainly contribution from scatterers within the radar resolution volume but may also be contaminated from clutter. To filter the clutter, signals from the auxiliary elements are weighted and subtracted from $X(mT_s)$. The expression of the output signal in terms of the signals from the auxiliary elements is

$$y(mT_s) = X(mT_s) - \mathbf{w}^H \mathbf{v}(mT_s). \tag{3.35}$$

In the following sections, techniques for obtaining $\mathbf{w}^H$ are presented.

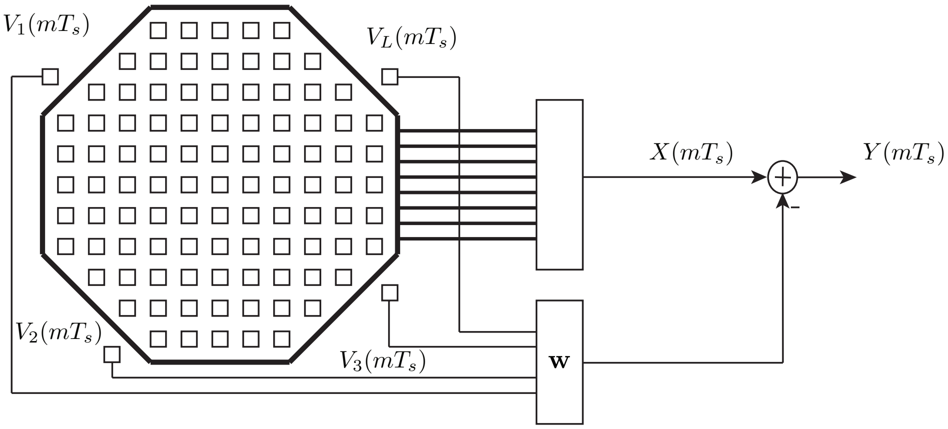

Figure 3.13: Architecture of partially adaptive array. The main antenna consists of many elements and uses conventional beamforming to steer the beampattern. The output signal can contain clutter contamination when the beampattern illuminates the clutter through either the main or sidelobe. When the clutter is in the sidelobe, auxiliary elements located around the main array can be used to mitigate the clutter contamination.

A simplified example of a partially adaptive array is illustrated in Figure 3.14. The example is shown for a main array, which is a ULA with $d/\lambda = 0.5$ and $d/\lambda L = 16$, and an auxiliary array of four elements that are equally distributed to the sides of the main array. The desired scatterer is located at 0° and denoted by the '◯' symbol, while the clutter source is located at -10° and denoted by the '☐' symbol. The beampattern of the main antenna, which was obtained using conventional Fourier beamforming, has a unity gain at 0° and a non-zero gain at the clutter source. The auxiliary array has a null at the angle of the desired scatterer and a gain that matches the main array at -10° when it is optimized. The composite beampattern, which is a combination of the main and auxiliary array, has a unity gain in the direction of the desired signal and a null at the clutter source.

3.4.3.1 Multiple Sidelobe Canceler (MSC)

One of the simplest techniques for designing the auxiliary weights of the SLC elements involves removing the correlation between the signal obtained by the main antenna and the signals obtained by the auxiliary elements (Widrow et al. 1967). Mathematically, the scheme is a minimization of the power and is expressed as

$$\min_{\mathbf{w}} \mathrm{E}\{y(mT_s)y^*(mT_s)\}. \tag{3.36}$$

One approach for solving (3.36) involves using the orthogonality principle, which states that the output signal is uncorrelated with the input signals of the auxiliary elements. Applying the orthogonality principle,

$$\mathrm{E}\{\mathbf{v}(mT_s)y^*(mT_s)\} \;=\; \mathbf{0}, \tag{3.37}$$

and substituting $y(mT_s) = X(mT_s) - \mathbf{w}^H\mathbf{v}(mT_s)$ and replacing $\mathbf{w} = \mathbf{w_o}$ give

$$\mathrm{E}\{\mathbf{v}(mT_s)(X^*(mT_s) - \mathbf{v}^H(mT_s)\mathbf{w}_o)\} \;=\; \mathbf{0}. \tag{3.38}$$

By defining $\mathbf{p} = \mathrm{E}\{\mathbf{v}(mT_s)X^*(mT_s)\}$, the optimal solution of the above minimization scheme is

$$\mathbf{w}_o \;=\; \mathbf{R}^{-1}\mathbf{p}, \tag{3.39}$$

where $\mathbf{R} = \mathrm{E}\{\mathbf{v}(mT_s)\mathbf{v}^H(mT_s)\}$ is the covariance matrix of the auxiliary time signals. The above solution was obtained independent of the steered vector and does not require any information about the auxiliary array.

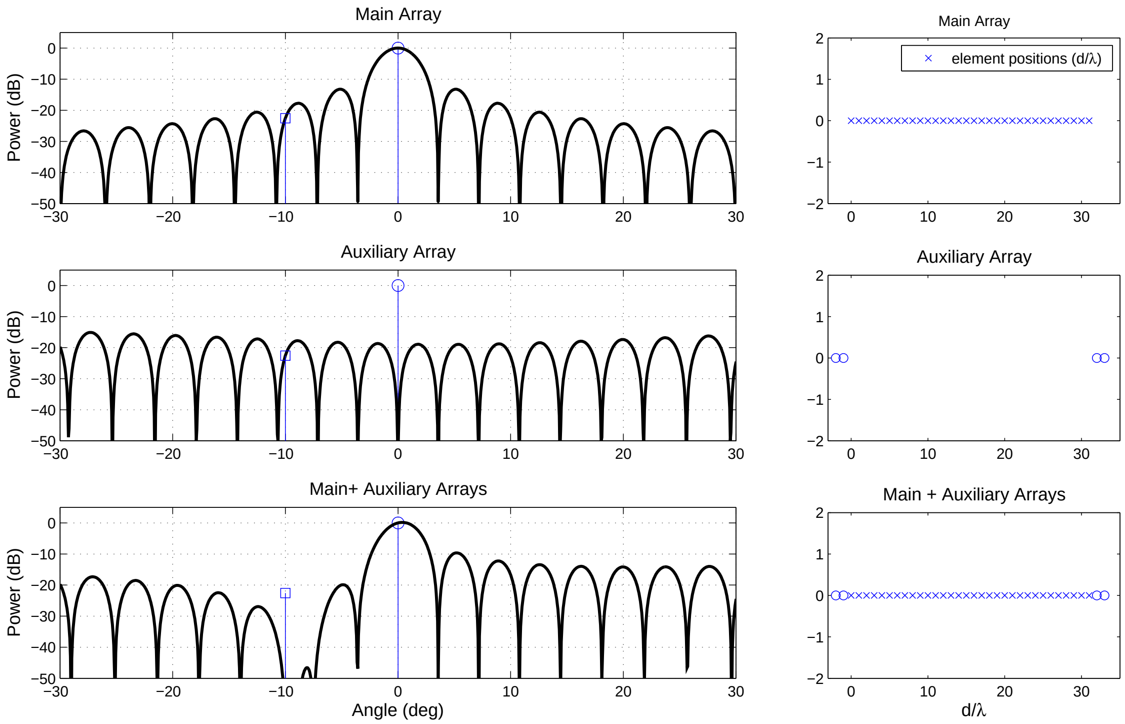

Figure 3.14: Illustrated concept of partially adaptive array. In this example, the main array is steered to 0°, denoted by the symbol '◯'. The beampattern that is produced using the main array has a non-zero gain at -10°, denoted by the symbol '□' where the clutter source is located. As a result, contamination from the clutter source is observed in the signal obtained from the main array. An auxiliary array then obtains an identical signal of the clutter by matching its gain to that of the main array at the location of the clutter. By subtracting this signal from that obtained using the main array, the clutter signal is effectively removed. This process is equivalent to producing a notch gain at the location of the clutter source in the beam pattern of the combined array.

3.4.3.2 Minimum Variance Distortionless Response (MVDR)

Another technique for designing the auxiliary weights is to extend the Capon beamformer approach to satisfy

$$\min_{\mathbf{w}} \mathrm{E}\{|X(mT_s) - \mathbf{w}^H\mathbf{v}(mT_s)|^2\} \quad \text{subject to} \quad \mathbf{w}^H\mathbf{a}(\theta) = 0. \tag{3.40}$$

The output power is also minimized, however the auxiliary array is constrained to produce a gain of zero in the steered direction. The constraint essentially limits the distortion introduced by the auxiliary elements to the mainlobe, which is important for weather radars. To obtain a matrix-form solution of $\mathbf{w}$, additional notations is needed. Begin with

$$\tilde{\mathbf{w}} = \begin{bmatrix} w_0 \\ -\mathbf{w} \end{bmatrix}, \tag{3.41}$$

and

$$\tilde{\mathbf{R}} = \mathrm{E}\left\{\begin{bmatrix} X(mT_s) \\ \mathbf{v}(mT_s) \end{bmatrix}\begin{bmatrix} X(mT_s) \\ \mathbf{v}(mT_s) \end{bmatrix}^H\right\}. \tag{3.42}$$

The output power of the array is

$$\begin{aligned} \mathrm{E}\{y(mT_s)y^*(mT_s)\} &= \mathrm{E}\left\{\left|\begin{bmatrix} w_0 \\ -\mathbf{w} \end{bmatrix}^H \begin{bmatrix} X(mT_s) \\ \mathbf{v}(mT_s) \end{bmatrix}\right|^2\right\} \\ &= \tilde{\mathbf{w}}^H\tilde{\mathbf{R}}\tilde{\mathbf{w}}. \end{aligned} \tag{3.43}$$

Let

$$\tilde{\mathbf{A}} = \begin{bmatrix} 1 & 1 \\ -\mathbf{a}(\theta) & \mathbf{0} \end{bmatrix}, \tag{3.44}$$

where $\mathbf{0}$ is a column zero vector with length equal to the number of auxiliary channels, and $\tilde{\mathbf{1}} = \begin{bmatrix} 1 & 1 \end{bmatrix}$. The second term forces w_0 to be unity.

Using the above notation, the minimization problem of (3.40) can be written as

$$\min_{\tilde{\mathbf{w}}} \tilde{\mathbf{w}}^H\tilde{\mathbf{R}}\tilde{\mathbf{w}} \quad \text{subject to} \quad \tilde{\mathbf{w}}^H\tilde{\mathbf{A}} = \tilde{\mathbf{1}} \tag{3.45}$$

and the solution is

$$\tilde{\mathbf{w}}_o = \tilde{\mathbf{R}}^{-1}\tilde{\mathbf{A}}\left(\tilde{\mathbf{A}}^H\tilde{\mathbf{R}}^{-1}\tilde{\mathbf{A}}\right)^{-1}\tilde{\mathbf{1}}^H. \tag{3.46}$$

The above solution is similar to (3.21).

3.4.3.3 Subspace Tracking Spatial Projection (STSP)

Another important technique for obtaining the auxiliary weights is the subspace technique of Ellingson and Hampson (2002) that uses the clutter subspace $\mathbf{R}_i$. The approach can be cast as the following minimization problem

$$\min_{\mathbf{w}} \mathrm{E}\{y(mT_s)y^*(mT_s)\} \quad \text{subject to} \quad \mathbf{w}_o \in \mathbf{R}_i, \tag{3.47}$$

where $\mathbf{w}_o \in \mathbf{R}_i$ is the projection of the multiple sidelobe canceler weights of Equation (3.39) into the clutter subspace. Thus,

$$\mathbf{w}_o \;=\; \mathbf{P}_i^{\|}\mathbf{R}^{-1}\mathbf{p}, \tag{3.48}$$

where $\mathbf{P}_i^{\|} = \mathbf{U}_i\mathbf{U}_i^{\dagger}$, with $\mathbf{U}_i^{\dagger} = (\mathbf{U}_i^H\mathbf{U}_i)^{-1}\mathbf{U}_i^H$ and $\mathbf{U}_i$ are the clutter eigenvectors. In essence, the projection matrix $\mathbf{P}_i^{\|}$ selects the subspace that is used in $\mathbf{R}^{-1}$.

In the example that follows, the clutter subspace is not known *a priori* and the clutter subspace is assumed to be from the dominant eigenvectors. The projection matrix is then composed of the eigenvectors obtained using some eigen decomposition. For a 6x6 covariance matrix, which is the size used in the simulation and validation analysis, its decomposition using eigenvalue analysis is expressed as

$$\mathbf{R}\mathbf{U}_6 \;=\; \mathbf{U}_6 \begin{bmatrix} \gamma_1 & 0 & 0 & 0 & 0 & 0 \\ 0 & \gamma_2 & 0 & 0 & 0 & 0 \\ 0 & 0 & \gamma_3 & 0 & 0 & 0 \\ 0 & 0 & 0 & \gamma_4 & 0 & 0 \\ 0 & 0 & 0 & 0 & \gamma_5 & 0 \\ 0 & 0 & 0 & 0 & 0 & \gamma_6 \end{bmatrix}, \tag{3.49}$$

where $\gamma_1 \geq \gamma_2 \geq \cdots \geq \gamma_6$, $\mathbf{U}_i = [\mathbf{u}_1 \cdots \mathbf{u}_i]$, and $\mathbf{u}_i$ is the eigenvector that corresponds to the γ_i eigenvalue. When $\mathbf{U}_6$ is used, $\mathbf{P}_i^{\|} = \mathbf{I}$ and the optimal weights reverts to $\mathbf{w}_o = \mathbf{R}^{-1}\mathbf{p}$, which is the optimal weights of the MSC. To distinguish the number of most dominant eigenvectors used in $\mathbf{P}_i^{\|}$, the notation STSP$_n$, where n is the number of eigenvectors, is employed.

3.4.4 Summary of Spatial Processing Techniques

In the last subsection, several spatial processing techniques were presented for obtaining weights that could be used to design the array factor. They included conventional non-adaptive as well as adaptive weights for both a fully and partially adaptive array. The objective of these spatial processing techniques was to preserve the desired signal and to mitigate the clutter contamination. Most often, the processing techniques use a steered direction constraint of unity and a minimization of the output power to achieve this objective. While it was shown that fully adaptive arrays are more desirable because they contain more degrees-of-freedom and are capable of mitigating mainlobe clutter, the fully adaptive systems are complex and expensive to constructive. Partially adaptive arrays are simpler and more cost effective, and could be used as a reasonable alternative solution to the fully adaptive arrays at the cost of mainlobe clutter mitigation and lower number of degrees-of-freedom.

Chapter 4

Algorithm Validation Using Numerical Simulation and Experimental Data

4.1 Simulation Approach

A simple approach consisting of using simulated time series signals has been employed to determine the performance of spatial adaptive arrays and clutter filtering. The approach uses time series signals of the weather, clutter, and noise that are independently simulated. The signals are injected into a spatial filter and processed using parameters such as diagonal loading, clutter-to-signal ratio (CSR), dwell time as defined by number-of-points (NPTS), signal-to-noise ratio, and clutter fading. The signals are also processed over a wide range of azimuth and elevation angles to provide robust estimates. At each location, the clutter filter ingests the time series signals and processes them based on the selected parameters. Results of the filtered weather, clutter, and noise are then saved so that they can be later examined.

4.1.1 Simulation of the Radar Environment

The design of the antenna that is used to obtain the simulated time series signals follows that of the NSSL NWRT PAR shown in Figure 4.1 and 4.2(Scudder and Sheppard 1974). The antenna consists of a main array with 4,352 elements that is approximately 3.84 m tall and 3.66 m wide and an auxiliary array with six elements. Conventional Fourier beamforming is used to steer the main array, while adaptive weights are applied to the signals of the auxiliary elements. Figures 4.3 and 4.4 show the beampattern of the main array when it is steered in the normal direction. The results show the beampattern is approximately symmetric with a beam that ranges between 1.42-1.62°.

Figure 4.1: Images of SPY1-A antenna of NSSL PAR (courtesy of Boon-Leng Cheong). Shown are some examples of the receive subarray and sidelobe canceling modules of the NSSL PAR. These elements combine to form the antenna that is used for transmitting, receiving, and for mitigating clutter.

4.1.2 Time Series Radar Simulator

The proven method of Cheong et al. (2004, 2008) is used to simulate the time series signals that are used in this study. The model has been previously shown to provide realistic temporal and spectral signatures of the simulated weather event using phased array radars of various configurations. The technique uses point targets enclosed in a simulation volume with targets that are each characterized with individual values of reflectivity and three-dimensional velocity obtained from the Advanced Regional Prediction System (Xue et al. 2000, 2001) numerical weather prediction model. At each sampled time, the contribution of each scatterer is summed using the radar range equation to obtain the time series signal.

The approach of using point targets is also used to simulate the time series signals of clutter returns:

- *Ground clutter:* A collection of point targets placed at the surface of the simulated enclosing volume was used to model the contamination caused by ground clutter. The targets were randomly placed and characterized with uniform reflectivity and a Gaussian distributed random motion. The simulated time series signals were observed to have a narrow spectrum width that is indicative of a slowly fading temporal response.

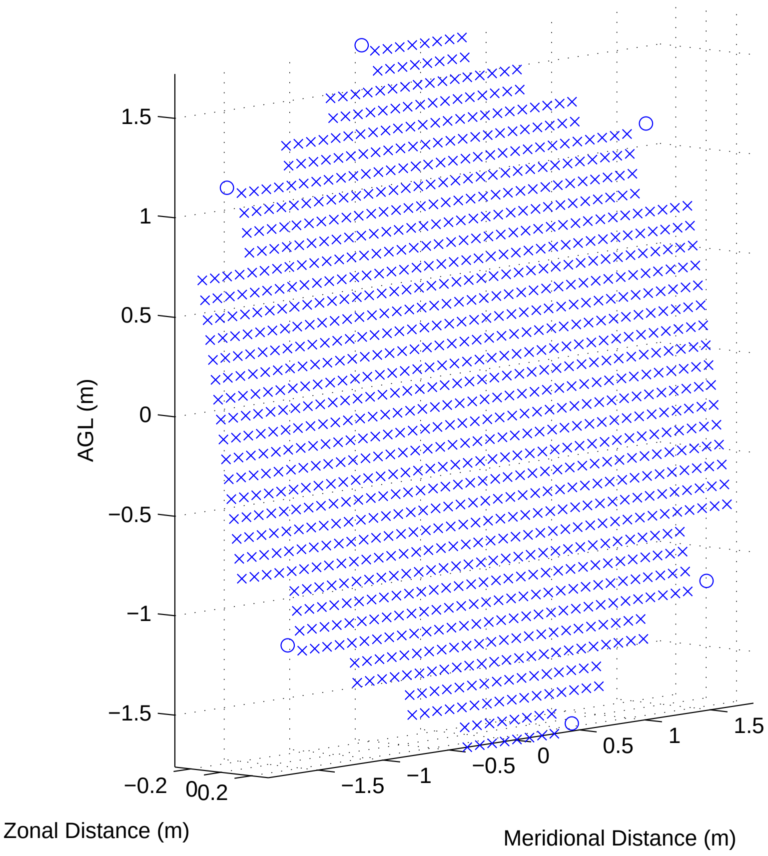

Figure 4.2: Positions of the antenna elements of the simulated array. Designed to match the SPY-1A antenna including the 10° elevation tilt, the simulated array consists of 4,352 elements and is physically the same size. Beamforming by the array is achieved by dividing the elements into 136 32-element subarrays and applying Fourier weighting to each of the subarray. Additionally, there are six auxiliary elements denoted with 'o' located around the main array that are used to mitigate clutter.

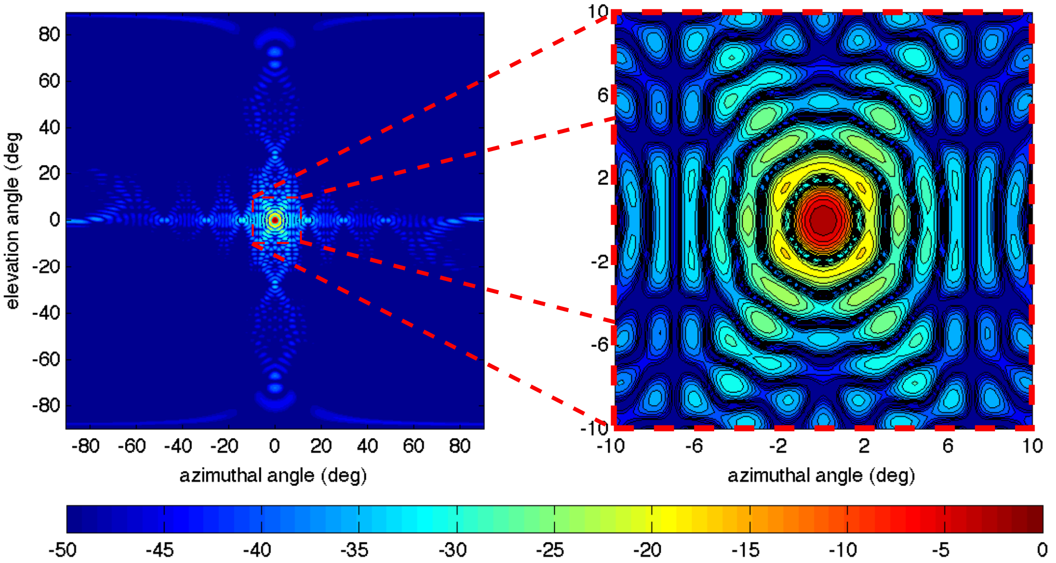

Figure 4.3: Beampattern of the simulated PAR antenna when steered normal to the array. Shown is the one-way receive pattern obtained using Fourier beamforming at wide and close-up views.

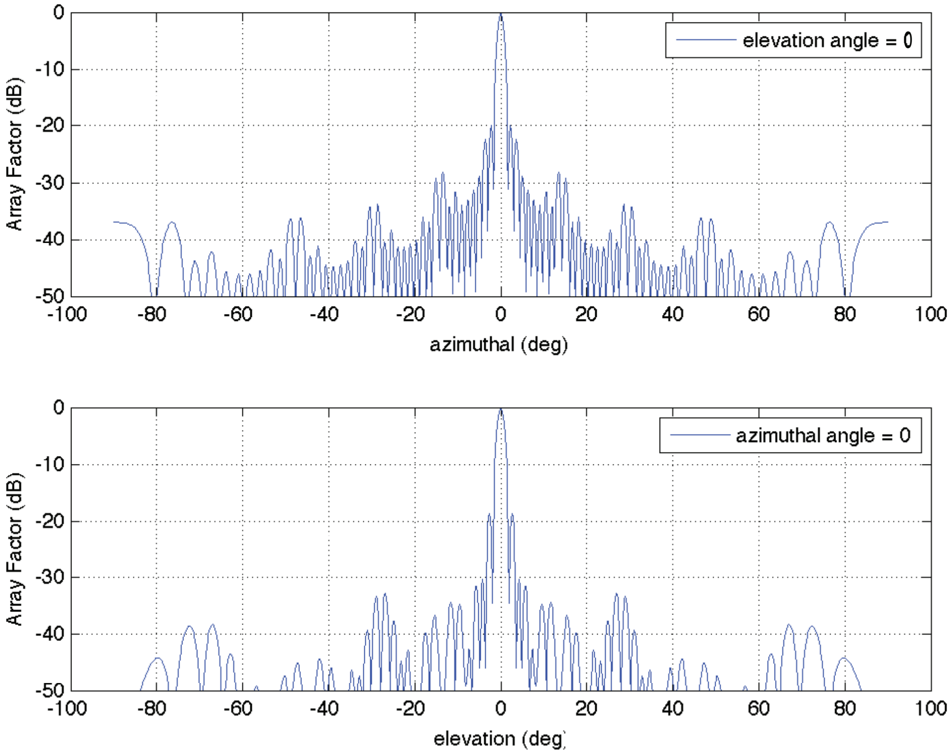

Figure 4.4: Vertical and horizontal cross sections of the beampattern of the simulated PAR. Same as Figure 4.3, except for cross section cuts.

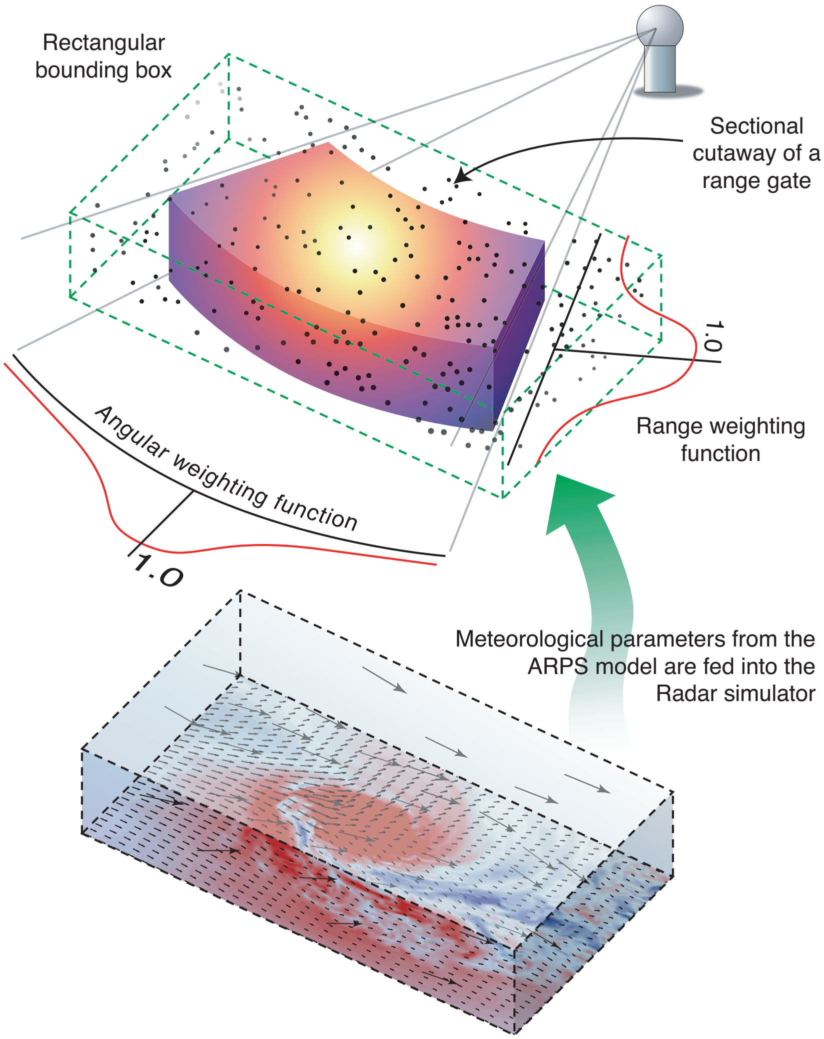

Figure 4.5: Depiction of point scattering model of Cheong et al. (2004, 2008). Using point targets, with characteristics obtained from the ARPS numerical weather prediction model, and the radar range equation, the fluctuations of the time series signals at each element can be obtained for a realistic weather field with this model (from Cheong et al. (2004, 2008)).

- *Moving clutter:* A single point target located near the surface of the simulated enclosing volume was used to model the contamination caused by a point scatterer. The target moved in a straight line its scattered signal is represented by a sinusoid whose amplitude is modulated by the gain of the radar resolution volume.

Besides the works of Cheong et al. (2004, 2008), a variety of other methods exist that can be used to generate time series signals (Zrnić 1975; Torres and Zrnić 2003; Holdsworth and Reid 1995; Capsoni and D'Amico 1998) and are worth mentioning. For example, the technique of Zrnić (1975) provides the time series by using the inverse Fourier transform to transform an arbitrary shaped Doppler to time series signals. The technique has an advantage of being computationally efficient but a limited radar resolution. Torres and Zrnić (2003) extended the technique to incorporate the spatial correlation of the radar waveform by filtering the independently generated time series with a range spatial response. While both techniques are computationally efficient, they do not incorporate the angular correlation. This effect was examined by Holdsworth and Reid (1995) using a random field of scatterers and an arbitrary array of receivers to simulate turbulence. A similar method was used by Capsoni and D'Amico (1998) to simulate time series signals of precipitation using proxy scatterers. The characteristics of the proxy scatterers were obtained by binning the drop size distribution and integrating the contribution within each bin. Due to their complexities, the last two models can only used to simulate scattering from small volumes.

4.1.3 Simulated Scattering Environment

Results of the simulated power and Doppler velocity fields obtained using the model of Cheong et al. (2004, 2008) are shown in Figure 4.6 and 4.7, respectively. Inputs to the model include the Del City, Oklahoma, 20 May 1977 upper-air sounding and other parameters listed in Table 4.1. The results are plotted for nine elevation angles from 0.5° to 4.5° and for an azimuth swath of 20°. The values were obtained by applying Fourier beamforming to the main array and are indicative of features observed in a developing tornadic storm. Near the ground, the weather is concentrated zonally with an average power of 34.6 dB and a maximum power is 50.6 dB. An observation of the corresponding Doppler velocity shows the scatterers are moving away from the radar. At higher elevations, the weather is concentrated in a toroid with an average power of 39.6 dB and a maximum power of 52.8 dB, while the corresponding Doppler velocity shows an upper-level rotation.

Table 4.1: Simulated NSSL PAR Specification

Transmitter	20° BW
Receiver	NSSL PAR
Frequency	3.2 GHz
Range Resolution	235 m
Pulse Frequency	1 kHz
Doppler Aliasing Velocity	23.4 m s^{-1}
Number of Weather Point Targets	50,000
Number of Ground Clutter Point Targets	1,000
Number of Moving Clutter Point Targets	1
Number of Points (NPTS)	256

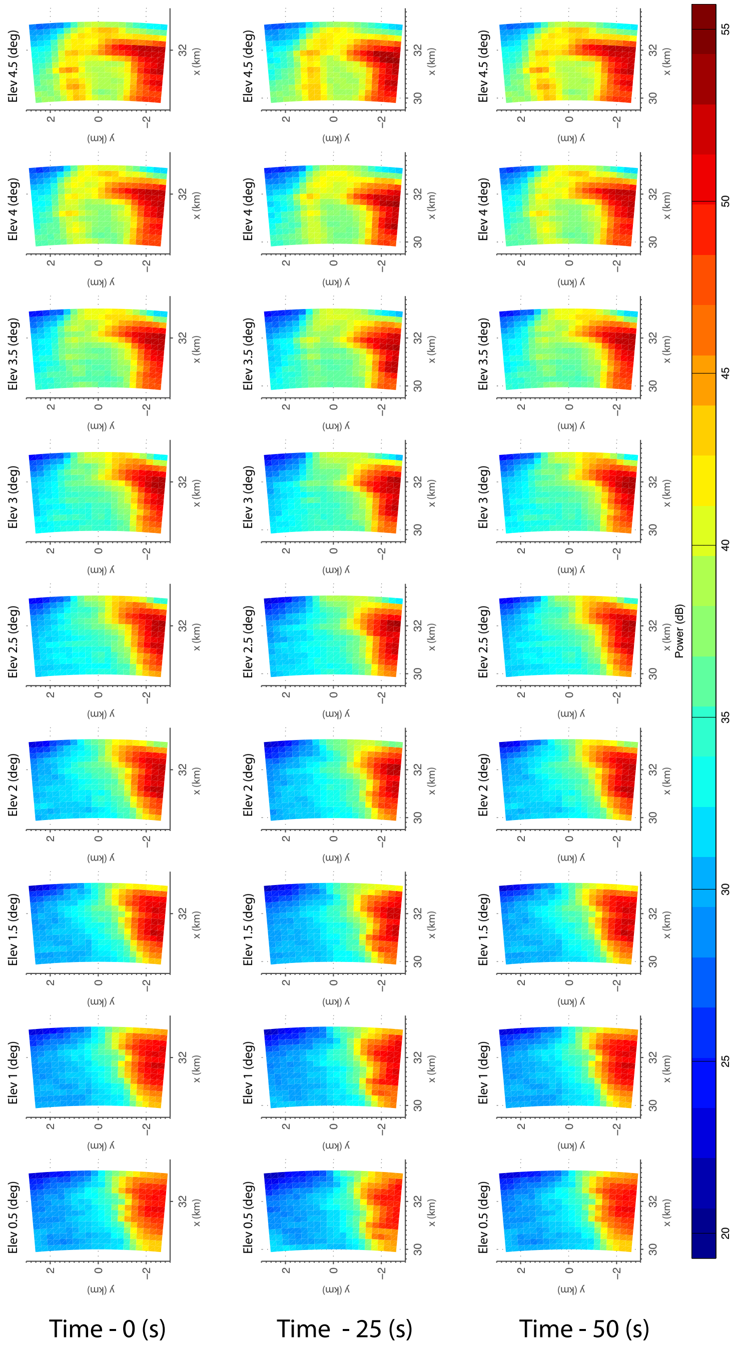

Figure 4.6: Power of simulated weather event. Shown is a power profile of a simulated weather events for three snapshots and for elevations from 0.5° to 4.5°. Each snapshot, separated by 25 s, was obtained by applying Fourier beamforming to the 256 time samples.

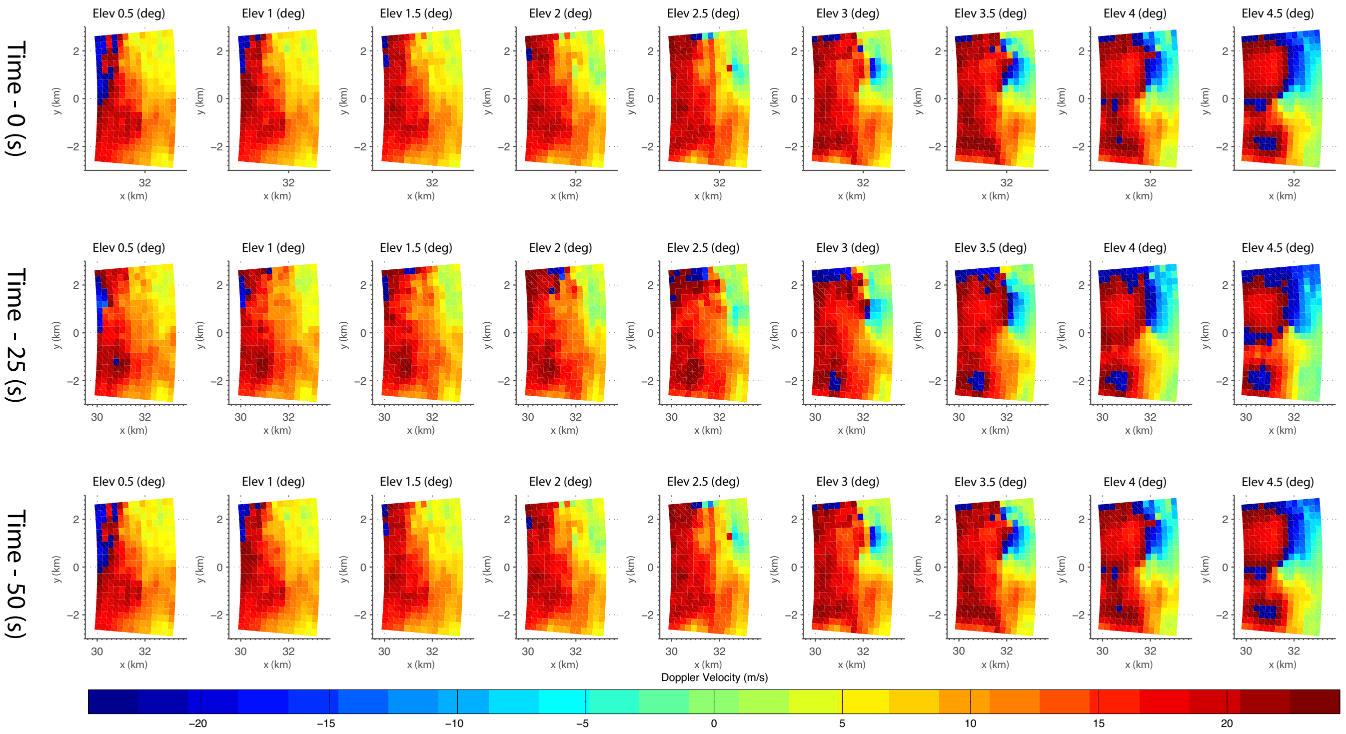

Figure 4.7: Same as Figure 4.6, except for Doppler velocity.

4.2 Platform for Experimental Validation

In an ideal situation, an actual radar platform that matches the simulated array would be used to validate the clutter filters. While no such platform currently exists, the situation may soon change when Yeary et al. (2008) introduce upgrades to the NWRT PAR for accessing to time series signals of the auxiliary elements. Validation is then obtained using data from a digital beamforming boundary layer radar. In this section, details of the radar and data are presented.

4.2.1 The Turbulent Eddy Profiler

The radar shown in Figure 4.8 with the specifications listed in Table 4.2 is used to validate the spatial filters. The transmitting components consist of a solid-state amplifier that outputs 0.22 μs pulses at 35 kHz with peak power of 4 kW and operates at 915 MHz. The receiving components consist of an array of 56 microstrip antennas, a collection of digital receivers, and a raid array. At each element, the echo signal is demodulated to baseband and sampled at 35 kHz, where two-hundred and fifty contiguous samples are then integrated. The final signal has an effective sampling rate of 140 Hz for an aliasing velocity of 11.48 m s^{-1}. The signals of all the elements are then stored, which allows for flexible implementation of sophisticated algorithms.

Table 4.2: TEP Specifications

Transmitter Antenna	Corrugated Horn
Receiver Antenna	Array of 50 microstrip elements
Frequency	915 MHz
Range Resolution	33.3 m
Pulse Frequency	35 kHz
Coherent Integration	250 samples
Effect Sampling Rate	7.15 m s^{-1}
Effective Aliasing Velocity	11.48 m s^{-1}
NPTS	256

While many data sets were collected using the TEP, only a short 20-minute sample of the data collected between 14-15 June 2003 was used for the experimental validation. The geometry of the received antenna array used to collect the data is shown in Figure 4.9. 50 elements denoted by the symbol 'x' compose the main array

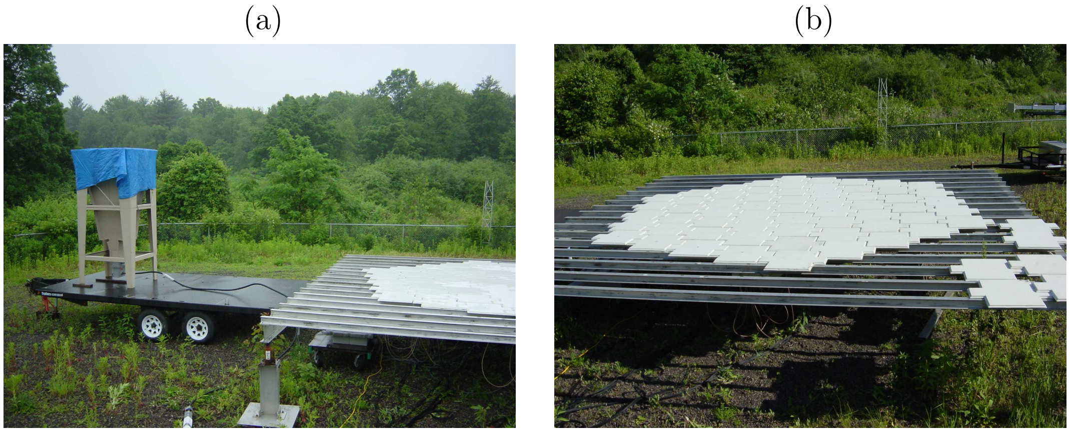

Figure 4.8: Images of the Turbulent Eddy Profiler (courtesy of Boon-Leng Cheong). The TEP is a vertically pointing radar that is used to observe atmospheric scatterers located in the boundary layer. The transmitting horn is located in the left image and is covered by a blue tarp. The receive antenna consists of an array of microstrip antennas shown in the right image. There are 56 elements and the time series of each element is independently recorded. As a result, post-processing using advanced spatial filtering schemes can be applied to the collected data set.

and conventional Fourier beamforming was used to steer its beam, while six elements denoted by the symbol 'o' compose the auxiliary array. The beampattern of the main array is shown in Figure 4.10 when the antenna is steered in the direction normal to the array. The results show the beampattern is approximately symmetric with a mainlobe width that ranges between 4.4-5.6° and six grating lobes that are located between 41.3-42.5°.

4.2.2 General Condition of the Validation Experiment

Plotted in Figures 4.11 and 4.12 are the results of the power and Doppler velocity fields, respectively, of the validated data set obtained using Fourier beamforming. The results near the surface show large power and near zero Doppler velocity. The features enclosed in brown oval are dominated by ground clutter, while the features at 15:43, 15:47, and 15:57 UTC and enclosed in red circles are dominated by moving targets, such as birds or possibly aircrafts. The weather features, which are everywhere else, are of clear-air turbulent scatterers and surface heating plumes. These features have fairly weak returns with wide spectrum widths and near-zero Doppler velocities.

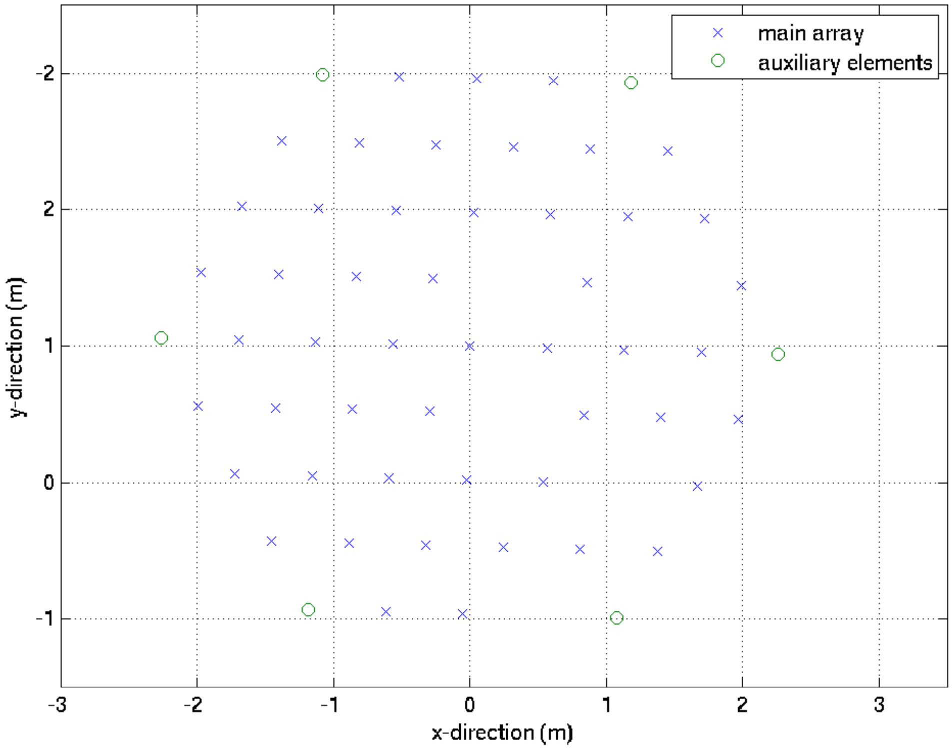

Figure 4.9: Configuration of TEP receive array. Shown is the layout of the receiving elements of the TEP. The main array is composed of the inner 50 elements. A single signal is then obtained from the array by applying Fourier beamforming to the individual signal of each of these elements. The auxiliary array is composed of six elements located at the corners of the main array, and adaptive weighting is applied to these signals. The output signal of the array is then obtained by subtracting the auxiliary signal from the output signal obtained using the main array.

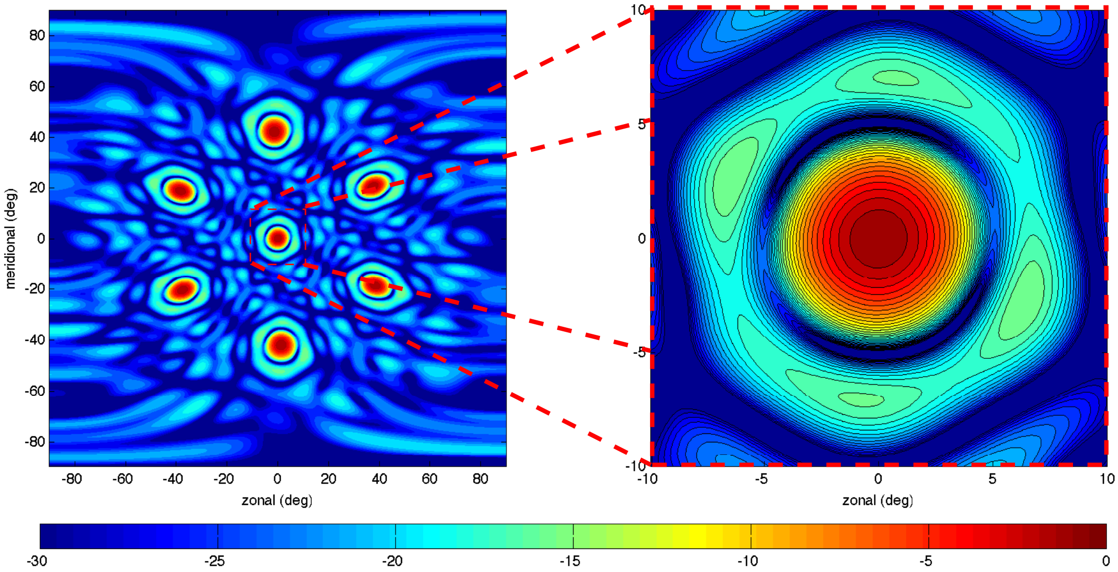

Figure 4.10: Beampattern of TEP antenna using the configuration described in Figure 4.9. The pattern was obtained by applying Fourier beamforming to the simulated antenna array. In this configuration, the mainlobe was calculated to have a 3-dB beamwidth of approximately 4.4° to 5.6° when the steered direction is normal to the array.

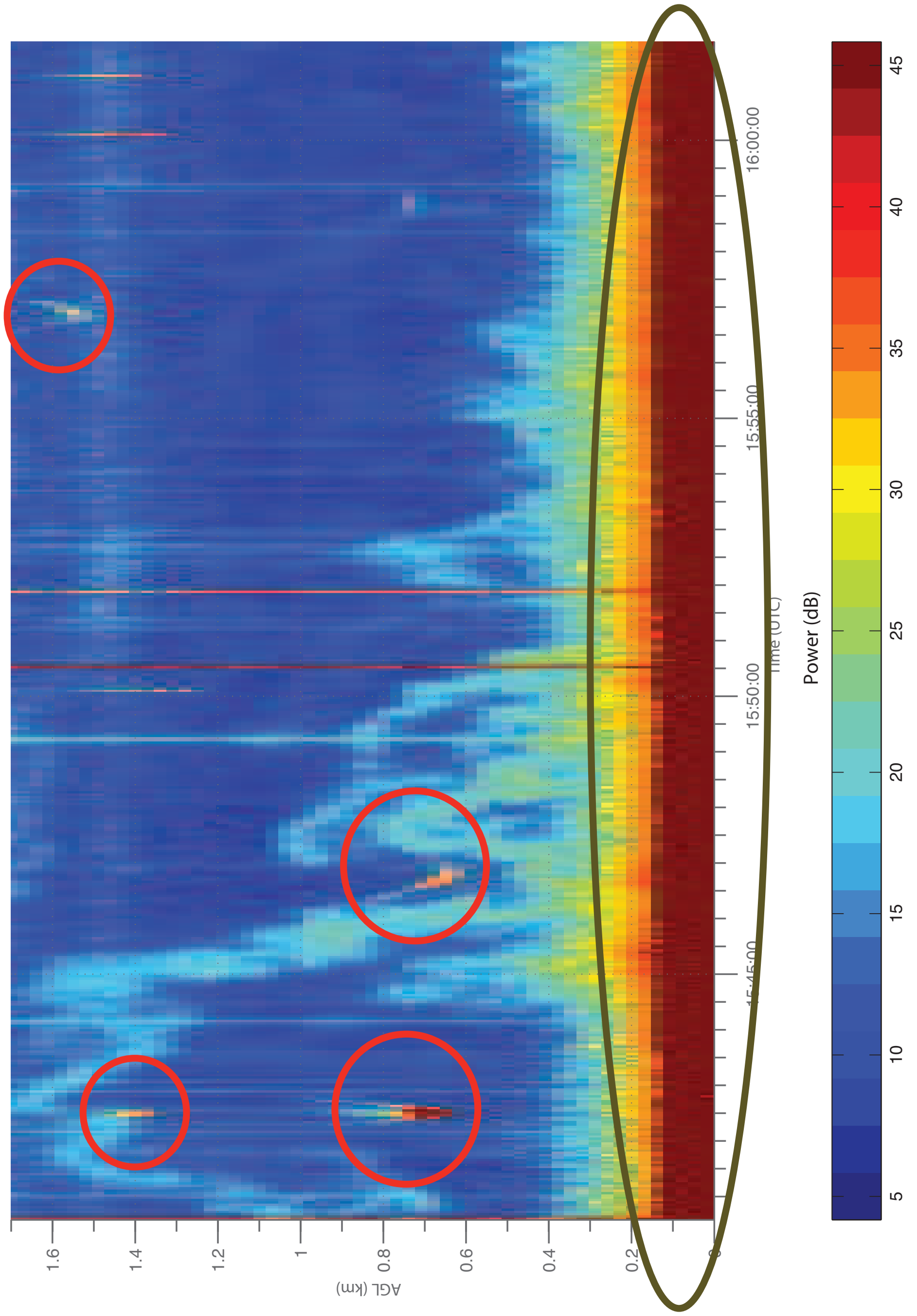

Figure 4.11: Echo Power profile obtained by the TEP that occurred between 1540 and 1602 UTC. The field consists primarily turbulent scatterers with persistent quasi-stationary ground clutter below 0.25 km outlined using a brown oval and intermittent non-stationary moving clutter above 0.5 km outlined using red circles.

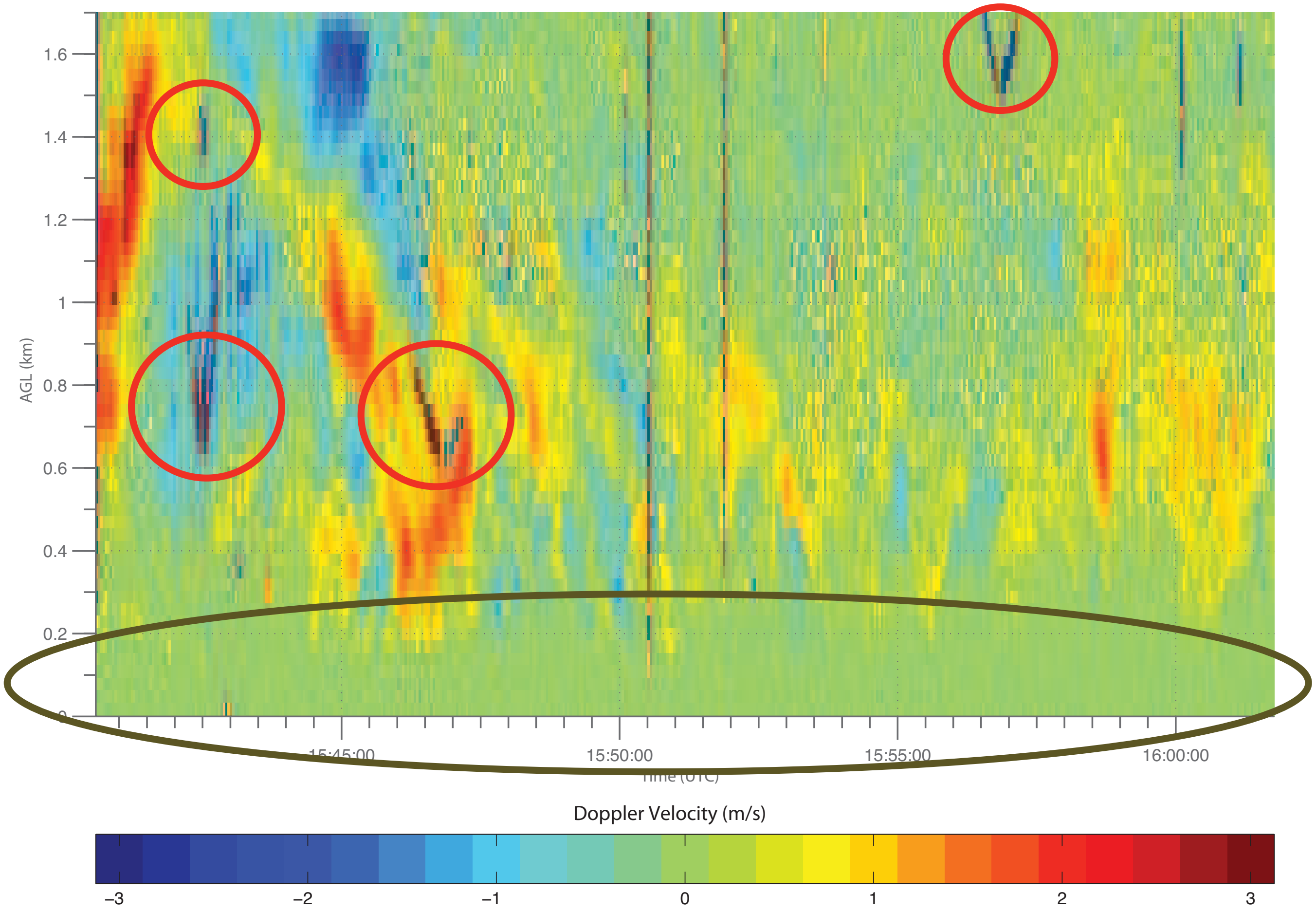

Figure 4.12: Same as Figure 4.11, except for Doppler velocity.

Chapter 5

Clutter Mitigation Using Partially Adaptive Arrays: Numerical Simulation and Experimental Validation

In this chapter, spatial arrays are used to investigate the performance of clutter filtering for weather radar data contaminated by ground and moving clutter sources for both real and simulated data. When simulated data are used, the return signals obtained using conventional Fourier beamforming without clutter are available and will be used as ground truth for comparison. The ground truth is not available when real data are used and the spatial and temporal continuity conditions of weather-dominated scattering are then used as qualitative measures of performance. While it is one of many possible criteria that can be used, the continuity condition is a relatively good measure to determine the accuracy of the extracted weather signal.

The parameters used to examine the performance of the spatial filters are listed in Table 5.1 and vary depending on the clutter source. When the clutter source is the ground, the parameters include SNR, CSR, NPTS, diagonal loading, and a fading clutter term. The SNR is defined as the ratio of the average weather to noise powers over a PPI measurement at 0.5°. The CSR is defined using the same angle while the fading clutter is defined as the random motion of the slow moving targets. All the parameters will be systematically varied to observe the performance of the clutter filters. When the clutter sources are moving scatterers, the clutter fading parameter is neglected and the clutter power is defined as the peak power at 1.5°.

When real data are used, the number of parameters that can be used to investigate the clutter filter performance decreases. A list of these parameters are shown in Table 5.2 along with values of the fixed parameters. These parameters include the

Table 5.1: Simulation Parameters

Parameter	Nominal Value	Variable Range
Partial Array with Ground Clutter:		
SNR	70 dB	10 — 70 dB
CSR	55 dB	35 — 65 dB
NPTS	8	2 — 32
γ	10^6	10^{-1} — 10^{-7}
σ_v	0.1 m s^{-1}	0.01 — 1.0 m s^{-1}
Partial Array with Moving Point Target:		
SNR	70 dB	10 — 70 dB
CSR	30 dB	10 —- 50 dB
NPTS	8	2 — 32
γ	10^5	10^{-1} — 10^8

dwell time and diagonal loading that are variable and SNR, CSR, and σ_v that are fixed.

Table 5.2: General Parameters Used In Validation

Parameter	Nominal Value	Variable Range
Partial Array with Ground Clutter:		
SNR	3.4 dB	
CSR	33.6 dB	
NPTS	8	2 — 64
γ	10^6	10^2 — 10^7
σ_v	variable	
Partial Array with Moving Point Target:		
SNR	3.4 dB	
CSR	33.5 dB	
NPTS	8	2 — 64
γ	10^5	10^2 — 10^7

For both real and simulated data, clutter filtering is applied to time series signals with a length of 256 samples to ensure that a fair comparison is made. The approach is illustrated in Figure 5.1 and consists of using a moving window with width NPTS = $\{2, 4, 8, \cdots\}$. After all 256 samples are processed, moment data are then obtained of the whole sequence. In this approach, the composite signal, which is also called the *combined* signal, is a coherent sum of the *weather*, *clutter*, and *noise* signals. The individual signals are separable when simulated data are used, while only the combined signal is available when real data are used.

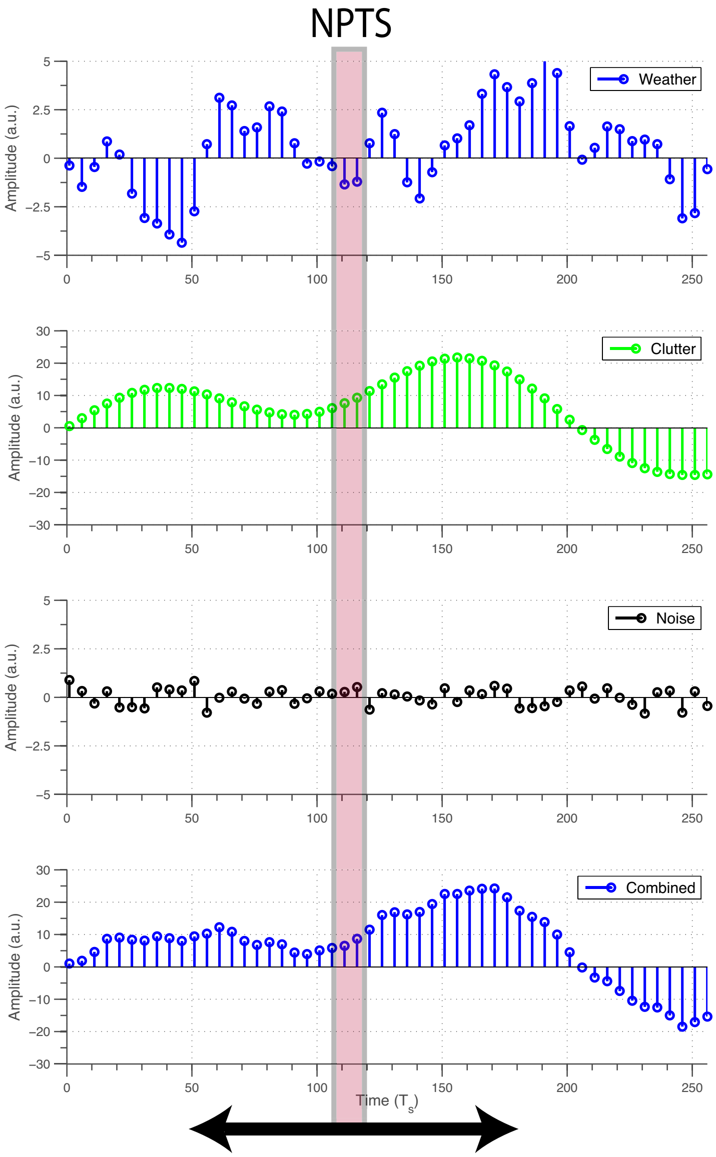

Figure 5.1: Conceptualized illustration of clutter filtering scheme. A non-overlapping moving window of width NPTS selects time series samples that will be ingested by the adaptive spatial filtering scheme and processed. Output signals include the *combined* and individual components of *weather*, *clutter*, and *noise* whenever possible. The characteristics of these components are obtained by averaging over a time series of 256 samples.

5.1 Quasi-Stationary Ground Clutter: Numerical Simulations

The performance of using a partially adaptive array to filter ground clutter is now examined with simulated data. Listed in Table 5.3 are the average powers of the combined, clutter, weather, and noise components that are obtained when ground clutter and other parameters listed in Table 5.1 are applied. The results show the steady-state conditions that are observed when conventional Fourier beamforming is used to process the contaminated data. Notice that the combined and clutter are similar and indicate that the clutter is the dominant component of the combined signal. In comparison, the noise and weather powers, which together have a maximum value of 40.3 dB, are significantly smaller and their contributions to the combined power are significantly less.

Table 5.3: Powers Obtained Using Fourier Beamforming (values in dB)

Elev (°)	0.5	1.0	1.5	2.0	2.5	3.0	3.5	4.0	4.5
Combined Power	95.5	91.7	84.9	81.6	81.9	78.7	76.5	76.5	74.6
Clutter Power	95.5	91.7	84.9	81.6	81.9	78.7	76.5	76.5	74.6
Weather Power	35.2	35.7	36.1	36.5	37.0	37.6	38.4	39.3	40.3
Noise Power	-28.1	-28.1	-28.1	-28.1	-28.1	-28.1	-28.1	-28.1	-28.1

5.1.1 Effects of Diagonal Loading

The parameter that is most commonly altered when a partially adaptive array is used is the diagonal loading. The parameter was previously discussed in Chapter 4 and is used as a means to control the adaptivity of the spatial filter and to provide improved numerical stability. In general, the diagonal loading ranges between the minimum and maximum values of the eigenvalues that are observed in the covariance matrix. It is used when either the array is miscalibrated or when a small number of samples is employed and the statistics of the covariance matrix are poorly estimated. In this subsection, the performance of the spatial filters is examined as the diagonal loading is varied from 10^{-1} to 10^{7} along with the parameters listed in Table 5.4.

When MVDR is applied to the contaminated signals and processed, the powers of the filtered signals are plotted in Figure 5.2. The results show the effects to the individual and combined powers as the diagonal loading is changed from 10^{-1} to

Table 5.4: Parameters Used in Varying Diagonal Loading

Parameter	Value Range
SNR	70 dB
CSR	55 dB
NPTS	8
γ	$\mathbf{10^{-1}}$**—**$\mathbf{10^{7}}$
σ_v	0.1 m s^{-1}

10^8. The combined power has a maximum of approximately 50 dB near 0.5° and a minimum of approximately 35 dB near 4.5°. These values are obtained when either a diagonal loading of 10^{-1} or 10^8 is used. In general, the combined power increases when the diagonal loading is changed from 10^{-1} to 10^8, however the rate of change is most significant after the diagonal loading has increased beyond 10^5 while the combined power is approximately minimum when the diagonal loading is below 10^5. While data from the combined power show that an attenuation of more than 40 dB is obtained and the results match well the desired power level at elevations above 4.0°, the combined power is still larger than the desired combined power below this angle and the difference can be up to 15 dB. The clutter power follows the combined power with difference less than a few dB, however its minimum values are obtained when a diagonal loading of 10^6-10^7. The weather power follows a similar trends as the combined and clutter powers, however its values tend to be slightly larger. While a small difference when compared to the original weather power at 4.5° is obtained using a diagonal loading of 10^6, the difference at 0.5° can be as much as 20 dB. The noise power is mostly below 0 dB and is the smallest of the four powers, playing a negligible role for the combined power.

Using STSP_1, STSP_2, and STSP_6 and the selected range of diagonal loading to process the time series signals, the powers obtained are plotted in Figures 5.3, 5.4, and 5.5. The values show the transition of the powers with different sets of eigenvectors and diagonal loadings. The powers using STSP_1 have a small variance that is essentially independent of the diagonal loading. Unfortunately, the primary component of the combined power is the clutter, which is observed for all values of diagonal loading. With STSP_2, an increase in the variance of the combined power is observed, which is caused by the effects of the diagonal loading to the clutter power. With STSP_6, additional increases to the variance of the combined power are observed

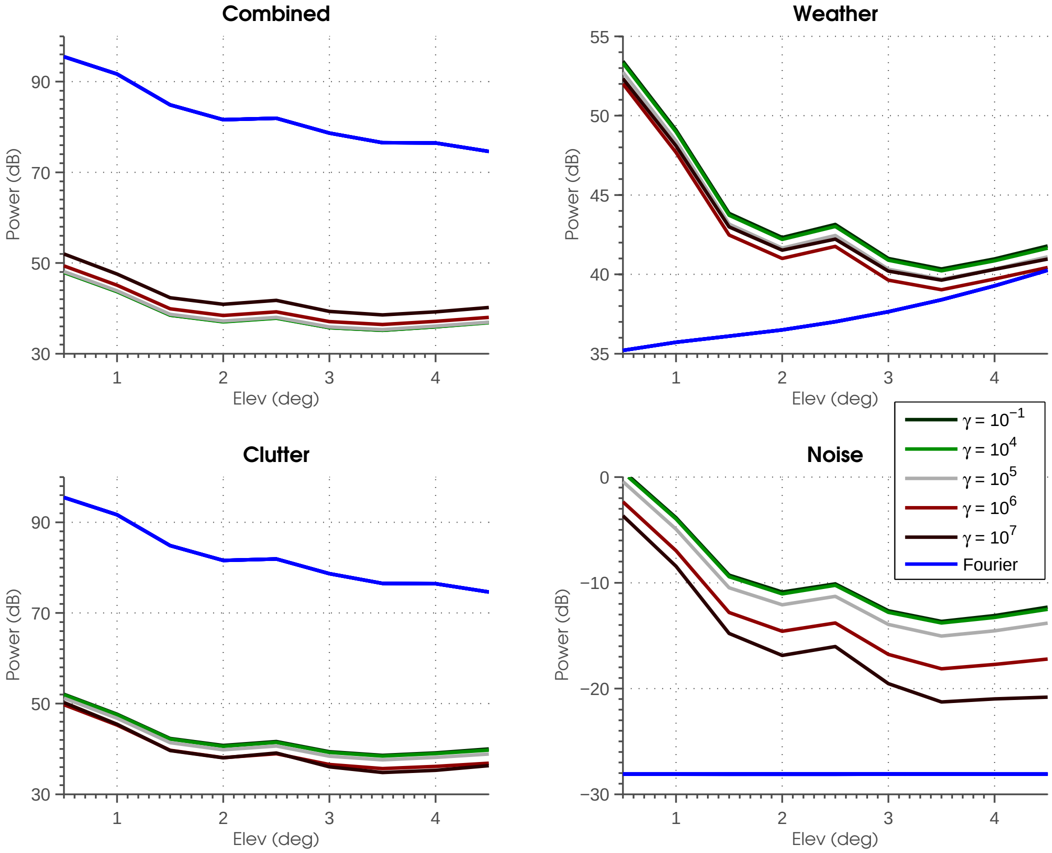

Figure 5.2: Powers obtained using MVDR with variable diagonal loading. The results show the average power with height for diagonal loading ranging from 10^{-1} to 10^{8}. For comparison, the power shown in the blue line is obtained using conventional Fourier beamforming.

since the changes are also effected by the weather and noise components. These effects show that STSP_1 and STSP_2 primarily affect the clutter, while the STSP_3 and STSP_6 affect both the clutter and weather.

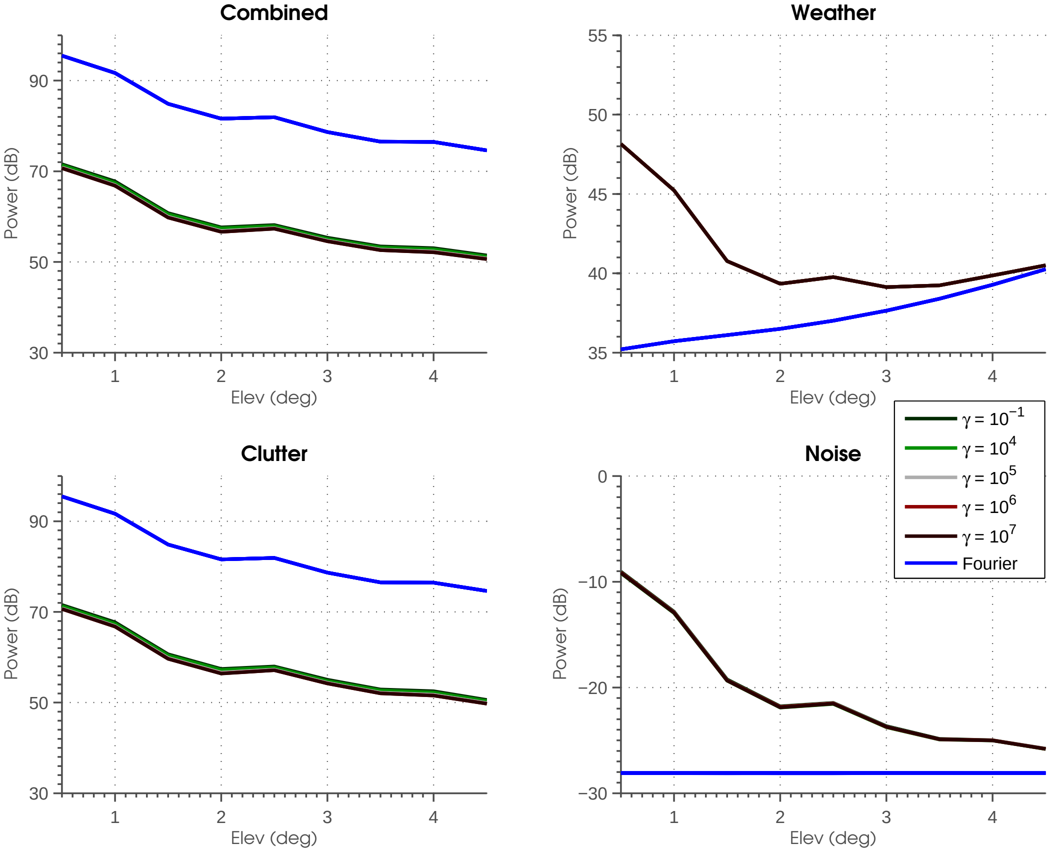

Figure 5.3: Same as Figure 5.2, except with STSP_1.

Based on the results, it can be concluded that the diagonal loading is an important parameter used in filtering ground clutter with a partially adaptive array. Its role in the combined power can be differentiated into two regions illustrated in Figure 5.6. When the steered angle is near the ground, the clutter is located in either the mainlobe or in a sidelobe with high gain. A high gain sidelobe pattern is needed in this case to produce a pattern that matches and to remove the clutter. The process requires a low diagonal loading and produces a composite beampattern that has a mainlobe that is dramatically altered and a high sidelobe level. In the simulated data, this scenario is manifested as an amplified weather power at low elevations. In contrast, when the beampattern is steered away from the ground, the clutter is located near sidelobes with significantly lower gains. In these cases, a lower sidelobe pattern obtained with lower values of diagonal loading is needed to minimize the clutter power, and the

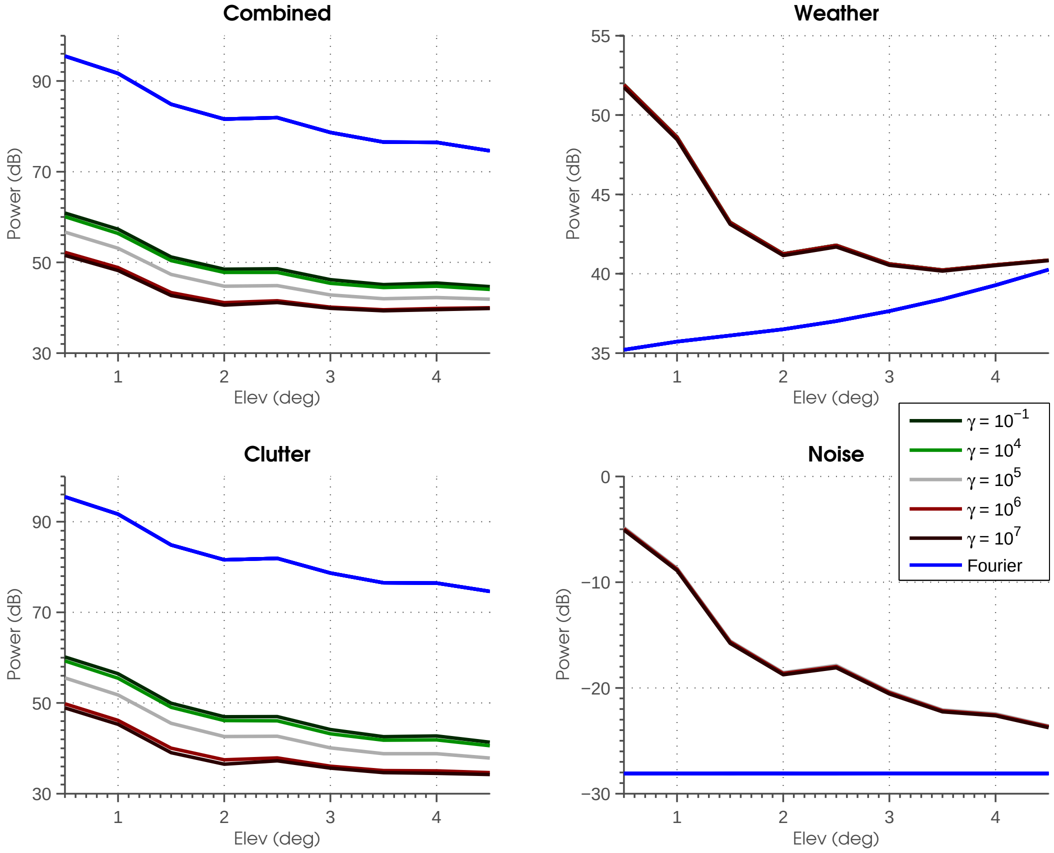

Figure 5.4: Same as Figure 5.2, except with STSP$_2$.

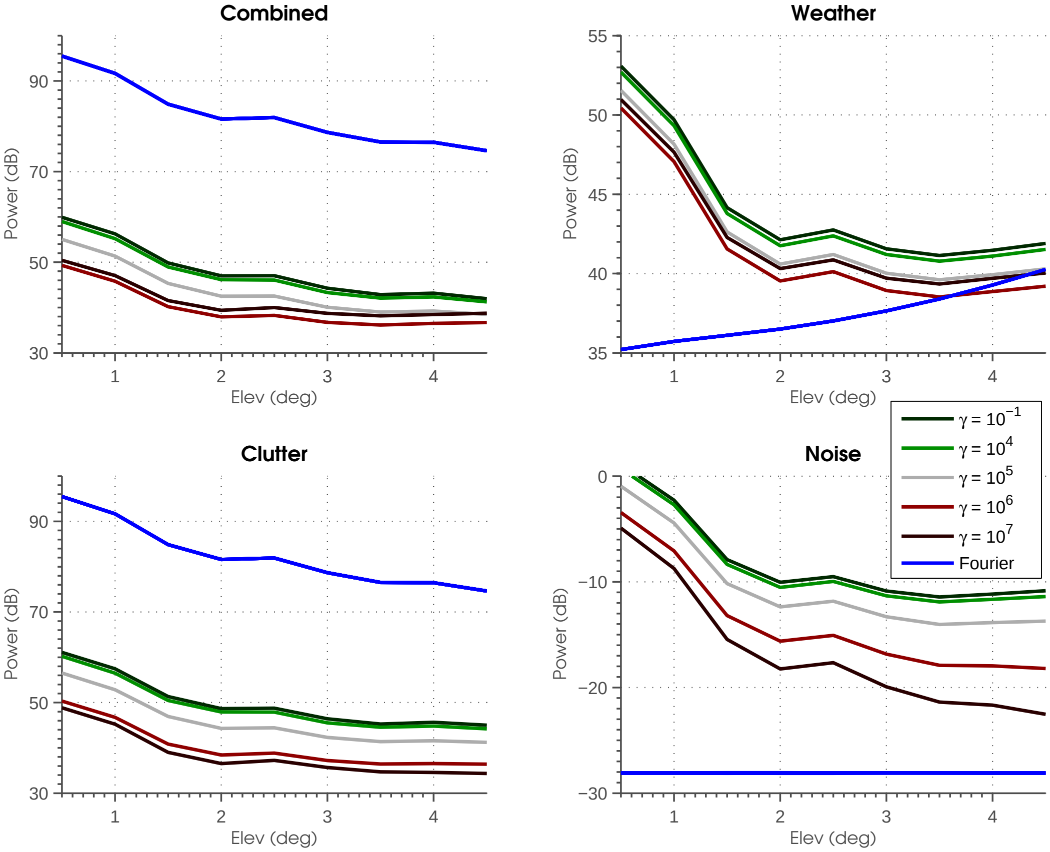

Figure 5.5: Same as Figure 5.2, except with STSP$_6$.

process produces a composite beampattern that has a more desirable mainlobe and lower level sidelobes.

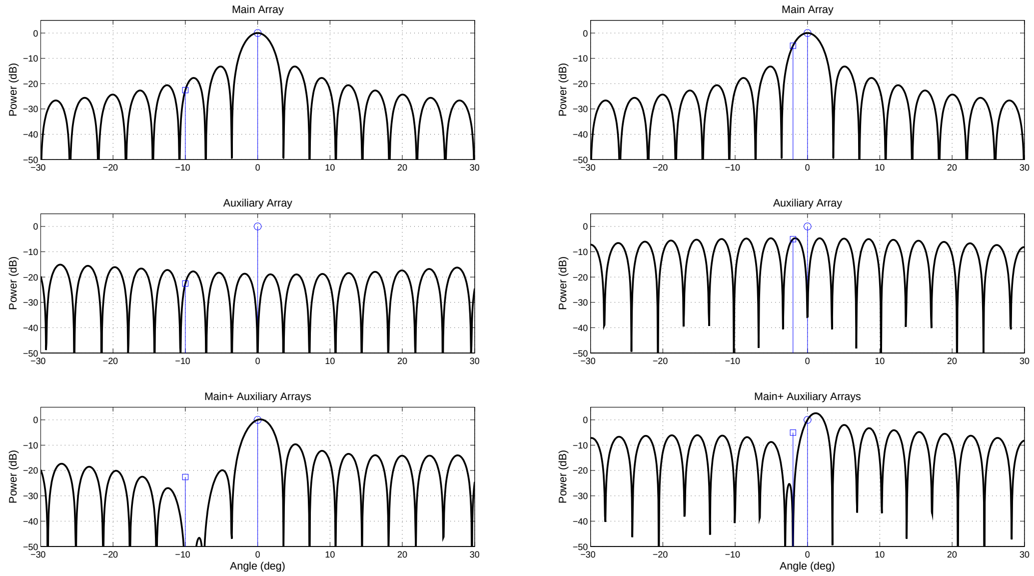
(a)

(b)

Figure 5.6: Example illustrating the beampatterns of original, auxiliary, and composite array when strong clutter is located in the sidelobe and near the mainlobe. Observe the differences of the mainlobe and sidelobes between between the two cases. When clutter is near the mainlobe, its presence introduce higher sidelobe levels as well as distortion to the mainlobe. In both cases, the steered direction is denoted by the symbol '◯', while the clutter position is denoted by the symbol '□'.

5.1.2 Effects of Dwell Time

Based on the setup previously described in Chapter 4, the adaptive techniques are minimized such that the minimum power is obtained over the applied dwell time. As a result, the approach may introduce signals that are correlated and the individual clutter, weather, and noise components may be undesirable in some situations. In this section, the effects caused by samples sizes of 2, 4, 8, 16, and 32 along with parameters listed in Table 5.5 are examined.

Table 5.5: Parameters Used in Varying Dwell Time

Parameter	Value Range
SNR	70 dB
CSR	55 dB
NPTS	**2 — 32**
γ	10^6
σ_v	0.1 m s^{-1}

The powers obtained using MVDR for different sample sizes are plotted in Figure 5.7. For small sample sizes on the order of less than the number of auxiliary elements, the combined power is smaller than the individual powers of the weather and clutter while the noise power is smallest. For example, the combined power is below 35 dB while the weather and clutter powers are both above 40 dB when NPTS of two samples is used. Upon closer inspection, the magnitudes of the clutter and weather powers have similar values and their difference is almost negligible. As a result, the weather and clutter signals must be correlated. At larger sample sizes that are more than the number of auxiliary elements, the combined power is slightly larger than the individual components and its values are in the expected range. The values above 4.0° are approximately equal to the original weather powers. While the results appear to be promising, the clutter and weather power obtained using 32 samples appear to be increasing.

The results of filtering ground clutter using STSP_1, STSP_2, STSP_3, and STSP_6 with the selected sample sizes are shown in Figures 5.8, 5.9, 5.10, and 5.11, respectively. These results show that the variance of the filtered power is affected by the sample size and the choice of the STSP technique. In general, the variance of the combined power is reduced when the filtering scheme is changed from STSP_1 to STSP_6,

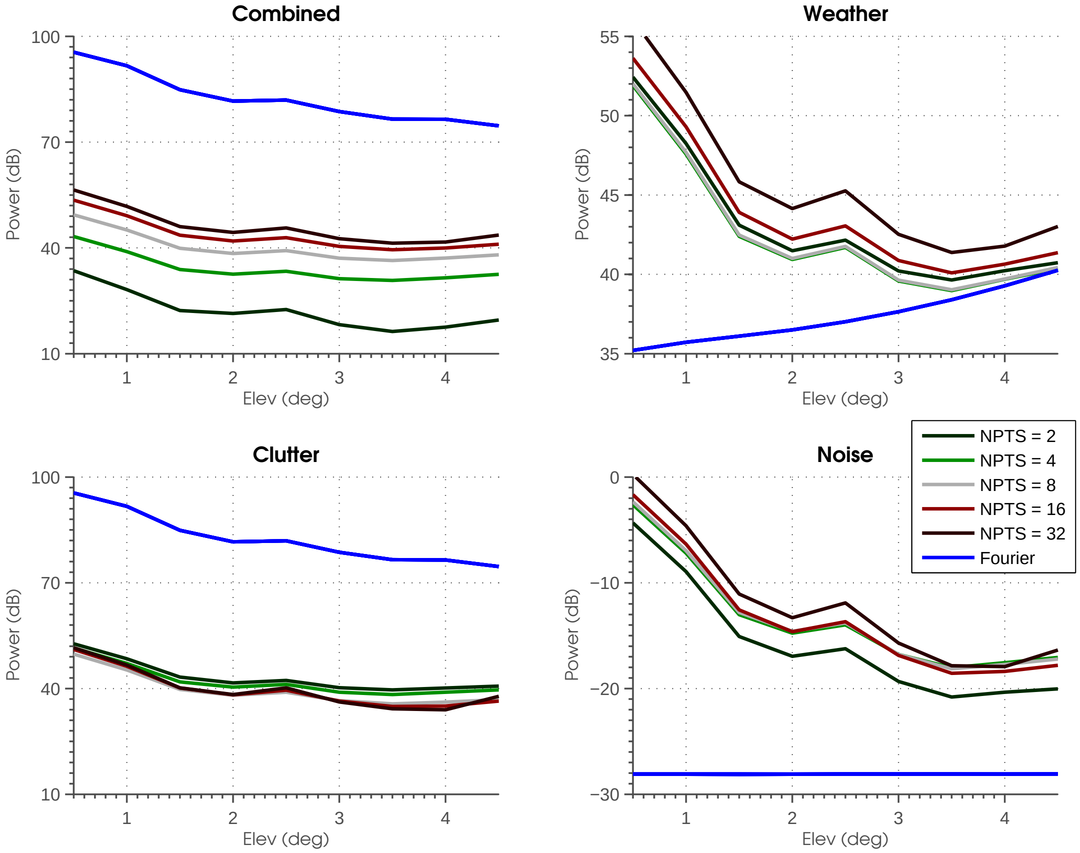

Figure 5.7: Powers obtained using MVDR with variable sample sizes. The results show the average power as a function of elevation angle for sample sizes from two to 32 samples. For comparison, the power shown in the blue line is obtained using conventional Fourier beamforming.

while its variance increases when the sample size is changed from two to 32 samples. Again, the changes can be differentiated into two regions with distinct level of variance. At lower elevations, the variance of the combined power is observed primarily using STSP_1 and STSP_2. Since these two techniques are associated with large eigenvalues and clutter, the output signals obtained when these two subspaces are not included should contain residual clutter.

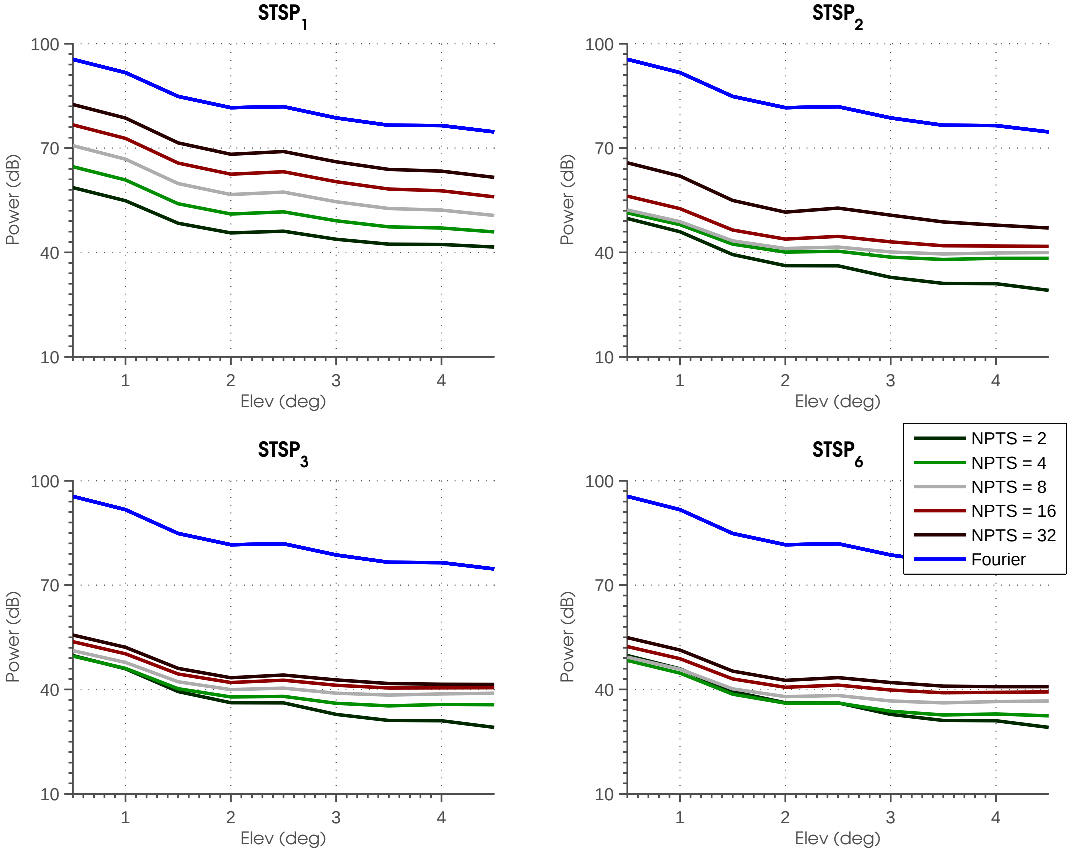

Figure 5.8: Same as Figure 5.7, except for STSP_1, STSP_2, STSP_3, and STSP_6, and only the combined power is plotted.

Based on the results, the dwell time is an important parameter of the covariance matrix and is related to the stability of these systems since the inverse of the covariance matrix is used to obtain the filter weights. The effects of the dwell time on clutter filtering can be observed by examining the output powers for cases with varying dwell times. For short dwell times, the variance of the covariance matrix is expected to be high and the covariance matrix is singular and rank deficient. When the weights are obtained using the inverse of the covariance matrix in this case, the poorly estimated covariance matrix can produce combined powers with smaller values

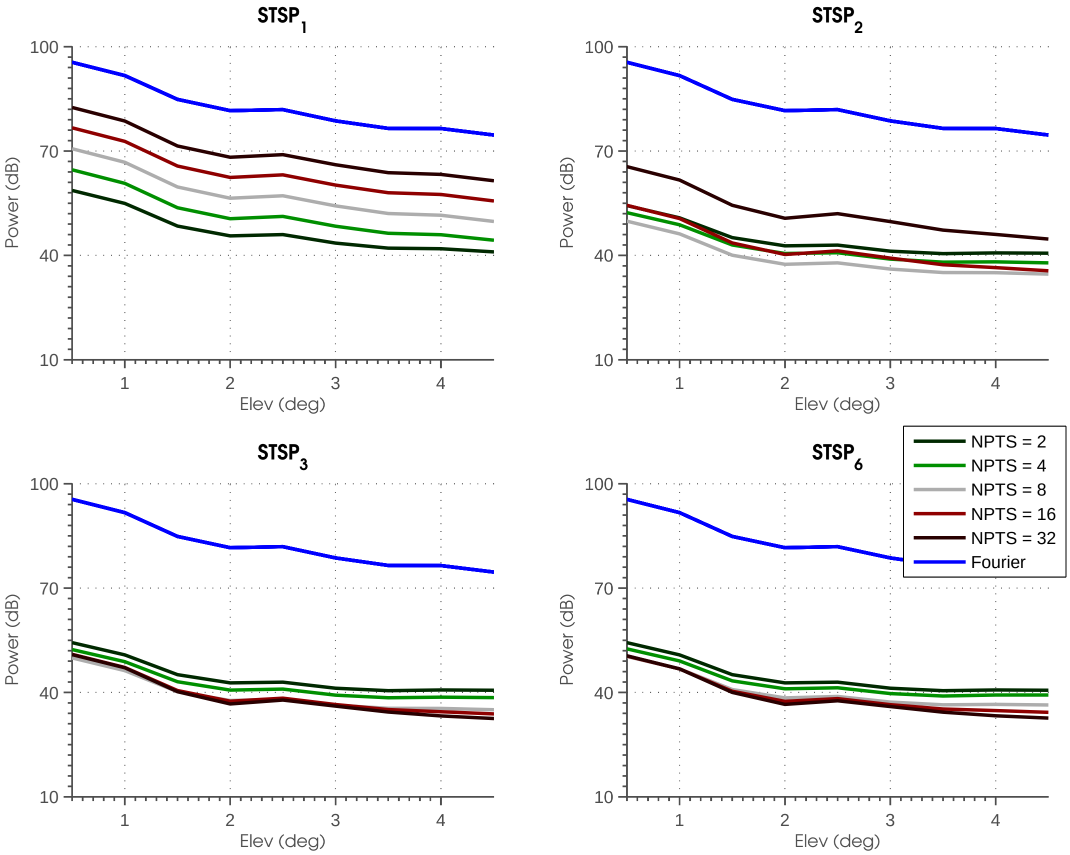

Figure 5.9: Same as Figure 5.7, except for STSP$_1$, STSP$_2$, STSP$_3$, and STSP$_6$, and only the clutter power is plotted.

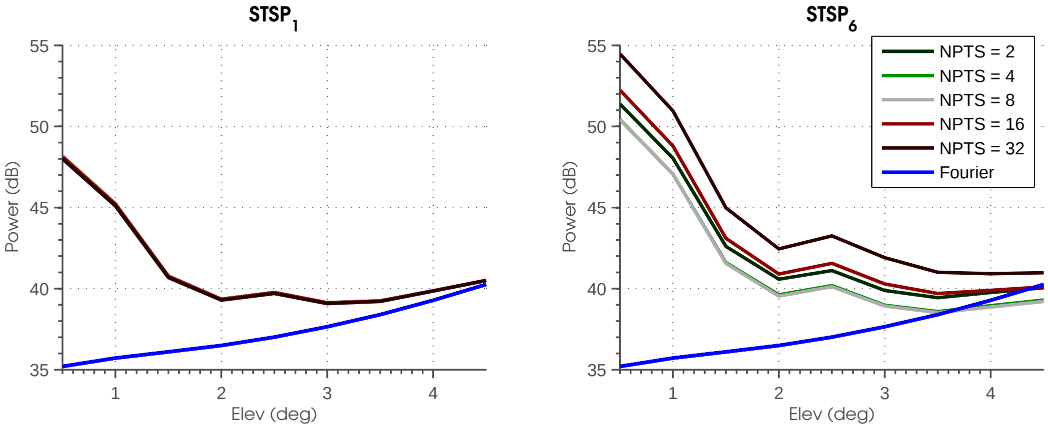

Figure 5.10: Same as Figure 5.7, except for STSP$_1$ and STSP$_6$, and only the weather power is plotted.

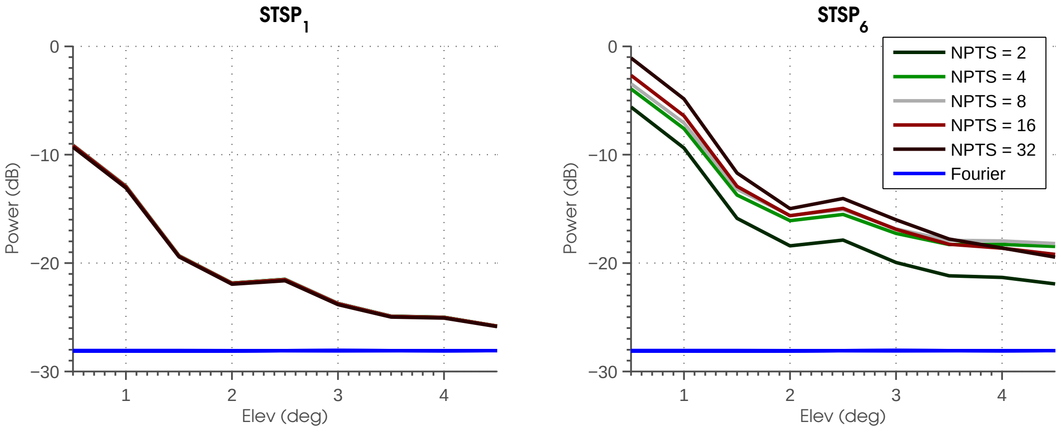

Figure 5.11: Same as Figure 5.7, except for STSP$_1$ and STSP$_6$, and only the noise power is plotted.

than the individual clutter and weather powers. In contrast, the covariance matrix is better estimated when longer dwell times are used, and better estimates of the combined power are produced in this case. Upon closer inspection of the results, clutter attenuation is maximized when a dwell time of 16 samples is used while the weather and clutter powers appear to be amplified when 32 samples are used.

5.1.3 Effects of Fading Clutter

The fading parameter for ground clutter describes the extent to which the clutter is in random motion. Large values of fading clutter indicate a high variance of the ground clutter motion, while small values describe essentially stationary ground scatterers. In this subsection, the performance of clutter filtering using spatial arrays is examined for fading clutter with values of 0.01, 0.05, 0.1, 0.5, and 1.0 m s^{-1} along with the other parameters listed in Table 5.6. While realistic values of fading clutter have been observed by Curtis (2009) with the NWRT PAR, only the effects caused by fading clutter with the selected values are examined.

Table 5.6: Parameters Used in Varying Fading Clutter

Parameter	Value
SNR	70 dB
CSR	55 dB
NPTS	8
γ	10^6
$\sigma_{\mathbf{v}}$	**0.01 — 1.0 m** $\mathbf{s}^{-1}$

Results of filtering ground clutter using MVDR for the selected range of fading clutter values are plotted in Figure 5.12, showing that the fading parameter differentiates the powers into two regions with boundaries that are determined by the magnitude of the fading parameter. When $\sigma_v \leq 0.1$ m s^{-1}, the filtered powers have low variance and similar values. The weather power has values that are similar to the original weather values when the elevation is above 4.0°. When $\sigma_v \geq 0.5$ m s^{-1} is observed, a larger difference in the output powers are obtained that increases when σ_v is changed from 0.5 m s^{-1} to 1.0 m s^{1}.

With the same setup, the results observed by processing the time series signals using STSP_1, STSP_2, STSP_3, and STSP_6 are plotted in Figure 5.13, 5.14, 5.15, and 5.16, respectively. Generally, the results also show two distinct regions with boundaries that are differentiated by the fading parameter and a third region that is present when STSP_1 is used. The localization of the powers is particularly evident when processed using STSP_2, STSP_3 or STSP_6, and shows that the powers cluster when $\sigma_v \leq 0.1$ m s^{-1} and when $\sigma_v \geq 0.5$ m s^{-1}. When STSP_1 is used, another region is observed when $\sigma_v = 0.01$ m s^{-1} that produces the minimum power. Overall, it was

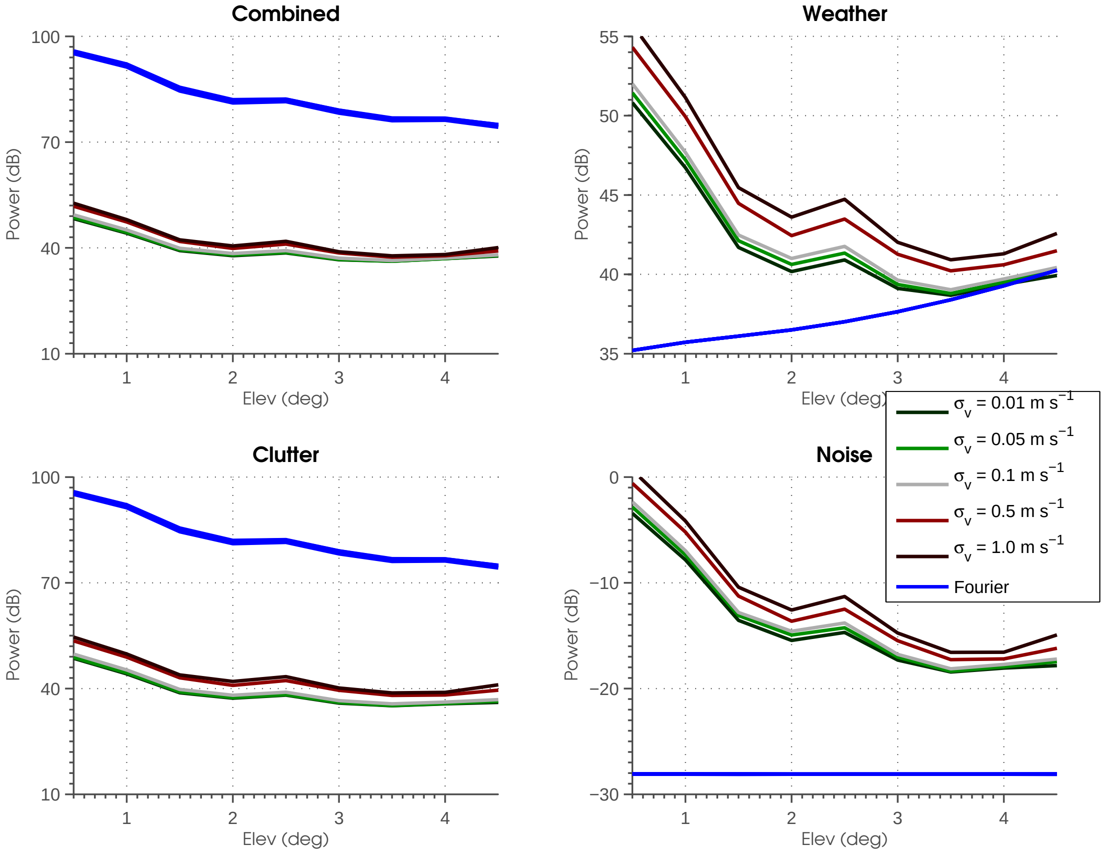

Figure 5.12: Powers obtained using MVDR with variable fading clutter. The results show the average power with height for fading clutter from 0.01 m s^{-1} to 1.0 m s^{-1}. For comparison, the power shown in the blue line is obtained using conventional Fourier beamforming.

observed that the clutter power and its variance decrease when STSP is changed from $STSP_1$ to $STSP_6$ with a significant portion of the change occurring before $STSP_3$ is applied. In contrast, the weather and noise powers and their variance increase for the same changes to the STSP techniques, this time with a significant portion of the change occurring when *after* $STSP_3$ is applied.

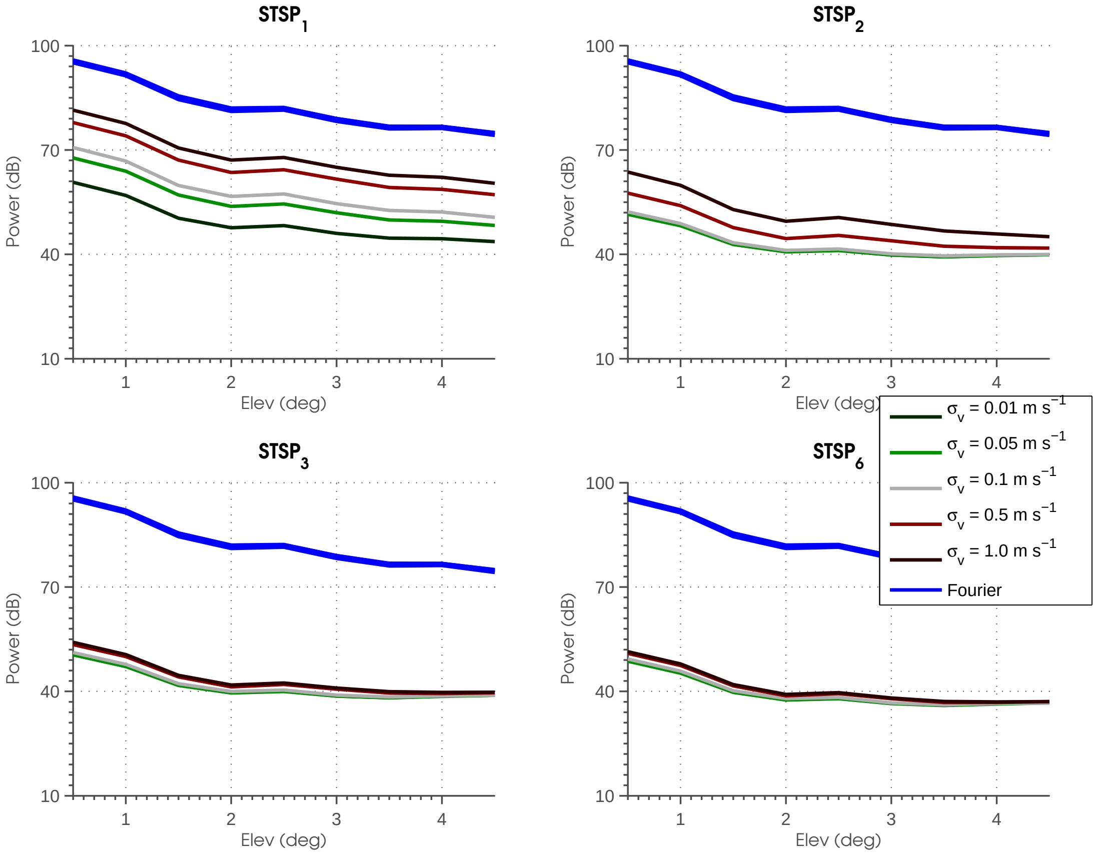

Figure 5.13: Same as Figure 5.12, except for $STSP_1$, $STSP_2$, $STSP_3$, and $STSP_6$, and only the combined power is plotted.

Another factor that determines the statistics of the covariance matrix is clutter fading. As previously discussed, the parameter details the relative motion of the ground targets. In the simulations, the results processed by the STSP techniques show that the residual clutter increases when larger values of clutter fading was using and imply that clutter fading spreads the eigenvalues of the clutter subspace. This phenomenon is illustrated in Figure 5.17. Intuitively, spreading the clutter implies that more independent samples of the clutter are observed and more degrees-of-freedom are needed to filter the contamination. With a limited number of degrees-of-freedom

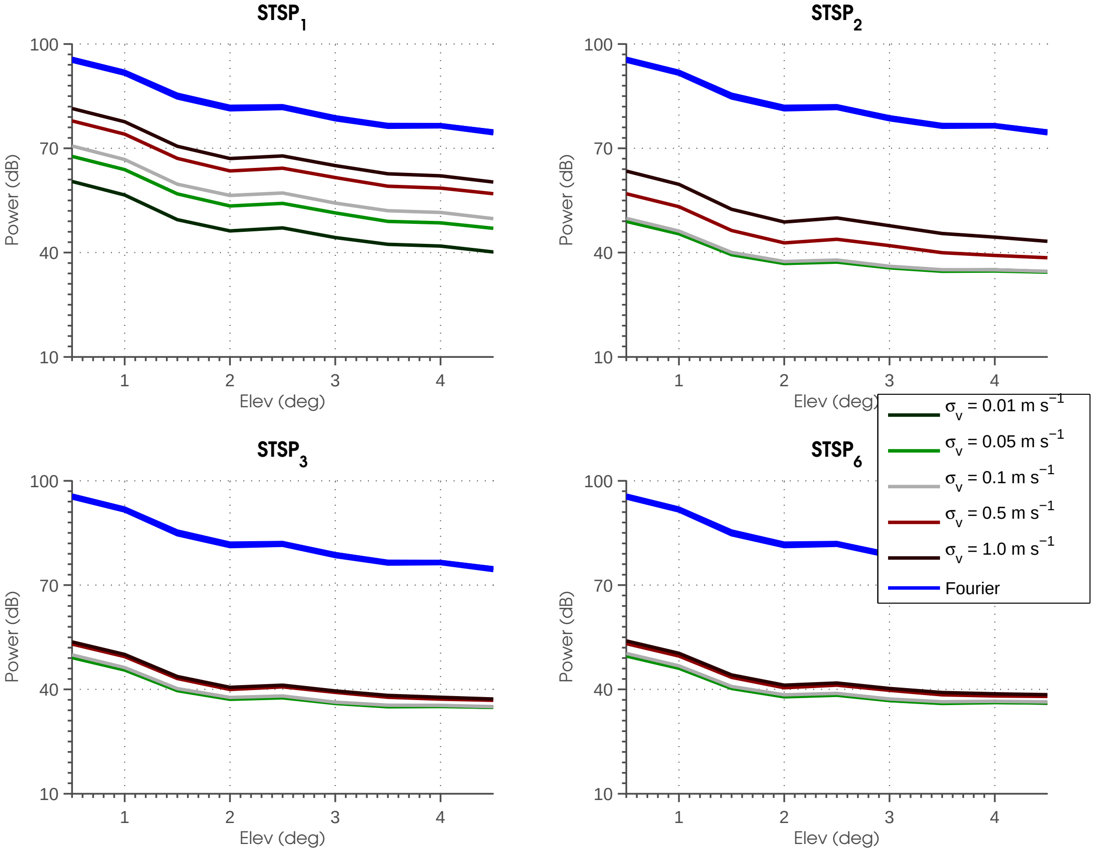

Figure 5.14: Same as Figure 5.12, except for STSP$_1$, STSP$_2$, STSP$_3$, and STSP$_6$, and only the clutter power is plotted.

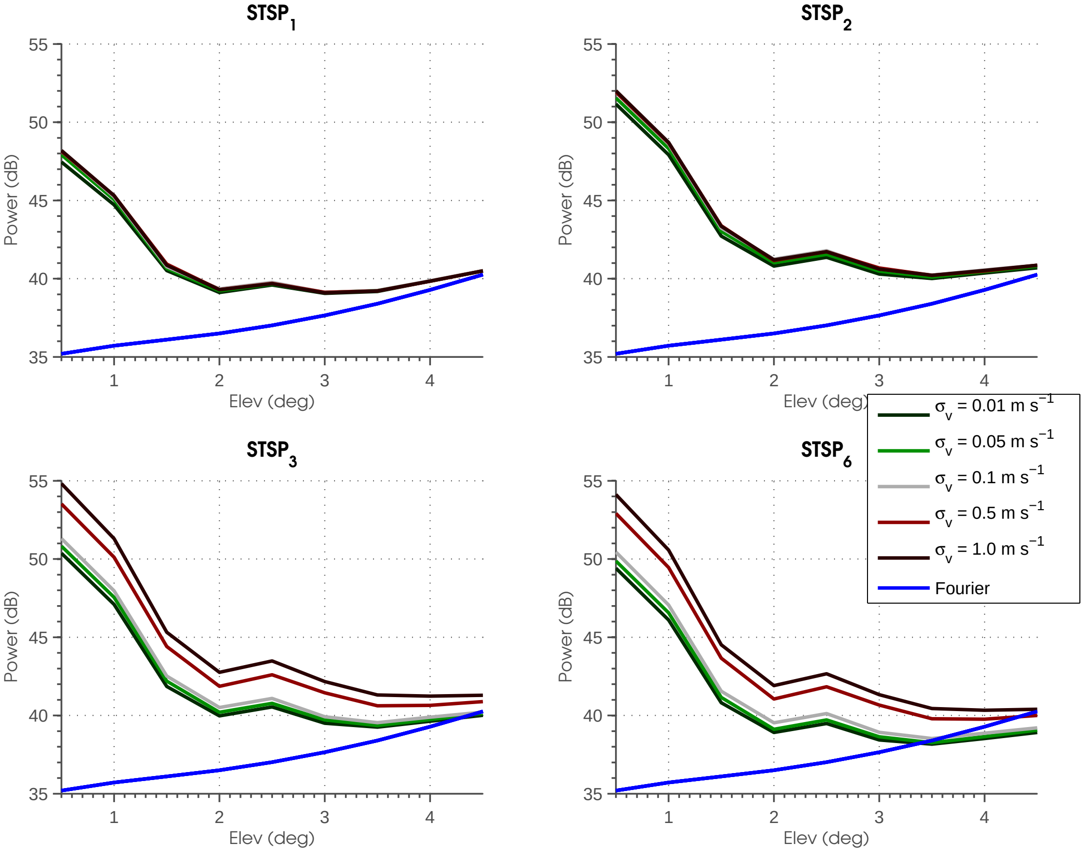

Figure 5.15: Same as Figure 5.12, except for STSP$_1$, STSP$_2$, STSP$_3$, and STSP$_6$, and only the weather power is plotted.

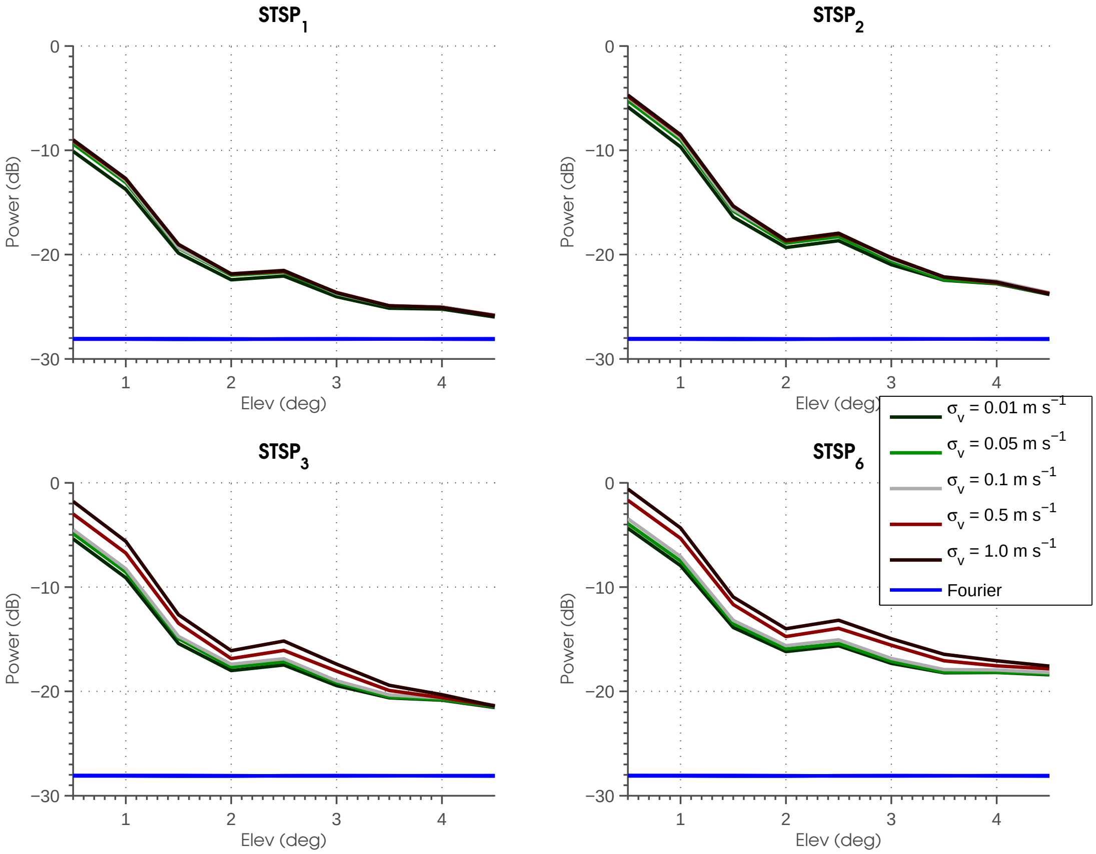

Figure 5.16: Same as Figure 5.12, except for STSP$_1$, STSP$_2$, STSP$_3$, and STSP$_6$, and only the noise power is plotted.

that are available in any SLC algorithm, the performance of the clutter filters is expected to degrade as longer dwell time is used.

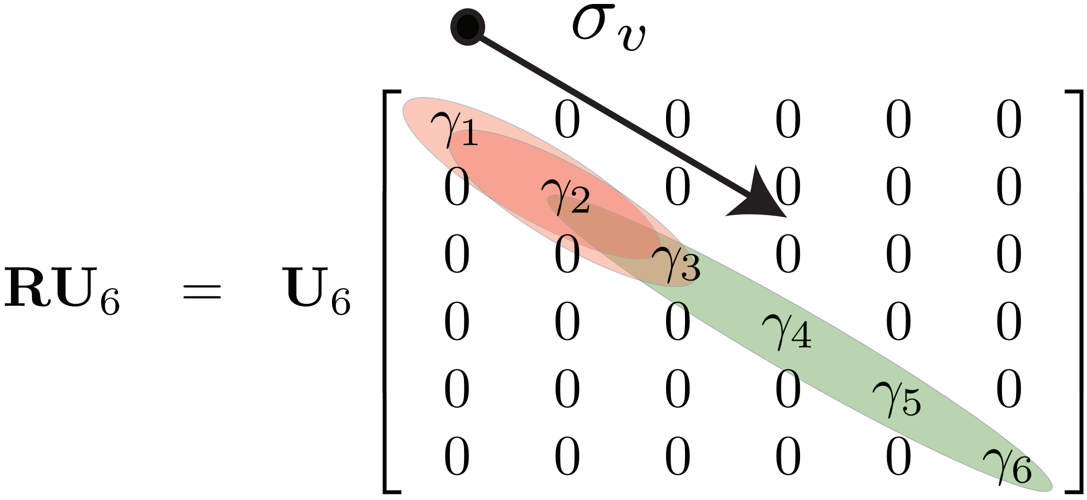

$$\mathbf{RU}_6 \quad = \quad \mathbf{U}_6 \begin{bmatrix} \gamma_1 & 0 & 0 & 0 & 0 & 0 \\ 0 & \gamma_2 & 0 & 0 & 0 & 0 \\ 0 & 0 & \gamma_3 & 0 & 0 & 0 \\ 0 & 0 & 0 & \gamma_4 & 0 & 0 \\ 0 & 0 & 0 & 0 & \gamma_5 & 0 \\ 0 & 0 & 0 & 0 & 0 & \gamma_6 \end{bmatrix}$$

Figure 5.17: Illustrated effects of clutter fading. With increase in the clutter fading, the eigenvalues are spread. Since there is a limited number of degrees-of-freedom in a sidelobe canceler, the performance of the clutter filter can degrade with increasing value of clutter fading.

5.1.4 Effects of Clutter-to-Signal Ratio

The clutter power relative to the signal power, which is called the clutter-to-signal ratio, is another parameter generally considered when filtering clutter with spatial arrays. The value is quite variable and depends on the target characteristics and the location of the clutter relative to the steered direction. It is generally largest when the clutter is located within the mainlobe and decreases when the clutter is located farther away from the mainlobe. In this section, the performance of ground clutter filtering is examined with CSR ranging from 35 dB to 65 dB along with parameters listed in Table 5.7.

Table 5.7: Parameters Used in Varying Clutter Power

Parameter	Value
SNR	70 dB
CSR	**35 — 65 dB**
NPTS	8
γ	10^6
σ_v	0.1 m s^{-1}

The results obtained using MVDR for the above setup are shown in Figure 5.18. The results show changes to the filtered powers with input CSR and indicate that an attenuation of over 55 dB could be attained. Additionally, the results appear to be relatively constant with a small variance of less than 6 dB and suggest that the output powers are independent of the input CSR level above 35 dB. In the setup, it was observed that the variance in the combined power is primarily caused by fluctuations between 4-6 dB of the weather power. While the clutter and noise powers also fluctuate, their magnitude and variation are slightly smaller. In particular, the clutter power is a few dB smaller than the weather power while the noise is significantly smaller. Additionally, MVDR retrieves the weather power with a small positive bias when the elevation angle is above 4.0° and the CSR is greater than 45 dB. At a CSR of 35 dB, the weather power is slightly negatively biased. Below this angle, the weather power is positively biased and increases until 0.5°, where it is largest.

When the time series signals were processed using STSP_1, STSP_2, STSP_3, and STSP_6, the results are plotted in Figures 5.19, 5.20, 5.21, and 5.22, respectively. The results show that the filtered powers have a large variance when STSP_1 is used, while

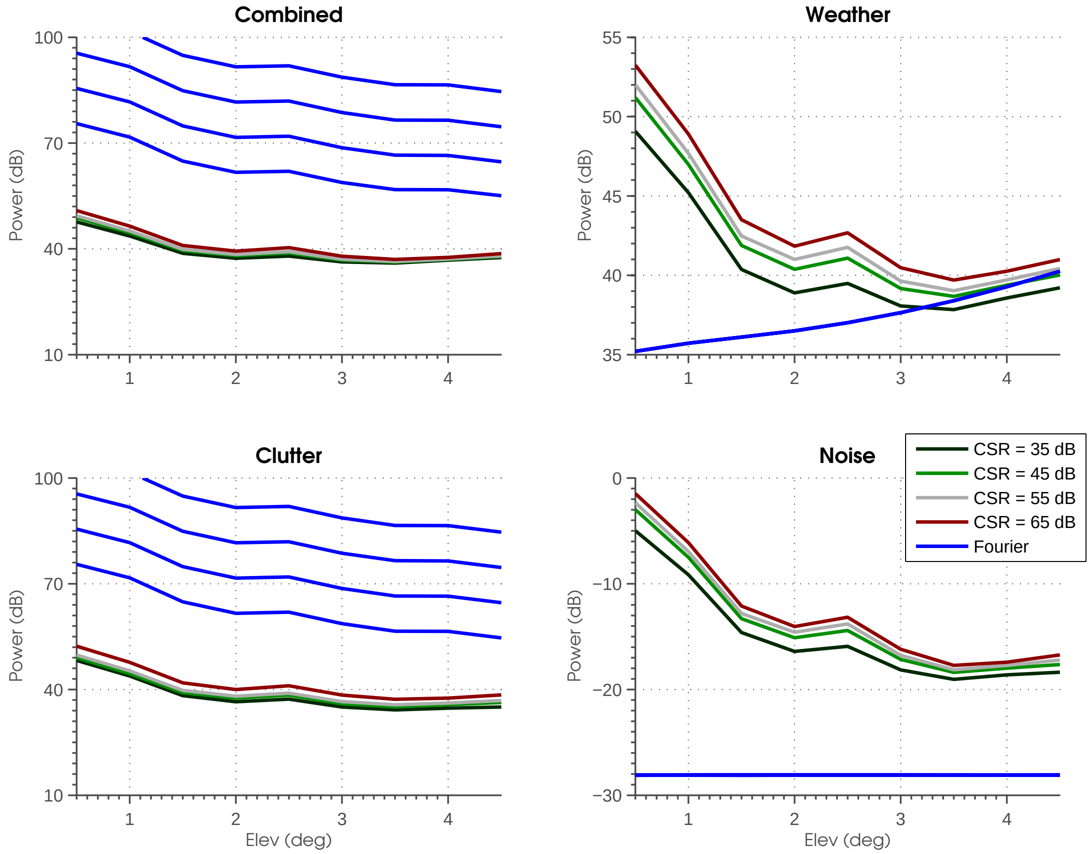

Figure 5.18: Powers obtained using MVDR with variable CSR. The results show the average power with height for CSR from 35 dB to 65 dB. For comparison, the power shown in the blue line is obtained using conventional Fourier beamforming.

the powers are relatively consistent with a small variance of less than 6 dB is observed when STSP$_2$, STSP$_3$, or STSP$_6$ is applied. An exception occurs when the input CSR is 65 dB, which produces an abnormal above average output power indicates the results were obtained using an unstable version of the estimated covariance matrix. Excluding this case and using only the dominant eigensubspace, clutter power and its variance are largest while the noise and weather powers are relatively consistent. Because of this, the clutter power is generally the dominant component of the combined power.

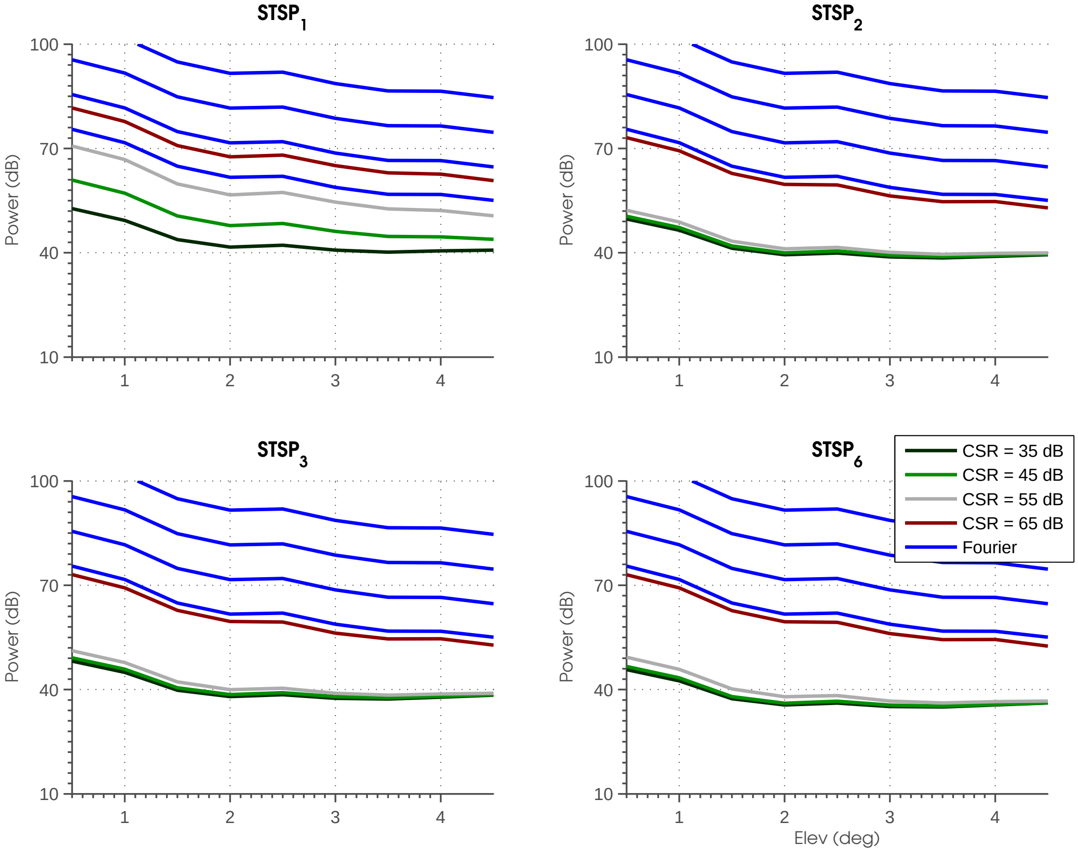

Figure 5.19: Same as Figure 5.18, except for STSP$_1$, STSP$_2$, STSP$_3$, and STSP$_6$, and only the combined power is plotted.

The effects of CSR to clutter filtering with SLC arrays can be simplified by first examining the results that are obtained when the CSR is large. Under this assumption and using an eigenvalue decomposition, the order of the eigenvalues of the covariance matrix has the form $\gamma_1 > \gamma_2 \gg \gamma_3 > \gamma_4 > \gamma_5 > \gamma_6$, where γ_1 and γ_2 are the clutter eigenvalues and they are significantly larger than $\gamma_{3\cdots6}$, which are the weather and noise eigenvalues. An illustrated example of this decomposition is shown in

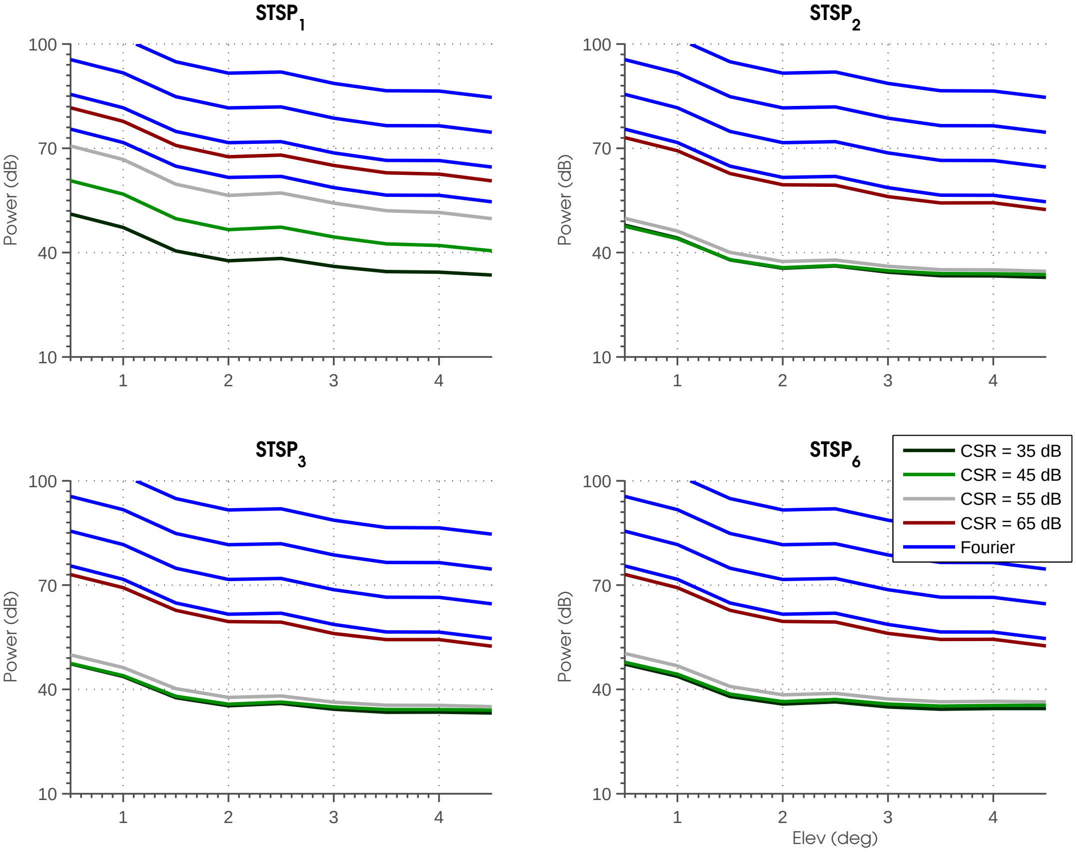

Figure 5.20: Same as Figure 5.18, except for STSP$_1$, STSP$_2$, STSP$_3$, and STSP$_6$, and only the clutter power is plotted.

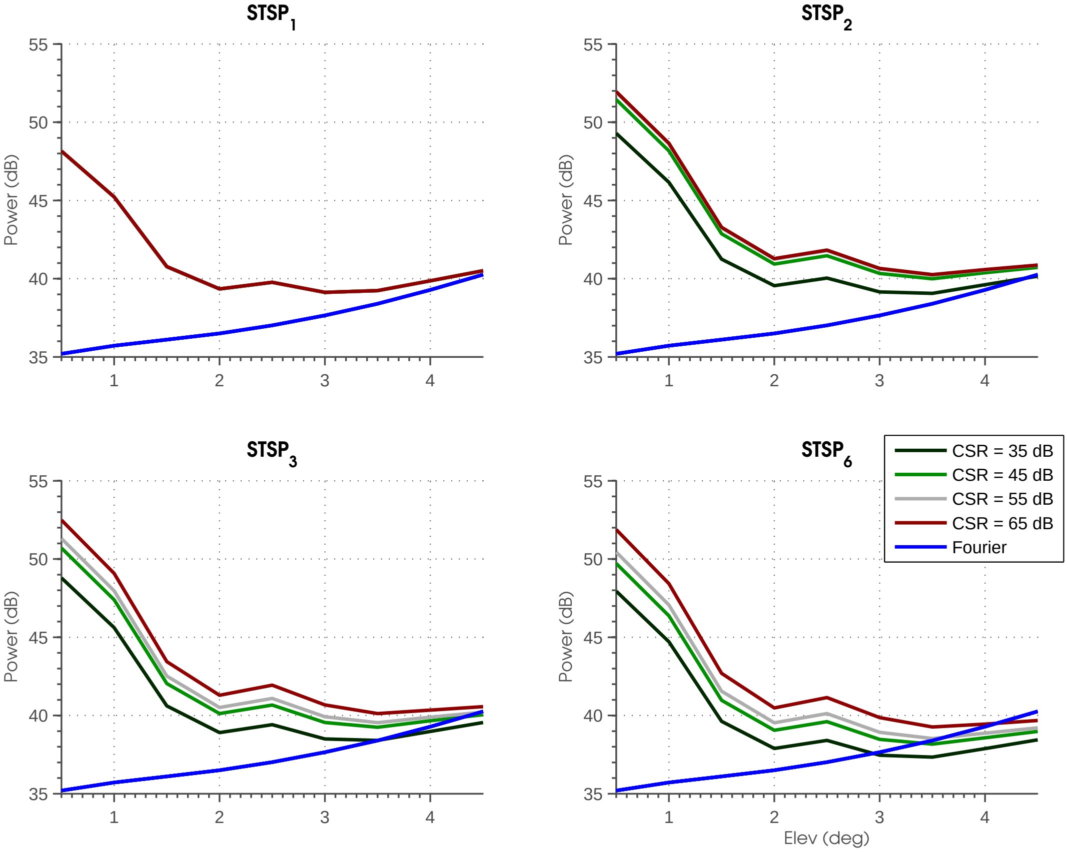

Figure 5.21: Same as Figure 5.18, except for STSP$_1$, STSP$_2$, STSP$_3$, and STSP$_6$, and only the weather power is plotted.

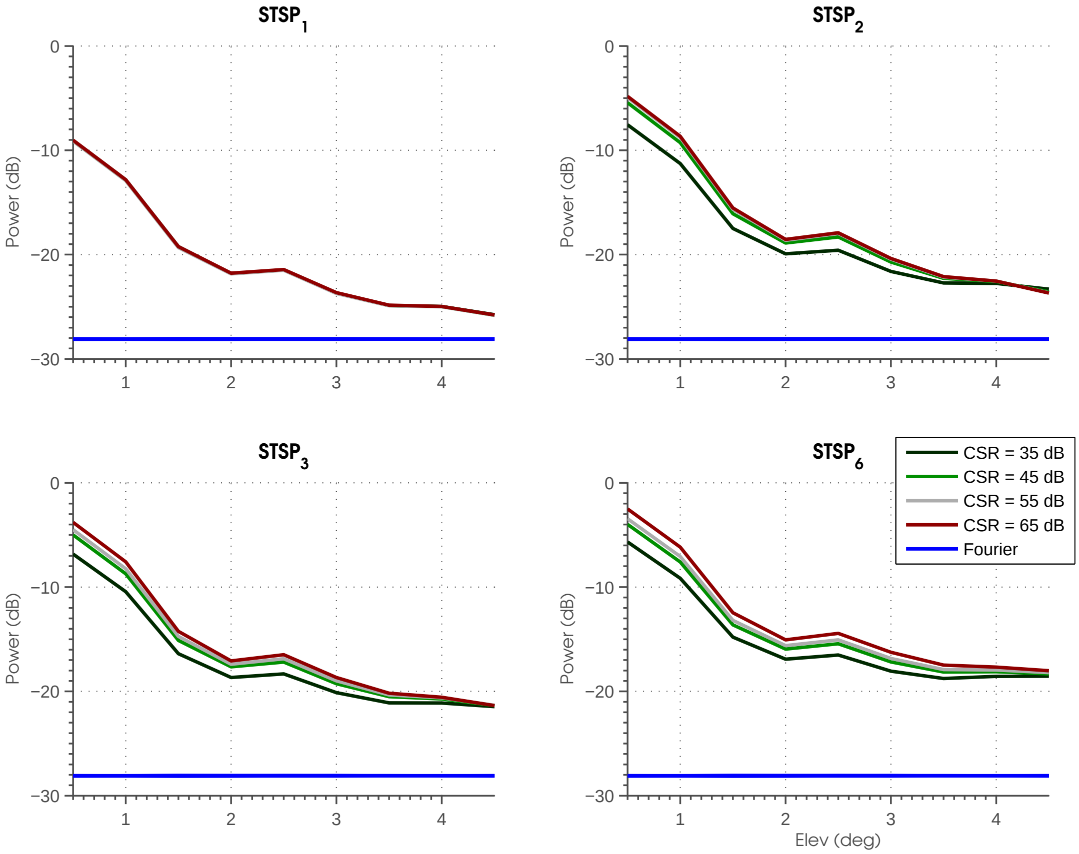

Figure 5.22: Same as Figure 5.18, except for STSP$_1$, STSP$_2$, STSP$_3$, and STSP$_6$, and only the noise power is plotted.

Figure 5.23. When the clutter power is changed, only the magnitude of the clutter eigenvalues are affected. Therefore, $\mathbf{R}^{'} \cong C^2\mathbf{R}$, where C is the clutter scaling factor, and its cross correlation as $\mathbf{p}^{'} \cong C_pC\mathbf{p}$, where C_p is the gain of the clutter in the time series signal of the main array.

Now observe the output power of the SLC using MSC which has the expression $\mathbf{w}_o^{'} = \left(\mathbf{R}^{'}\right)^{-1}\mathbf{p}^{'}$ with original weights $\mathbf{w}_0 = \left(\mathbf{R}\right)^{-1}\mathbf{p}$. Using the assumption, $\left(\mathbf{R}^{'}\right)^{-1} \cong \frac{1}{C^2}\mathbf{R}^{-1}$ when a sufficiently large diagonal loading is used. The output power with the scaled correlation matrix is

$$\begin{aligned} \left(\mathbf{w}_o^{'}\right)^H \mathbf{R}^{'}\mathbf{w}_o^{'} &\cong \left(CC_p\mathbf{p}\tfrac{1}{C^2}\mathbf{R}^{-1}\right)^H C^2\mathbf{R}\left(CC_p\mathbf{p}\tfrac{1}{C^2}\mathbf{R}^{-1}\right) \\ &= C_p^2\mathbf{w}_o^H\mathbf{R}\mathbf{w}_o. \end{aligned} \tag{5.1}$$

It is a scaled version of the original clutter power, which when subtracted from the signal of the main array produces a consistent power. Another view of this process is that the orthogonal projection matrix, i.e. $\mathbf{R}^{-1} = \frac{1}{\gamma}\mathbf{P}^{\perp}$ is only a scaled factor.

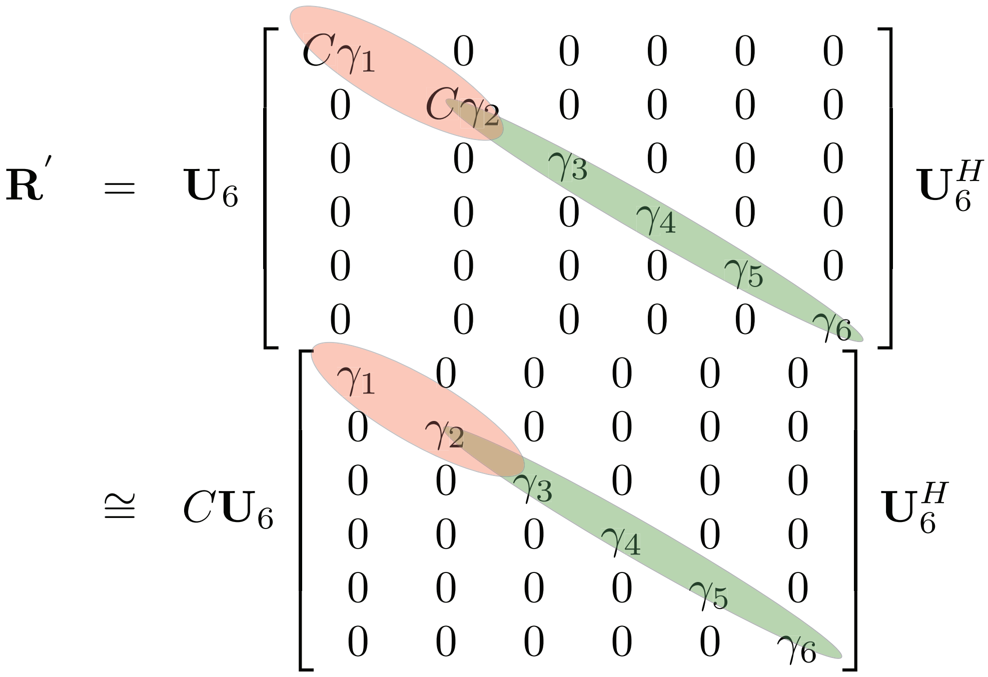

$$\begin{aligned} \mathbf{R}^{'} &= \mathbf{U}_6 \begin{bmatrix} C\gamma_1 & 0 & 0 & 0 & 0 & 0 \\ 0 & C\gamma_2 & 0 & 0 & 0 & 0 \\ 0 & 0 & \gamma_3 & 0 & 0 & 0 \\ 0 & 0 & 0 & \gamma_4 & 0 & 0 \\ 0 & 0 & 0 & 0 & \gamma_5 & 0 \\ 0 & 0 & 0 & 0 & 0 & \gamma_6 \end{bmatrix} \mathbf{U}_6^H \\ &\cong C\mathbf{U}_6 \begin{bmatrix} \gamma_1 & 0 & 0 & 0 & 0 & 0 \\ 0 & \gamma_2 & 0 & 0 & 0 & 0 \\ 0 & 0 & \gamma_3 & 0 & 0 & 0 \\ 0 & 0 & 0 & \gamma_4 & 0 & 0 \\ 0 & 0 & 0 & 0 & \gamma_5 & 0 \\ 0 & 0 & 0 & 0 & 0 & \gamma_6 \end{bmatrix} \mathbf{U}_6^H \end{aligned}$$

Figure 5.23: Illustrated effects of CSR at high values. Under this assumption, the correlation matrix is dominated by a few eigenvalues of the clutter and can be approximated by a constant multiplication to the eigenmatrix. Using this assumption, it can be easily shown that the inverse of the correlation matrix is also a multiple of the constant.

5.1.5 Effects of Signal-to-Noise Ratio

The ratio of the signal to noise powers is the final parameter examined. In general, the noise power is caused by thermal fluctuations of the receiver and is generally assumed to be constant over the measurement duration, while the weather power has a large range and depends on the scattering field, which can vary from clear air to heavy rain for atmospheric radars. The composite values make up the spatial covariance matrix that is used by the spatial filters to obtain the weights and determines the SNR. As a result, the SNR is an important parameter of spatial arrays and its effect on the performance of these filters is examined along with other parameters listed in Table 5.8 in this subsection.

Table 5.8: Parameters Used in Varying Noise Power

Parameter	Value
SNR	**10 — 70 dB**
CSR	55 dB
NPTS	8
γ	10^6
σ_v	0.1 m s^{-1}

The results obtained using MVDR are shown in Figure 5.24. The results show the filtered powers when processed with SNR levels ranging from 10-70 dB and indicate that the filtered powers are consistent when the SNR is high. For example, the results when the SNR is at least 30 dB show negligible differences. On the other hand, a large deviation from the other results is observed when the SNR is 10 dB. The effect manifests as an increase to the weather power of approximately less than 2.0 dB, while it manifests as a larger increase in the combined and clutter powers of up to 5.0 dB. The noise power, which in other cases is significantly below the other powers, is now at some angles larger than the weather power. Its contribution to the combined power now can not be neglected.

With the same setup, the results observed by processing the time series signals using STSP are plotted in Figures 5.25, 5.26, 5.27, and 5.28, respectively. The results show that the results are relatively consistent when the SNR is above 30 dB while the performance of the filters is more sensitive when the SNR is below this value. For example, only a negligible difference in the output powers is observed when the SNR

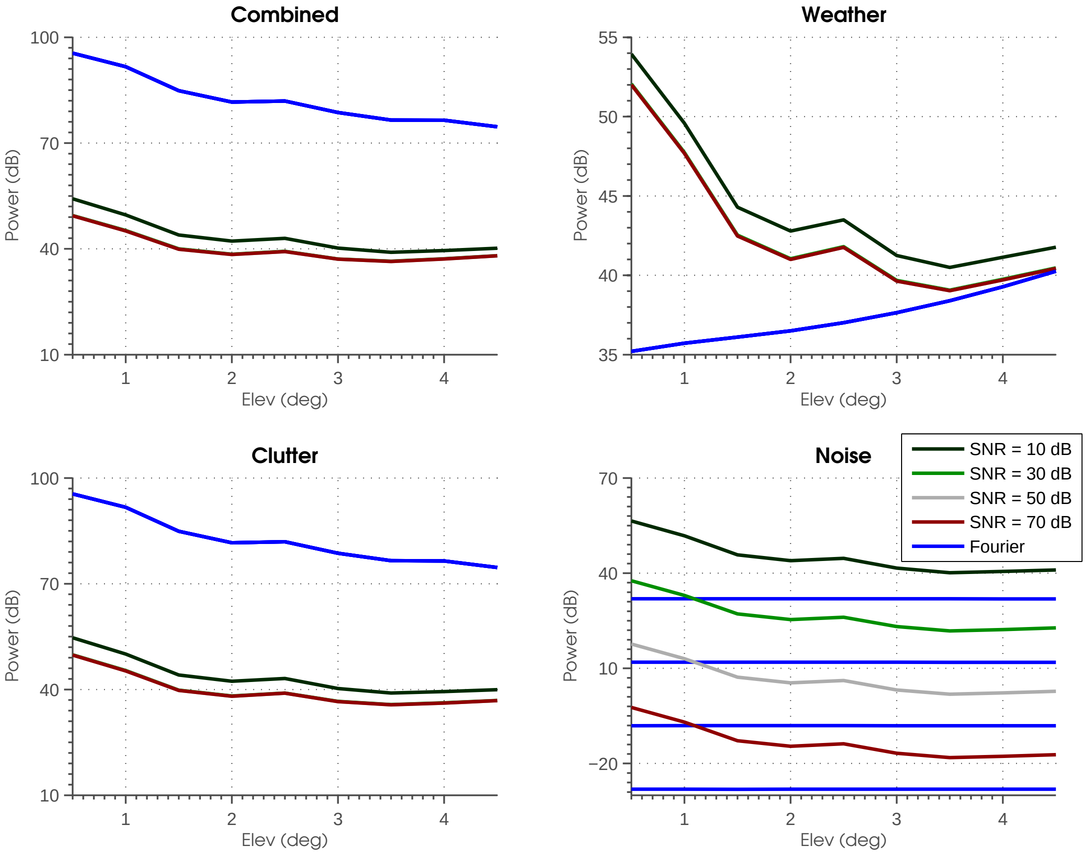

Figure 5.24: Powers obtained using MVDR with variable SNR. The results show the average power with height for SNR from 10 dB to 70 dB. For comparison, the power shown in the blue line is obtained using conventional Fourier beamforming.

is above 30 dB. In contrast, a noticeable change to the processed powers is observed when the SNR is 10 dB with the largest change occurring when STSP_6 is used and negligible change when STSP_1 is used. Upon closer inspection, the weather and noise powers are increased and in some cases a positive bias of the weather power is observed. Overall, the increase in the noise power due to the SNR is fairly consistent. The noise power when the SNR = 10 dB is approximately equal to the clutter power and larger than the weather power for some angles.

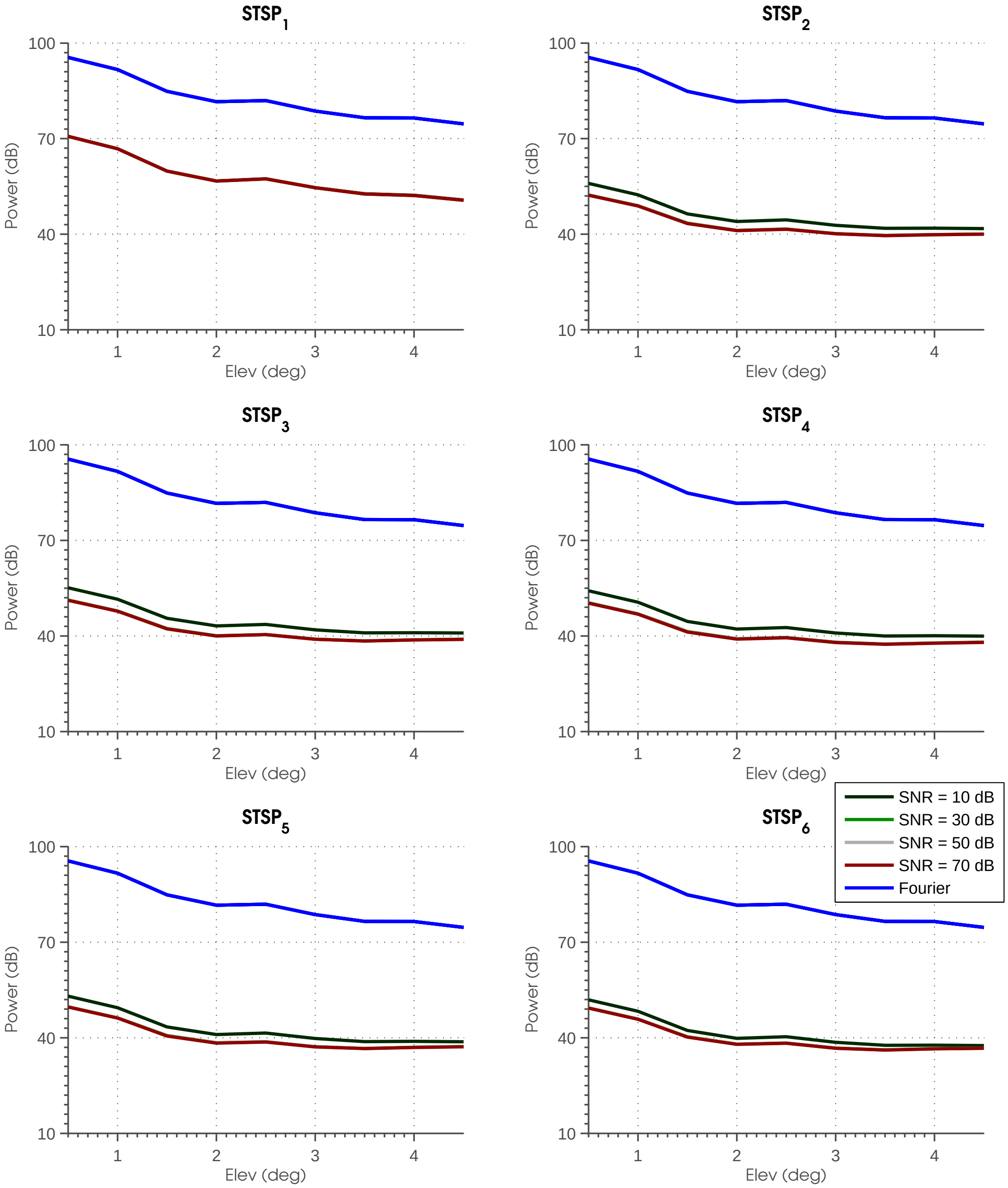

Figure 5.25: Same as Figure 5.24, except for STSP_1, STSP_2, STSP_3, STSP_4, STSP_5, and STSP_6, and only the combined power is plotted.

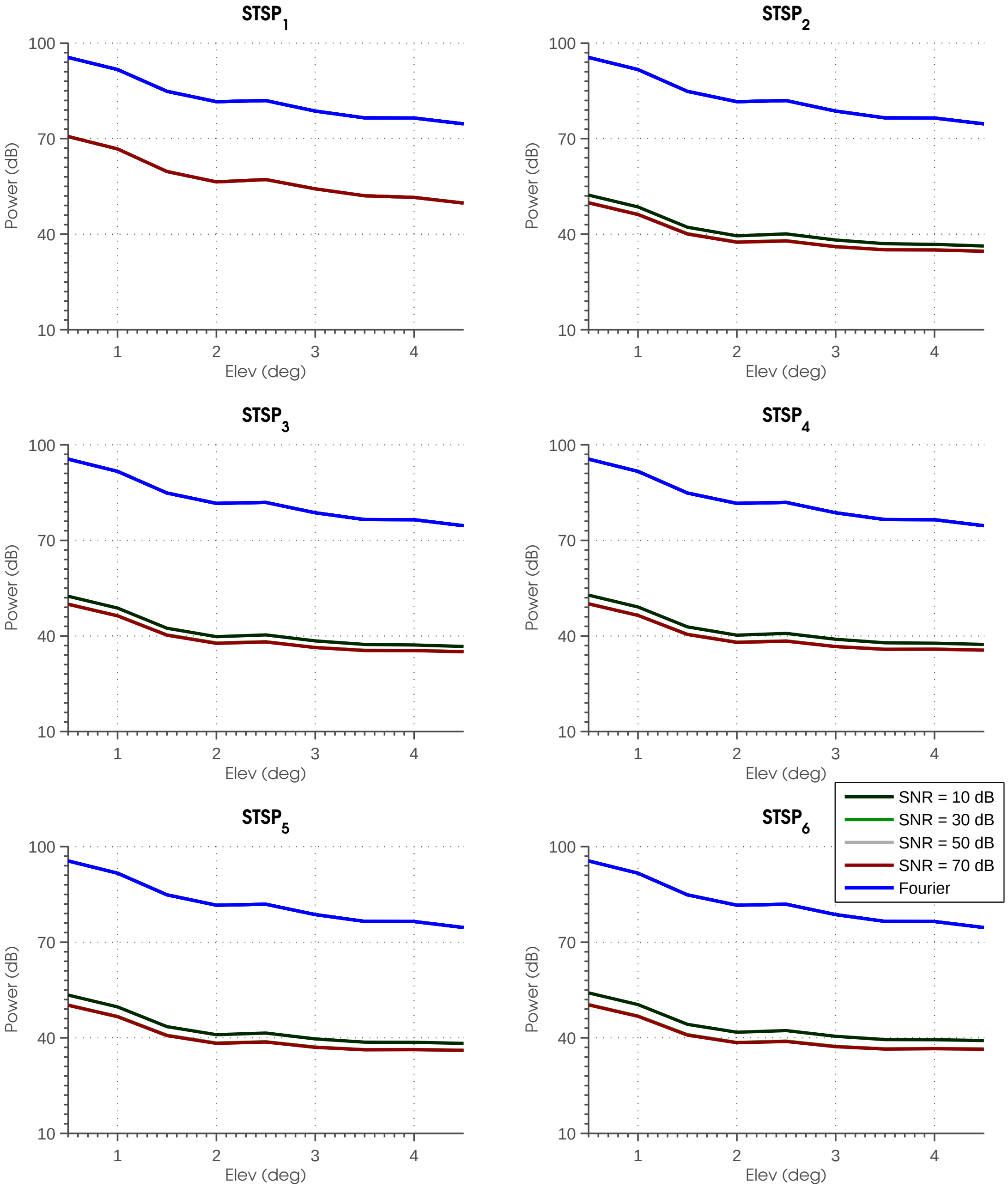

Figure 5.26: Same as Figure 5.24, except for STSP_1, STSP_2, STSP_3, STSP_4, STSP_5, and STSP_6, and only the clutter power is plotted.

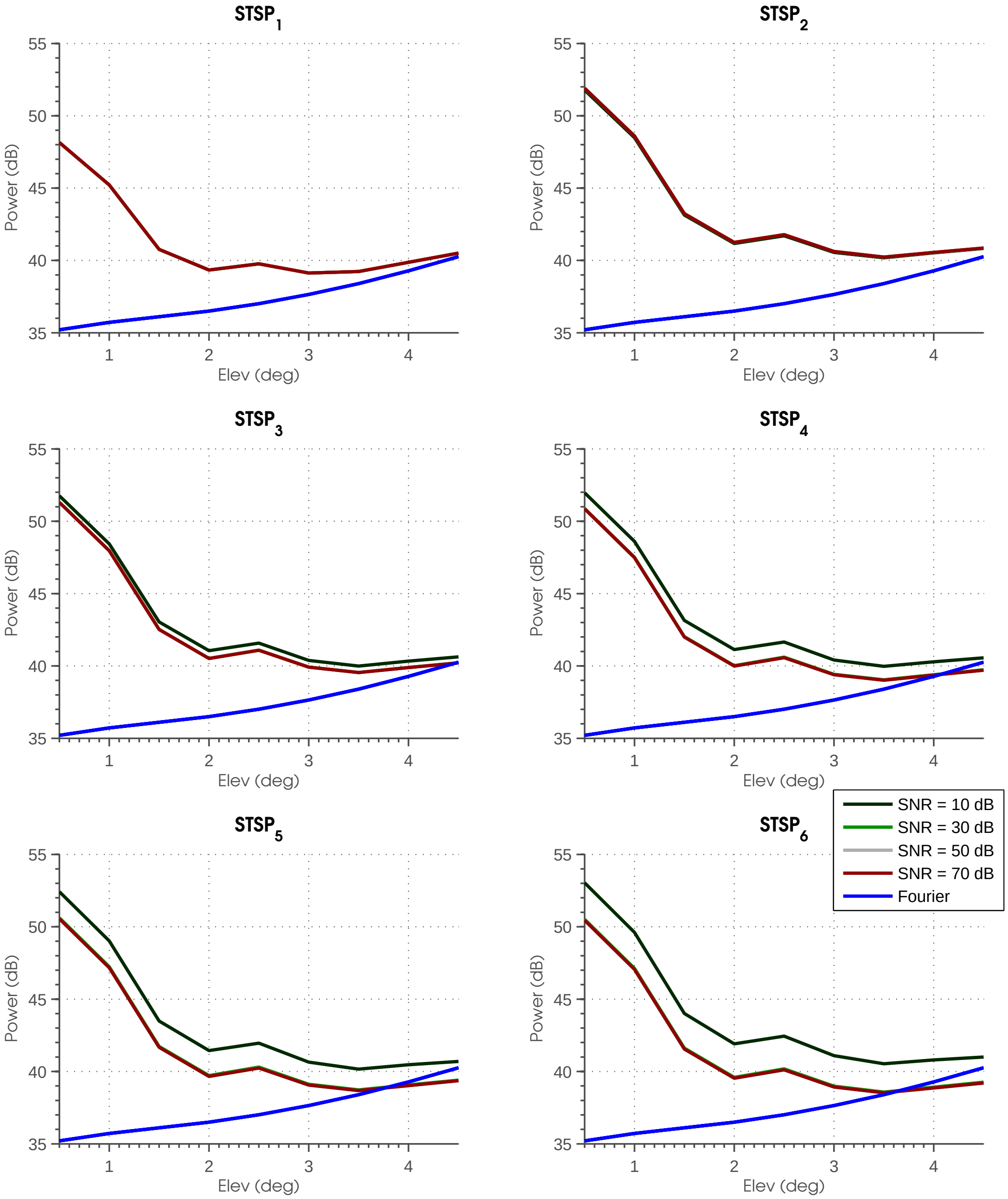

Figure 5.27: Same as Figure 5.24, except for STSP$_1$, STSP$_2$, STSP$_3$, STSP$_4$, STSP$_5$, and STSP$_6$, and only the weather power is plotted.

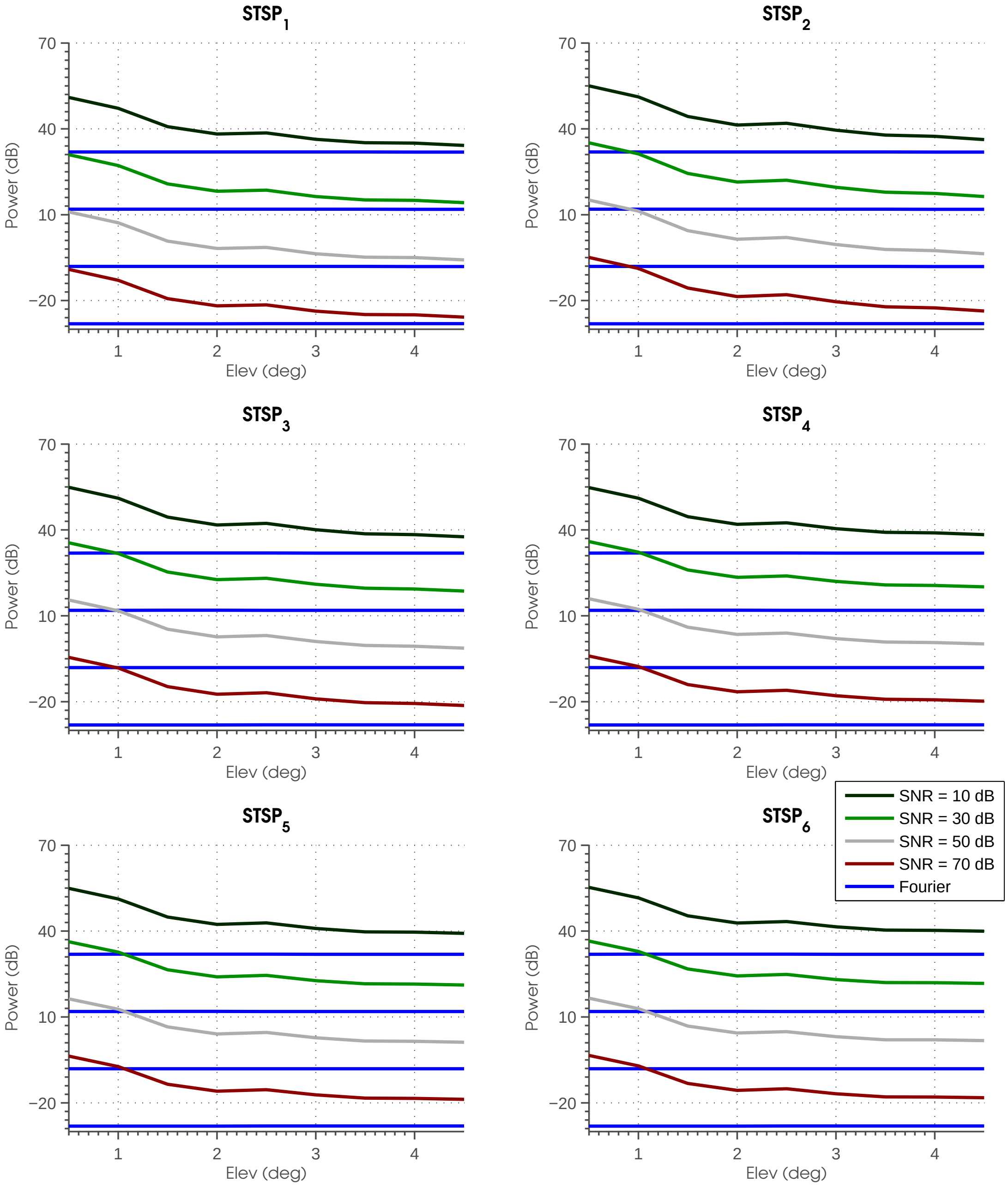

Figure 5.28: Same as Figure 5.24, except for STSP$_1$, STSP$_2$, STSP$_3$, STSP$_4$, STSP$_5$, and STSP$_6$, and only the noise power is plotted.

5.1.6 Discussion of Simulation Results

In the previous subsections, the performance of clutter filtering by a partially adaptive array with ground clutter contamination was investigated for changes in diagonal loading, dwell time, fading clutter level, CSR, and SNR. The overall objective was to determine the capabilities of the spatial array to retrieve the weather signal while mitigating clutter contamination in each case. With the foreseeable application of such systems in weather observations, the observations made of these results will be important for spatial filters with SLC designs. Based on the results obtained, the performance of spatial clutter filtering has some limitations but the results are promising even when only a few samples are used.

Some qualitative results obtained after processing contaminated time series signals with 55 dB of ground clutter are shown in Figure 5.29. The results include the powers and Doppler velocities for the combined component and constituents such as the weather, clutter, and noise. In particular, the components shown are obtained by applying STSP_6 and a diagonal loading of 10^7 to the contaminated signals. Compared to the original simulated fields in Figures 4.6 and 4.7, the results show that a relatively accurate field of the weather is retrieved when the elevation is above 3.5°. The weather component have powers that are near the original value with Doppler velocities that have slightly positive Doppler velocities. The clutter and noise constituents are smaller than the combined and weather powers. At elevations below 3.5°, the retrieved fields are less accurate with powers that are significantly biased and Doppler velocities that are difficult to qualitatively analyzed while the clutter power is relatively large. While being only a single case, the results in Figure 5.29 show some of the difficulties as well as successes that were obtained.

Additionally, it was observed that a small combined power was generally obtained when the sample size was less than the number of auxiliary elements. The phenomenon is illustrated in Figure 5.30. The powers and Doppler velocities for the combined component and its constituents are shown after MVDR with a diagonal loading of 10^6 was applied to time signals contaminated with 55 dB of ground clutter. Compared to the original simulated fields shown in Figures 4.6 and 4.7, the estimate of the weather component is relatively accurate when the elevation is above 3.5°. Interestingly, the clutter power does not have characteristics of the clutter. Instead, its characteristics matches almost exactly the weather characteristics with almost similar power and Doppler velocity. Since the combined power is smaller than both the weather and clutter signals and the weather and clutter signals are coherently

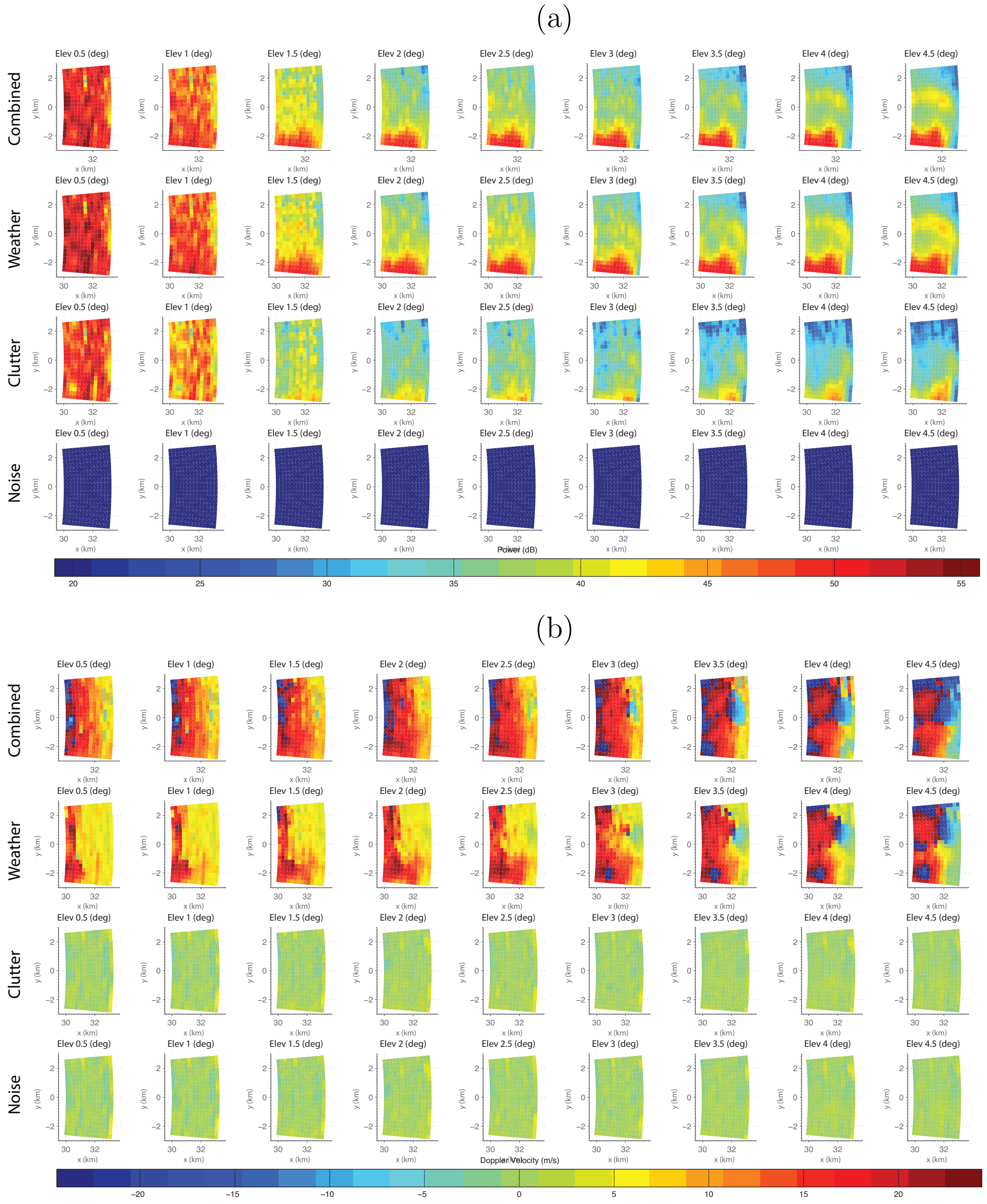

Figure 5.29: (a) Power of the simulated weather event and its (b) corresponding Doppler velocity as obtained using MSC with a dwell time of 8 samples.

added, the results imply that the time series of the weather and clutter must be approximately identical and out of phase.

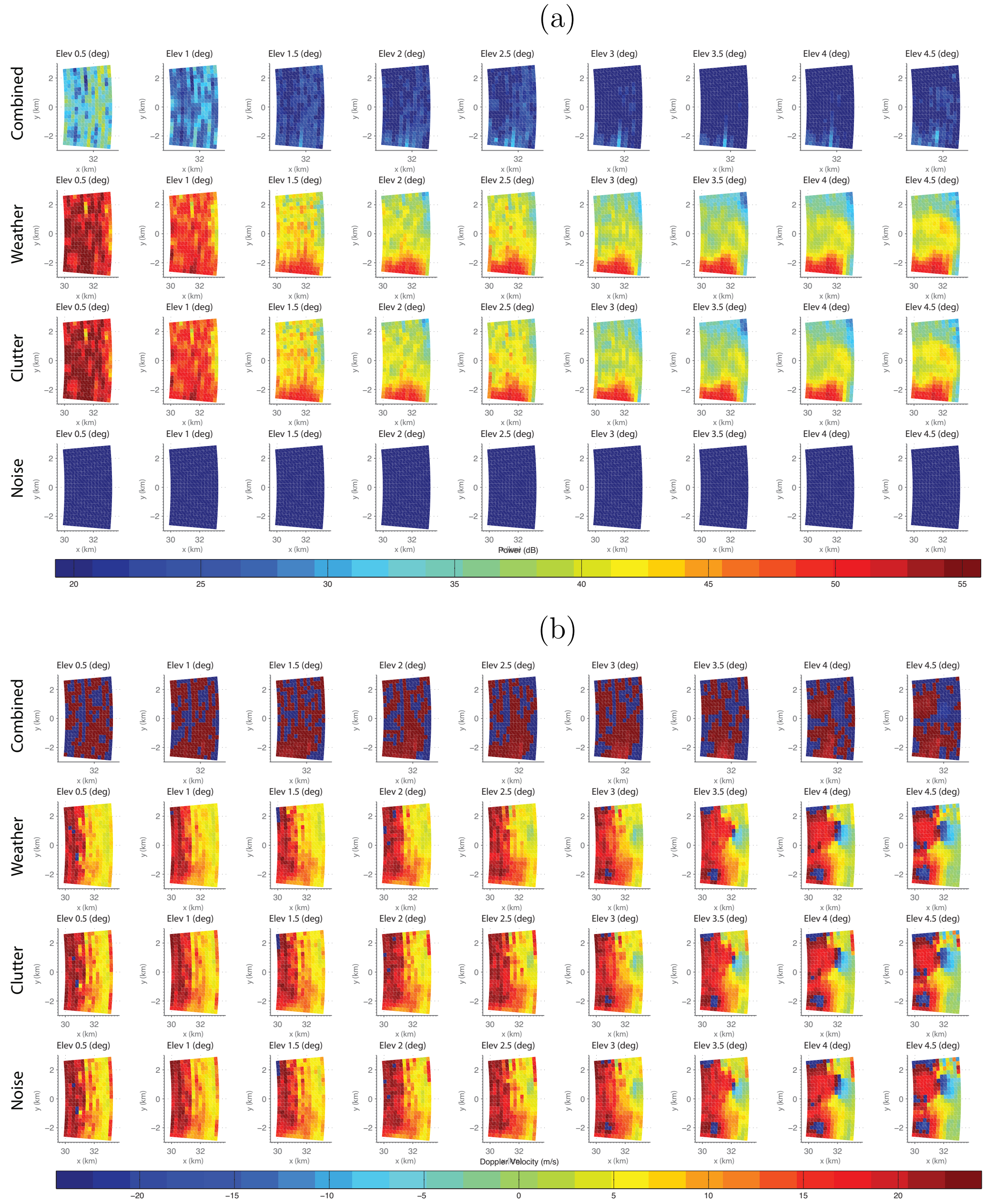

Figure 5.30: (a) Power of the simulated weather event and its (b) corresponding Doppler velocity as obtained using MVDR with a sample size of two. The effects of correlation between the weather and clutter signals can be observed from the power and Doppler velocity fields.

From the simulated data, it was noticed that two approaches which include employing diagonal and subspace constraints could be used to alleviate some of the problems observed when using small sample sizes. In essence, the approaches constrain the adaptivity of the spatial filters to produce more positive results. Some results obtained after reprocessing the contaminated signals with a subspace constraint are shown in Figure 5.31. The results were obtained by processing the contaminated signals using STSP_1 with a diagonal loading of 10^6. The results show that the weather power is retrieved with better accuracy but its Doppler velocity is significantly biased. Nevertheless, the results are significant improvements over those shown in Figure 5.30. While preliminary, subspace constraints appear effective and show promise for mitigating some of the problems that are observed when using small sample sizes.

While the above results are shown for the signals after spatial filtering is applied, the connection of the spatial filters to the scattering field is represented in terms of the beampatterns of the main, auxiliary, and composite arrays. An example of some beampatterns after spatial filtering was applied to time series signals with 55 dB of ground clutter are plotted in Figure 5.32. The example shows changes to the received beampatterns as the elevation is changed from 0.5° to 4.5°. When the steered angle is close to the ground, the clutter is in sidelobes or in the mainlobe with relatively large gains. The beampattern of the auxiliary array has large gains that are on the order of the mainlobe of the mainlobe of the main array. As a result, the composite array has a relatively distorted mainlobe and large sidelobe levels. On the other hand, the clutter is in sidelobes with lower gain when the steered angle is closer to 4.5°. The beampattern of the auxiliary array has smaller overall gain, and the beampattern of the composite is less distorted.

The effects of power minimization, which is employed as a means for determining the filter weights in schemes such as MVDR and STSP, play an important role in of filtered time series signals and the retrieved Doppler velocities. The minimization scheme ultimately determines the final values of the combined, weather, clutter, and noise signals that are obtained. When processed using moment estimators, the temporal correlation of the combined component determines the retrieved Doppler velocity. Shown in Figure 5.33 is a scatter plot of the estimated Doppler velocities versus ground truth for the combined signals at elevations from 0.5° to 4.5° obtained using MVDR with a diagonal loading of 10^6. The retrieved Doppler velocities generally match at most elevation angles the ground truth even when the clutter is in the mainlobe at 0.5°. A small positive bias is observed at each angle when the velocities are greater than 0 m s^{-1}, and it is negative when the Doppler velocity of ground truth

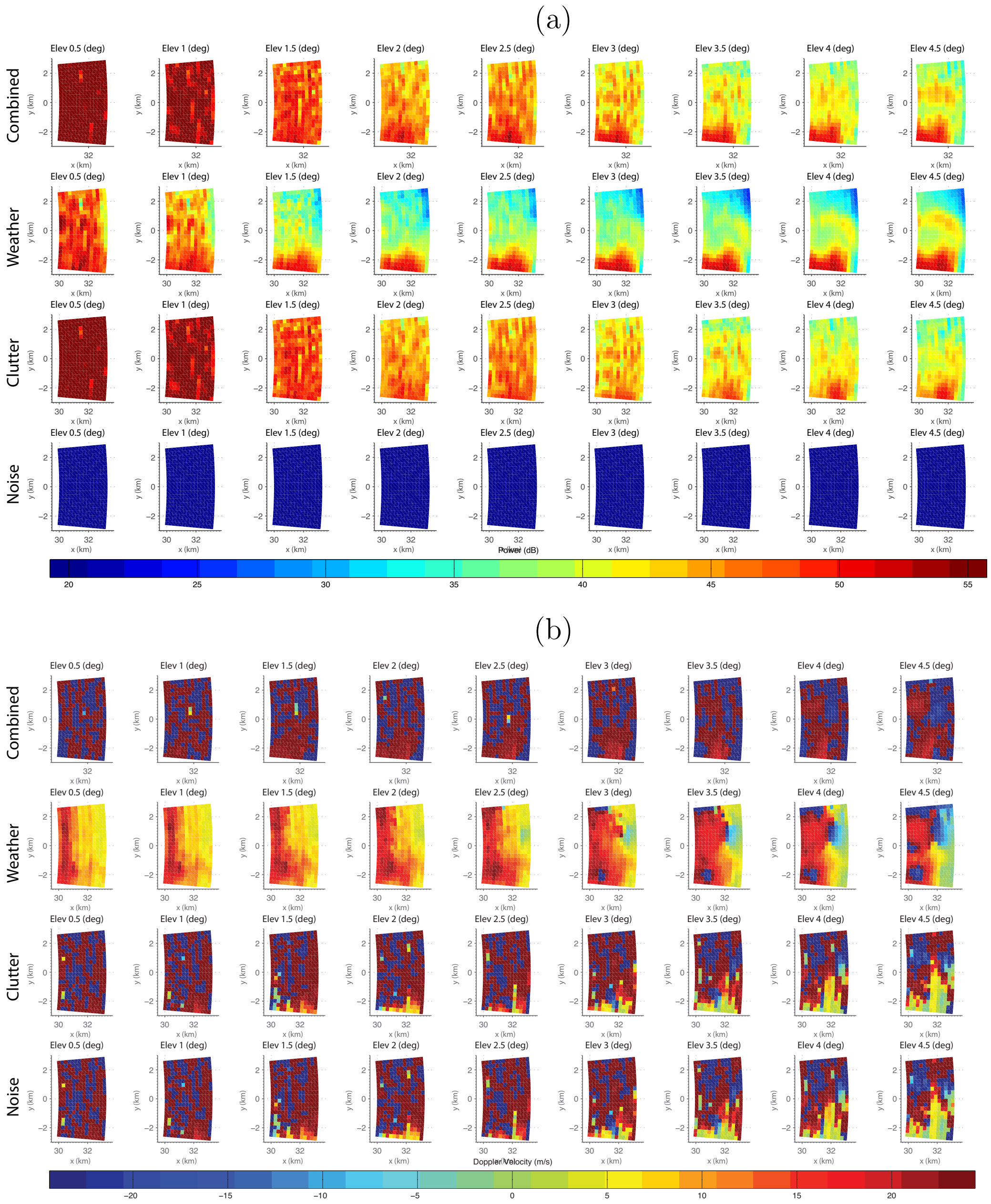

Figure 5.31: (a) Power of the simulated weather event and its (b) corresponding Doppler velocity as obtained using STSP$_1$ with a sample size of two samples. The effects of using subspace constraint can be exploited to reduce the effect of signal correlation introduced by a small sample size.

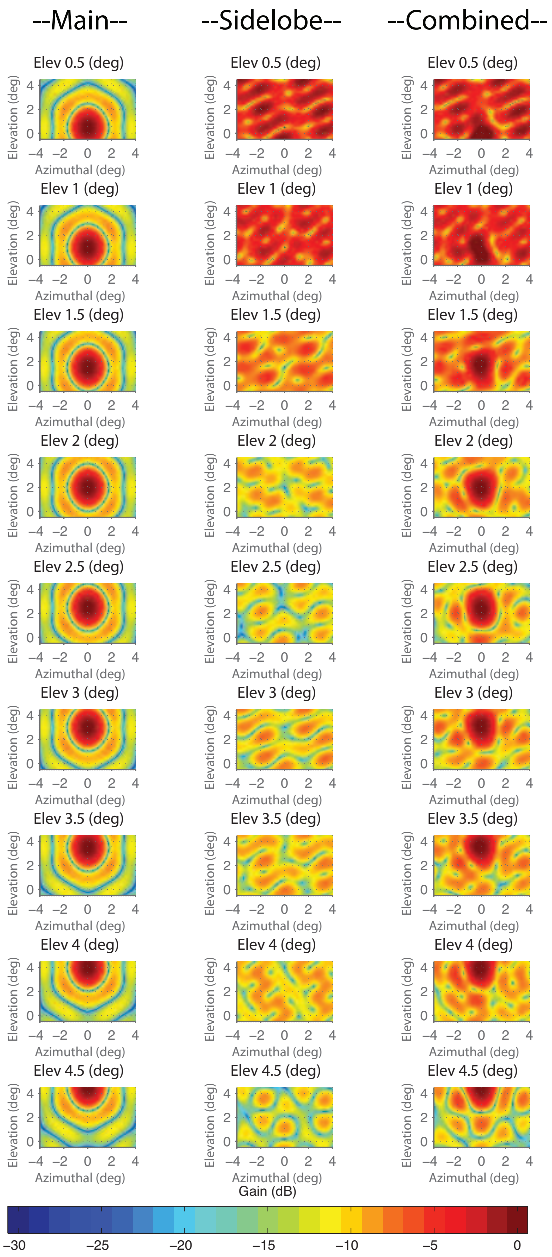

Figure 5.32: Example showing beampatterns of main, auxiliary, and composite arrays when spatial filtering is applied. The example shows changes to the received beampatterns when different elevations are used. The degree to which the beampattern changes depends on the relative positions of the clutter and the steered direction.

is less than 0 m s^{-1}. The magnitude of the bias increases when the elevation angle is changed from 0.5° to 4.5°. Though not shown, the bias decreases when either subspace or diagonal loading is applied. These results show some of the effects observed on the retrieved Doppler velocities when spatial filtering with SLC is applied.

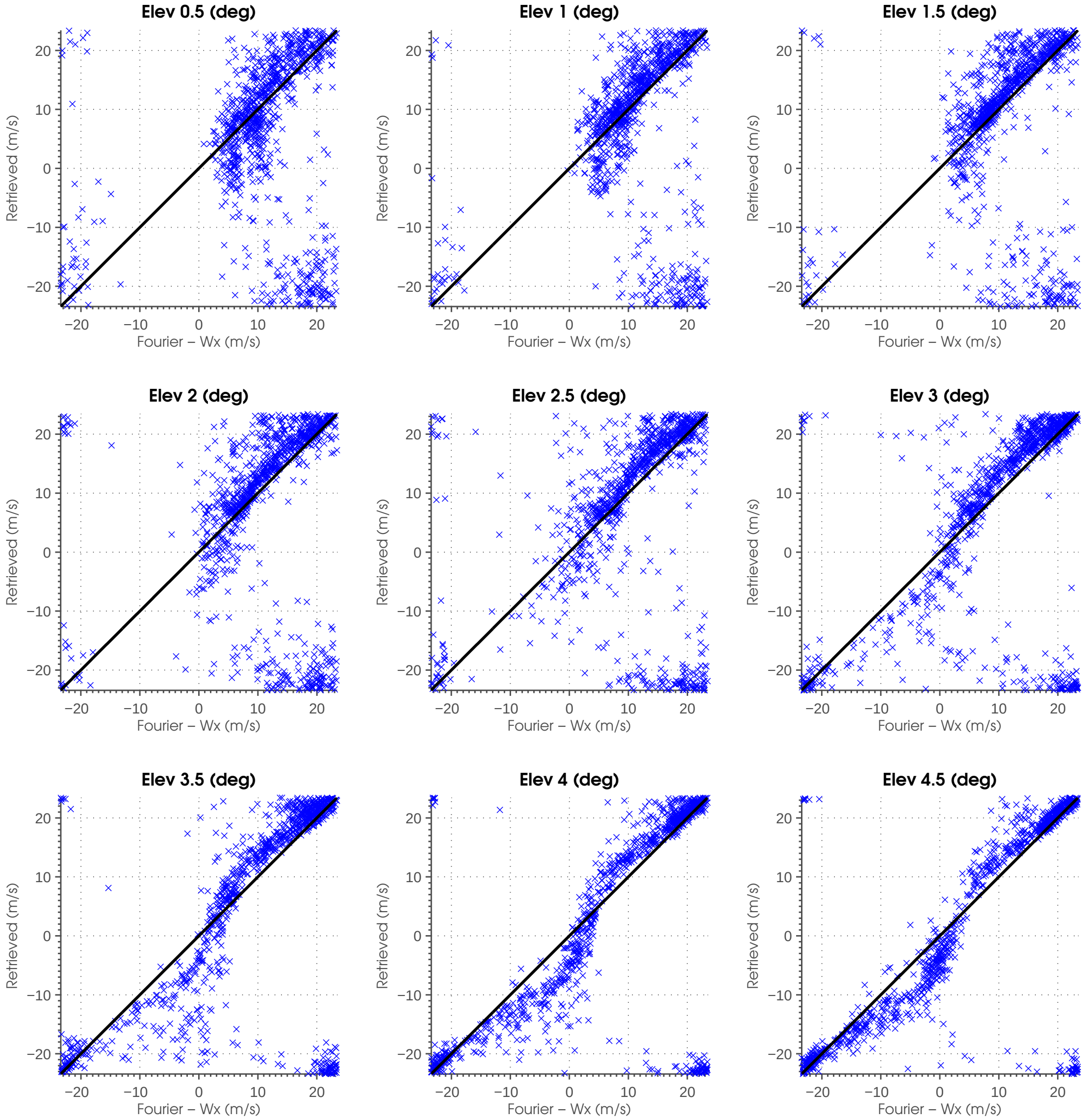

Figure 5.33: Scatter plots of velocities obtained using MVDR with a diagonal loading of 10^6. The results show the effects of velocity bias on the combined filtered signal.

In the next section, the techniques and observations made here are applied to real data from the Turbulent Eddy Profiler radar.

5.2 Quasi-Stationary Ground Clutter: Validation Using the Turbulent Eddy Profiler

The spatial filtering techniques previously applied in a numerical simulation environment are now validated using real data obtained with the Turbulent Eddy Profiler. Previously, preliminary observations using conventional Fourier beamforming showed that the return signals below 0.2 km are primarily contaminated by ground clutter Moment data processed of the signals showed significantly above-average values of the power and near-zero Doppler velocities. These qualities are often observed in high CSR cases with ground clutter. In this section, the performance of spatial filtering is examined by applying them to this data set. For comparison, it was pointed out that the average weather power is estimated from scatterers located between 0.25-0.5 km, the clutter power from scatterers below 0.25 km, and the noise power from scatterers located between 1.0-1.2 km. The CSR is then obtained by taking a ratio of the clutter to signal powers while the SNR is obtained by taking a ratio of the signal to noise powers. Since real data are used, the number of flexible parameters consists of only the diagonal loading and dwell time. In the following subsections, the effects spatial filtering using SLC and these two parameters are examined.

5.2.1 Effects of Diagonal Loading

Results of processing the time series signals with the selected range of diagonal loading along with parameters listed in Table 5.9 are plotted in Figure 5.34. The results were obtained using MVDR, $STSP_1$, $STSP_2$, and $STSP_6$ and show the average power with height and the transition of the average power when the diagonal loading is changed from 10^2 to 10^7. The average power is maximum near the ground with a peak value of approximately 75 dB, and the peak value decreases to approximately 25 dB when the height is changed to 0.4 km. Additionally, the average power of MVDR decreases as the diagonal loading changes from 10^7 to 10^2 with differences that appear systematic as the diagonal loading is varied. When the diagonal loadings is above 10^5, the decrease to the average power near the ground appears to be constant with a difference of approximately 8-10 dB, while the decrease to the average power is significantly smaller with magnitudes less than 3 dB when the height is above 0.22 km. With smaller diagonal loading ranging from 10^2 to 10^4, a minimum in the power is observed near the ground, while larger decreases of the average power are continued to be observed at heights above 0.22 km. When these results are compared to those obtained using STSP$_6$, the values appear to be similar with differences of less than 1 dB when the same diagonal loading are compared. The difference in the average power is larger when compared to the results obtained using STSP$_1$ and STSP$_2$, while the average powers obtained using STSP$_1$ and STSP$_2$ are generally larger for the same diagonal loading. The smallest difference that is obtained is approximately 1 dB when a diagonal loading of 10^8 is used.

Table 5.9: Parameters Used in Varying Diagonal Loading

Parameter	Value
SNR	3.4 dB
CSR	33.5 dB
NPTS	8
γ	$\mathbf{10^2}$ — $\mathbf{10^7}$
σ_v	variable

The power and Doppler velocity of the processed data are plotted in Figures 5.35, 5.36, 5.37, 5.38, 5.39, and 5.40, respectively. These results relate the data shown previously to the individual power and Doppler velocity. Results of the MVDR show that using a single diagonal loading produces non-optimal power and Doppler velocities. Near the ground, a diagonal loading ranging between 10^5 and 10^6 produce the most reasonable results based on the spatial and temporal continuity conditions, while the moments obtained using other diagonal loading appears to contain either residual clutter or Doppler velocities with magnitudes greater than 3 m s^{-1} that are unreasonable for the turbulent scatterers. Near 0.4 km, the results obtained using diagonal loading ranging between 10^3 and 10^4 appear to produce the optimal results, while using diagonal loading with other values appear to produce suboptimal results. The results obtained using STSP$_1$ and STSP$_2$, however, show that a significantly smaller diagonal loading can be applied to produce reasonable results even when a single small diagonal loading is used. A reasonable estimate was obtained of the turbulent scatterer even when the diagonal was 10^2. However, it was observed that a combination of diagonal loading and STSP produced the best result, and the combination of the two constraints varied with height.

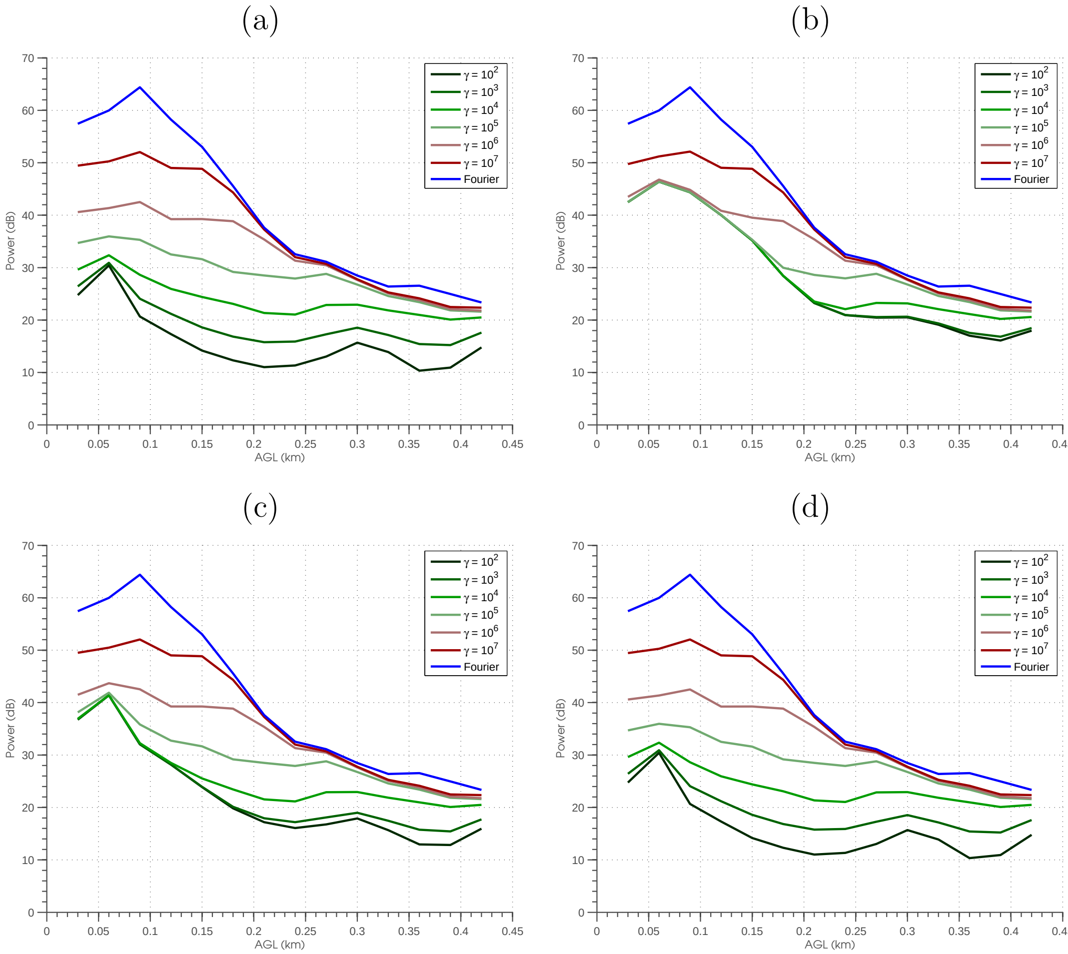

Figure 5.34: Powers obtained using MVDR and STSP with variable diagonal loading. The results show the average power with height using MVDR (a), STSP$_1$ (b), STSP$_2$ (c), and STSP$_6$ for diagonal loading from 10^2 to 10^7. For comparison, the power shown in the blue line is obtained using conventional Fourier beamforming.

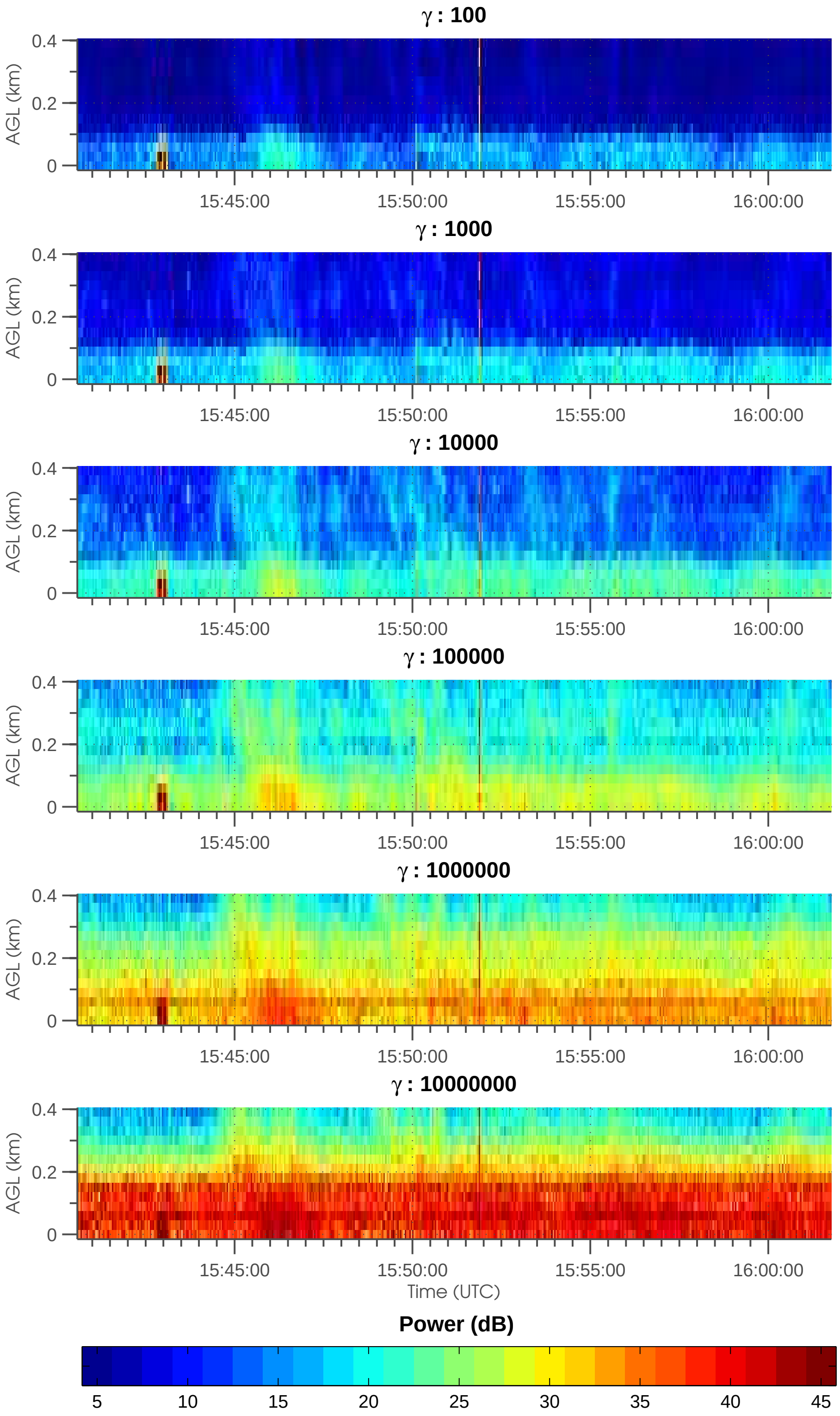

Figure 5.35: Power obtained of the combined signal for near surface scattering after applying MVDR with a dwell time of eight samples. The diagonal loadings that were used to calculate these powers range from 10^2-10^7. As can be observed, the performance of the clutter filter depends on an optimal diagonal loading.

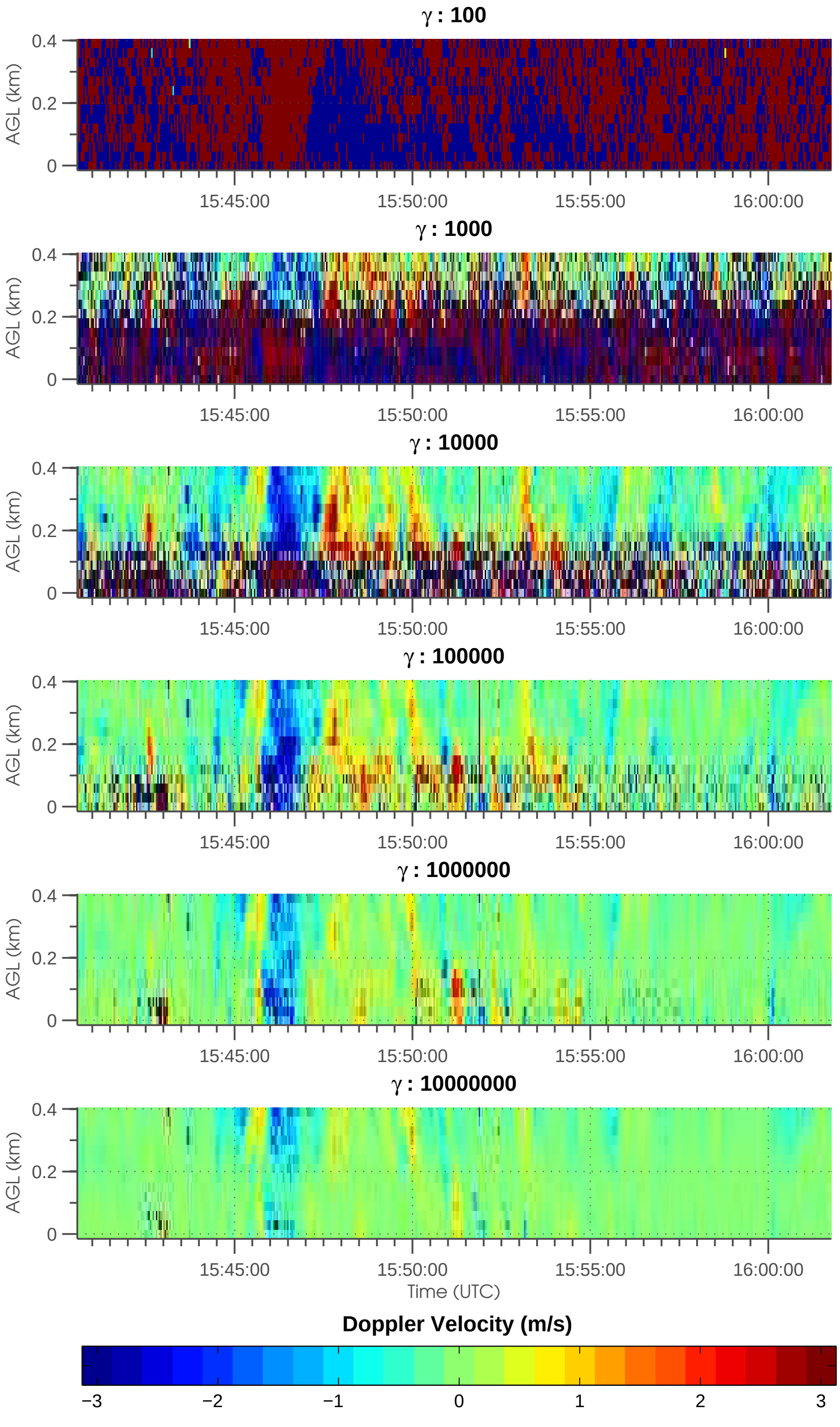

Figure 5.36: Same as Figure 5.35, except for Doppler velocity.

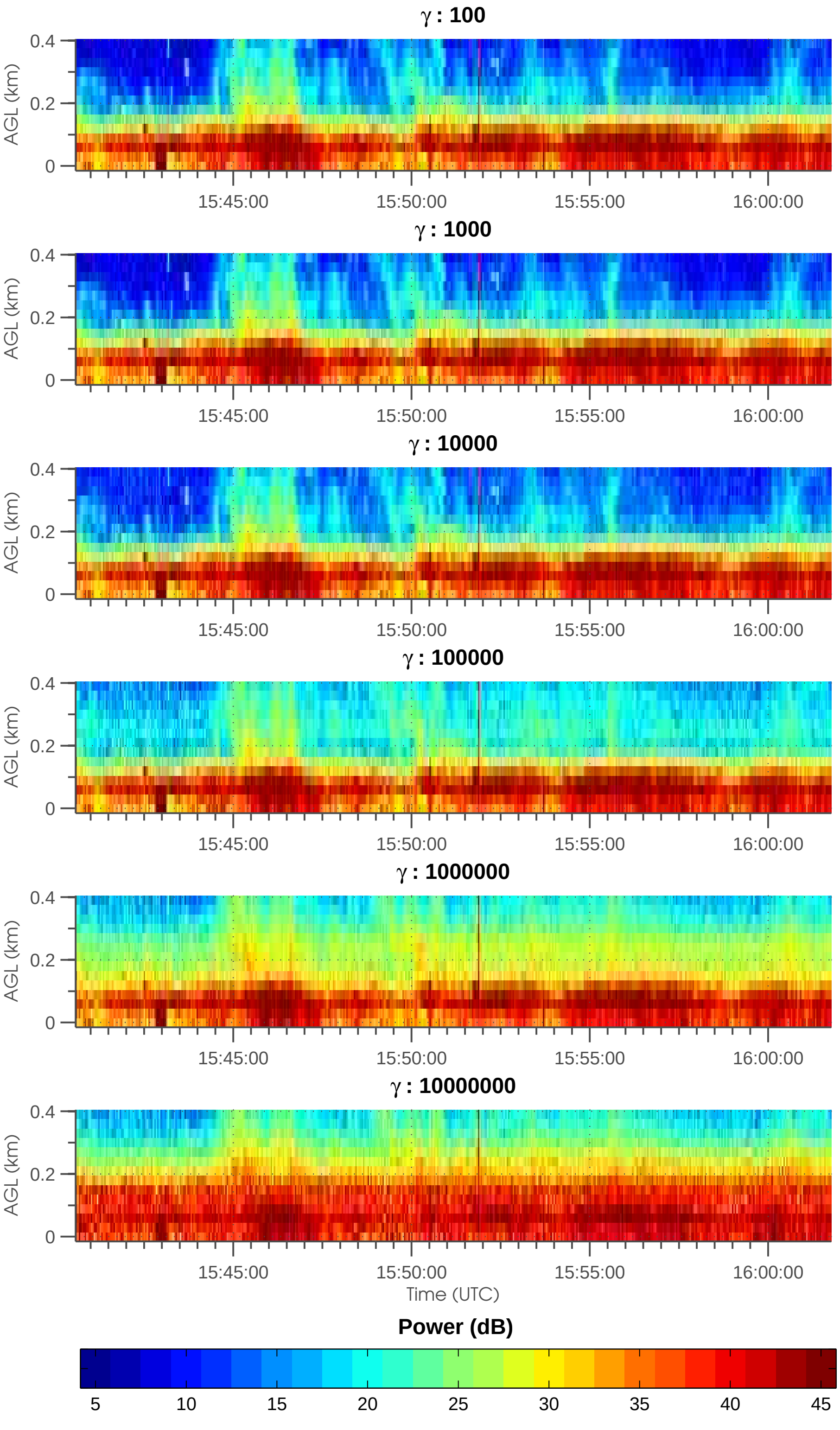

Figure 5.37: Same as 5.35, except for STSP_1.

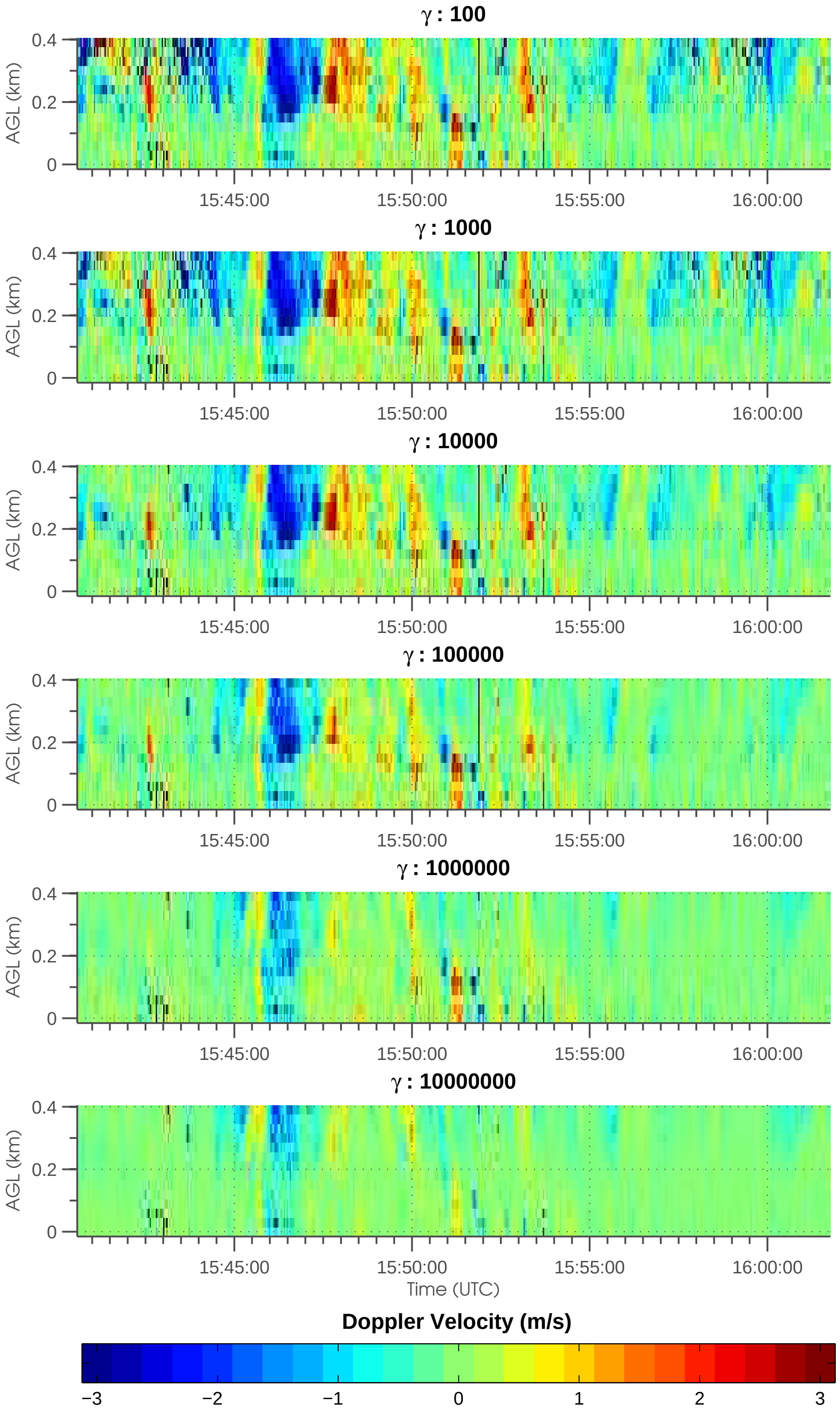

Figure 5.38: Same as 5.36, except for STSP$_1$.

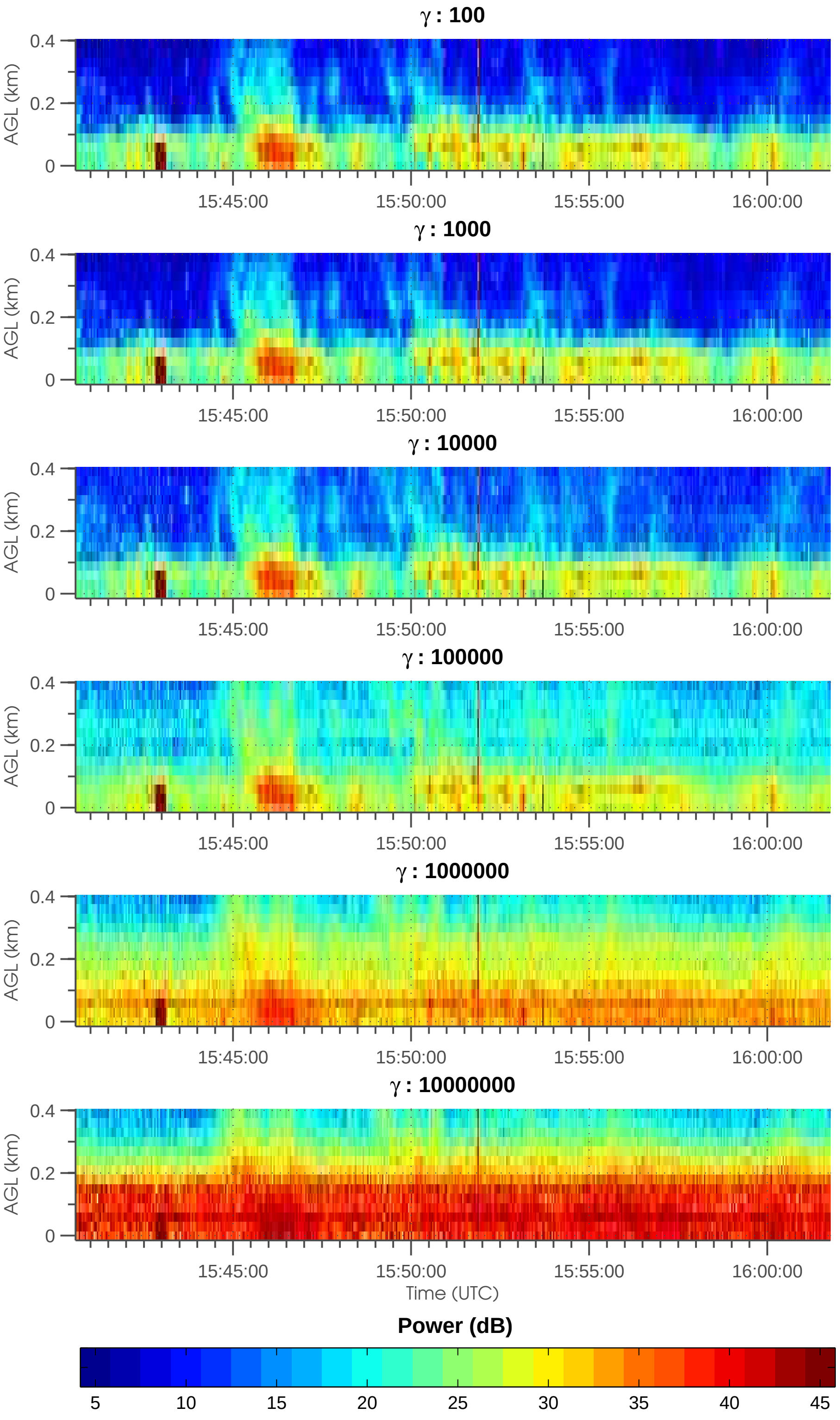

Figure 5.39: Same as 5.35, except for $STSP_2$.

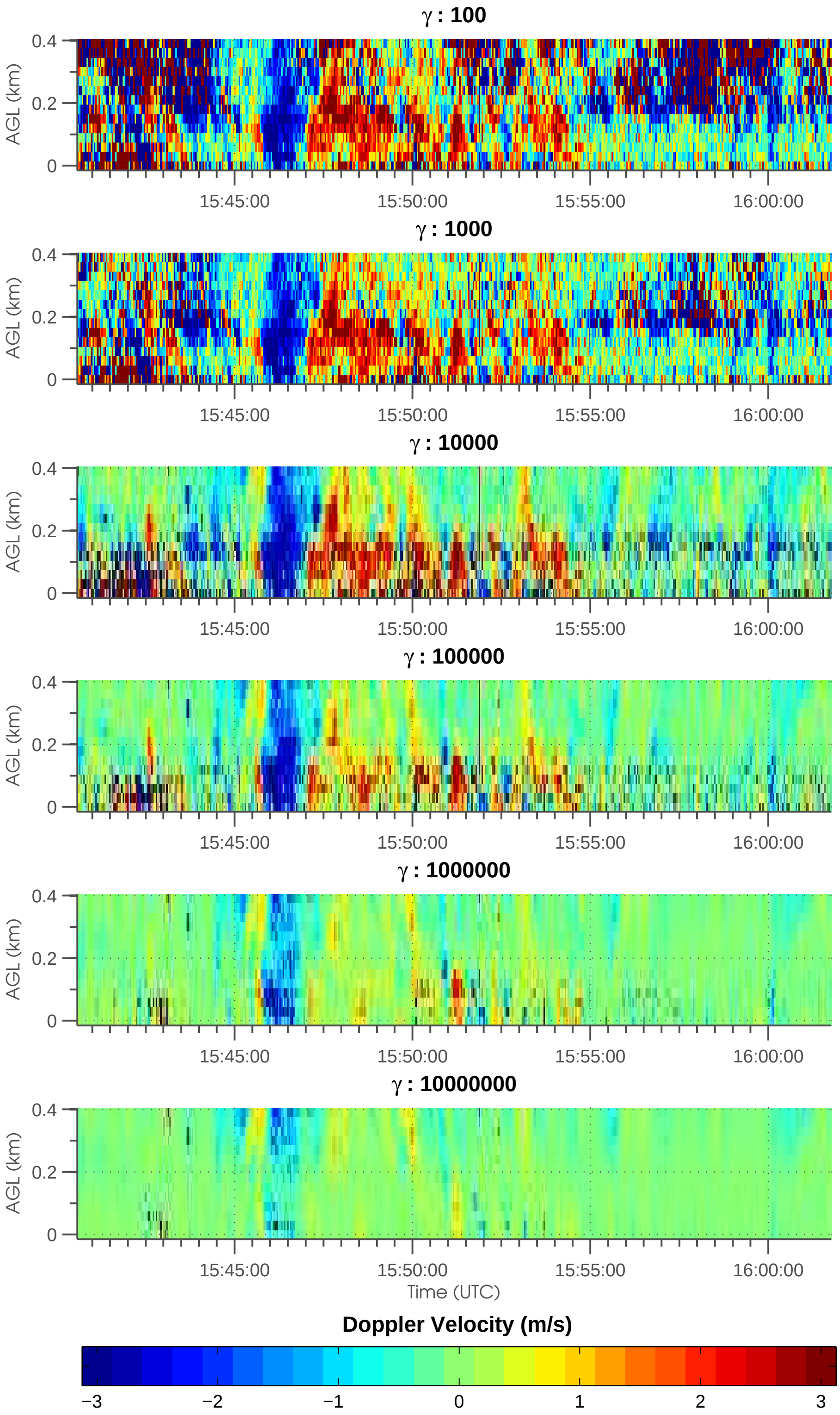

Figure 5.40: Same as 5.36, except for $STSP_2$.

5.2.2 Effects of Dwell Time

Results of processing the time series signals when the dwell time is varied along with parameters listed in Table 5.10 are plotted in Figure 5.41. The results are obtained using MVDR, STSP$_1$, STSP$_2$, and STSP$_6$ and show the average power with heights as the sample size is varied. Similar to the results obtained when the diagonal loading is varied from two to 64 samples The average power near the ground appears to increase between 3-6 dB every time the sample size is doubled, while the increases is less than 2 dB for the same change near 0.4 km. Additionally, it was observed that the minimum power varies when different spatial filtering techniques are applied. While the difference of the output power between STSP$_6$ and MVDR is relatively small, the difference can be up to approximately 15 dB between the two techniques and STSP$_1$ when the same diagonal loading and sample size are used to process the contaminated signals. The difference is largest near the ground where strong clutter powers are observed and the difference is smaller at heights near 0.4 km where weaker clutter are observed. Additionally, the differences are smaller when the values between MVDR and STSP$_2$ are compared.

Table 5.10: Parameters Used in Varying Dwell Time

Parameter	Value
SNR	3.4 dB
CSR	33.6 dB
NPTS	**2 — 64**
γ	10^5
σ_v	variable

Corresponding plots of the power and Doppler velocities obtained by applying the above parameters are shown in Figures 5.42, 5.43, 5.44, 5.45, 5.46, and 5.47, respectively. These results relate the data shown previously to the individual power and Doppler velocity as was similarly observed when diagonal loading was varied. The results with the most reasonable powers and Doppler velocities are observed when the sample size is 8 even though details of the scatterers are difficult to observed from images of the powers. The velocities were reasonable and showed expected spatial and temporal continuity indicative of scattering primarily from atmospheric

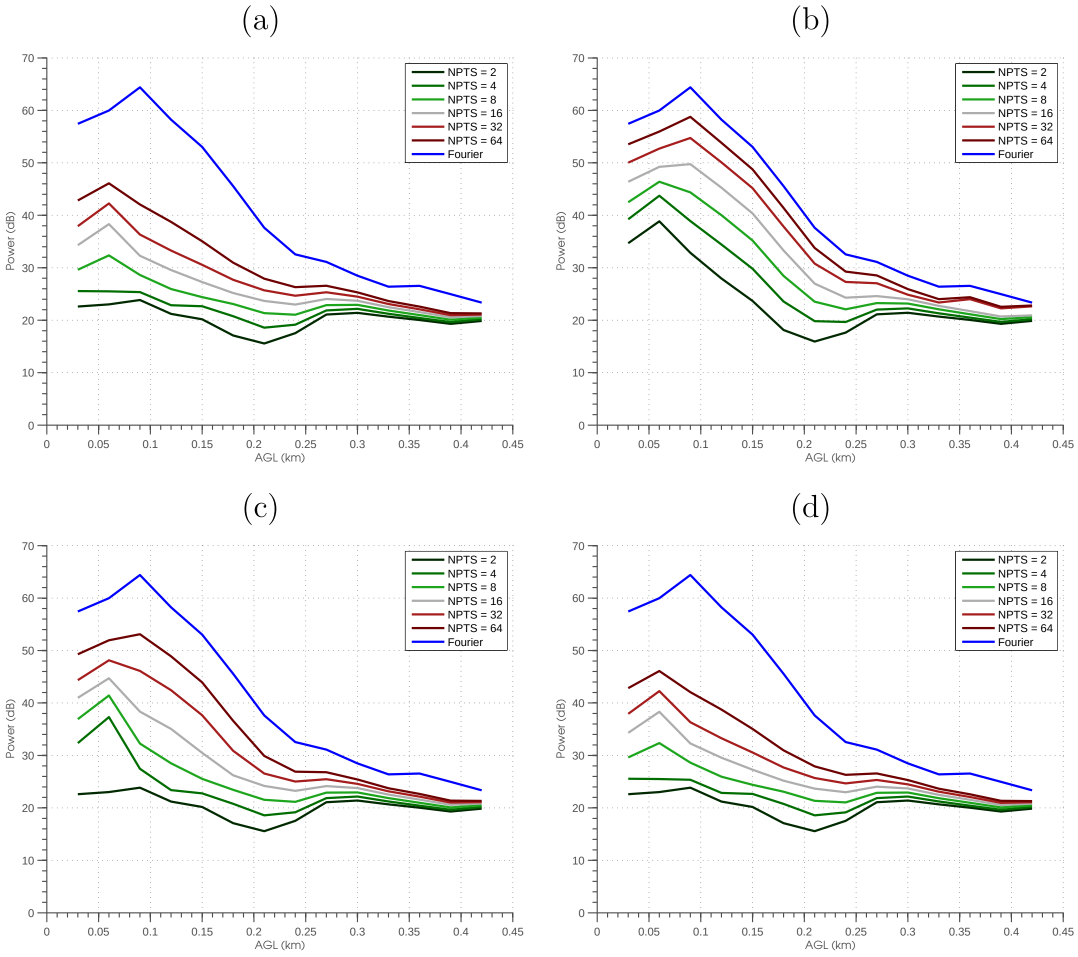

Figure 5.41: Powers obtained using MVDR and STSP with variable sample sizes. The results show the average power with height using MVDR (a), STSP_1 (b), STSP_2 (c), and STSP_6 for sample sizes from two to 32 samples. For comparison, the power shown in the blue line is obtained using conventional Fourier beamforming.

scatterers. With smaller samples sizes, the powers are abnormally small with values slightly above the noise level while the the corresponding Doppler velocities have values greater than 3 m s^{-1}. In contrast, the powers are larger than expected and the Doppler velocities are near zero and are indicative of clutter contamination when more than 8 samples were processed.

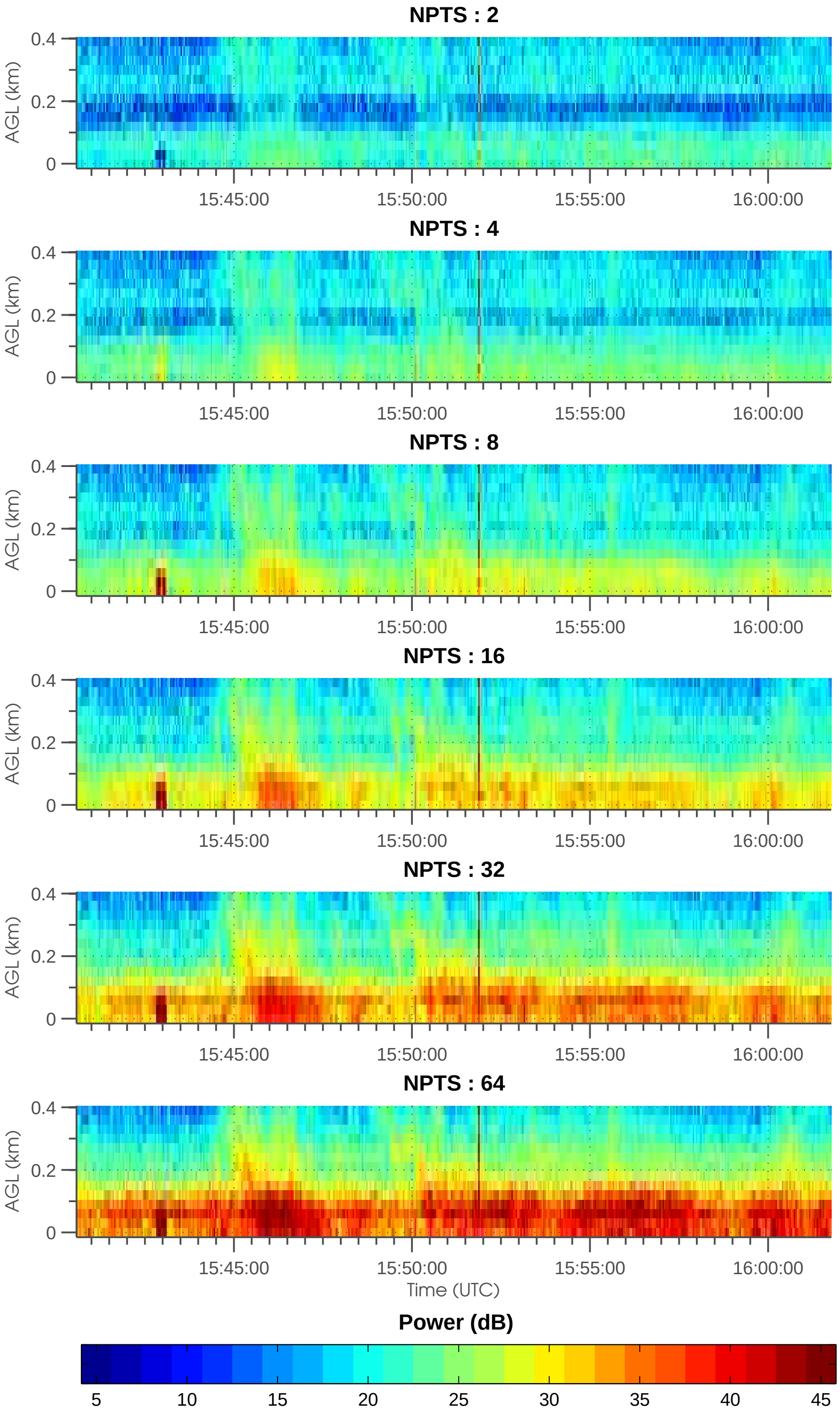

Figure 5.42: Power of the combined signal for near surface scattering after applying MVDR with a diagonal loading of 10^5 and a dwell time ranging from 2-64 samples. The results appear to be optimal when 8-16 samples are used based on the spatial and temporal continuity conditions.

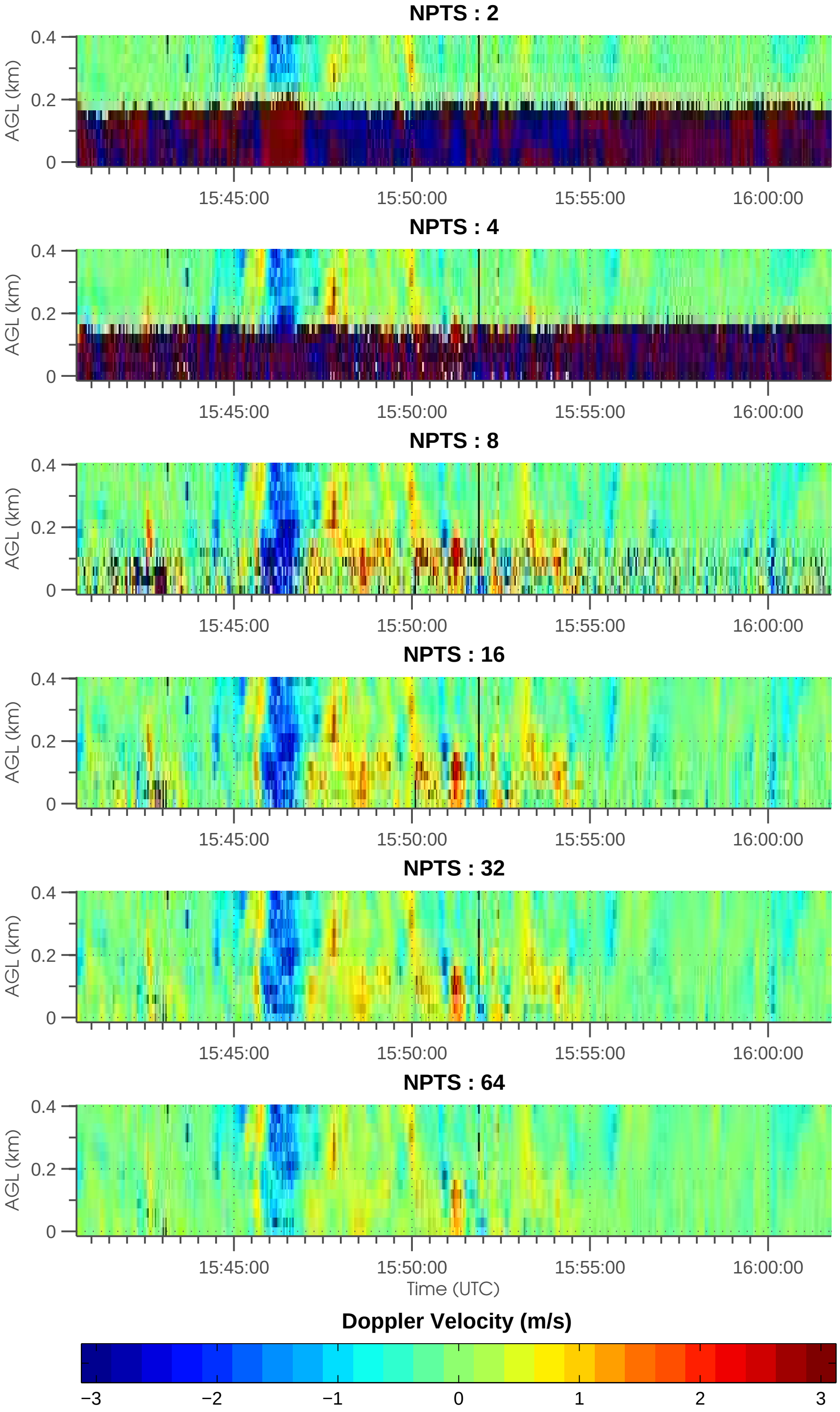

Figure 5.43: Same as Figure 5.42, except for Doppler velocity.

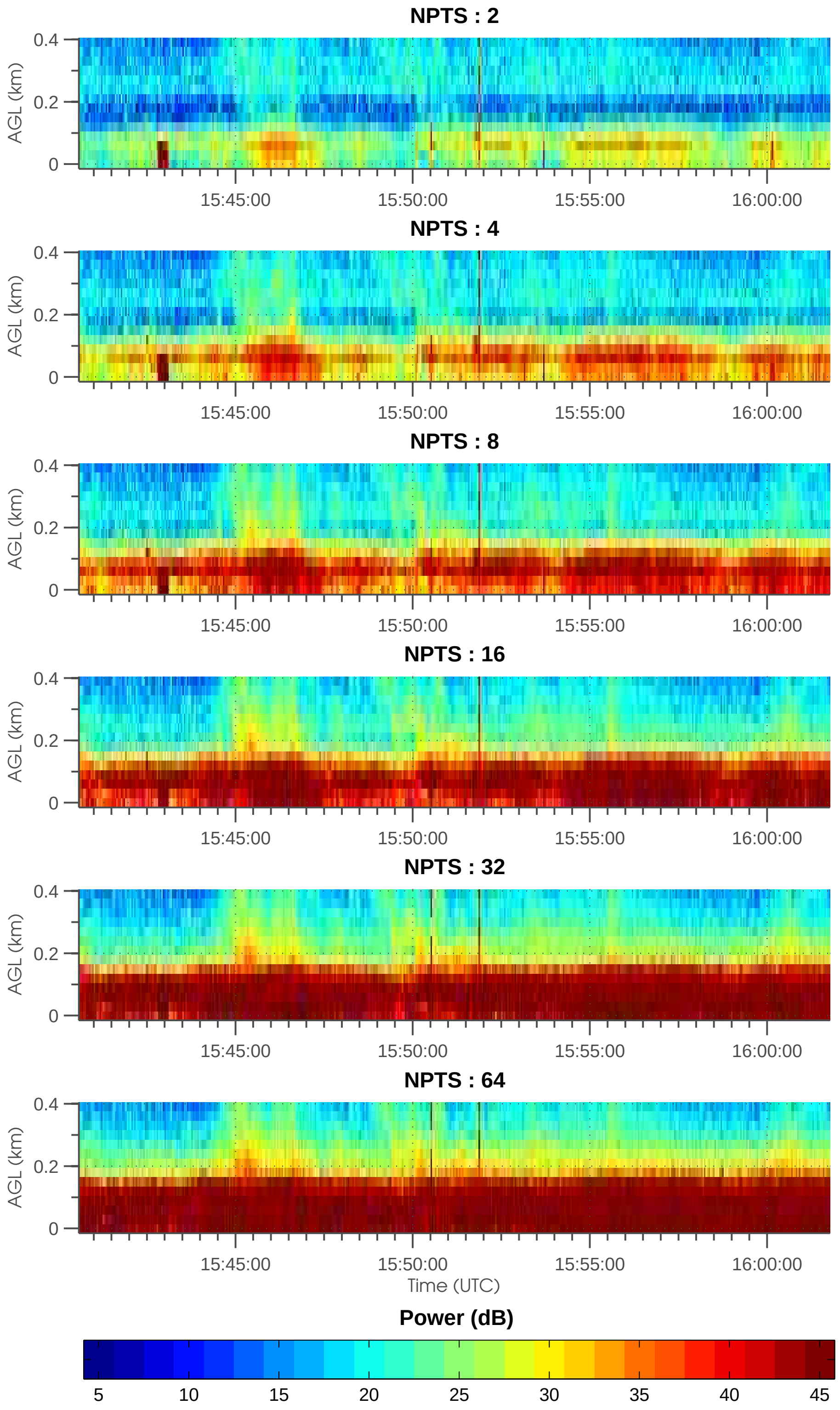

Figure 5.44: Same as Figure 5.42, except for STSP$_1$.

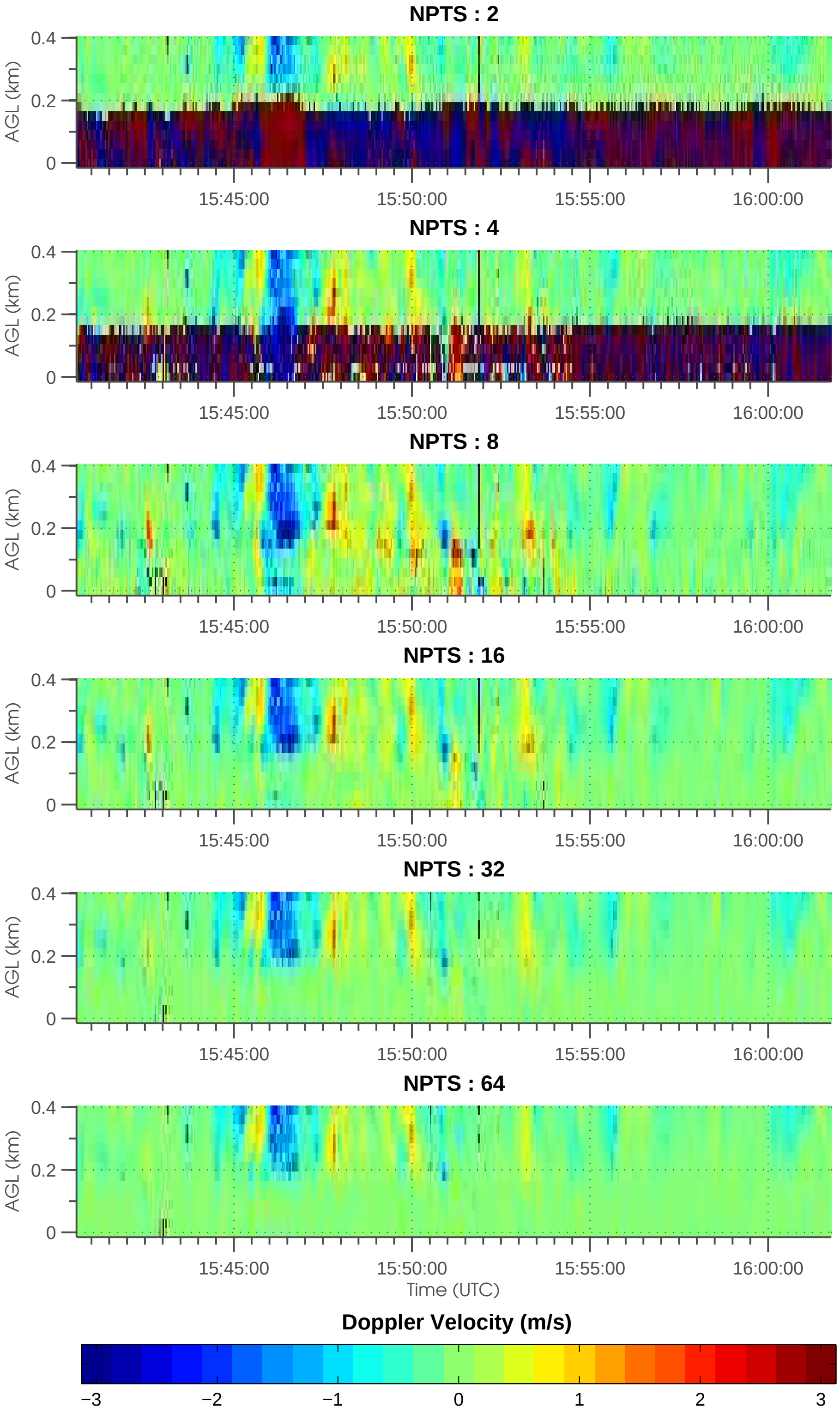

Figure 5.45: Same as Figure 5.43, except for STSP_1.

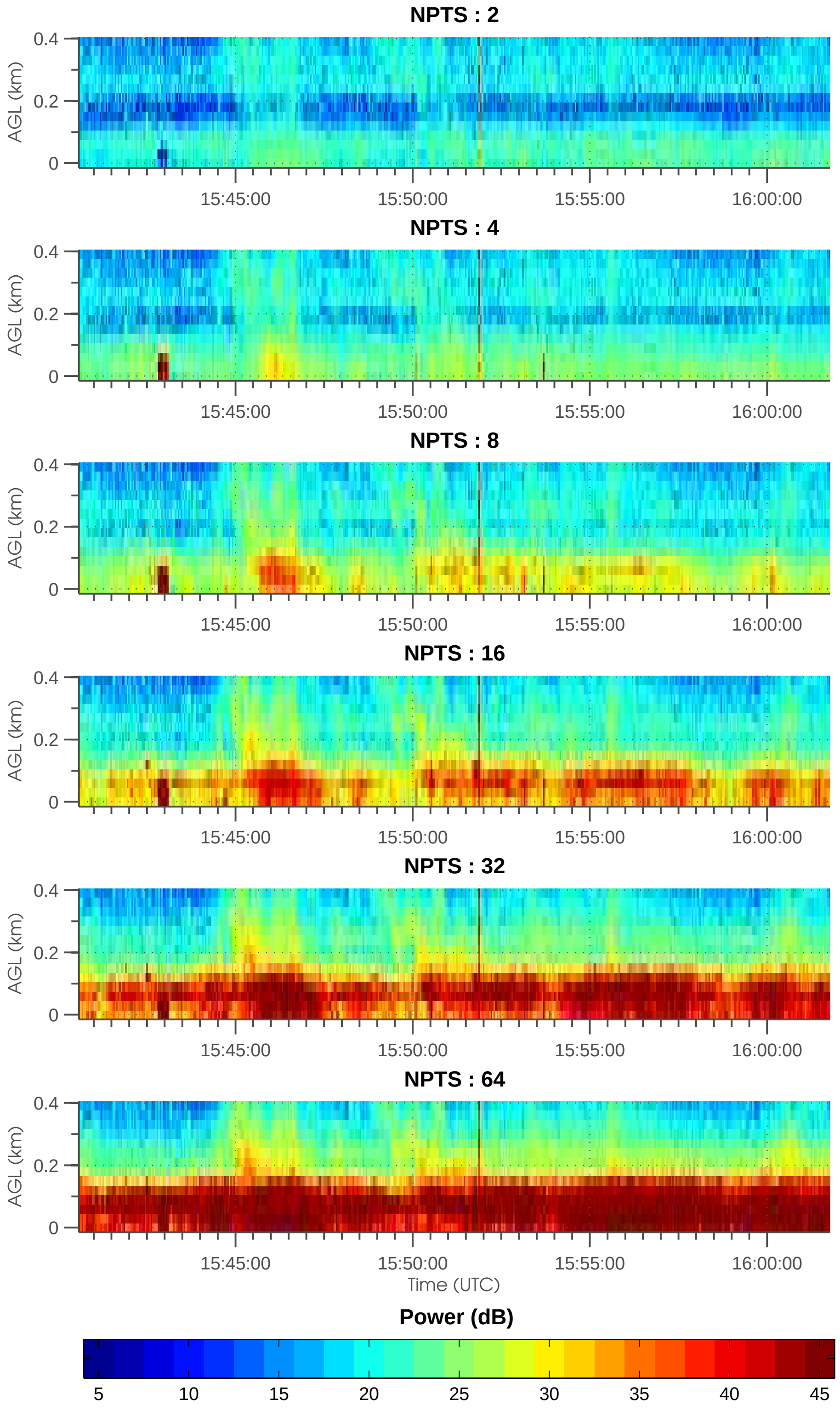

Figure 5.46: Same as Figure 5.42, except for STSP$_2$.

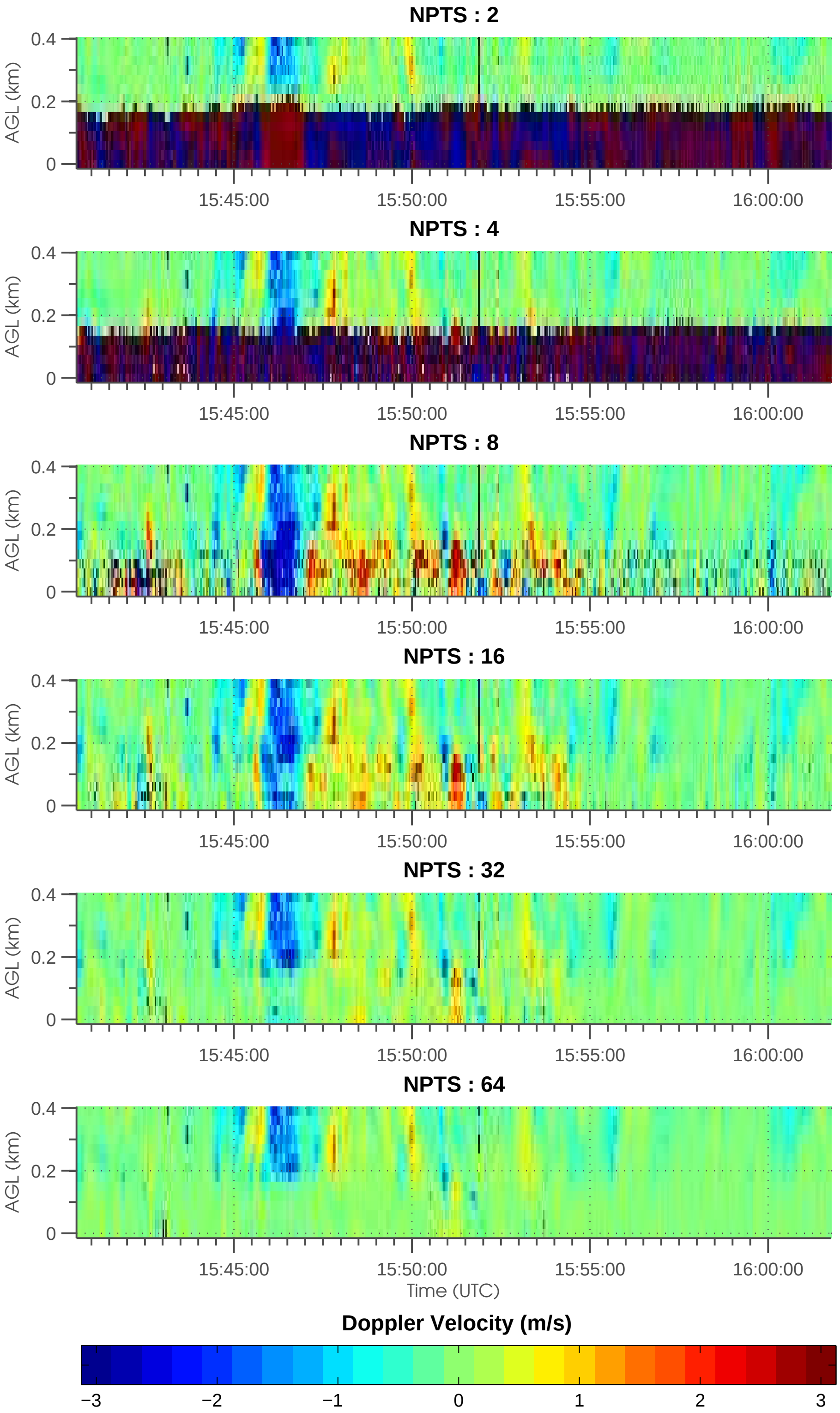

Figure 5.47: Same as Figure 5.43, except for STSP$_2$.

5.3 Non-Stationary Clutter Targets: Numerical Simulations

The setup used in Section 5.1, which was designed to investigate clutter filtering of quasi-stationary ground targets, is now used to investigate clutter filtering of moving targets. With the new clutter source, a few changes to the setup were applied to make the investigation possible. This includes redefining CSR to be the ratio of the maximum clutter power to the average weather power and ignoring the fading clutter parameter. Additionally, the stationary scatterers that represented the ground clutter are now replaced with a single target located at (30.9 km, 2.0 km) that moves radially with speeds of -20, -25, -10, -5, 5, 10, 15, and 20 m s^{-1} to sample uniformly the received Doppler spectrum. Additionally, the region over which the filtering will be examined is now limited since the main factors that affect the powers are the range weighting function and radiation pattern. As a result, the performance of the clutter filters is limited to a single range gate and for azimuth up to 8° from the clutter. The effects of the clutter to the received signal are assumed to be negligible beyond these ranges.

With the setup presented, the combined, clutter, weather, and noise powers as measured of the contaminated data are listed in Table 5.11. The results show the steady state conditions when conventional Fourier beamforming is used. The combined power has a maximum value of 62.4 dB at 0°. It slowly decreases until 6.0°, where it then increases from there to 8.0°. The clutter power ranges from 28.5 dB to 62.4 dB and has a pattern that is similar to the combined power up to approximately 3.0°, where the two patterns becomes different as the angle is further increased. The weather power is smallest at 1.0° and increases steadily to 8.0°. At 6.0°, it is larger than the clutter power. The noise power, on the other hand, is approximately constant at all angles.

Table 5.11: Powers Obtained Using Fourier Beamforming

Elev Angle (°)	0.0	1.0	2.0	3.0	4.0	5.0	6.0	7.0	8.0
	Fourier Beamforming: All Powers (dB)								
Combined Power	62.4	56.0	45.8	40.9	40.2	39.9	38.7	43.4	45.6
Clutter Power	62.4	55.9	45.1	37.9	36.2	36.6	29.9	28.5	31.6
Weather Power	29.4	28.8	29.5	30.7	31.7	33.6	36.5	42.6	45.0
Noise Power	-31.6	-31.5	-31.6	-31.6	-31.4	-31.5	-31.4	-31.5	-31.6

5.3.1 Effects of Diagonal Loading

As discussed previously, diagonal loading is the most commonly used technique in adaptive spatial arrays. It is often used as a means for controlling the adaptivity of the filters and is needed when the array is miscalibrated or when a small number of samples is used. In this subsection, the performance of the spatial filters is examined for changes in diagonal loading with values along with the parameters listed in Table 5.4 when a single moving target produces clutter contamination.

Table 5.12: Parameters Used in Varying Diagonal Loading

Parameter	Value
SNR	70 dB
CSR	30 dB
NPTS	8
γ	$\mathbf{10^{-1}}$ — $\mathbf{10^{8}}$

When MVDR is applied to the time series signals with the selected range of diagonal loading and processed, the powers of the filtered signals are plotted in Figure 5.48. The results show the variation of the individual powers and its contribution to the combined power over the selected diagonal loading range. While the combined power decreases with diagonal loading less than 10^5, the results are not always desirable. At angles below 4.0°, a change in the diagonal loading from 10^8 to 10^{-1} leads to lower clutter power at a cost of increased weather power. For example, the weather power increases from 41.6 dB to 50.1 dB while the clutter attenuates from 58.2 dB to 47.8 dB when the loading range is changed from 10^8 to 10^{-1} at 0.0°. The trade-off is reversed at the further angles away from the clutter source where an increase in clutter power is observed when the diagonal loading is changed from 10^8 to 10^{-1}. As another example, the clutter power increases from 22.3 dB to 28.9 dB while the weather power decreases from 36.4 dB to 33.6 dB over the same diagonal loading range at 8.0°. Additionally, the decrease of the combined power at this angle leads to a negatively biased estimate of the weather power.

Using STSP_1, STSP_3, STSP_5, and STSP_6 and the selected range of diagonal loading to process the time series signals, the results are plotted in Figures 5.49, 5.50, 5.51, and 5.52, respectively. The results show the transition of the powers with different

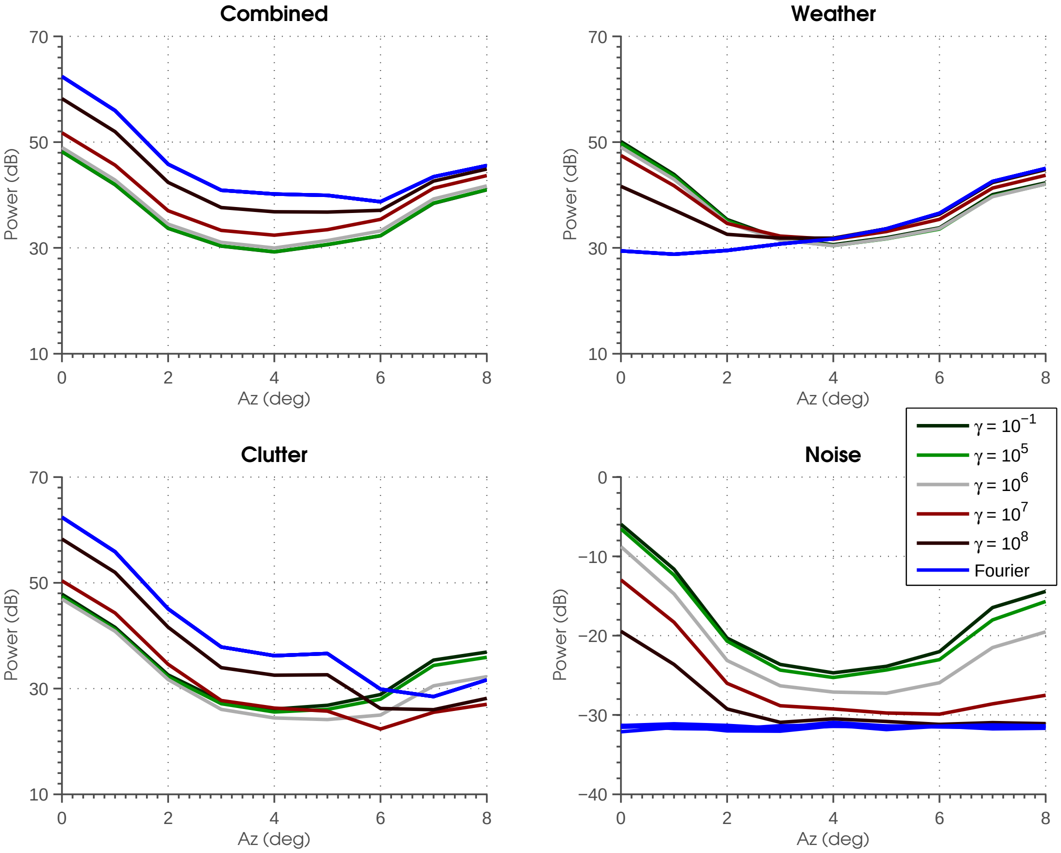

Figure 5.48: Powers obtained using MVDR with variable diagonal loading. The results show the average power as the angle is steered away from the clutter source for diagonal loading from 10^{-1} to 10^{8}. For comparison, the power shown in the blue line is obtained using conventional Fourier beamforming.

diagonal loading and set of eigenvectors. The powers obtained using STSP$_1$ show the smallest variance with values that appear to be most desirable. The combined power decreases and becomes minimum when diagonal loading less than 10^7 is used. Additionally, it is observed that the clutter power is reduced when the diagonal loading is changed to 10^6. The real benefit of using STSP$_1$, however, is observed when weather power is observed. At angles above 4°, the weather power is constant and its bias is relatively low compared to the original weather power. Compared to the results obtained using STSP$_3$, STSP$_5$ and STSP$_6$, a larger attenuation of the combined power can be obtained. However, the attenuation comes at the cost of increased clutter power and negative bias in the estimate of the weather power.

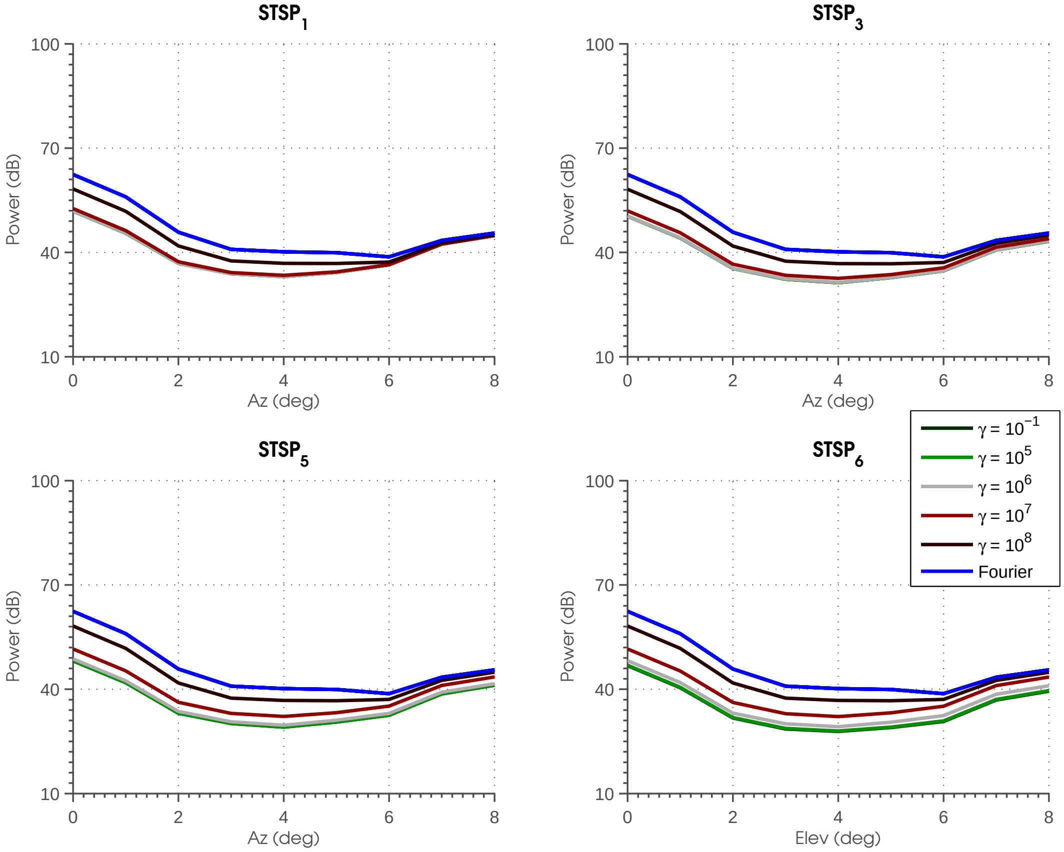

Figure 5.49: Same as Figure 5.48, except for STSP$_1$, STSP$_3$, STSP$_5$ and STSP$_6$, and only the combined power is plotted.

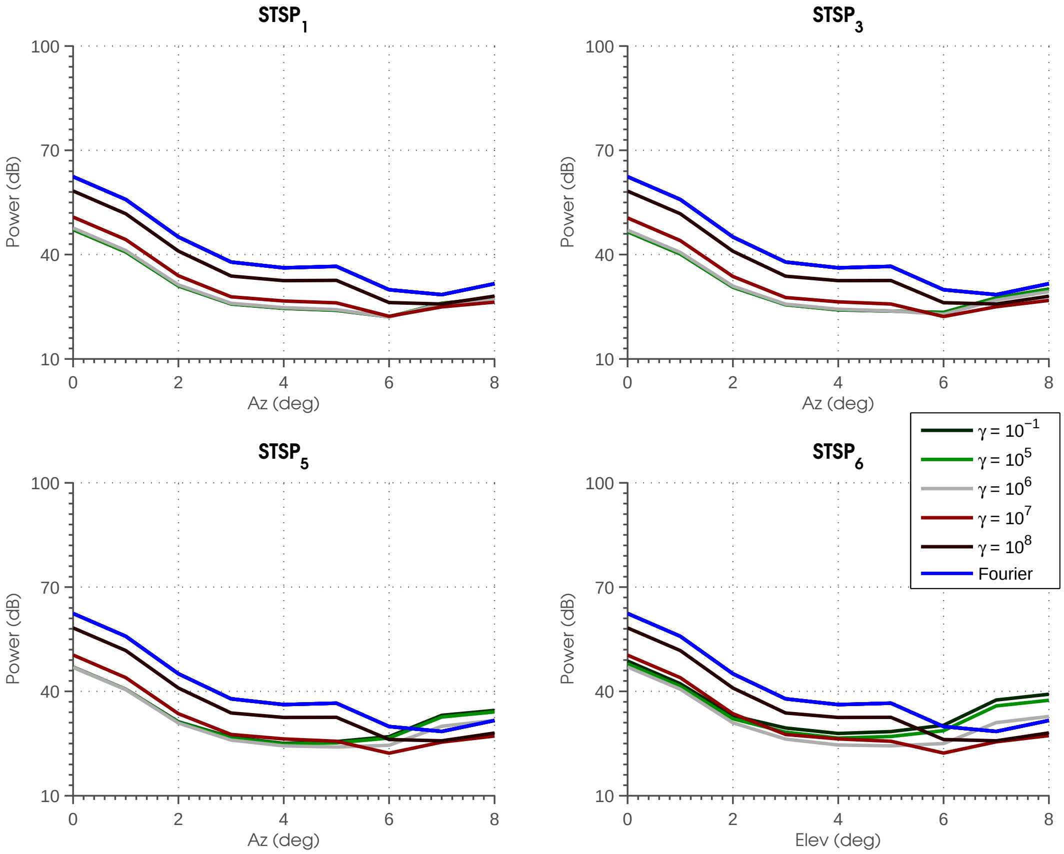

Figure 5.50: Same as Figure 5.48, except for STSP$_1$, STSP$_3$, STSP$_5$ and STSP$_6$, and only the clutter power is plotted.

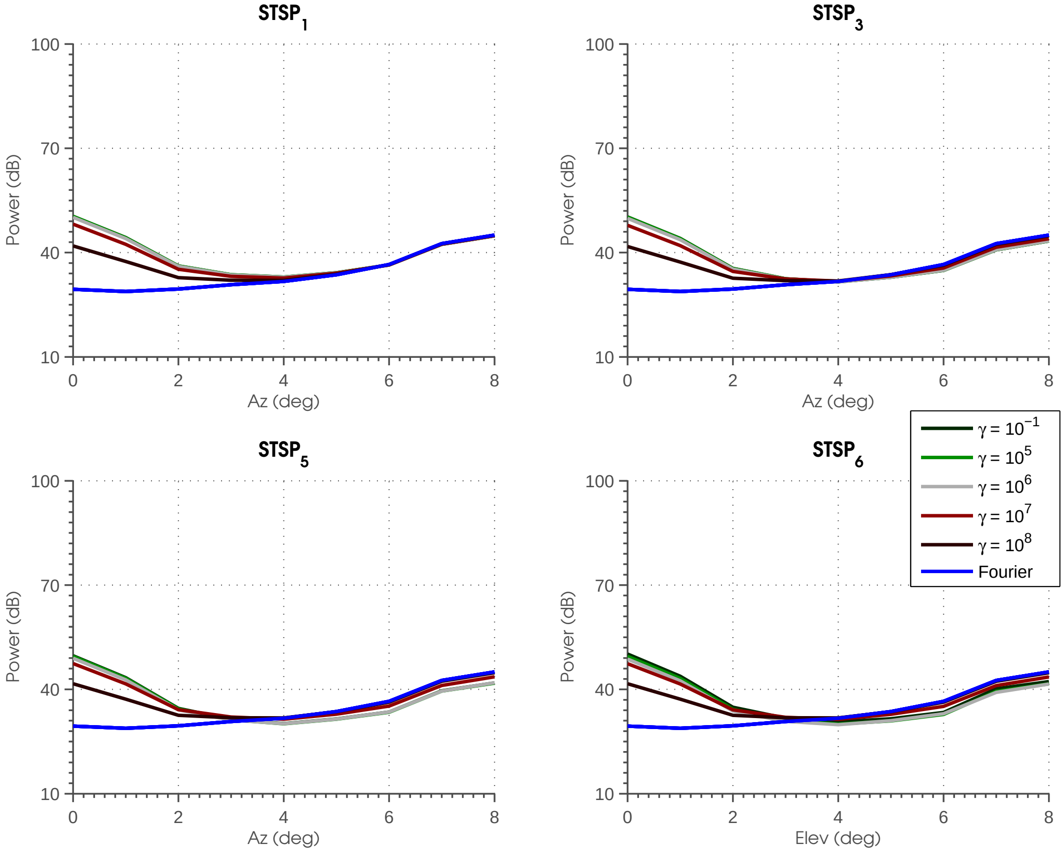

Figure 5.51: Same as Figure 5.48, except for STSP$_1$, STSP$_3$, STSP$_5$ and STSP$_6$, and only the weather power is plotted.

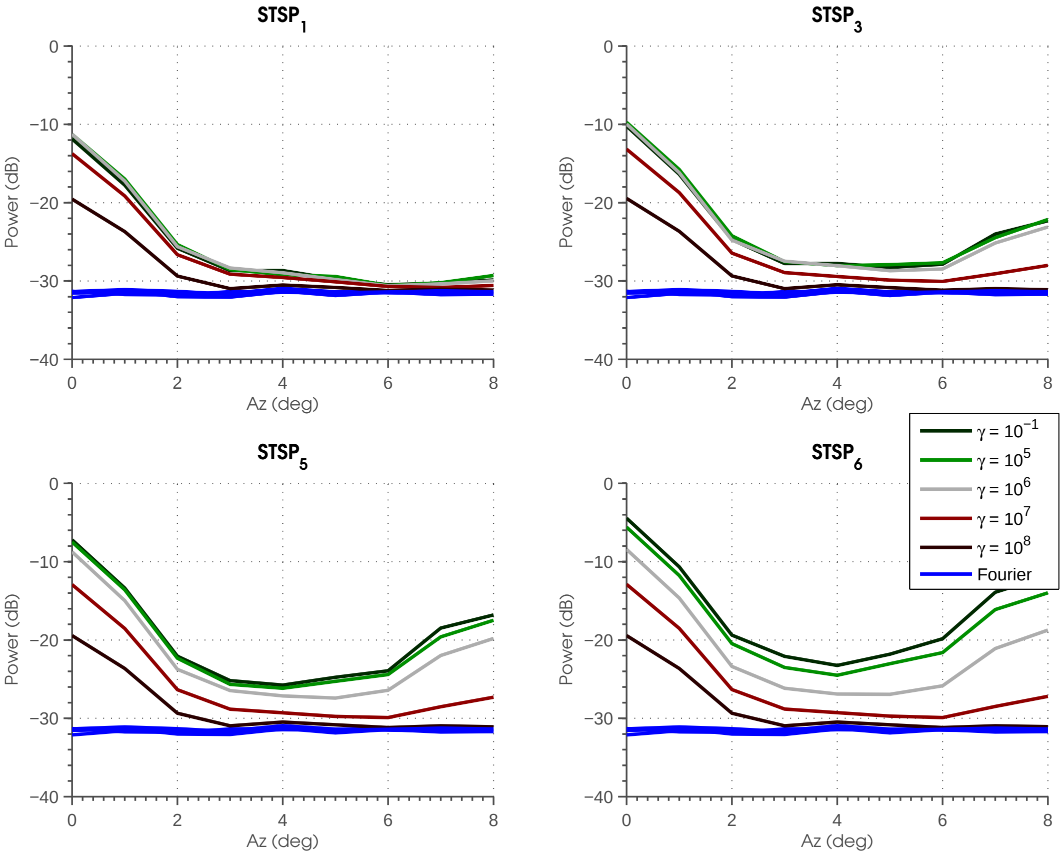

Figure 5.52: Same as Figure 5.48, except for STSP$_1$, STSP$_3$, STSP$_5$ and STSP$_6$, and only the noise power is plotted.

5.3.2 Effects of Dwell Time

Like diagonal loading, the dwell time is another commonly used parameter that is varied when clutter filtering is examined using spatial arrays. This parameter determines the variance of the covariance matrix as well as its accuracy. For a single moving scatterer, it will be shown that the dwell time is an important parameter that determines the success to which clutter is attenuated. In this subsection, the performance of filtering a moving clutter source is examined for changes to the dwell time using samples sizes ranging from two to 32 samples along with parameters listed in Table 5.13.

Table 5.13: Parameters Used in Dwell Time Variation

Parameter	Value
SNR	70 dB
CSR	30 dB
NPTS	**2 — 32**
γ	10^5

The results obtained using MVDR and the selected sample sizes are plotted in Figure 5.53. The results show changes of the power and the individual powers as the sample size is varied. The combined power increases when the sample size is changed from two to 32 samples. However, it is still smaller than the individual weather and clutter powers when the sample size is less than the number of auxiliary elements. When the sample size is two, the combined power ranges between -2.5 dB to 17.9 dB while the clutter and weather powers are significantly larger with values that range between 29.9 dB and 51.2 dB. Upon closer inspection, a negligible difference of less than 0.1 dB is observed between the clutter and weather powers that implies these two components destructively combined when added. At sample sizes larger than the number of auxiliary elements, the magnitudes of the combined and weather powers increase. In contrast, they decrease for the clutter and noise powers when the sample size is changed from eight to 32 samples. Additionally, the combined power appears to be steady when more than 16 samples are used even though the weather power continues to further increase at angles larger than 2.0° away from the clutter source as well as the clutter attenuation at these angles.

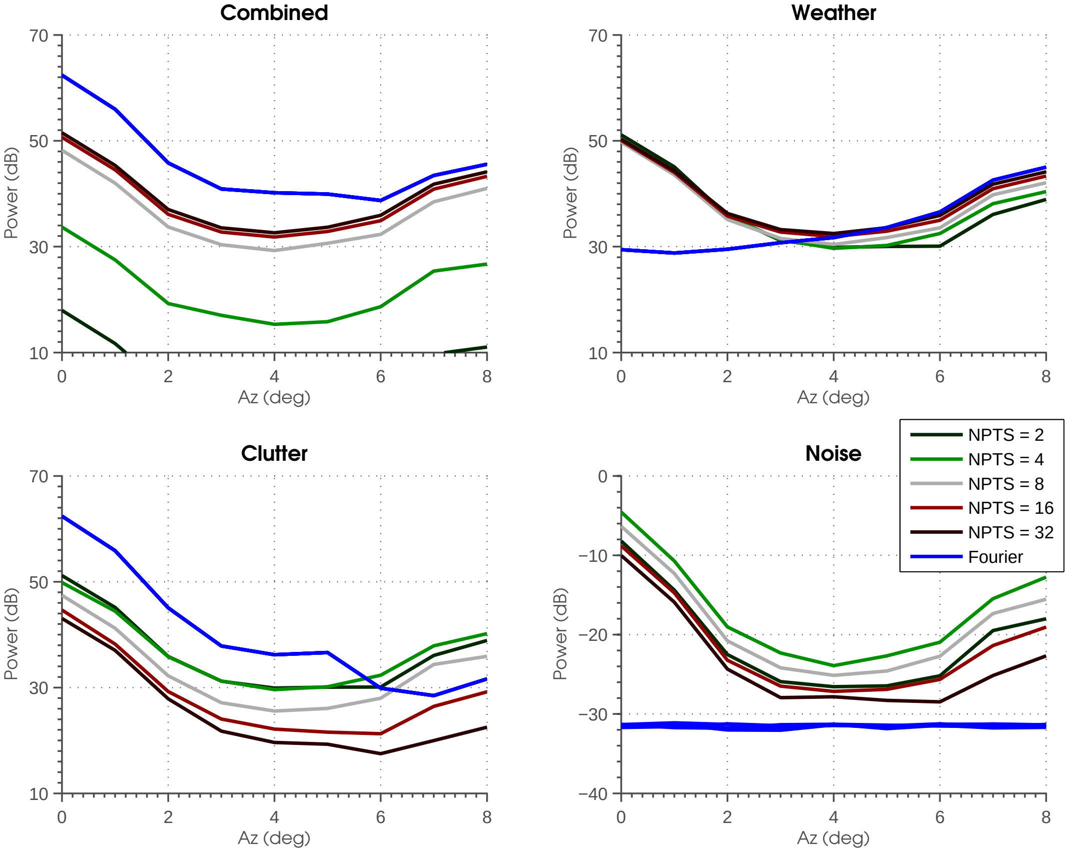

Figure 5.53: Powers obtained using MVDR with variable sample sizes. The results show the average power as the angle is steered away from the clutter source for sample sizes from two to 32 samples. For comparison, the power shown in the blue line is obtained using conventional Fourier beamforming.

Using STSP and the selected range of sample sizes, results processed using STSP_1, STSP_2, STSP_3, STSP_4 and STSP_6 are plotted in Figures 5.54, 5.55, 5.56, and 5.57, respectively. In general, it was observed that the variance of the combined power is changed from STSP_1 to STSP_6. The difference between the maximum and minimum values that are obtained of the combined power at any angle is less than 3.3 dB when STSP_1 is used, while the difference increases significantly when two or four samples are used or when STSP_2 thru STSP_6 are used. Additionally, the clutter attenuation increases when the sample size is changed from two to 32 samples and the clutter filter is changed from STSP_1 to STSP_6. Unfortunately, the weather powers obtained above 4.0° with STSP_2 to STSP_6 are not as desirable as those obtained using STSP_1

since a negative bias is observed at these angles. The effects can be reduced by using only STSP_1 which shows that only a negligible difference between the weather powers is observed at the cost of reduced clutter attenuation.

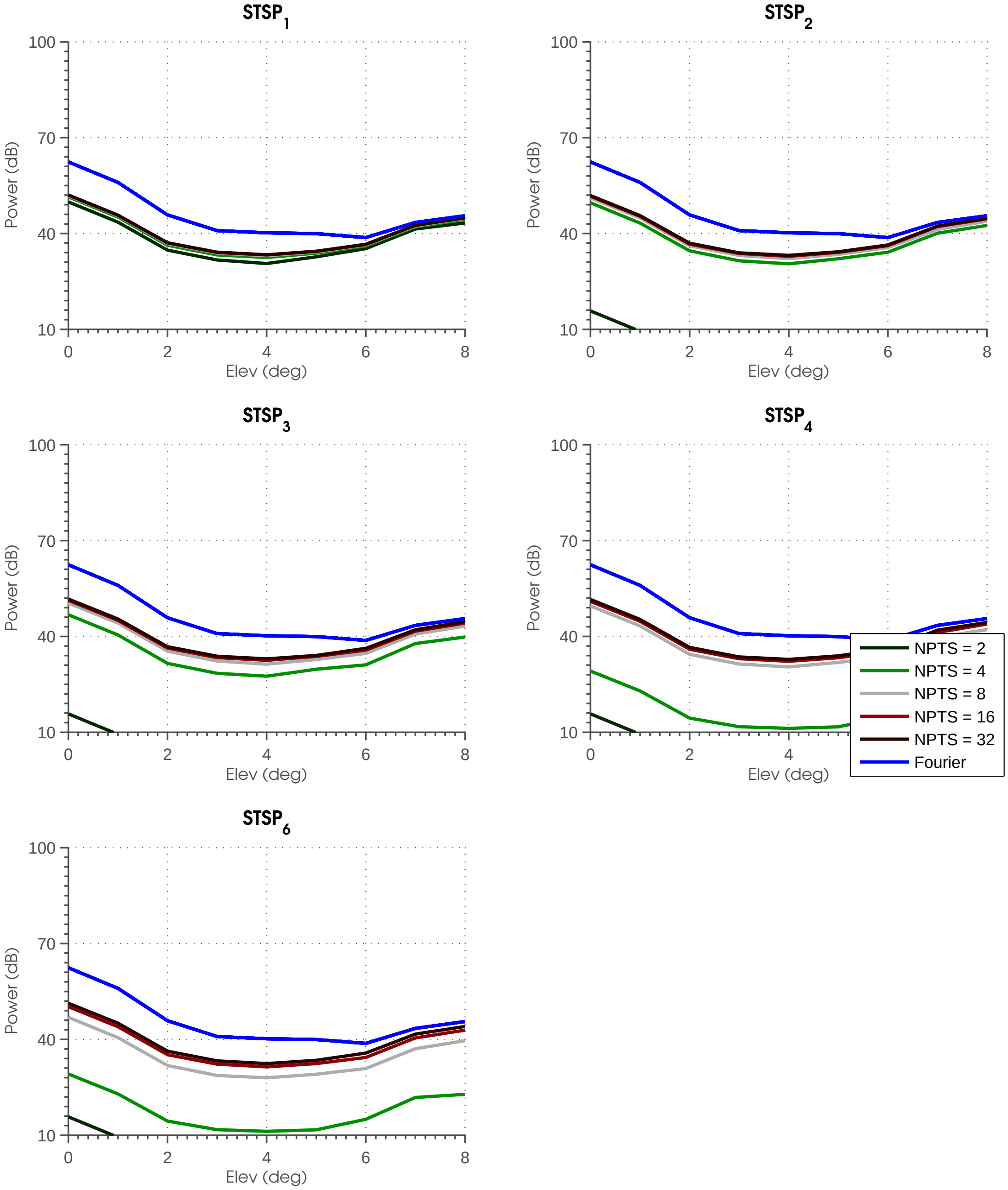

Figure 5.54: Same as Figure 5.53, except for STSP_1, STSP_2, STSP_3, STSP_4, and STSP_6, and only the combined power is plotted.

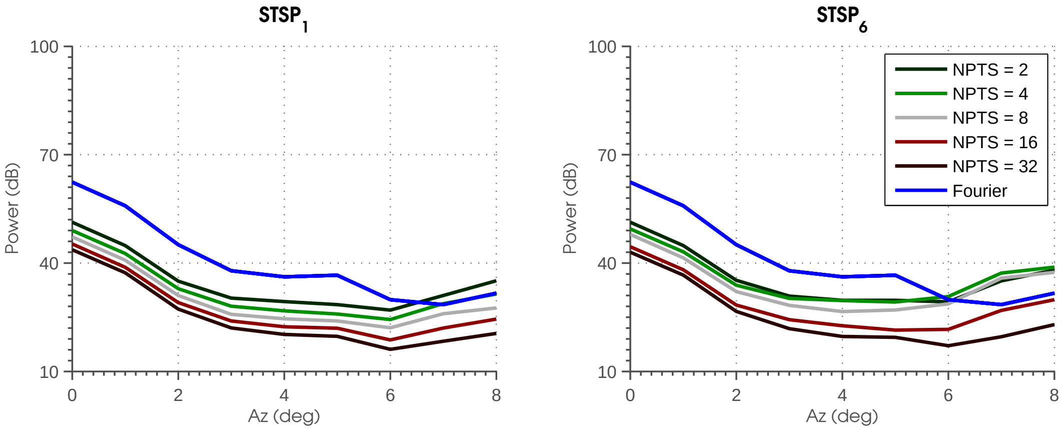

Figure 5.55: Same as Figure 5.53, except for STSP$_1$ and STSP$_6$, and only the clutter power is plotted.

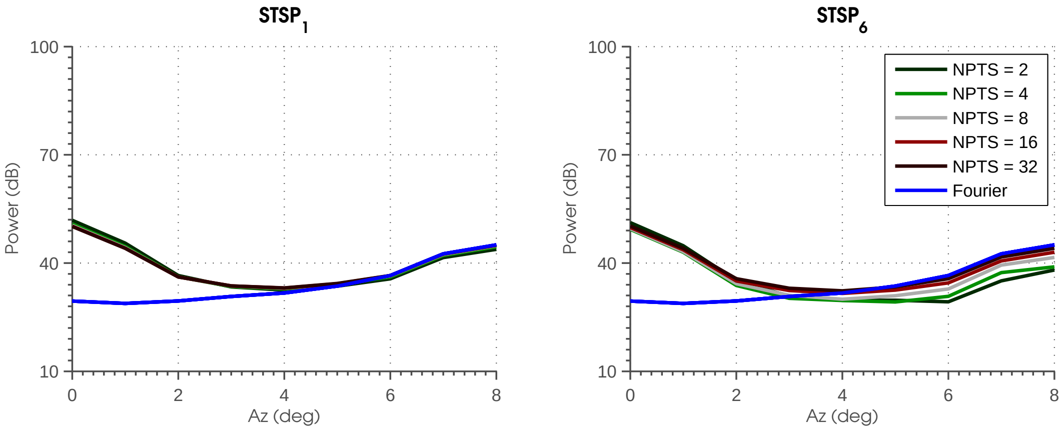

Figure 5.56: Same as Figure 5.53, except for STSP$_1$ and STSP$_6$, and only the weather power is plotted.

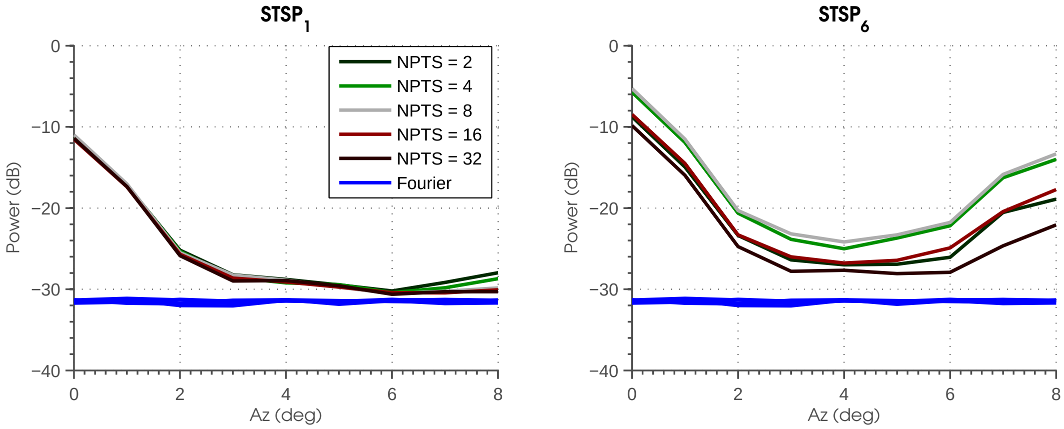

Figure 5.57: Same as Figure 5.53, except for STSP$_1$ and STSP$_6$, and only the noise power is plotted.

As discussed previously, the dwell time is an important parameter that determines the variance of the covariance matrix and the performance of the clutter filters. When a short dwell time is used, the variance of the covariance matrix is high and the covariance matrix can be singular and rank deficient. When clutter filtering is applied in this case, the filtered clutter and weather signals are partially correlated and the combined power that is produced is smaller than the individual power of the weather and clutter. In contrast, when more samples than the number of auxiliary elements are used, the variance of the covariance matrix decreases and better estimates of the individual powers are obtained. While the performance of clutter filtering of a single source has results that are similar to those obtained from filtering ground clutter, the two cases are still different because the clutter source in this case is localized whereas it is distributed with ground clutter. As a result, the number of degrees of freedom is more than the number of clutter sources and a better attenuation of the clutter can be obtained when longer dwell times are used in this case.

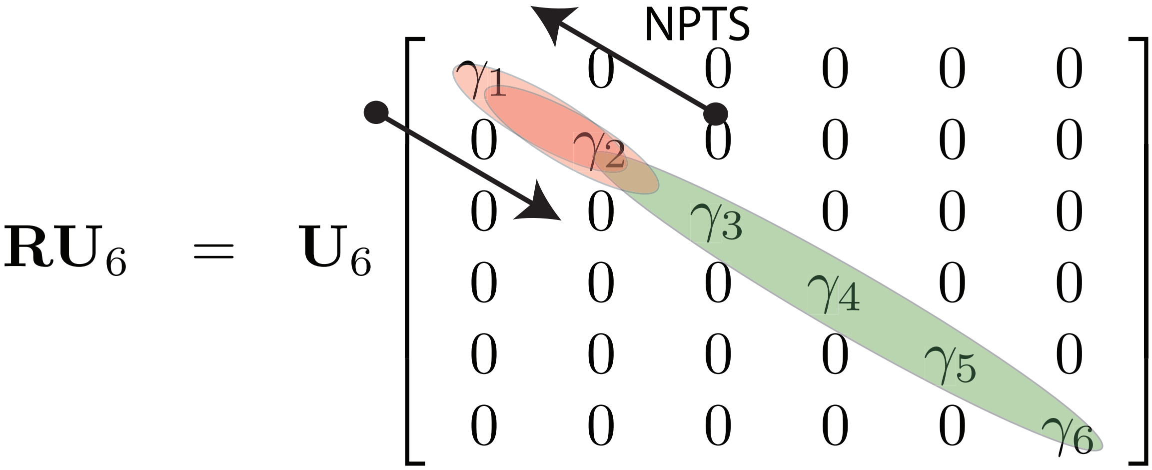

Figure 5.58: Illustrated effects of CSR at high values. Under this assumption, the correlation matrix is dominated by a few eigenvalues of the clutter and can be approximated by a constant multiplication to the eigenmatrix. Using this assumption, it can be easily shown that the inverse of the correlation matrix is also a multiple of that constant.

5.3.3 Effects of Clutter-to-Signal Ratio

The CSR is another parameter generally considered when filtering clutter with spatial arrays. As discussed, its value depends on the location of the clutter relative to the radar resolution volume, and is determined by both the range and relative position of the clutter to the steered direction. In this section, the performance of clutter filtering using a spatial array is examined with CSR ranging from 10 dB to 50 dB along with parameters listed in Table 5.7.

Table 5.14: Parameters Used in Varying Clutter Power

Parameter	Value
SNR	70 dB
CSR	**10 — 50 dB**
NPTS	8
γ	10^5

The powers obtained using MVDR for the selected range of CSR are plotted in Figure 5.59. The results show changes to these values when different clutter powers are processed. The combined power is variable near the clutter source while being relatively consistent when the clutter is at least 4.0° away. Upon closer inspection, the variation near the clutter depends on the CSR and is caused by fluctuations in the weather power. When the angle is steered away from the clutter, smaller fluctuations of the weather power and combined power are observed. Additionally, it was observed that while the minimum combined power depends on the CSR, its maximum value reaches a steady state when the CSR is above 30 dB. As a result, the combined powers obtained using CSR of 30 dB and 50 dB are approximately the same. The weather and noise powers follow similar trends even though their magnitudes are many orders of magnitude apart. In particular, the weather power near the clutter is increased beyond the original value in some cases up to 30 dB. However, the weather power is negatively biased when the clutter is at least 4.0° away.

Results of using STSP with the range of CSR are plotted in Figures 5.60, 5.61, 5.62, and 5.63. The results show that a trade-off between minimum combined power and bias to the weather power when the filtering scheme is changed from STSP_1 to STSP_6. When STSP_1 is used, the combined power at each angle is maximum,

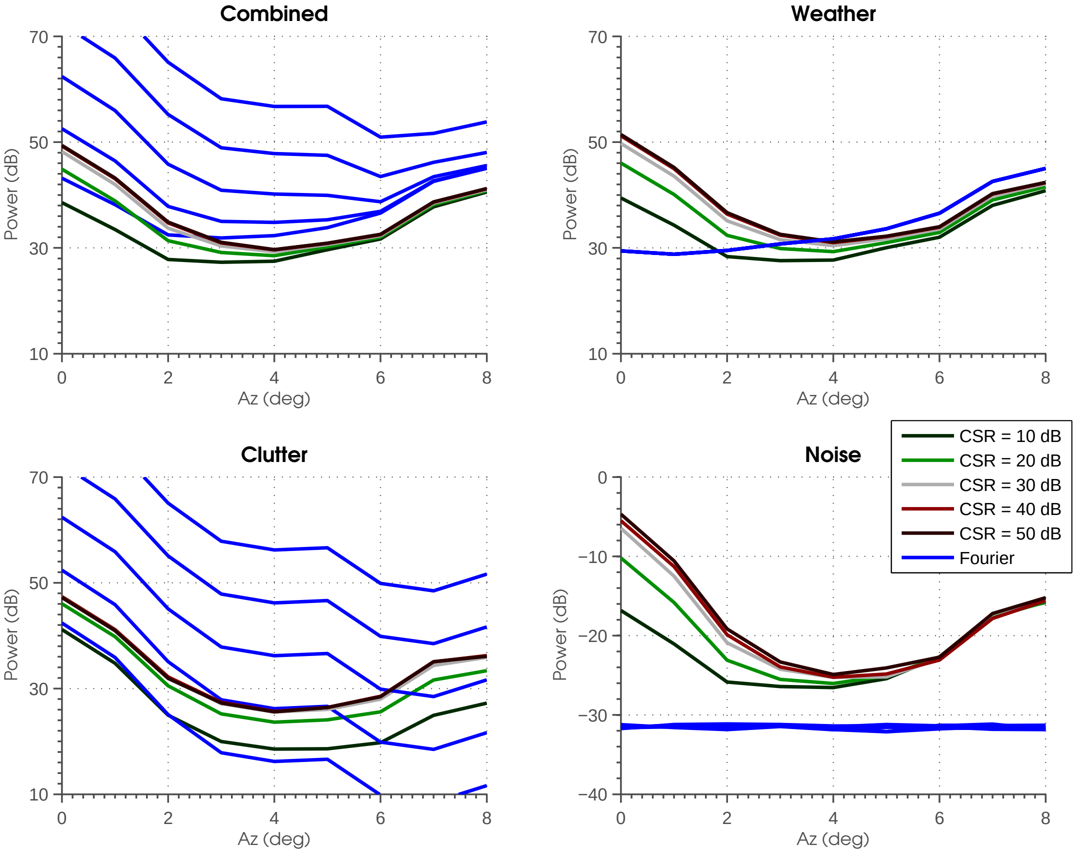

Figure 5.59: Powers obtained using MVDR with variable CSR. The results show the average power as the angle is steered away from the clutter source for CSR from 10 dB to 50 dB. For comparison, the power shown in the blue line is obtained using conventional Fourier beamforming.

however the power that it measures of the weather when the angle is larger than 4.0° is generally below 1.0 dB and has smallest negative biases compared to the other techniques. When other STSP techniques are applied, the combined power decreases, which is important for removing the power near the clutter source, at the cost of increased bias to the weather signals at angles above 4.0°. For example, a difference up to 8 dB is observed at 8.0° when STSP_6 was used.

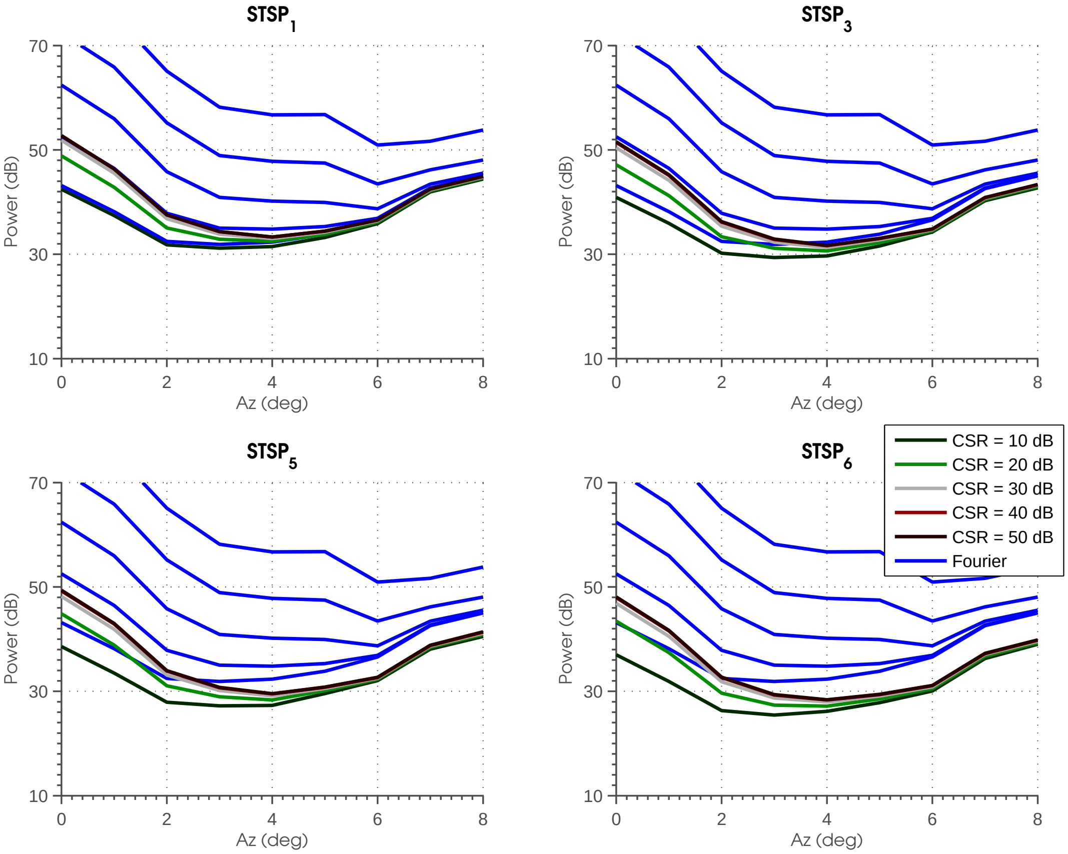

Figure 5.60: Same as Figure 5.59, except for STSP_1, STSP_3, STSP_5, and STSP_6, and only the combined power is plotted.

In the previous results of clutter filtering with ground clutter, it was shown that the effects of CSR could be best observed by starting from a high CSR case and then decreasing the CSR. The same approach can be used to examine the effects of CSR in these situations. Observed that in the case with high CSR (i.e., > 30 dB), the combined, clutter, and weather powers obtained from clutter filtering have approximately the same values. However, as the clutter power becomes smaller than this "threshold", the results from each technique begin to differ, which is because a balance is being made between minimum power and constraint. Additionally, the

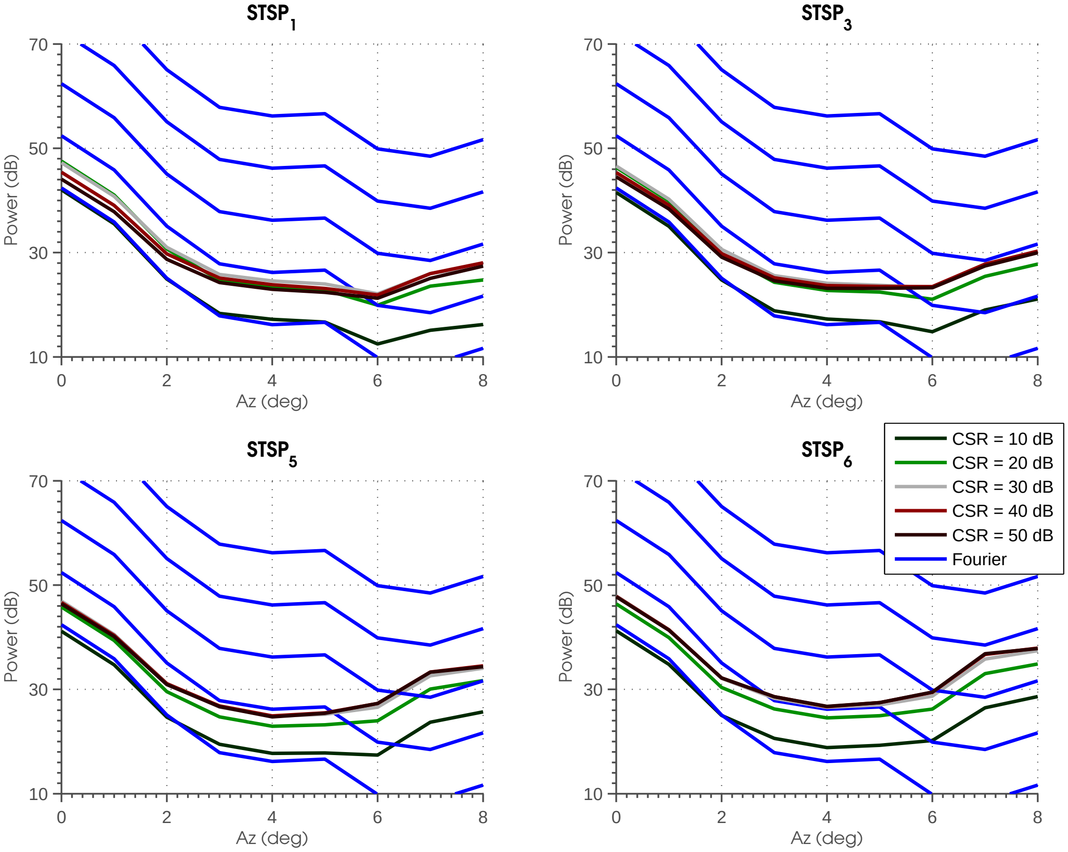

Figure 5.61: Same as Figure 5.59, except for STSP$_1$, STSP$_3$, STSP$_5$, and STSP$_6$, and only the clutter power is plotted.

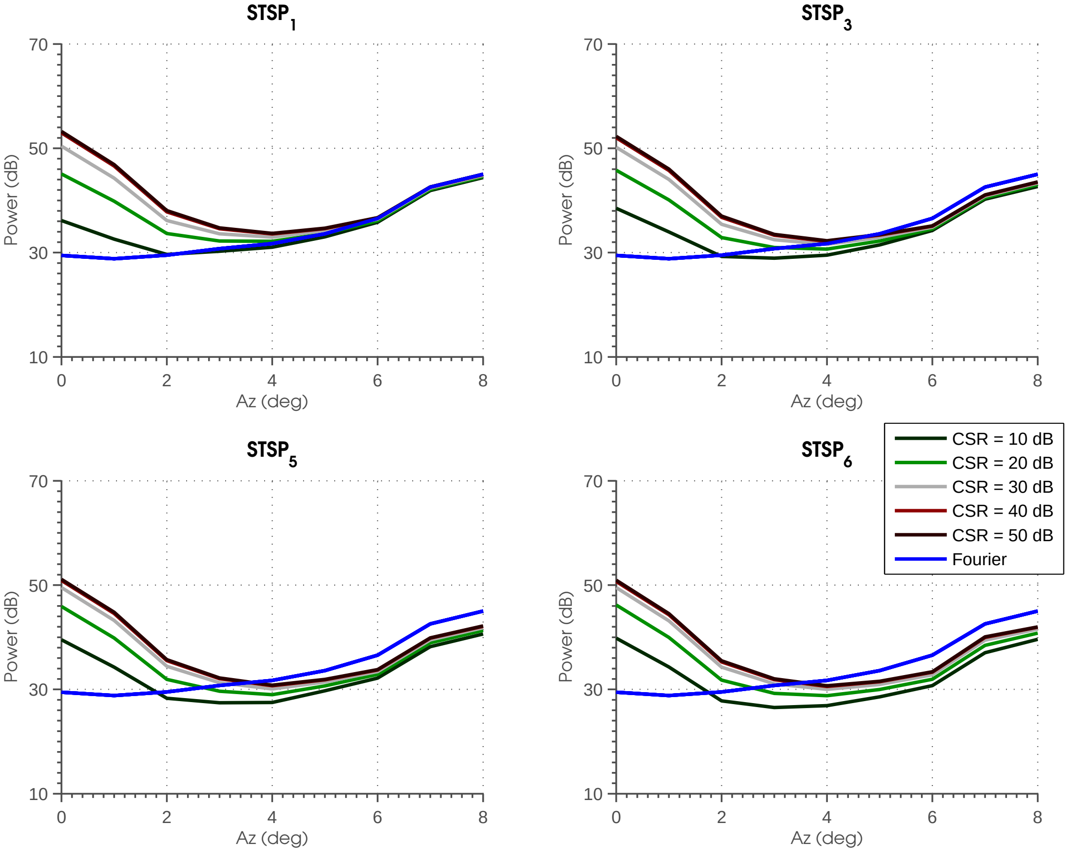

Figure 5.62: Same as Figure 5.59, except for STSP$_1$, STSP$_3$, STSP$_5$, and STSP$_6$, and only the weather power is plotted.

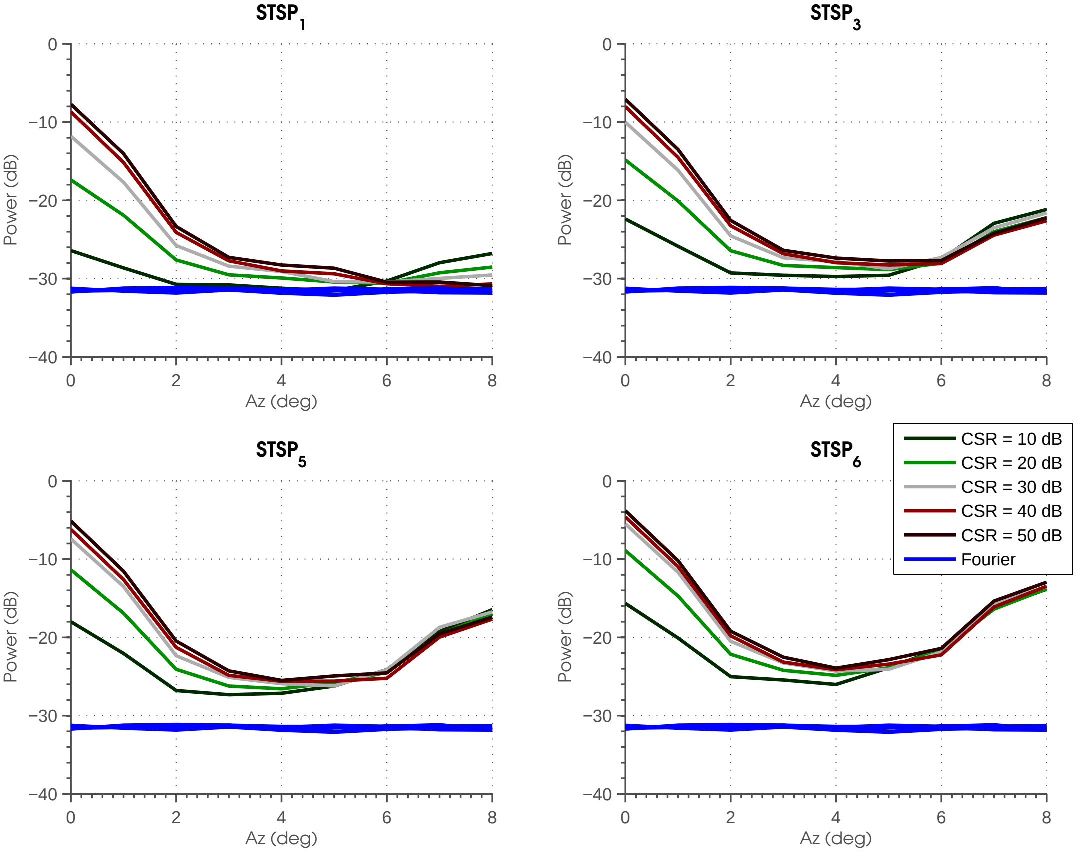

Figure 5.63: Same as Figure 5.59, except for STSP$_1$, STSP$_3$, STSP$_5$, and STSP$_6$, and only the noise power is plotted.

location of the clutter subspace may shift as the power of the weather in a low CSR now becomes a major factor and takes on eigenvalues that are equally as large as the clutter. An illustration of this effect is shown in Figure 5.64. As a result, the assumption previously made that the clutter is observed in only the largest eigenvalues may become invalid, and the weather signal can be accidently removed when clutter filtering is applied to these corresponding eigensubspaces. As shown with the STSP techniques, the weather signal power that was obtained without clutter had values that were lower than those obtained without clutter. However, the constraint of zero gain in the steered direction that was applied by the MVDR alleviates this problem and keeps the weather power at the correct level in these situations.

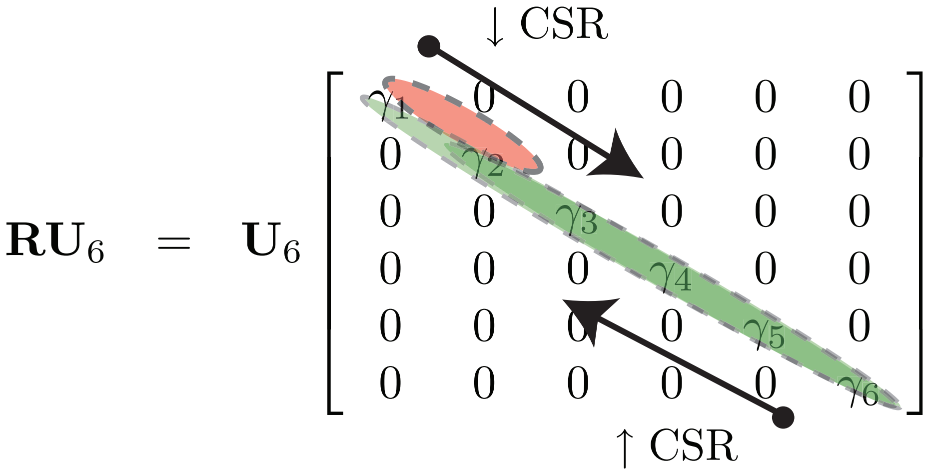

Figure 5.64: Illustrated effects of CSR for a single moving target. As can be observed, the eigenvalue belonging to the clutter shifts downward as the CSR decreases and is replaced by eigenvalues of the weather signal. In this point-of-view, the original assumption that the clutter exists in only the largest eigenvalue becomes invalid.

5.3.4 Effects of Signal-to-Noise Ratio

The ratio of the signal to noise powers is the final parameter that is examined of these spatial arrays. As was previously discussed, it has a large range that depends on the scattering field, which can vary from clear air to heavy rain, and its value is used to estimate the covariance matrix that is then employed by the spatial filters to obtain their weights. While birds are not expected to be moving in the latter situation, the performance of clutter filtering of a moving target is still examined for all the conditions along with parameters listed in Table 5.15.

Table 5.15: Parameters Used in Varying Noise Power

Parameter	Value
SNR	**10 — 70 dB**
CSR	30 dB
NPTS	8
γ	10^5

The results obtained using MVDR and the above parameters are plotted in Figure 5.65. The results show the powers of the time series signals when processed with SNR that range from 10-70 dB. The results indicate that the filtered powers are consistent with differences that are negligible when the SNR is at least 30 dB. When the SNR is lower with a value of 10 dB, the powers that are obtained deviate from these results. The combined and clutter powers are increased by approximately 2 dB while the weather power increases by 1 dB. Additionally, the noise power, which was previously relatively small, is now comparable to the weather and clutter powers. As a result, it is now a major component when the SNR is 10 dB of the combined power value.

With the same setup, the results observed by processing the time series signals using STSP are plotted in Figures 5.66, 5.67, 5.68, and 5.69. They are consistent with differences that are negligible when the SNR is at least 30 dB, while the power is slightly amplified when the SNR is 10 dB. The change is negligible when STSP_1 is used however it is more evident when the filtering scheme is changed from STSP_2 to STSP_6. Upon closer inspection, the clutter power is amplified by up to 2 dB at angles below 6.0° and with smaller values above this angle. Similarly, the weather

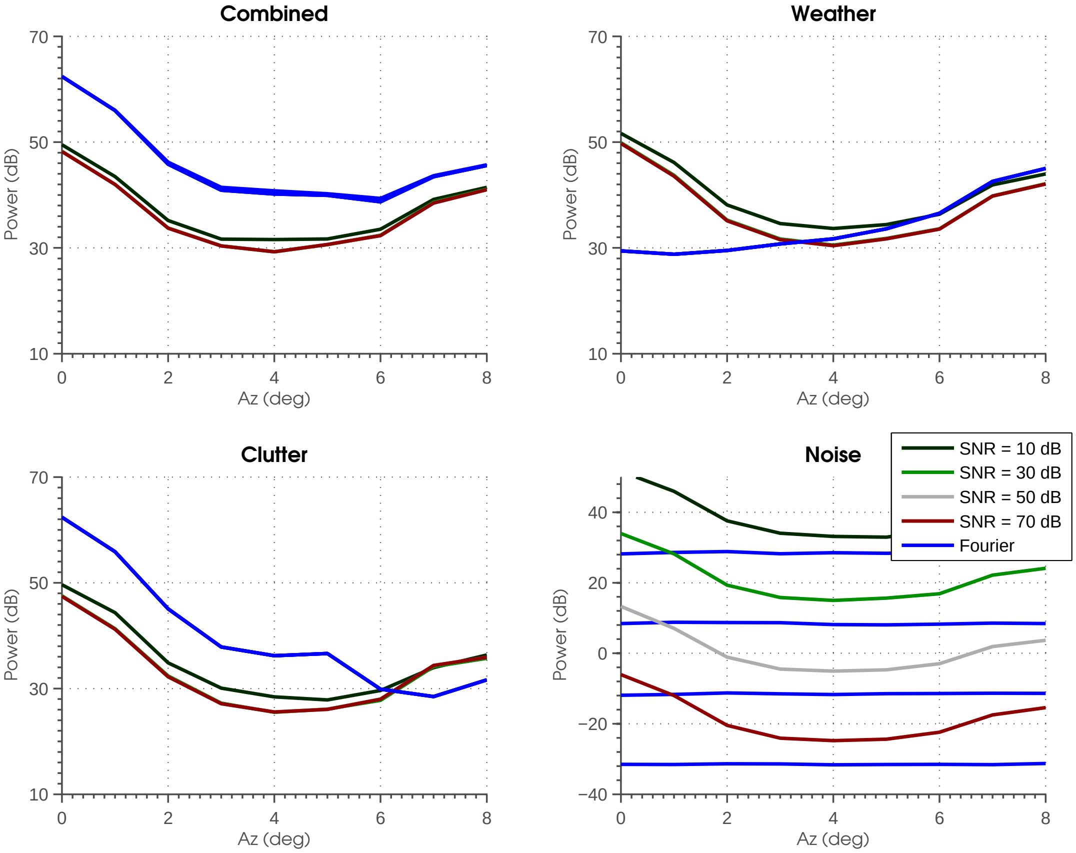

Figure 5.65: Powers obtained using MVDR with variable SNR. The results show the average power as the angle is steered away from the clutter source for SNR from 10 dB to 70 dB. For comparison, the power shown in the blue line is obtained using conventional Fourier beamforming.

power is amplified when the SNR is 10 dB, and its bias above 6.0° is reduced because of this change.

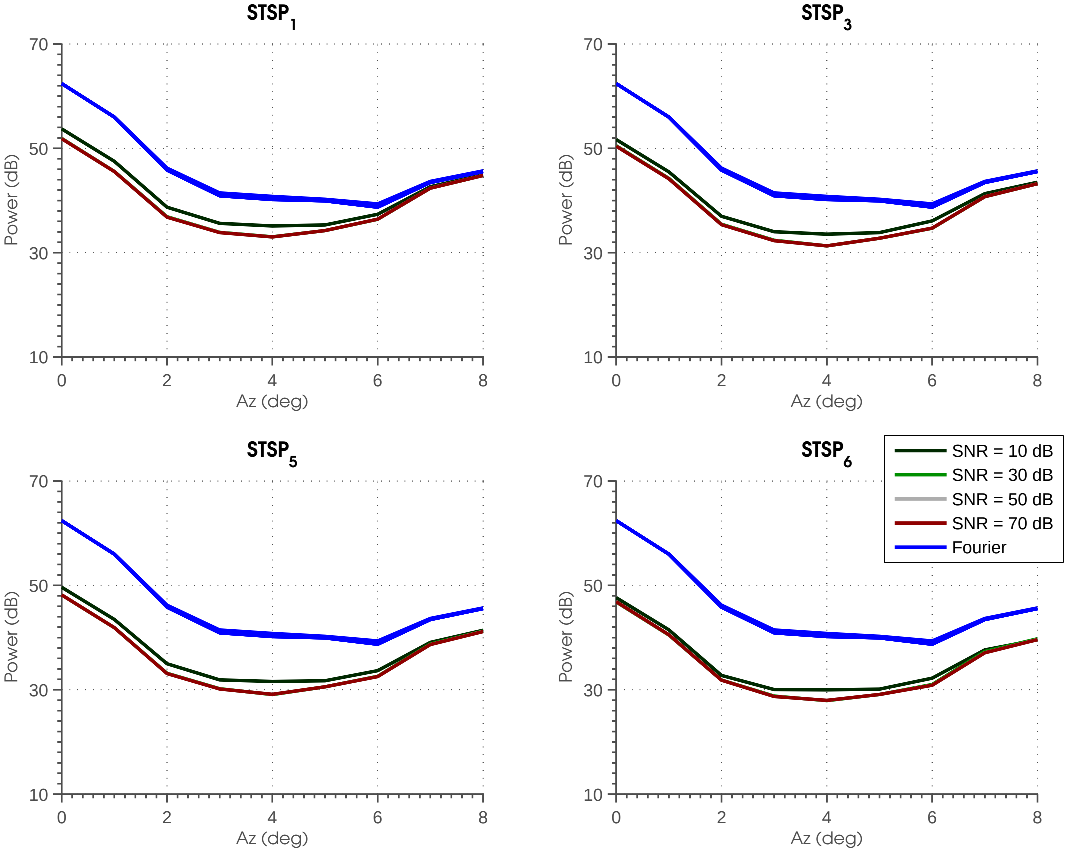

Figure 5.66: Same as Figure 5.65, except for STSP_1, STSP_3, STSP_5, and STSP_6, and only the combined power is plotted.

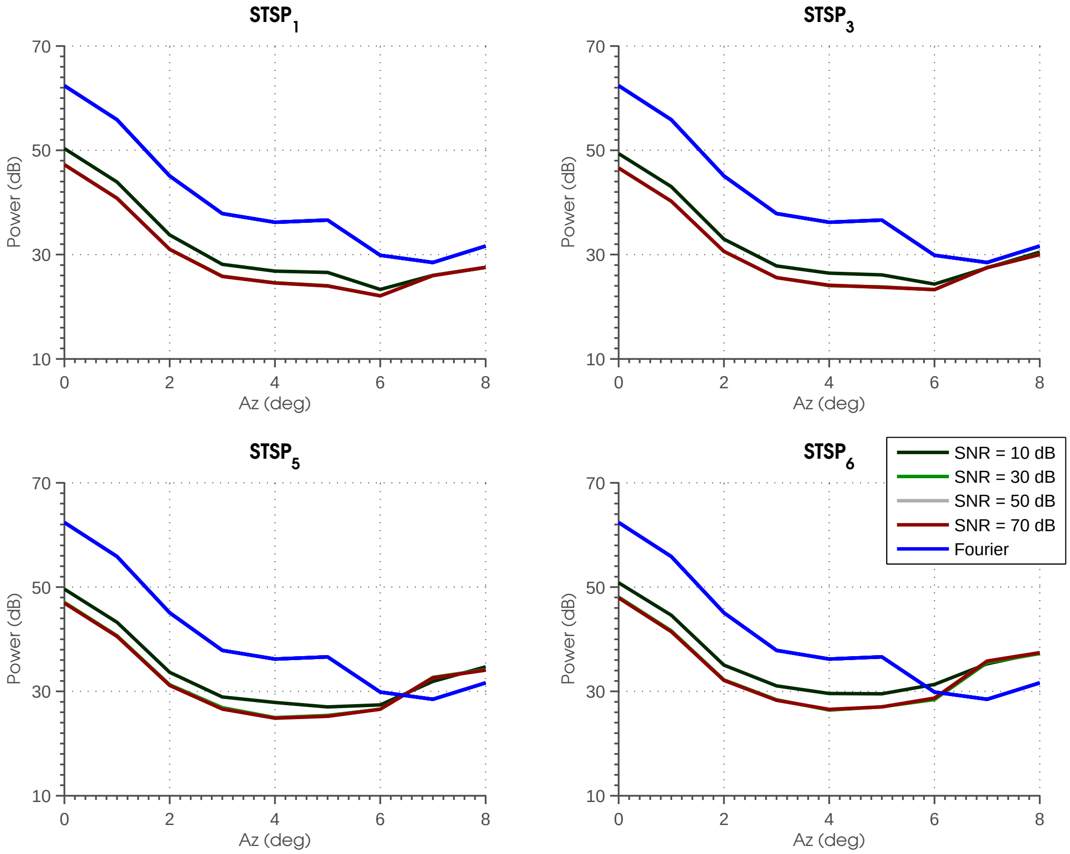

Figure 5.67: Same as Figure 5.65, except for STSP_1, STSP_3, STSP_5, and STSP_6, and only the clutter power is plotted.

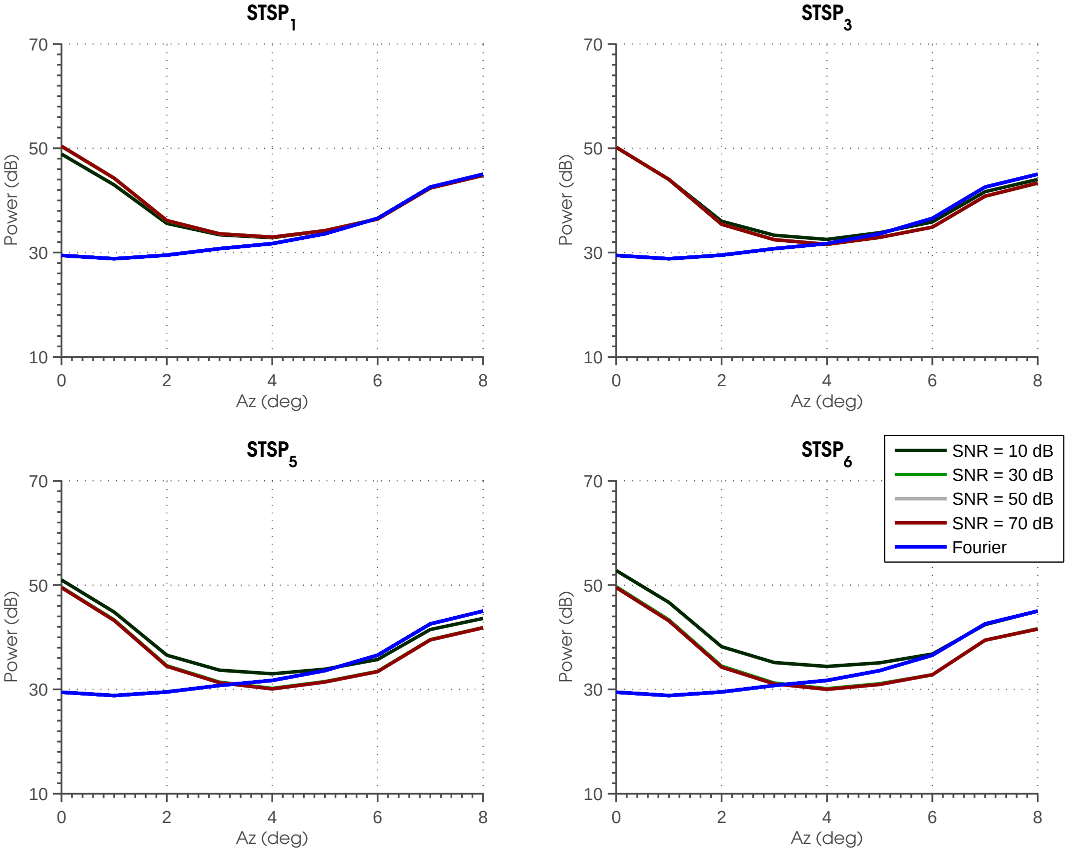

Figure 5.68: Same as Figure 5.65, except for STSP$_1$, STSP$_3$, STSP$_5$, and STSP$_6$, and only the weather power is plotted.

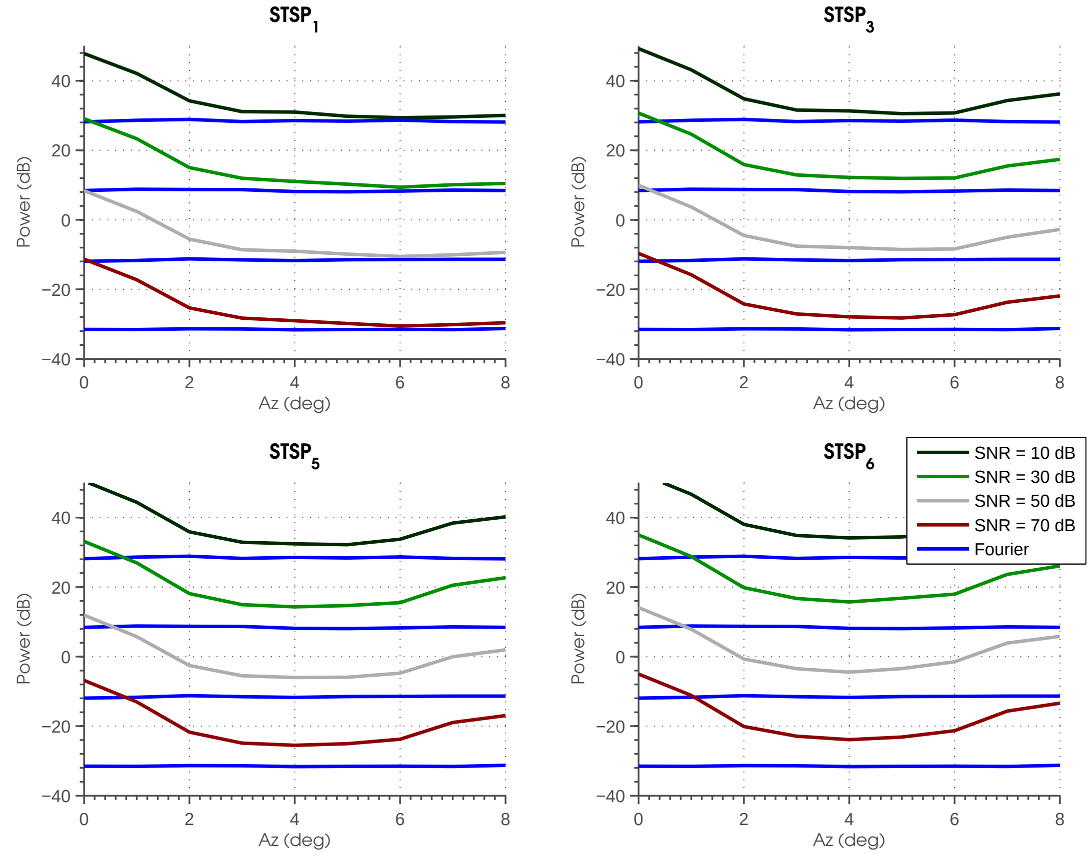

Figure 5.69: Same as Figure 5.65, except for STSP$_1$, STSP$_3$, STSP$_5$, and STSP$_6$, and only the noise power is plotted.

5.3.5 Discussion of the Simulation Results

In the previous subsections, the performance of clutter filtering by a partially adaptive array contaminated by moving clutter was examined for changes in diagonal loading, dwell time, clutter-to-signal ratio, and signal-to-noise ratio. The overall objective was to determine the capabilities of the spatial array to retrieve the weather signals while mitigating as much of the clutter as possible in the different cases. As with the previous study of mitigating quasi-stationary ground clutter, the contaminated signals were processed and values of the combined and individual powers of the clutter, weather and noise were obtained. These values were then compared to results obtained without clutter, and the differences of the powers between the two cases were used to judge the performance of the filters.

Based on the results obtained from these simulations, the sidelobe canceler exhibited many of the same effects that were previously observed when spatial arrays were used to filter ground clutter. Namely, the problem that the filtered power is composed of partially correlated signals and is problematic for estimating the correct power when short dwell time and small diagonal loading were used was observed. Additionally, it was observed that when the spatial filtering techniques were changed from STSP_1 to STSP_6, the results of the weather signals that were observed were negatively biased in many situations. To produce better estimates of the weather signals, it was observed that the results using fewer of the eigensubspace should be used. Another case that was similar involves the weather power being amplified significantly near the clutter sources. These three primary cases are evidence that similar results are obtained and that the minimization schemes approaches clutter filtering in the same manner.

Differences in the effects are also observed when clutter filtering is applied to moving scatterers. One obvious situation involves the case when the weather power is larger than the clutter power even without filtering. This scenario was not previously observed, as the ground clutter power was always larger than the weather power at all elevations. As a result, they do not show that the clutter power could be amplified to minimize the combined power. This phenomenon was observed when the sample size was less than eight samples, diagonal loadings was less than 10^6, and the CSR was less than 30 dB, and contrasts those previously obtained in which the clutter power was always attenuated. Another situation that showed some differences was the case that the estimates improved when long dwell times were used. In these situations, the attenuation of the moving clutter improved as well as the bias of the weather power.

A possible difference is because the number of degrees-of-freedom that are needed to mitigate moving targets are significantly less than the number of degrees-of-freedom that are required to mitigate ground clutter, which is one for the case of a moving target. As a result, the long dwell time improves the statistics of the covariance matrix that helps to match the beampatterns between the auxiliary and main arrays that is used to attenuate the clutter.

5.4 Non-Stationary Clutter Targets: Validation Using the Turbulent Eddy Profiler

The techniques used previously to simulate clutter filtering of a moving target are now validated with real data obtained from the Turbulent Eddy Profiler. The power and Doppler velocity that are processed using conventional Fourier beamforming are shown in Figure 5.70, and from preliminary observations, clutter contamination from moving targets are readily observed above 0.4 km. The returns from these scatterers are outlined using red circles and are characterized by spatially discontinuous powers with peak values of more than 12 dB above their nearby neighbors and spatially discontinuous Doppler velocities with non-zero values.

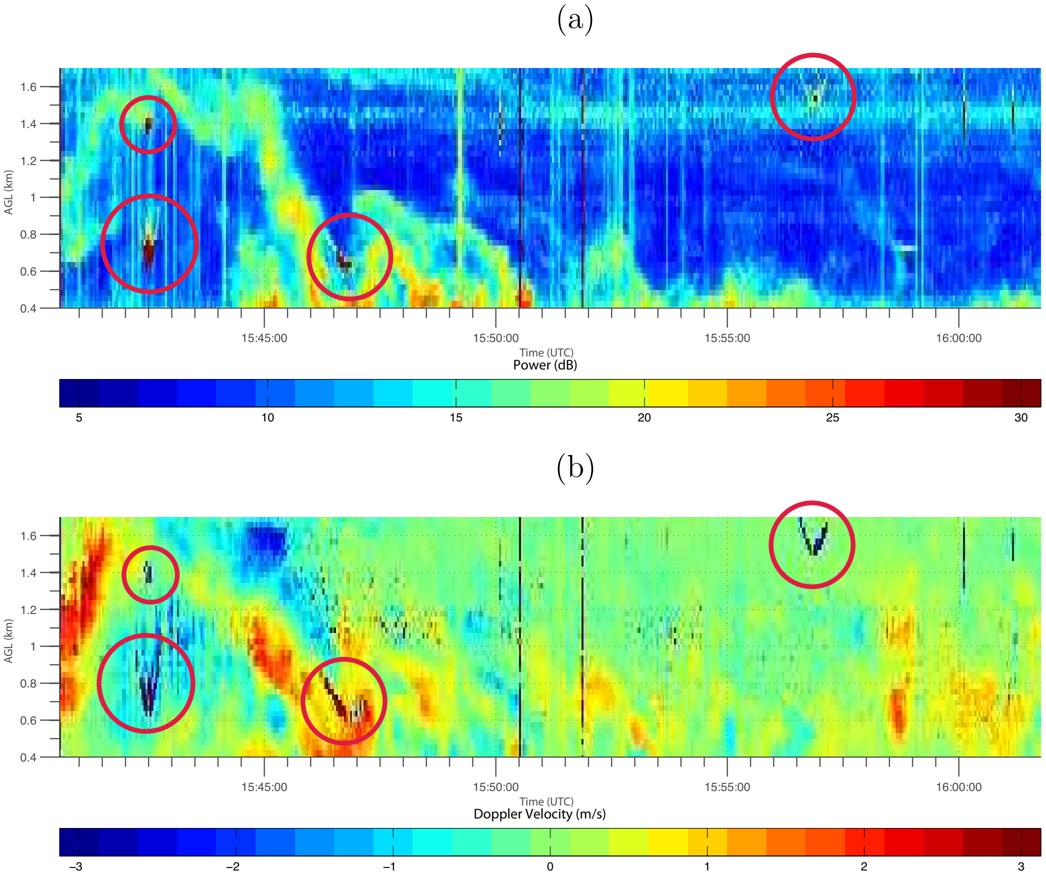

Figure 5.70: Power and Doppler velocity obtained of the combined signal for above surface scattering. Circled at 15:43, 15:47, and 15:57 UTC are the returns assumed from point targets. These features have powers that are much larger than the background and non-zero Doppler velocities.

5.4.1 Effects of Diagonal Loading

Using parameters listed in Table 5.9, spatial filtering was applied to the TEP data to investigate the performance of the clutter filtering with contamination caused by moving targets.

Table 5.16: Parameters Used in Varying Diagonal Loading

Parameter	Value
SNR	3.4 dB
CSR	33.5 dB
NPTS	8
γ	$\mathbf{10^2}$ — $\mathbf{10^7}$
σ_v	variable

With the above parameters, the results of the power and Doppler velocity obtained using MVDR are plotted in Figures 5.71 and 5.72 along with the temporal evolution of the corresponding peak power in Figure 5.73(a). These results in terms of clutter attenuation of the peaks at at 15:43, 15:47, and 15:57 UTC appear to improve when the diagonal loading decreases from 10^8 to 10^2. The best trade-off between mitigating clutter and preserving the weather appears to be obtained when a diagonal loading of approximately 10^5 is used. The weather signal is maximized while regions where the clutters existed have values that are similar to the background weather. When the diagonal loading is further decreased to 10^2, the powers where the clutter sources exist is attenuated to values that are slightly above the noise level. Nevertheless, the estimated velocities of the clutter are still observed and the power of the received signals are adversely affected. At 10^2, the power where the weather scatterers are located also have values that are slightly above the noise level with corresponding Doppler velocities that have magnitudes above 3 m s^{-1}.

When the time series signals are processed using STSP$_1$, the results obtained are plotted in Figures 5.74 and 5.75 along with the corresponding peak powers along time in Figure 5.73(b). They show the power and Doppler velocity as different values of diagonal loading are applied. When the diagonal loading is 10^2, most of the power have values near the background noise level while the corresponding Doppler velocities are generally poorly estimated with values that are approximately above 3.0 m s^{-1}.

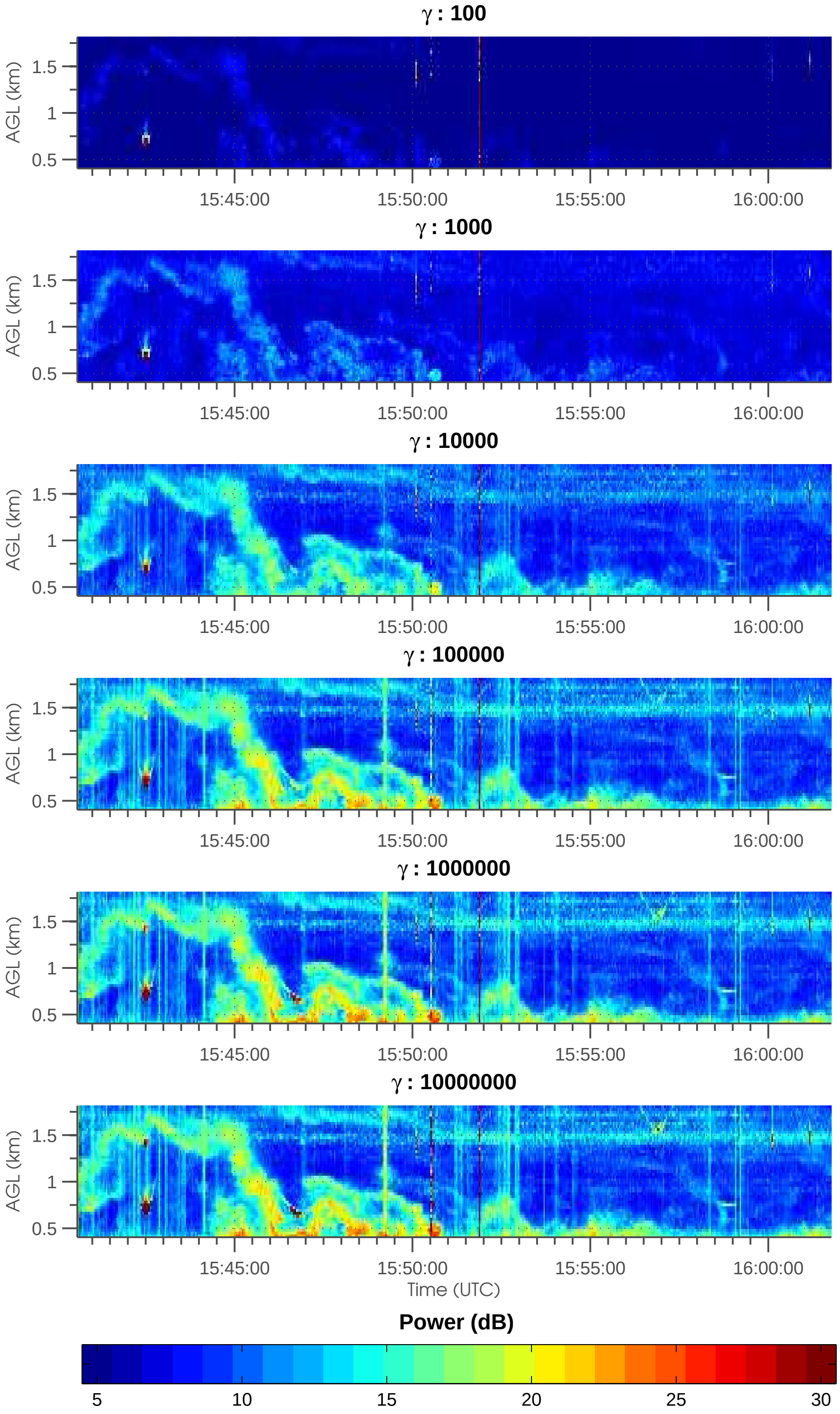

Figure 5.71: Power obtained of the combined signal for above surface scattering after applying MVDR with a dwell time of eight samples. Diagonal loading ranging from 10^2-10^8 was used to obtain the results. The results show that with increasing use of aggressive loading, clutter is first removed then correlation is introduced to reduce the combined power.

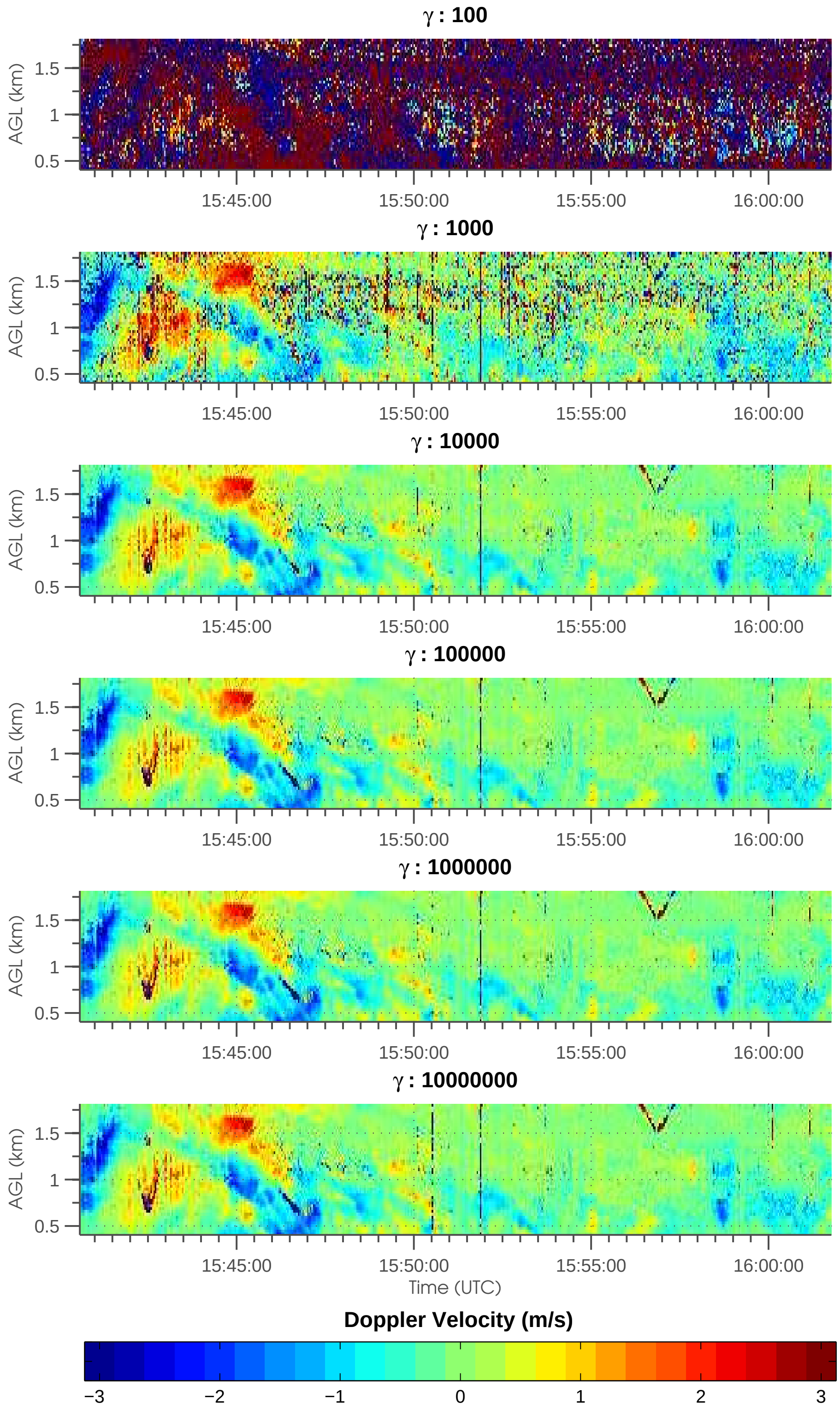

Figure 5.72: Same as Figure 5.71, except for Doppler velocity.

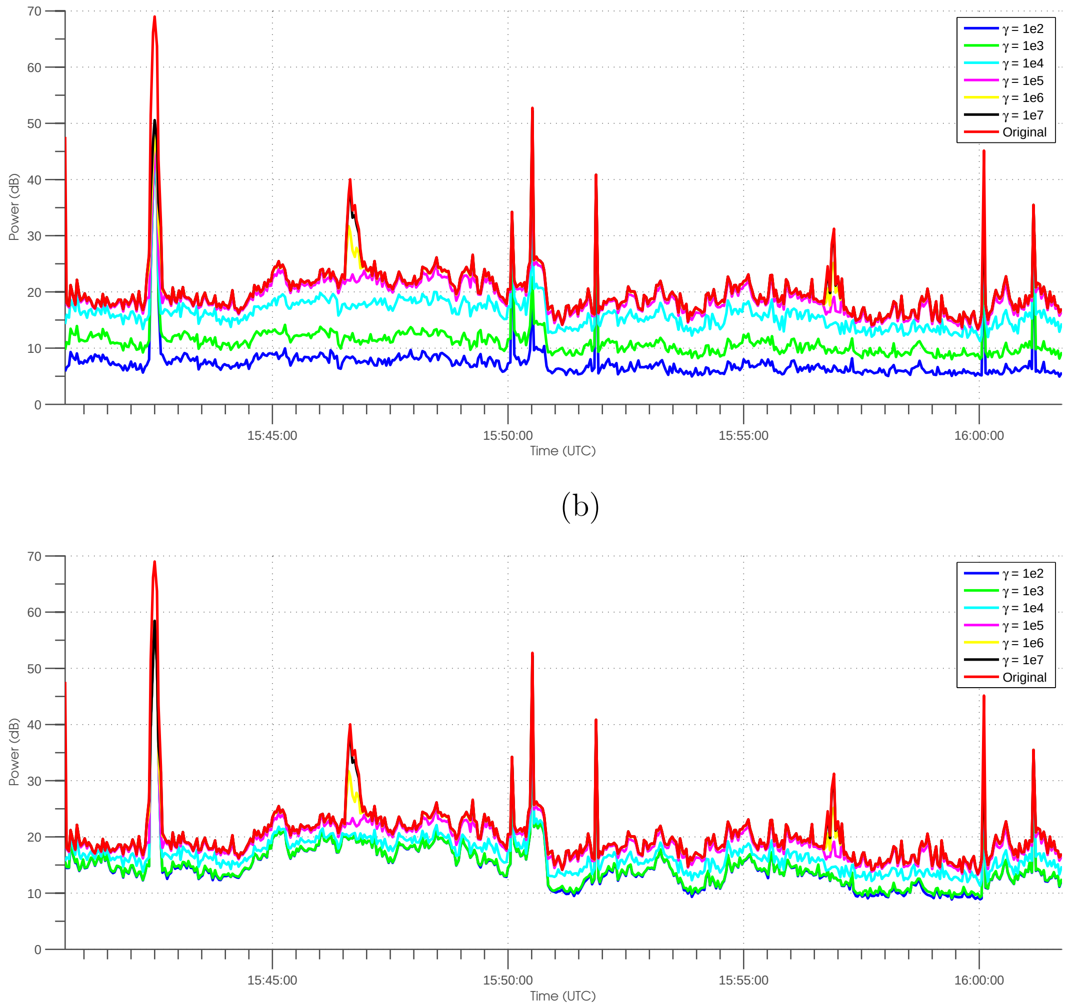

(a)

(b)

Figure 5.73: Temporal evolution of peak power obtained using (a) MVDR and (b) STSP_1. The peak power is obtained by taking the maximum value of a vertical slice. The results show the attenuation of the clutter and the preservation of the clutter signal when the diagonal loading is varied from 10^2-10^7.

While the estimates of the Doppler velocity improve when a diagonal loading of 10^3 is used, the corresponding estimates of the power are still significantly biased below the expected background level where weather is observed. With further increases of the diagonal loading, both the estimates of the power and Doppler velocity background weather continue to improve. The difference between the retrieved power and the background weather becomes significantly small when a diagonal loading of 10^5 is used and the power observed where the clutter is located is approximately the background weather power. As the diagonal loading is increased further from 10^5 to 10^7, the estimate of the background weather is not changed, however the attenuation of the moving clutter is now diminished.

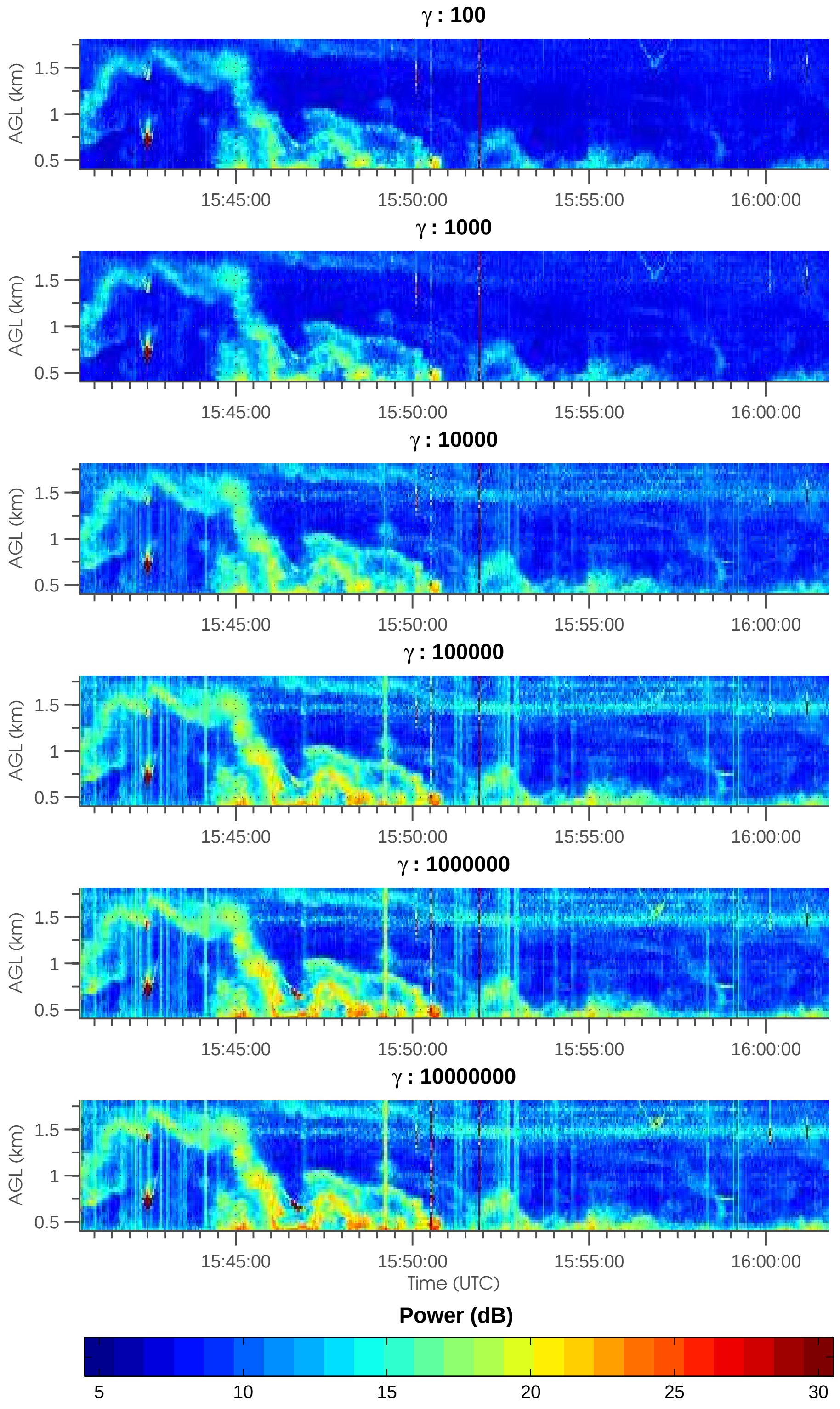

Figure 5.74: Same as Figure 5.71, except for $STSP_1$.

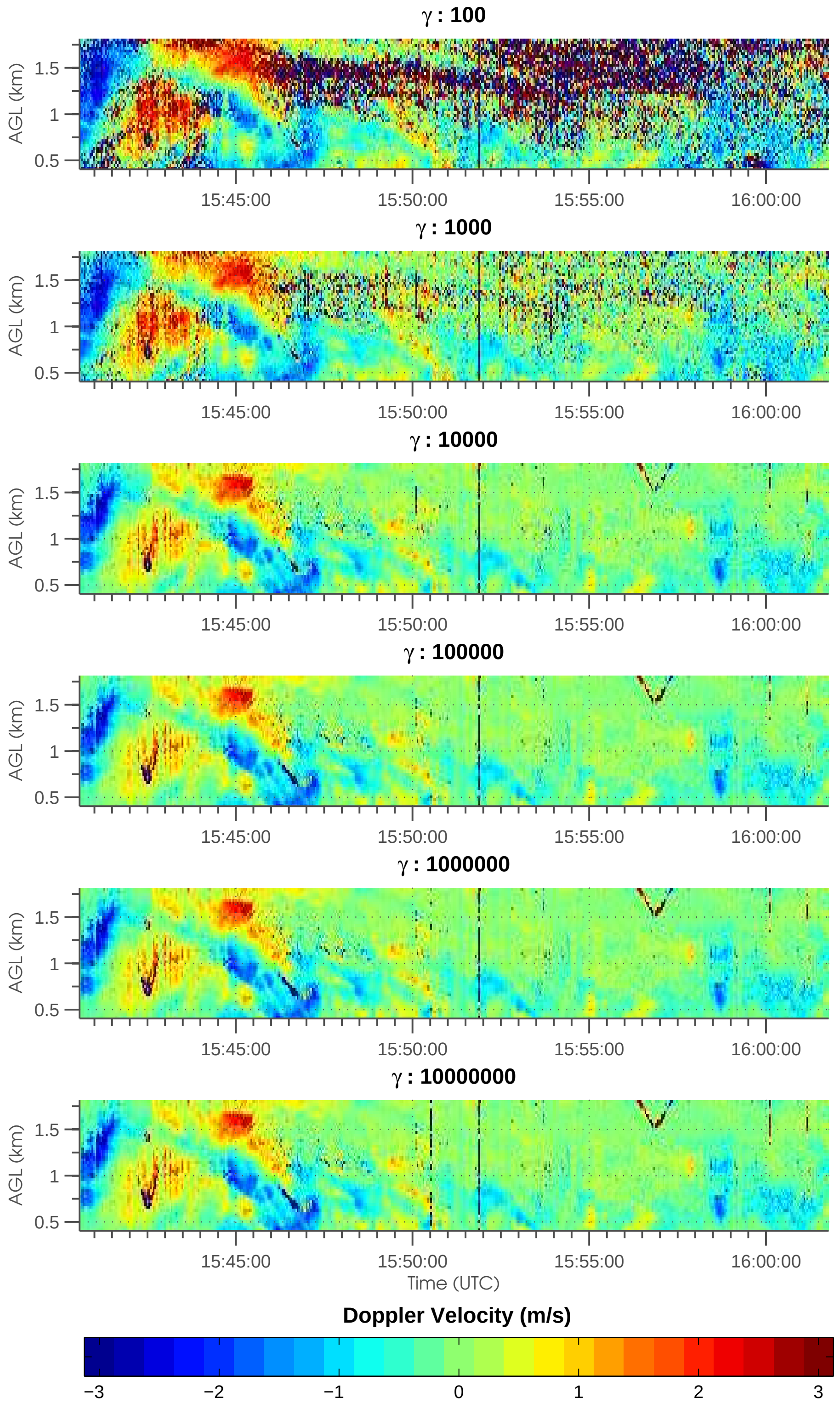
γ : 100

γ : 1000

γ : 10000

γ : 100000

γ : 1000000

γ : 10000000

Figure 5.75: Same as Figure 5.72, except for STSP_1.

5.4.2 Effects of Dwell Time

The performance of spatial filtering to mitigate moving clutter is again examined. In this case, the dwell time is varied from two to 32 samples along with other parameters listed in Table 5.17.

Table 5.17: Parameters Used in Varying Dwell Time

Parameter	Value
SNR	3.4 dB
CSR	33.6 dB
NPTS	**2 — 64**
γ	10^3
σ_v	variable

For time series signals with moving clutters processed using the above parameters and MVDR, the results are plotted in Figures 5.76 and 5.77, along with the temporal evolution in Figure 5.78(a). The results show a general improvement of the retrieved power and Doppler velocity as longer dwell times are used. When a dwell time of two samples is used, the power is significantly small with values that are slightly above the noise floor and corresponding Doppler velocities with magnitudes of about 3.0 m s^{-1}. While a small power is always desired at the clutter locations, these values are also observed where weather is located. In these regions, the values inaccurately represent the weather scatterers and are undesired. With longer duration, estimates of power and Doppler velocities of the weather scatterers improve as its magnitude better matches the expected values of weather scatterers.

Results of the processed data obtained using STSP_1 are plotted in Figures 5.79 and 5.80 along with the temporal evolution in Figure 5.78(b). The results similarly show a general improvement of the estimated power and Doppler velocity of the weather scatterers as longer dwell times are used. Additionally, they show that a steady state of the background weather is reached using only 16 samples as compared to the results obtained using MVDR, which requires 64 samples. In particular, the difference is relatively small between the steady state and the background weather powers. Assuming the background profile is the true field where only weather is

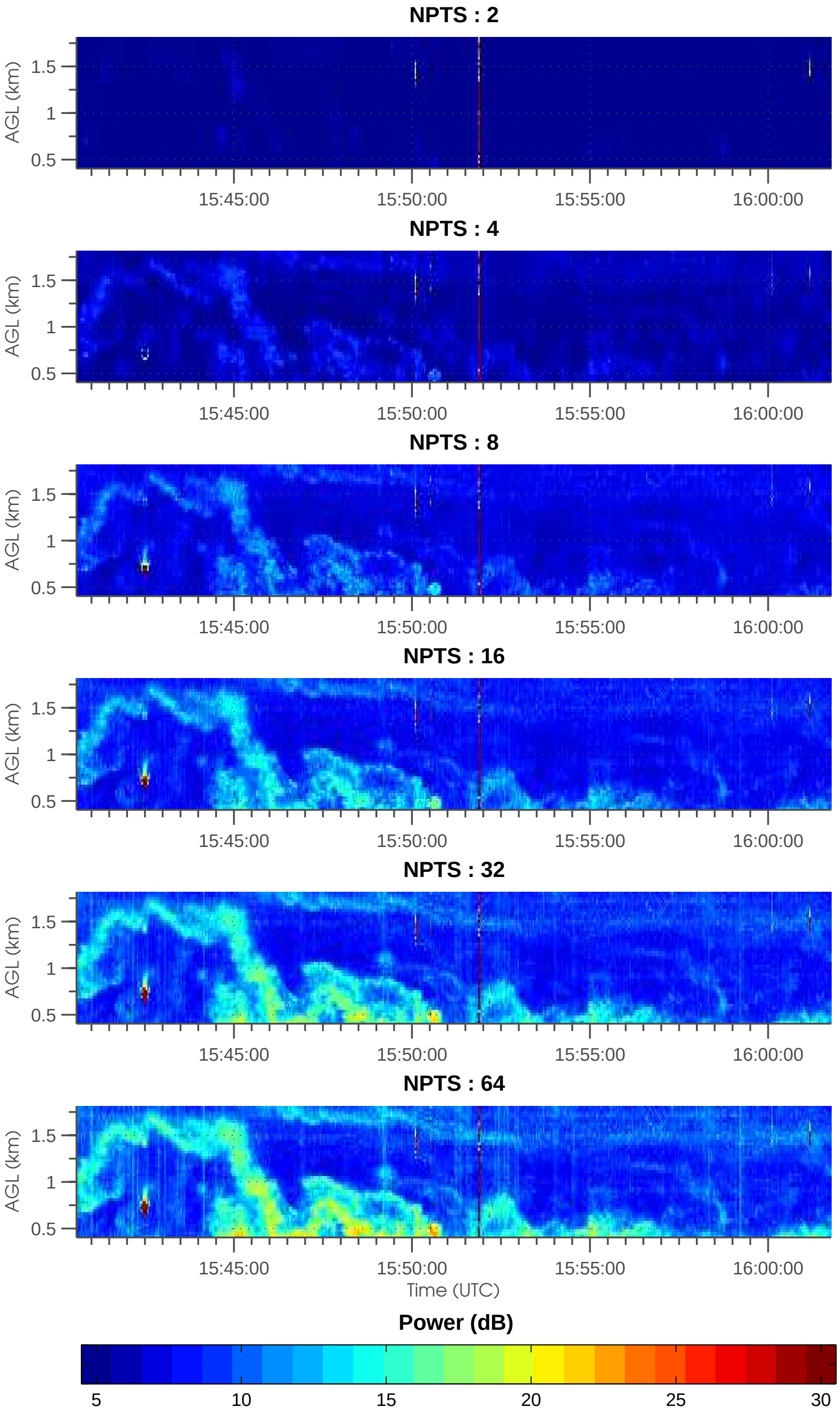

Figure 5.76: Power obtained of the combined signal for above surface scattering after applying MVDR with a diagonal loading of 10^3. A dwell time ranging from 2-32 samples was used to obtain the results. Based on the results, the estimate power of the weather signal improves with dwell time.

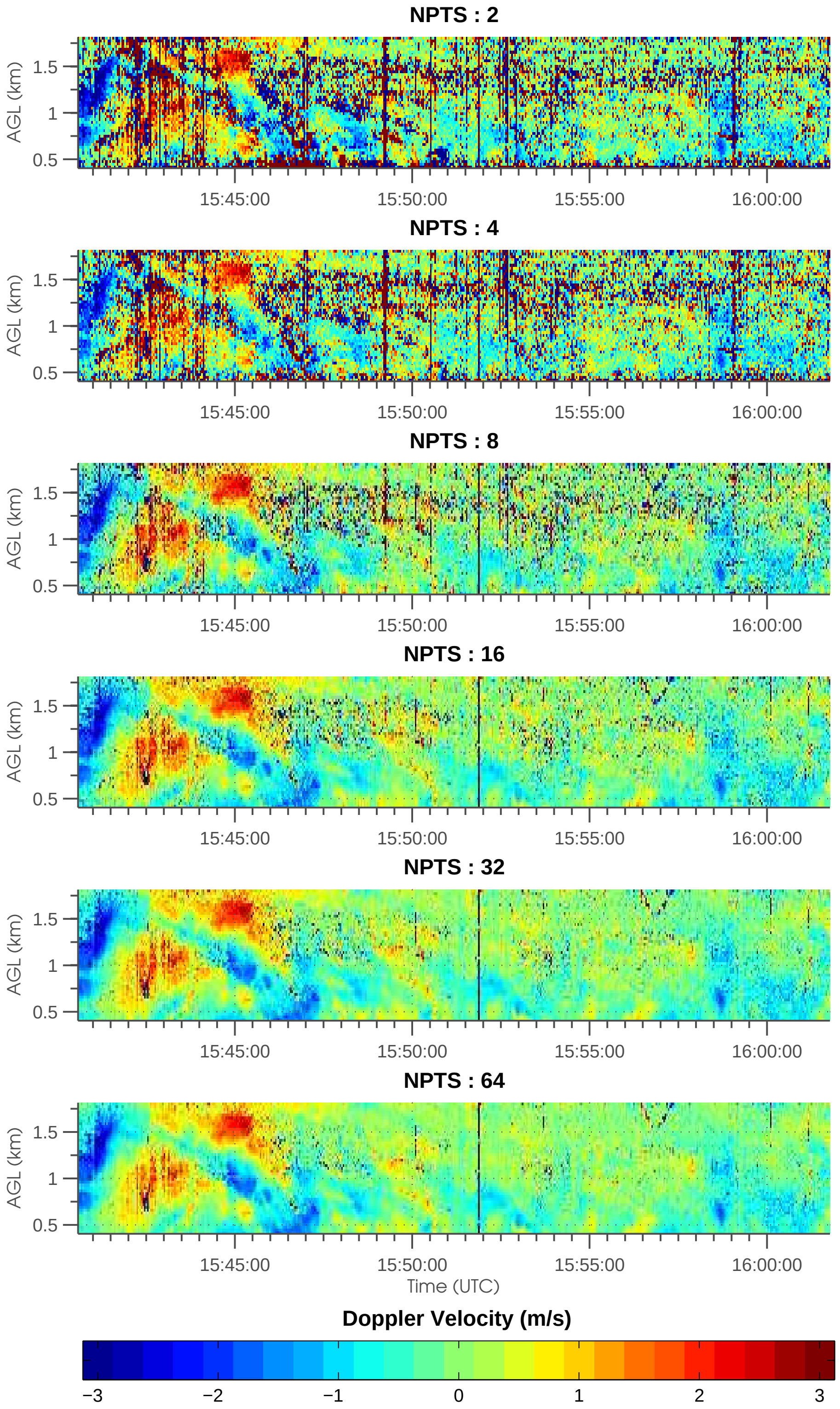

Figure 5.77: Same as Figure 5.76, except for Doppler velocity.

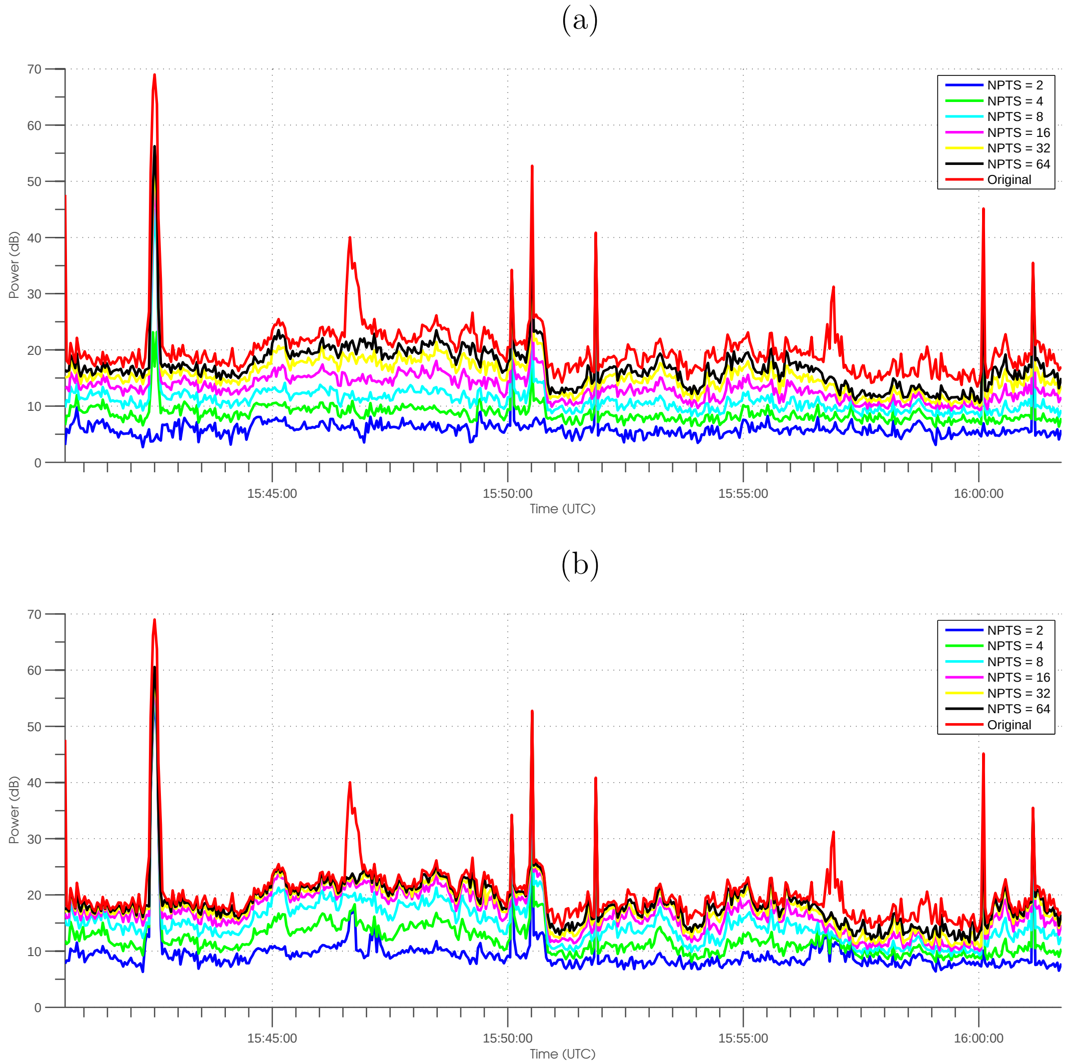

Figure 5.78: Temporal evolution of peak power obtained using (a) MVDR and (b) STSP_1. The peak power is obtained by taking the maximum value of a vertical slice. The results show the attenuation of the clutter and the preservation of the clutter signal when the sample size is varied from 2-64 samples.

located, the use of STSP$_1$ produces a relatively insignificant bias of the estimated power.

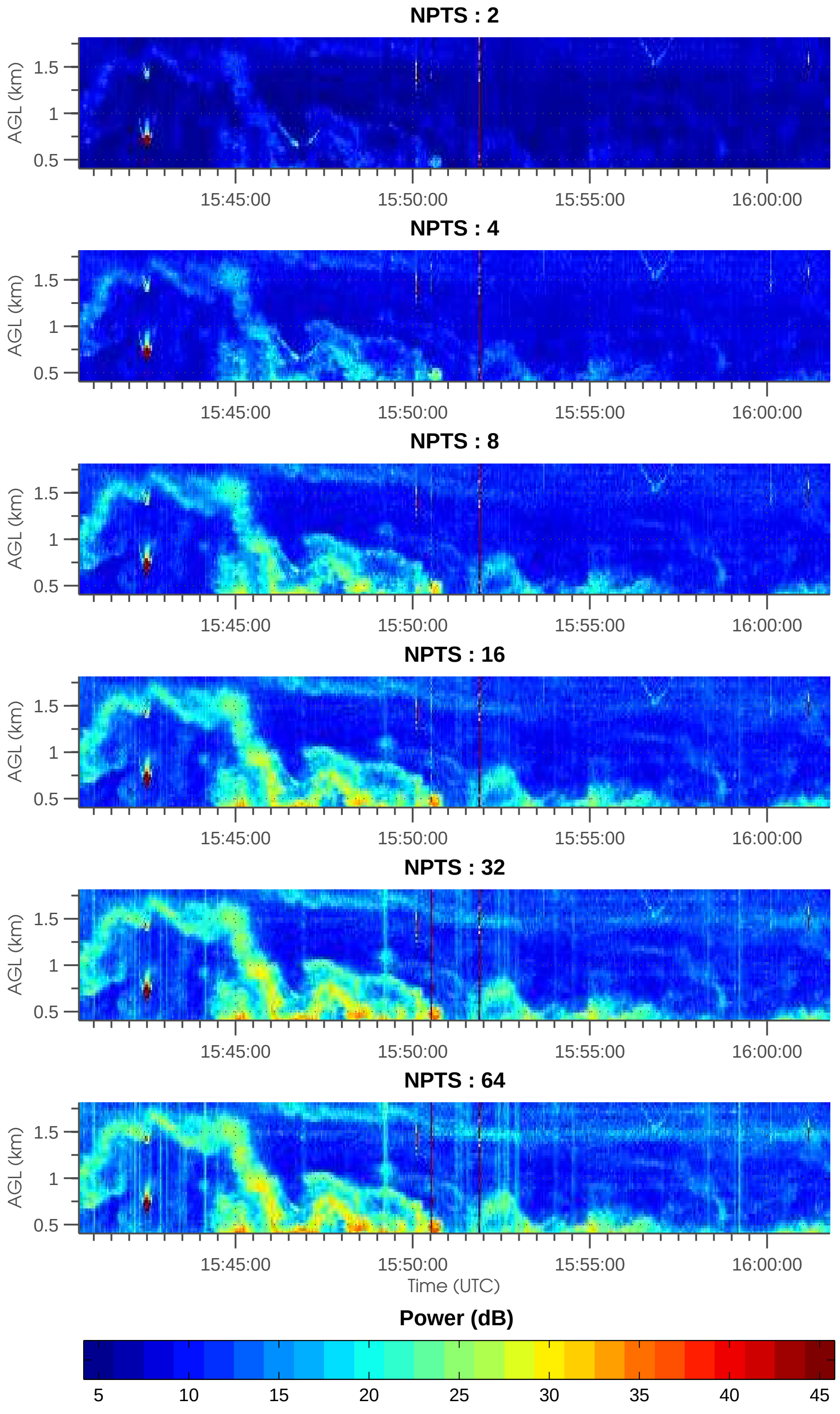
NPTS : 2

NPTS : 4

NPTS : 8

NPTS : 16

NPTS : 32

NPTS : 64

Power (dB)

Figure 5.79: Same as Figure 5.76, except for STSP$_1$.

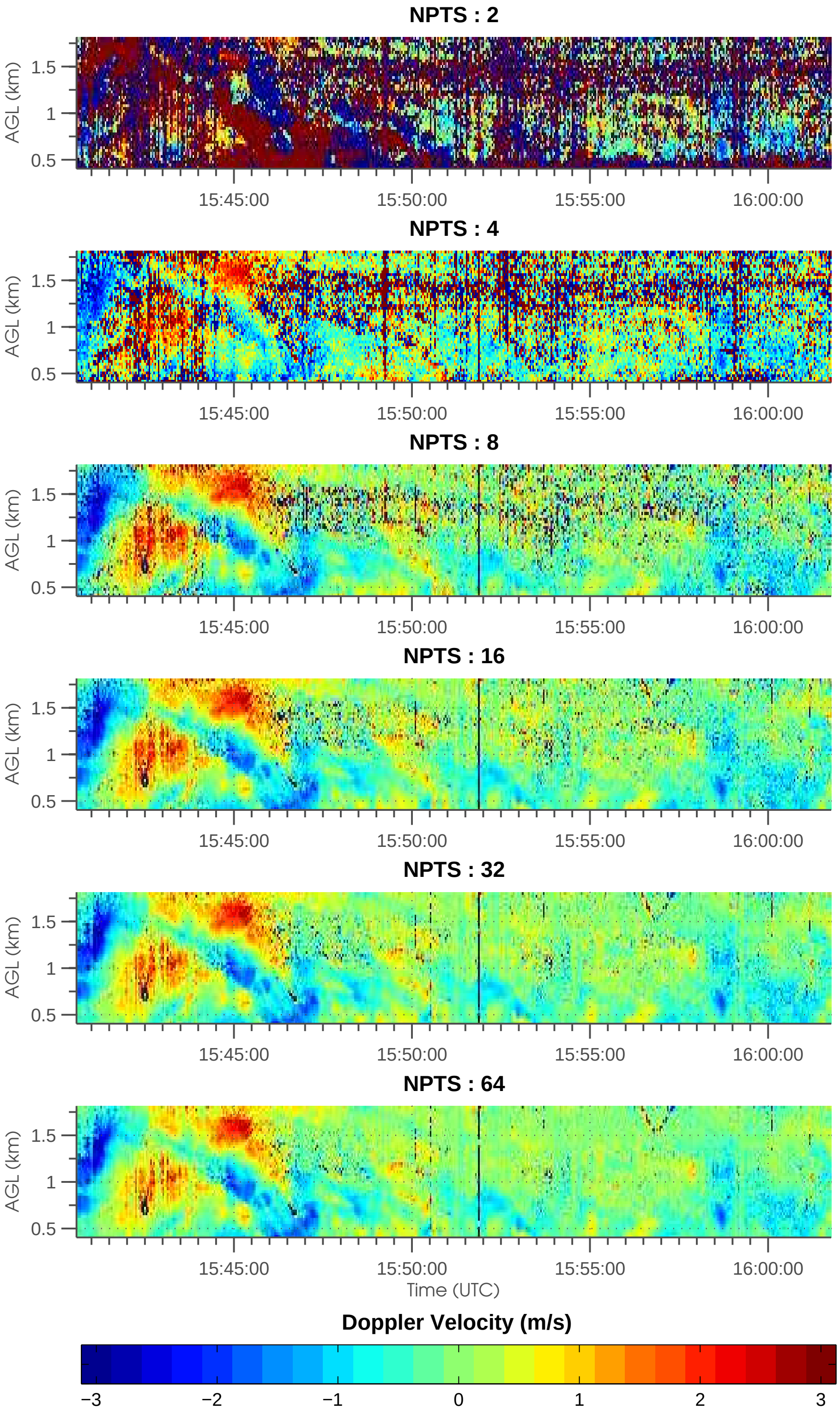

Figure 5.80: Same as Figure 5.77, except for STSP$_1$.

Chapter 6

Conclusions and Suggestions for Future Studies

The motivation of this study was to examine spatial filtering and its capability to remove clutter contamination in a weather radar environment. The impacts caused by both quasi-stationary and non-stationary clutter sources are pertinent in this work and were examined for changes to parameters such as *dwell time*, *relative clutter position and characteristics*, and *adaptive filtering approaches.* The primary catalyst of this study is the impending use of phased array radars, which was discussed as a means for resolving some of the limitations imposed by mechanically steered and fixed radiation pattern radars, to replace the aging NEXRAD network (Weber et al. 2007; Zrnić et al. 2007) as operational tools for monitoring the weather. Currently, this technology is being tested in Norman, Oklahoma with the NWRT PAR (Forsyth et al. 2007) in the most basic setup of only rapid beam steering. However, a multichannel receiver for this radar that would provide real-time access to six auxiliary elements (Yeary et al. 2008) and allow for application of clutter filtering is currently in development. With this in mind, the analyses made in this study will be useful for such future research and development.

6.1 Conclusions

Spatial clutter filtering was applied to a pre-determined array setup and the performance of the clutter filter was obtained specifically for the simulated scattering conditions. The results of a comprehensive set of simulations and validations showed that these algorithms could mitigate the clutter contamination significantly but at the price of undesired mainlobe distortion under some limited cases. However, the results also showed that:

- *Correlated Combined Signal:* When a short dwell time with low number of samples was used (approximately less than twice the number of elements), the output signal can be correlated and the combined power may be reduced. However, the individual components that are observed in the output signal of the weather and clutter can have powers that are much higher. They are, unfortunately, correlated and out of phase, and when added result in a combined signal with smaller power. But, by examining only the combined signal, the effects of the weather and clutter power may be masked.

  Two approaches have been shown that can be used to reduce the effects of a correlated combined signal. The first approach is to reduce the adaptability of the auxiliary array, which can be achieved by introducing a larger diagonal loading before calculating the inverse of the correlation matrix. This procedure results in a set of filter weights with a smaller magnitude. However, it reduces the adaptability of the clutter filter and can result in a residual clutter signal with more power. The second approach is to limit the adaptability of the auxiliary array, which can be achieved by forcing the clutter filter to adapt only to the clutter subspace. In the simulations, the clutter subspace was not known, however and was assumed to be the eigensubspace with the largest eigenvalue. While this subspace may not truly represent only the clutter signal, it is a reasonable approximation when the clutter-to-signal ratio is high. The results of the simulations showed that an increased power in the combined signal was obtained using this approach.

- *Quasi-Stationary Clutter:* Ground clutter was simulated with a plane of scatterers located at the ground. The statistics of the covariance matrix of the clutter is more accurately described when the dwell time is longer. However, the clutter filter may not perform well in this situation. The main reason is the number of degrees of freedom of the clutter filter is equal to the number of sidelobe canceling elements. With a long dwell time, the clutter field observed by the sidelobe canceler must match that observed by the main array to significantly mitigate the clutter. Since the clutter field is a collection of scatterers along the ground plane and the main array is configured differently than the auxiliary array, there may not be enough degrees of freedom in the auxiliary array to match the observed clutter statistics in the main array when the dwell time is long. As a result, it may not be possible to remove all of the clutter. The optimal solution in these cases is a set of filter weights that produces the minimum power. To allow for the clutter filter to perform optimally, a shorter dwell time should be used.

- *Non-Stationary Clutter:* In contrast to ground clutter, the performance of filtering moving clutter will improve with dwell time if the target is localized. Assuming that the number of moving targets is less than the number of auxiliary elements, there is a sufficient amount of freedom that could be used to match the gains of the auxiliary elements to the gain of the main array at the clutter positions. With increasing dwell time, the auxiliary array can better localize the targets as the estimate of the covariance matrix of the clutter becomes more accurate. The result is an improved match of the gains of the auxiliary array to the main array at the clutter positions. However, a possible upper limit of the dwell time is limited by the temporal statistics of the weather signal.

- *Advantages of MSC:* The multiple-sidelobe-canceling technique is extremely robust and useful in real-life application and has three advantages that can be explicitly stated. The first is that it produces the maximum possible attenuation that can be obtained. The attenuation obtained by other spatial clutter filtering techniques is always larger due to their inherent spatial constraint. Additionally, the weights of the MSC spatial filter can be used to obtain the weights of other spatial filtering techniques through a matrix transformation. This implies that the solution of the other spatial filters are embedded in the solution obtained of the MSC spatial filter. Moreover, the filter weights of the MSC was obtained without using a steering vector. In real life, the gains and positions of each antenna may not be known, and this simplicity can be exploited.

6.2 Suggestions for Future Studies

There are still some promising and intriguing problems of clutter filtering with phased arrays in the weather radar environment as well as some fundamental problems that are predicted of future adaptive arrays with many elements:

- *Real Application to a Weather Radar:* While the results showed that clutter filtering could be successfully applied to attenuate ground and moving clutter using the Turbulent Eddy Profiler, the spatial filters were validated only with real data obtained from a vertically pointed radar. As a result, the assessment of clutter filtering with real life data has not yet been achieved when the clutter is located near the mainlobe. As observed in the simulations, it is expected that the shape of the mainlobe will be compromised in this situation, however this effect has not yet been verified with real data. But with the multi-channel receiver being developed to access the auxiliary elements that are available in National Weather Radar Testbed phased array radar, the study of this effect can be obtained in the near future.

- *Clutter Subspace Characterization:* In the subspace tracking spatial projection technique, the clutter subspace was assumed to be one of the eigenvector obtained using eigenvalue decomposition. This is a fairly good approximation that can be used for any type of clutter when the clutter-to-signal ratio is high. In contrast, this assumption can fail when the clutter-to-signal ratio becomes smaller. However, when the clutter field is stationary, its spatial distribution and clutter statistics may be constant. As a result, a preliminary assessment of the clutter field can be made and be used as a projection of the clutter eigen-subspace. This eliminates the need for using eigenvalue decomposition on all the received signals and can be used even when the clutter-to-signal ratio is low.
- *Reduced-Rank Fully Adaptive Canceling:* As was suggested in the conclusion, a reduced-rank beamformer will be necessary for an adaptive array with many elements that employs a short-dwell time with low number of samples. This is because the combined power will be biased unless a large diagonal loading is used. Unfortunately, this reduces the adaptability and defeats the purpose of using an adaptive array. Additionally, since the combined power is related to precipitation rate, the bias in the combined signal may become a limiting factor of adaptive phased array that are used to observe the weather. As a result, a study will be needed to investigate the optimal dwell time for variation in clutter rejection and weather signal bias. Based on the simulated results obtained in this study, the optimal dwell time depends many variables of which the main ones are the illuminated field and the number of antenna elements used.

Bibliography

Ahrens, C., N. Horne, and R. Alvelais, 2001: *Essentials of Meteorology : An Invitation to the Atmosphere*. Brooks/Cole.

Applebaum, S., 1976: Adaptive Arrays. *IEEE Trans. Antennas Propag.*, **AP-24 (5)**, 385–398.

Atlas, D., (Ed.) , 1990: *Radar in Meteorology*. Amer. Meteor. Soc., Boston, MA.

Bachmann, S., 2008: Phase-Base Clutter Identification in Spectra of Weather Radar Signals. *IEEE Geosci. Remote Sens. Lett.*, **5 (3)**, 487–491.

Bachmann, S. and D. Zrnić, 2008: Suppression of Clutter Residue in Weather Radar Reveals Birds' Corridors Over Urban Area. *IEEE Geo. Rem. Sens. Let.*, **5 (2)**, 128–132.

Balanis, C., 2005: *Antenna Theory Analysis and Design*. Wiley-Interscience, New Jersey.

Balsley, B., W. Ecklund, D. Carter, and P. Johnston, 1980: The MST Radar at Poker Flat, Alaska. *Radio Sci.*, **15 (2)**, 213–223.

Balsley, B. and K. Gage, 1980: The MST Radar Technique: Potential for Middle Atmospheric Studies. *Pure Appl. Geophys.*, **118 (1-2)**, 452–493.

Battan, L., 1962: *Radar Observes the Weather*. A DoubleDay Anchor Original, Garden City, New York.

Beverage, H., 1921: Radio Receiving System. U.S. Patent 1381089.

Bhattacharyya, A., 2006: *Phased Array Antennas: Floquet Analysis, Synthesis, BFNs, and Active Array Systems*. Wiley-Interscience, New Jersey.

Bigler, S., P. Hexter, Jr, and F. Wells, 1962: The Radar Program of the U.S. Weather Bureau. *Bull. Amer. Meteor. Soc.*, **43 (11)**, 591–603.

Billetter, D., 1989: *Multifunction Array Radar*. Artech House Inc, Mass.

Billingsley, J., 2002: *Low-Angle Radar Land Clutter Measurements and Empirical Models*. William Andrew Pub., Norwich, N.Y.

Brookner, E., 2002: Phased Array Radars - Past, Present, and Future. *2002 International Radar Conference*, London, UK.

Brookner, E., 2008: Phased Array and Radar Astounding Breakthroughs - an Update. *2008 IEEE Radar Conference*, Rome, Italy, IEEE, 6.

Brown, R. and J. Lewis, 2005: Path to NEXRAD: Doppler Radar Development at the National Severe Storms Laboratory. *Bull. Amer. Meteor. Soc.*, **86 (10)**, 1459–1470.

Capon, J., 1969: High-Resolution Frequency-Wavenumber Spectrum Analysis. *Proc. IEEE*, **57**, 1408–1419.

Capsoni, C. and M. D'Amico, 1998: A Physically Based Radar Simulator. *J. Atmos. Oceanic. Technol.*, **15 (2)**, 593–598.

Chadwick, R. and E. Gossard, 1983: Radar Remote Sensing of the Clear Atmosphere - Review and Applications. *Proc. IEEE*, **71 (6)**, 738–753.

Cheong, B., M. Hoffman, and R. Palmer, 2004: Efficient Atmospheric Simulation for High-Resolution Radar Imaging Applications. *J. Atmos. Oceanic. Technol.*, **21**, 374–378.

Cheong, B., M. Hoffman, R. Palmer, S. Frasier, and F. Lopez-Dekker, 2006: Phased-Array Design for Biological Clutter Rejection: Simulation and Experimental Validation. *J. Atmos. Oceanic. Technol.*, **23 (4)**, 585–598.

Cheong, B., R. Palmer, and M. Xue, 2008: A Time-Series Weather Radar Simulator Based on High-Resolution Atmospheric Models. *J. Atmos. Oceanic. Technol.*, **25 (22)**, 230–243.

Cichon, D. and W. Wiesbeck, 1995: The Heinrich Hertz Wireless Experiments at Karlsruhe in the View of Modern Communication. *International Conference on 100 Years of Radio*, London, 1–6.

Cooley, J. and J. Tukey, 1965: An Algorithm for the Machine Calculation of Complex Fourier Series. *Math Comp.*, **19**, 297–301.

Cornman, L., R. Goodrich, C. Morse, and W. Ecklund, 1998: A fuzzy logic method for improved moment estimation from Doppler spectra. *J. Atmos. Oceanic. Technol.*, **15**, 1287–1305.

Curtis, C., 2009: Exploring the Capabilities of the Agile Beam Phased Array Weather Radar. Ph.D. thesis, University of Oklahoma.

Czechowsky, P., J. Klostermeyer, J. Rottger, R. Ruster, G. Schmidt, and R. Woodman, 1976: The SOUSY-VHF-Radar for Tropo-, Strato- and Mesospheric Sounding. *17th Radar Meteorology Conf.*, Seattle, WA, Amer. Meteor. Soc., 349–353.

Doviak, R. and D. Zrnić, 1985: Sitting of Doppler Weather Radars to Shield Ground Targets. *IEEE Trans. Antennas Propag.*, **AP-33 (7)**, 685–689.

Doviak, R. and D. Zrnić, 1993: *Doppler Radar and Weather Observations.* Academic Press, San Diego.

Durden, S., E. Im, F. Li, R. Girard, and K. Pak, 2001: Surface Clutter Due to Antenna Sidelobes for Spaceborne Atmospheric Radar. *IEEE Trans. Geosci. Remote Sens.*, **39 (9)**, 1916–1921.

Ellingson, S. and G. Hampson, 2002: A Subspace-Tracking Approach to Interference Nulling for Phased Array-Based Radio Telescope. *IEEE Trans. Antennas Propag.*, **50 (1)**, 25–30.

Forsyth, D., et al., 2002: The National Weather Radar Testbed (Phased-Array). *Preprints, 18th International Conference on Interactive Information and Processing Systems (IIPS)*, Orlando, FL, Amer. Meteor. Soc., 140–141.

Forsyth, D., et al., 2007: Update on The National Weather Radar Testbed (Phased-Array). *23rd Conference on IIPS*, San Antonio, TX, Amer. Meteor. Soc.

Forsyth, D., et al., 2008: Another Update on the National Weather Radar Testbed (Phased-Array. *The 24th Conference on Interactive Information Processing Systems (IIPS) for Meteorology, Oceanography, and Hydrology*, New Orleans, LA, Amer. Meteor. Soc., 9A.1.

Fowler, C., 1998: Old Radar Types Never Die; They just Phased Array or... 55 Years of Trying to Avoid Mechanical Scan. *IEEE Trans. Aerosp. Electron. Syst. Mag.*, **13 (9)**, 24A–24L.

Friis, H., 1925: A New Directional Receiving System. *Proc. IRE*, **13 (6)**, 685–707.

Friis, H. and C. Feldman, 1937: A Multiple Unit Steerable Antenna for Short-Wave Reception. *Proc. IRE*, **25 (7)**, 841–917.

Fukao, S., 2007: Recent Advances in Atmospheric Radar Study. *J. Meteor. Soc. Japan*, **85B**, 215–239.

Fukao, S., S. Kato, T. Aso, M. Sasada, and T. Makihira, 1980: Middle and Upper Atmosphere Radar (MUR) under design in Japan. *Radio Sci.*, **15 (2)**, 225–231.

Gage, K. and B. Balsley, 1978: Doppler Radar Probing of the Clear Atmosphere. *Bull. Amer. Meteor. Soc.*, **59 (9)**, 1074–1093.

Gage, K., C. Williams, and W. Ecklund, 1994: UHF Wind Profilers: A New Tool for Diagnosing Tropical Convective Cloud Systems. *Bull. Amer. Meteor. Soc.*, **75 (12)**, 2289–2294.

Galati, G., (Ed.) , 1993: *Advanced Radar Techniques and Systems.* Peter Peringrinus Ltd., England.

Gray, G., R. Serafin, D. Atlas, R. Rinehart, and J. Boyajian, 1975: Real-time Color Doppler Radar Display. *Bull. Amer. Meteor. Soc.*, **56**, 580–588.

Green, J., J. Warnock, R. Winkler, and T. Van Zandt, 1975: Studies of Winds in the Upper Troposphere with a Sensitive VHF Radar. *Geophys. Res. Lett.*, **2 (1)**, 19–21.

Griffiths, H., L. Vinagre, and W. Lee, 1998: Developments in Radar Waveform Designs. *12th International Conference on Microwaves and Radar*, Krakow, Poland, Vol. 4, 56–76.

Guerlac, H., 1987: *Radar in World War II.* Tomash Publishers, Los Angeles.

Hall, M., L. Barclay, and M. Hewitt, 1996: *Propagation of Radio Waves.* IEEE, U.K.

Hanado, H. and T. Ihara, 1992: Evaluation of Surface Clutter for the Design of the TRMM Spaceborne Radar. *IEEE Trans. Geosci. Remote Sens.*, **30 (3)**, 444–453.

Harper, R. and W. Gordon, 1980: A Review of Radar Studies of the Middle Atmosphere. *Radio Sci.*, **15 (2)**, 195–211.

Harris, F., 1978: On the Use of Windows for Harmonic Analysis with the Discrete Fourier Transform. *Proc. IEEE*, **66 (1)**, 51–83.

Hashiguchi, H., S. Fukao, Y. Moritani, T. Wakayama, and S. Wantanbe, 2004: A Lower Troposphere Radar: 1.3-GHz Active Phased-Array Type Wind Profiler with RASS. *J. Meteor. Soc. Japan*, **82 (3)**, 915–931.

Haykin, S., 1996: *Adaptive Filter Theory: Third Edition.* Prentice Hall, New Jersey.

Haykin, S., S. Kessler, and B. Currie, 1979: An Experimental Classification of Radar Clutter. *Proc. IEEE*, **67 (2)**, 322–323.

Haykin, S., W. Stehwien, C. Deng, P. Weber, and R. Mann, 1991: Classification of Radar Clutter in an Air Traffic Control Environment. *Proc. IEEE*, **79 (6)**, 742–772.

Hobbs, P., N. Funk, R. Weiss, Sr., J. Locatelli, and K. Biswas, 1985: Evaluation of a 35 GHz Radar for Cloud Physics Research. *J. Atmos. Oceanic. Technol.*, **2**, 35–48.

Hocking, W., 1997: Recent Advances in Radar Instrumentation and Techniques for Studies of the Mesosphere, Stratosphere, and Troposphere. *Radio Sci.*, **32 (6)**, 2241–2270.

Holdsworth, D. and I. Reid, 1995: A Simple Model of Atmospheric Radar Backscatter: Description and Application to the Full Correlation Analysis of Spaced Antenna Data. *Radio Sci.*, **30**, 1263–1280.

Hubbert, J., M. Dixon, S. Ellis, and G. Meymaris, 2009: Weather Radar Ground Clutter, Part I: Identification, Modeling and Simulation. *J. Atmos. Oceanic. Technol.*, in press.

Hyde, G. and K. Perry, 1958: Doppler Phase Difference Integrator. Tech. rep., M.I.T. Tech. Rep.

Im, E., C. Wu, and S. Durden, 2005: Cloud Profiling Radar for the CloudSat Mission. *IEEE Trans. Aerosp. Electron. Syst. Mag.*, **20 (10)**, 15–18.

Isom, B., 2007: Characterization and Mitigation of Wind Turbine Clutter for the WSR-88D Radar Network. M.S. thesis, University of Oklahoma.

Isom, B., et al., 2009: Detailed Observations of Wind Turbine Clutter With Scanning Weather Radars. *J. Atmos. Oceanic. Technol.*, **26 (5)**, 894–910.

Jagodnik, A., L. Novick, and K. Glover, 1975: A Weather Radar Scan Converter/Color Display. *16th Radar Meteor. Conf.*, Houston, TX, Amer. Meteor. Soc., 14–20.

Janssen, L. and G. Van der Spek, 1985: The Shape of Doppler Spectra From Precipitation. *IEEE Trans. Aerosp. Electron. Syst.*, **AES-21**, 208–219.

Johnson, D. and D. Dudgeon, 1993: *Array Signal Processing: Concepts and Techniques*. Prentice Hall, New Jersey.

Jordan, J., R. Lataitis, and D. Carter, 1997: Removing Ground and Intermittent Clutter Contamination from Wind Profiler Signals Using Wavelet Transforms. *J. Atmos. Oceanic. Technol.*, **14 (6)**, 1280–1297.

Kamio, K. and T. Sato, 2003: An Adaptive Sidelobe Cancellation Algorithm for High-Gain Antenna Arrays. *Trans. Inst. Electron. Inf. Commun. Eng. B*, **J86-B (5)**, 790–797.

Kay, S., 1988: *Modern Spectral Estimation: Theory and Application*. Prentice Hall.

Kollias, P., E. Clouthiaux, M. Miller, and B. Albrecht, 2007: Millimeter-Wavelength Radars: New Frontier in Atmospheric Cloud and Precipitation Research. *Bull. Amer. Meteor. Soc.*, **88 (10)**, 1608–1624.

Kropfli, R., 1981: A Review of Microwave Radar Observations in the Planetary Boundary Layer. *Atmos. Technol.*, **13**, 87–97.

Laws, J. and D. Parsons, 1943: The Relationship of Raindrop Size to Intensity. *Trans. Am. Geophys. Union*, **24 (452-460)**.

Lhermitte, R., 1987: A 94-GHz Doppler Radar for Cloud Observations. *J. Atmos. Oceanic. Technol.*, **4**, 36–48.

Long, M., 2001: *Radar Reflectivity of Land and Sea*. Artech House Inc, Boston, MA.

Lutgens, K., E. Tarbuck, and D. Tasa, 1979: *The Atmosphere: An Introduction to Meteorology*. Englewood Cliffs, New Jersey.

Mailloux, R., 2005: *Phased Array Antenna Handbook*. Artech House Inc, Boston, MA.

Manolakis, D., V. Ingle, and S. Kogon, 2000: *Statistical and Adaptive Signal Processing: Spectral Estimation, Signal Modeling, Adaptive Filtering and Array Processing*. McGraw-Hill, Boston, MA.

Martin, W. and A. Shapiro, 2007: Discrimination of Bird and Insect Radar Echoes in Clear Air Using High-Resolution Radars. *J. Atmos. Oceanic. Technol.*, **24 (7)**, 1215–1230.

Martner, B., et al., 1993: An Evaluation of Wind Profiler, RASS, and Microwave Radiometer Performance. *Bull. Amer. Meteor. Soc.*, **74 (4)**, 599–613.

Matlzer, C., 2002: MATLAB Functions for Mie Scattering and Absorption. Tech. Rep. 2002-08, Institut fur Angewandte Physik.

Mead, J., G. Hopcraft, S. Frasier, B. Pollard, C. Cherry, D. Schaubert, and R. McIntosh, 1998: A Volume-Imaging Radar Wind Profiler for Atmospheric Boundary Layer Turbulence Studies. *J. Atmos. Oceanic. Technol.*, **14 (4)**, 849–859.

Mead, J., A. Pazmany, S. Sekelsky, and R. McIntosh, 1994: Millimeter-Wave Radars for Remotely Sensing Clouds and Precipitation. *Proc. IEEE*, **82 (12)**, 1891–1906.

Miller, A., J. Thompson, R. Peterson, and D. Haragan, 1983: *Elements of Meteorology*. Charles E. Merrill Publishing Company, Columbus.

Monzingo, R., T. Miller, and W. Thomas, 2004: *Introduction to Adaptive Arrays*. SciTech Publishing, Rayleigh, NC.

Moran, K., B. Martner, M. Post, R. Kropfli, D. Welsh, and K. Widener, 1998: An Unattended Cloud-Profiling Radar for Use in Climate Research. *Bull. Amer. Meteor. Soc.*, **79 (3)**, 443–455.

Morse, C., R. Goodrich, and L. Cornman, 20002: The NIMA Method for Improved Moment Estimation from Doppler Spectra. *J. Atmos. Oceanic. Technol.*, **19**, 274–295.

Naidu, M. and V. Kamaraju, 1996: *High Voltage Engineering*. McGraw-Hill, New York.

National Research Council, 2002: *Weather radar technology beyond NEXRAD*. National Academy Press.

Nelder, J. and R. Mead, 1965: A Simplex Method for Function Minimization. *Comput. J.*, **7**, 308–313.

Nguyen, C., D. Moisseev, and V. Chandrasekar, 2008: A Parametric Time Domain Method for Spectral Moment Estimation and Clutter Mitigation for Weather Radars . *J. Atmos. Oceanic. Technol.*, **25 (1)**, 83–92.

Nicholas, F., 2000: *Advanced Array Systems, Applications and RF TEchnologies*. Academic Press, San Diego.

Oppenheim, A. and R. Schafer, 1989: *Discrete-Time Signal Processing*. Prentice Hall, New Jersey.

Palmer, R., B. Cheong, M. Hoffman, S. Frasier, and F. Lopez-Dekker, 2005: Observations of the Small-Scale Variability of Precipitation Using an Imaging Radar. *J. Atmos. Oceanic. Technol.*, **22**, 1122–1137.

Palmer, R., P. Chilson, and T.-Y. Yu, 1995: Range Imaging Using Frequency Diversity. *Radio Sci.*, **34**, 1485–1496.

Palmer, R., S. Gopalam, T.-Y. Yu, and S. Fukao, 1998: Coherent radar imaging using Capon's method . *Radio Sci.*, **33 (6)**, 1585–1598.

Parker, D. and D. Zimmermann, 2002: Phased Arrays - Part 1: Theory and Architectures. *IEEE Trans. Microw. Theory Tech.*, **50 (3)**, 678–687.

Pasqualucci, F., B. Bartram, R. Kropfli, and W. Moninger, 1983: A Millimeter-Wavelength Dual-Polarization Doppler Radar for Cloud and Precipitation Studies. *J. Climate Appl. Meteor.*, **22**, 758–765.

Pazmany, A., R. McIntosh, R. Kelley, and G. Vali, 1994: An Airborne 95 GHz Dual-Polarized Radar for Cloud Studies. *IEEE Trans. Geo. Rem. Sens.*, **32 (4)**, 731–739.

PopStefanija, I., J. Knorr, P. Buczynski, and B. Bluth, 2005: Advanced Weather Surveillance Algorithms and Techniques Using a Rapid Scanning X-band Radar - First Results. *32nd Conference on Radar Meteorology*, Albuquerque, NM.

Press, W., S. Taukolsky, W. Vetterling, and B. Flannery, 1992: *Numerical Recipes in C.* Cambridge University Press, Cambridge, Massachusetts.

Richards, M., 2005: *Fundamental of Radar Signal Processing.* McGraw-Hill, New York.

Rico-Ramirez, M. and I. Cluckie, 2008: Classification of Ground Clutter and Anomalous Propagation Using Dual-Polarization Weather Radar. *IEEE Trans. Geosci. Remote Sens.*, **46 (7)**, 1892–1904.

Rockney, V. and L. Jay, 1953: The Radar Storm Detection Program of the U.S. Weather Bureau. *Conference in Radio Meteorology*, Austin, TX, X–2.

Rogers, R., W. Ecklund, D. Carter, K. Gage, and S. Ethier, 1993: Research Applications of a Boundary-Layer Wind Profiler. *Bull. Amer. Meteor. Soc.*, **74 (4)**, 567–580.

Rummler, W., 1968: Introduction of a New Estimator for Velocity Spectral Parameters. Tech. Memo MM-68-4121-5, Bell Telephone Laboratories, Whippany, New Jersey.

Rutkowski, W. and A. Fleisher, 1955: R-meter: An Instrument for Measuring Gustiness. Tech. Rep. 24, M.I.T. Weather Radar Research Rep.

Ryzhkov, A., T. Schuur, D. Burgess, P. Heinselman, S. Giangrande, and D. Zrnić, 2005: The Joint Polarization Experiment: Polarimetric Rainfall Measurements and Hydrometeor Classification. *Bull. Amer. Meteor. Soc.*, **86 (6)**, 809–824.

Sarkar, T., R. Mailloux, A. Oliner, M. Salazar-Palma, and D. Sengupta, 2006: *History of Wireless*. John Wiley & Son, New Jersey.

Sato, T. and R. Woodman, 1982: Spectral Parameter Estimation of CAT Radar Echoes in the Presence of Fading Clutter. *Radio Sci.*, **17 (4)**, 817–826.

Sauvageot, H., 1992: *Radar Meteorology*. Artech House Inc, Mass.

Scannlan, M., 1993: Chain Home Radar – A Personal Reminiscence. *GEC Rev*, **8 (3)**, 171–183.

Scharfenberg, K., et al., 2005: The Joint Polarization Experiment: Polarimetric Radar in Forecasting and Warning Decision Making. *Wea. Forecasting*, **20 (5)**, 775–788.

Scudder, R. and W. Sheppard, 1974: AN/SPY-1 Phased-Array Antenna. *Microw. J.*, **17 (5)**, 51–55.

Sekelsky, S., 1995: A 33 GHz and 95 GHz Cloud Profiling Radar System (CPRS): Preliminary Estimates of Particle Size in Precipitation and Cloud. Ph.D. thesis, University of Massachusetts.

Sekine, M., 1996: Weather Radar Clutter and Its Suppression. *IEICE Trans. Commun.*, **E79-B (6)**, 736–743.

Selvan, K., 2007: Engineering Education: Presentation of Maxwell's Equations in Historical Perspective and the Likely Desirable Outcomes. *IEEE Antennas Propag. Mag.*, **40**, 155–160.

Sengupta, D. and T. Sarkar, 2003: Maxwell, Hertz, the Maxwellians, and the Early History of Electromagnetic Waves. *IEEE Antennas Propag. Mag.*, **45 (2)**, 155–160.

Siggia, A. and R. Passarell, Jr., 2004: Gaussian Model Adaptive Processing (GMAP) for Improved Ground Clutter Cancelation and Moment Calculation. *Proc. Eur. Radar Conf.*, 67–73.

Skolnik, M., 1990: *Radar Handbook*. McGraw-Hill, New York.

Skolnik, M., 2001: *Introduction to Radar Systems*. McGraw-Hill, Boston, MA.

Spilhaus, A., 1948: Raindrop Size, Shape, and Falling Speed. *J. Meteorol.*, **5**, 108–110.

Stoica, P. and R. Moses, 2005: *Spectral Analysis of Signals*. Prentice Hall, New Jersey.

Straka, J., D. Zrnić, and A. Ryzhkov, 2000: Bulk Hydrometeor Classification and Quantification Using Polarimetric Radar Data: Synthesis of Relations. *J. Appl. Meteor.*, **39 (8)**, 1341–1372.

Strauch, R., D. Merritt, K. Moran, K. Earnshaw, and D. Van De Kamp, 1984: The Colorado Wind-Profiling Network. *J. Atmos. Oceanic. Technol.*, **1 (1)**, 37–49.

Tang, R. and R. Burns, 1993: *Antenna Engineering Handbook*, chap. Phased Arrays. 3d ed., McGraw-Hill, New York.

Torres, S. and D. Zrnić, 1999: Ground Clutter Canceling with a Regression Filter. *J. Atmos. Oceanic. Technol.*, **16**, 1364–1371.

Torres, S. and D. Zrnić, 2003: Whitening in Range to Improve Weather Radar Spectral Moment Estimates. Part I: Formulation and Simulation. *J. Atmos. Oceanic. Technol.*, **20 (11)**, 1433–1448.

Uda, S., 1926: Wireless Beam of Short Electric Waves. *J. IEE*, 273–282.

van Loon, B., 2005: Radar 101: Celebrating 101 Years of Development. *Proc. IEEE*, **93 (4)**, 844–846.

Van Trees, H., 2002: *Optimum Array Processing: Part IV*. John Wiley & Sons, New York.

Wallace, J. and P. Hobbs, 1977: *Atmospheric Science: An Introductory Survey*. Academic Press, San Diego.

Weber, B., et al., 1990: Preliminary Evaluation of the First NOAA Demonstration Network Wind Profiler. *J. Atmos. Oceanic. Technol.*, **7 (6)**, 909–918.

Weber, M., J.-Y. Cho, J. Herd, J. Flavin, W. Benner, and G. Torok, 2007: The Next-Generation Multimission U.S. Surveillance Radar Network. *Bull. Amer. Meteor. Soc.*, **88 (11)**, 1739–1751.

Whiton, R., P. Smith, S. Bigler, K. Wilk, and A. Harbuck, 1998: History of Operational Use of Weather Radar by U.S. Weather Services. Part I: The Pre-NEXRAD era. *Wea. Forecasting*, **13 (2)**, 219–243.

Widrow, B., P. Mantey, L. Griffiths, and B. Goode, 1967: Adaptive Antenna Systems. *Proc. IEEE*, **55 (12)**, 2143–2159.

Xue, M., K. Droegemeier, V. W. A. Shapiro, K. Brewster, F. Carr, D. Weber, Y. Liu, and D. Wang, 2001: The Advanced Regional Prediction System (ARPS) - A Multi-Scale Nonhydrostatic Atmospheric Simulation and Prediction Model. Part II: Model Physics and Applications. *Meteor. Atmos. Physics.*, **76 (3-4)**, 143–165.

Xue, M., K. Droegemeier, and V. Wong, 2000: The Advanced Regional Prediction System (ARPS) - A Multi-Scale Nonhydrostatic Atmospheric Simulation and Prediction Model. Part I: Model Dynamics and Verification. *Meteor. Atmos. Physics.*, **75 (3-4)**, 161–193.

Yagi, H., 1928: Beam Transmission of Ultra Short Waves. *Proc. IRE*, **16 (715-741)**.

Yeary, M., et al., 2008: Introduction to Multi-Channel Receiver Development for the Realization of Multi-Mission Capabilities at the National Weather Radar Testbed. *24rd Conference on Interactive Information Processing Systems (IIPS)*, New Orleans, LA, 9A.3.

Yu, T., R. Rondinel, and R. Palmer, 2009: Investigation of Non-Gaussian Doppler Spectra Observed by Weather Radar in a Tornadic Supercell. *J. Atmos. Oceanic. Technol.*, **26**, 444–461.

Yu, T.-Y., M. Orescanin, C. Curtis, D. Zrnić, and D. Forsyth, 2007: Beam Multiplexing Using the Phased-Array Weather Radar. *J. Atmos. Oceanic. Technol.*, **24 (4)**, 616–626.

Yu, T.-Y. and R. Palmer, 2001: Atmospheric Radar Imaging Using Multiple-Receiver and Multiple-Frequency Techniques. *Radio Sci.*, **36 (6)**, 1493–1503.

Zrnić, D., 1975: Simulation of Weatherlike Doppler Spectra and Signals. *J. Appl. Meteor.*, **14**, 619–620.

Zrnić, D., 1977: Spectral Moment Estimates from Correlated Pulse Pairs. *IEEE Trans. Aerosp. Electron. Syst.*, **AES-13 (4)**, 344–354.

Zrnić, D., 1979: Estimation of Spectral Moments for Weather Echoes. *IEEE Geo. Rem. Sens. Let.*, **GE-17 (4)**, 113–128.

Zrnić, D. and A. Ryzhkov, 1999: Polarimetry for Weather Surveillance Radars. *Bull. Amer. Meteor. Soc.*, **80 (3)**, 389–406.

Zrnić, D., et al., 2007: Agile-Beam Phased Array Radar For Weather Observations. *Bull. Amer. Meteor. Soc.*, **88 (11)**, 1753–1766.

Appendix A - List Of Symbols

$\mathbf{a}(\theta)$	Steering Vector
$\mathbf{A}(\theta)$	Steering Matrix
A_e	Effective Aperture of Received Antenna
AC	Alternating Current
$AF(\theta)$	Array Factor
c	Speed of Light
C_n^2	Structure Function
D	Diameter
$E_\theta(R)$	Far-Field Electrical Intensity
f	Frequency
f_D	Doppler Frequency
GHz	Gigahertz, 10^9 Hz
Hz	Hertz, unit increment of frequency
$I(t)$	In-phase Signal
K	Kelvin, unit increment of temperature
kW	Kilowatts, 10^3 Watts
l	Path Loss
mb	Millibar, 10^{-3} bar
mm	Millimeter, 10^{-3} meters
MHz	Megahertz, 10^6 Hz
N	Refractivity Factor
$N(D)$	Particle Size Distribution
$\mathbf{P}$	Projection Matrix
P_r	Peak Receive Power
$\mathbf{P}_i$	Projection Matrix created from $\mathbf{U}_i$
$\bar{P}_r$	Average Receive Power
P_t	Peak Transmit Power
$Q(t)$	Quadrature Signal

R	Range
$\mathbf{R}$	Correlation Matrix
$\mathbf{R}^{-1}$	Inverse of Correlation Matrix
T	Temperature
T_s	Interpulse Period
$\mathbf{U}_i$	Eigenvector matrix
$V(mT_s)$	Baseband Time Series Signal
$\mathbf{v}(mT_s)$	Column Vector of Time Series Signals
v_a	Aliasing Velocity
$\mathbf{w}(mT_s)$	Column Vector of Complex Filter Weights
$\mathbf{w}_o(mT_s)$	Optimal Set of Complex Filter Weights
$y(mT_s)$	Output Signal
Z	Volume Reflectivity Factor
ϵ	Permittivity
η	Average Radar Cross-Section Per Unit Volume
λ	Diagonal Loading
μ	Permeability
$\sigma(D)$	Radar Cross Section
$\sigma_e(D)$	Extinction Cross Section
$\triangle V$	Differential Volume
τ	Pulse Duration

Appendix B - List Of Acronyms and Abbreviations

AC	Alternating Current
AF	Array Factor
AMF	Advanced Multi-Frequency
ARPS	Advanced Regional Prediction System
CASA	Collaborative Adaptive Sensing of the Atmosphere
CH	Chain Home
CSR	Clutter-to-Signal Ratio
DC	Direct Current
ESAR	Electronically Steerable Array Radar
FIR	Finite Impulse Response
JPL	Jet Propulsion Laboratory
JPOLE	Joint Polarization Experiment
MSC	Multiple Sidelobe Canceler
MST	Mesosphere-Stratosphere-Troposphere
MU	Middle and Upper
MUSA	Multiple Unit Steerable Antenna
MVDR	Minimum Variance Distortionless Response
NASA	National Aeronautics and Space Administration
NEXRAD	Next-Generation Radar
NSSL	National Severe Storms Laboratory
NPN	NOAA Profiling Network
NPTS	Number of Points
NWRT	National Weather Radar Testbed
NWS	National Weather Service
PTDF	Parametric Time Domain Filtering
PAR	Phased Array Radar
PRT	Pulse Repetition Time

RADAR	Radio-Detection-And-Ranging
SNR	Signal-to-Noise Ratio
ST	Stratosphere-Troposphere
STSP	Subspace Tracking Spatial Projection
STALO	Stable Local Oscillator
TEP	Turbulent Eddy Profiler
TRMM	Tropical Rainfall Measuring Mission
UHF	Ultra High Frequency
ULA	Uniform Linear Array
VHF	Very High Frequency
WSR	Weather Surveillance Radar

Index